Spectropolarimetric analysis of magnetic stars

Alexander John Martin

Doctor of Philosophy

Armagh Observatory &
Astrophysics Group, Keele University.

March 2017

Keele University

Declaration Part 1. To be bound in the thesis

SUBMISSION OF THESIS FOR A RESEARCH DEGREE

Part I. DECLARATION by the candidate for a research degree. To be bound in the thesis

Degree for which thesis being submitted **PhD**

Title of thesis **Spectropolarimetric analysis of magnetic stars**

This thesis contains confidential information and is subject to the protocol set down for the submission and examination of such a thesis.

YES/NO [please delete as appropriate; if YES the box in Part II should be completed]

Date of submission (Date of submission must comply with Regulation 2D)	03/02/2017	Original registration date	01/08/2012
Name of candidate	Alexander John Martin		
Research Institute	EPSAM	Name of Lead Supervisor	Dr Barry Smalley

I certify that:

(a) The thesis being submitted for examination is my own account of my own research
(b) My research has been conducted ethically. Where relevant a letter from the approving body confirming that ethical approval has been given has been bound in the thesis as an Annex
(c) The data and results presented are the genuine data and results actually obtained by me during the conduct of the research
(d) Where I have drawn on the work, ideas and results of others this has been appropriately acknowledged in the thesis
(e) Where any collaboration has taken place with one or more other researchers, I have included within an 'Acknowledgments' section in the thesis a clear statement of their contributions, in line with the relevant statement in the Code of Practice (see Note overleaf).
(f) The greater portion of the work described in the thesis has been undertaken subsequent to my registration for the higher degree for which I am submitting for examination
(g) Where part of the work described in the thesis has previously been incorporated in another thesis submitted by me for a higher degree (if any), this has been identified and acknowledged in the thesis
(h) The thesis submitted is within the required word limit as specified in the Regulations

Total words in submitted thesis (including text and footnotes, but excluding references and appendices) **33899**

Signature of candidate ..... Date 20/2/17

Note
Extract from Code of Practice: If the research degree is set within a broader programme of work involving a group of investigators – particularly if this programme of work predates the candidate's registration – the candidate should provide an explicit statement (in an 'Acknowledgments' section) of the respective roles of the candidate and these other individuals in relevant aspects of the work reported in the thesis. For example, it should make clear, where relevant, the candidate's role in designing the study, developing data collection instruments, collecting primary data, analysing such data, and formulating conclusions from the analysis. Others involved in these aspects of the research should be named, and their contributions relative to that of the candidate should be specified (*this does not apply to the ordinary supervision, only if the supervisor or supervisory team has had greater than usual involvement*).

Abstract

The spectra of Ap and Bp stars show evidence of non-homogenous distributions of chemical elements both vertically and horizontally, along with the presence of large-scale ordered magnetic fields. The atomic diffusion theory in stellar atmospheres explains the presence of the non-homogenous element distributions as a result of the magnetic field's effect on the radiative pressure in the photosphere. Recent modelling of the abundance distributions in Ap and Bp stars has questioned the results determined theoretically. In addition, there has been a debate over the uniqueness and reliability of the results determined using Zeeman/Magnetic Doppler Imaging (Z/MDI). To provide the tools necessary to determine further observational constraints for diffusion theory and to check the uniqueness and reliability of current MDI measurements, this thesis presents the development of two codes: Sparti Simple for the analysis of spectra formed in non-magnetic stellar atmospheres; and Sparti for the analysis of Stokes $IQUV$ profiles formed in magnetic stellar atmospheres.

Before the application of these two codes to observational data, testing was carried out to confirm the functionality and ability to cope with the challenges introduced as a result of the observation of Stokes $IQUV$ profiles.

The analysis of non-magnetic stellar spectra is a first step in the analysis of magnetic stellar spectra and also provides important observational constraints to diffusion theory. The member stars of the cluster NGC6250 were analysed using Sparti Simple as part of a larger collaborative effort to analyse the member stars of a variety of open stellar clusters. A cluster membership analysis of the stars in NGC6250 was performed and the fundamental parameters and photospheric chemical abundances were determined for each of the 19 member stars. Finally, the magnetic roAp star HD24712 and Ap star HD137909 were analysed using Sparti to determine its ability to recover unique and reliable results.

Acknowledgments

I am grateful to have had the opportunity to work with so many people, who have continually offered advice and support throughout my PhD.

I would like to thank my supervisors Dr. Stefano Bagnulo and Dr. Barry Smalley. Our many discussions have been extremely beneficial to my understanding of the challenging topics which are part of this thesis and of course for their many helpful comments on my thesis and paper. Thank you to Dr. Stefano Bagnulo for giving me the opportunity to travel so extensively to enrich my learning experience.

Thank you to Prof. Martin Stift for providing COSSAM and for producing the new code COSSAM SIMPLE. For introducing me to the wonderful world of Ada, and for correcting the layout of my early attempts of learning the language.

Thanks to Dr. Luca Fossati for providing the data for NGC 6250 and for giving me instruction on various techniques to perform chemical abundance analysis and the many, many ways in which it can go wrong.

Thank you to Prof. John Landstreet for allowing me to participate in the survey to search for weak magnetic fields in white dwarf stars and the many discussions during our work together.

Thank you to Prof. Franco Leone for the use of the Serra La Nave facilities and CAOS. For being such a welcoming host and also for providing the grid of ATLAS09 models.

Thanks to Cesare Scalia for reducing the HD24712 and βCrB data, for completing the K-means clustering of NGC 6250 and for leading the analysis of NGC 6633.

Thank you to AdaCore for providing the GNAT GPL Edition of its Ada compiler.

Finally, special thanks go to my family and friends (including the members of the Armagh St. John Ambulance division) for supporting me, occasionally managing to take my mind off research and for putting up with me through the tough times and the slightly less tough times! I would especially like to thank my Mum and Coral for always being there and looking out for me, even when I was a "wee" bit stressed.

"... It has been said that astronomy is a humbling and character-building experience. There is perhaps no better demonstration of the folly of human conceits than this distant image of our tiny world. To me, it underscores our responsibility to deal more kindly with one another, and to preserve and cherish the pale blue dot, the only home we've ever known."

- Carl Sagan, *Pale Blue Dot: A Vision of the Human Future in Space*

Contents

List of Figures

List of Tables

1 Introduction

Magnetic fields are observed in stars throughout the Hertzsprung-Russell (H-R) diagram and in the interstellar medium (ISM), ranging in strength from $\sim$1 μG in the ISM to 10^{12} G in some rotating neutron stars. Where present, magnetic fields are important during stellar evolution, from the very first stages of stellar formation in the ISM where the magnetic energies are comparable to the gravitational energies (Crutcher 1999), to the end of the star's life in white dwarfs, neutron stars, and black holes (e.g., Mestel 1999 and Ferrario & Wickramasinghe 2007).

The observations of the magnetic fields in the Sun provide excellent constraints for theories. Since the Sun is visually resolved we can observe the spectrum of various surface features separately. This allows us to detect the Zeeman splitting of spectral lines formed in surface features such as sunspots (e.g., Hale 1908) as shown by Fig. 1.1. The Sun, however, is only one type of star and, therefore, we must look further afield to gain a complete understanding of stellar magnetic fields.

Outside our solar system magnetic fields are most often observed in chemically peculiar A- and B-type stars, the Ap and Bp stars. These stars account for $\sim$10% of all A- and B-type stars (e.g., Donati & Landstreet 2009) and host large-scale ordered magnetic fields. These stars are especially interesting to study since their spectra contain the signatures of a variety of stellar processes, including diffusion, which theory predicts is strongly affected by magnetic fields.

The aim of this thesis is to create and use the new spectropolarimetric inversion code, Sparti, for the detection and characterisation of magnetic fields in main-sequence Ap and Bp stars. Sparti is also able to model magnetic fields in all main-sequence stars, as long as no molecular lines are considered in the analysis and the spectra have a sufficiently high signal-to-noise ratio (SNR) and spectral resolution (R); i.e. SNR $\gtrsim$ 200 and R $\gtrsim$ 60000 (see Section 5.4).

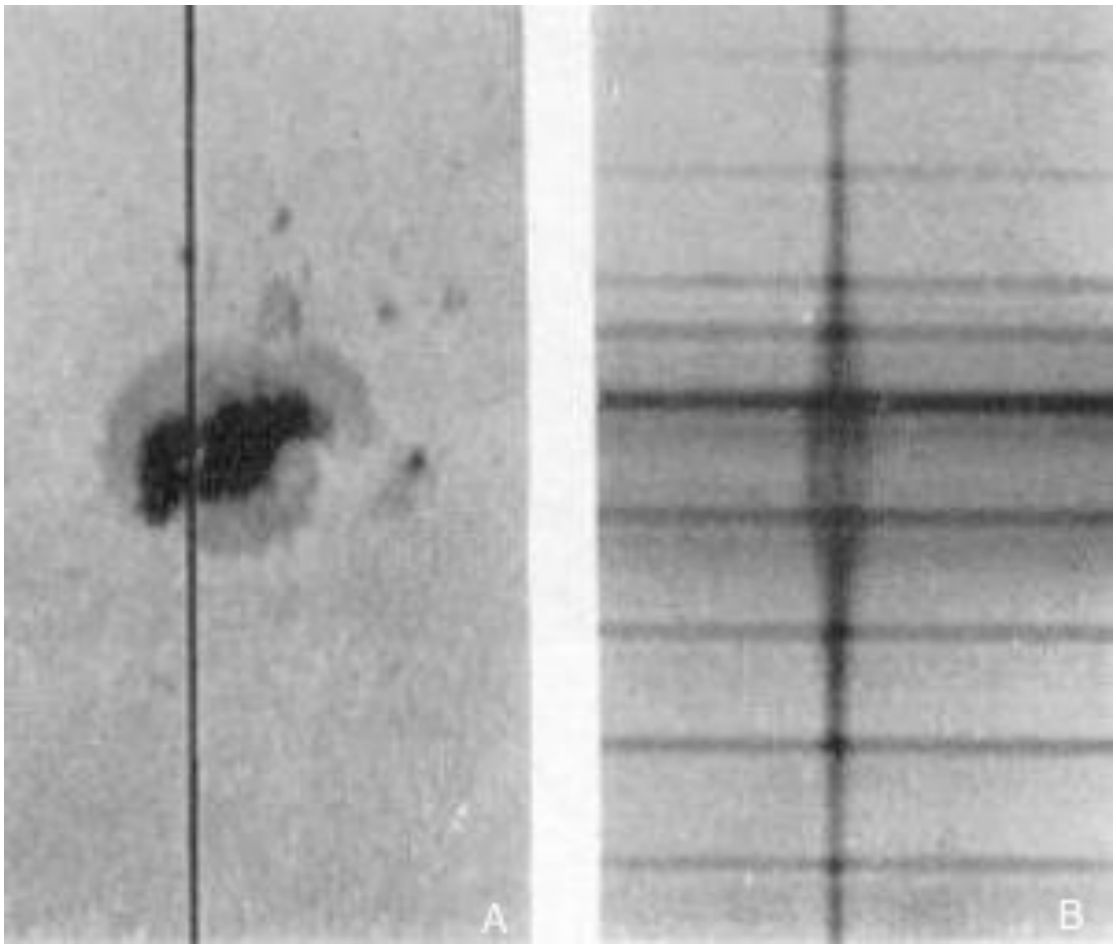

Figure 1.1: A: A sunspot photographed on 9$^{\text{th}}$ March 1916 at 23°W longitude. B: The iron triplet at 6173 Å, the slit is position as per the vertical line in image A. Image credit Hale et al. (1919)[1].

[1]Plate VII - parts a and b in *The Magnetic Polarity of Sun-Spots*, G. E. Hale, F. Ellerman, S. B. Nicholson, and A. H. Joy, 1919, ApJ, Vol. 49, p.153, © AAS. Reproduced with permission. `http://dx.doi.org/10.1086/142452`

1.1 Where are magnetic fields found?

Evidence of magnetic fields has been observed in a variety of stars of many spectral types across the H-R diagram. However, there are stars which after various surveys show no signatures of a magnetic field. Studying these types of stars allows us to determine which factors are responsible for magnetic fields and which signatures may appear as a result of the presence of a magnetic field. Surveys of the following stars have failed to detect any magnetic fields: HgMn Stars (Shorlin et al. 2002 and Makaganiuk et al. 2011); RR Lyrae Stars (Kolenberg & Bagnulo 2009); and A and B supergiants (Shultz et al. 2014). Initially the surveys of hot subdwarfs (O'Toole et al. 2005), emission line B-Type Stars (Hubrig et al. 2007 and Hubrig et al. 2009), and central stars of planetary nebulae (Jordan, Werner & O'Toole 2005) showed evidence of magnetic fields. However these results were called into question and later shown to be spurious (Petit et al. 2012; Bagnulo et al. 2012; Leone et al. 2011). Indeed further surveys of hot subdwarfs (Mathys et al. 2012 and Landstreet et al. 2012a) and central stars of planetary nebulae (Jordan et al. 2012 and Leone et al. 2014) show no evidence of magnetic fields.

We do not know whether the lack of detection is a result of instrument limitations or whether these stars truly have no magnetic fields. However we are able to give upper limits for magnetic field strengths in these stars: in most cases between 100–500 G.

The stars for which we observe magnetic field signatures can be split into two formation mechanisms. Those of "dynamo origin" (e.g., Charbonneau 2014) which form as a result of a dynamo process in the inner layers of the star and those of "fossil field" (e.g., Braithwaite & Spruit 2004) origin with fields which are created earlier in the star's evolution.

1.1.1 Dynamo origin magnetic field

The Sun was the first star found to have a magnetic field (Hale 1908). Since the Sun is the closest star to Earth and it is visually resolved, it has been very well studied. We now know that the magnetic field is comprised of magnetic flux tubes (Parker 1979); evidence of which comes in the form of sunspots, flares and prominences. The strongest fields on the surface of the Sun are observed in the umbrae of sunspots (e.g, Livingston et al. 2006). The Sun is often used as a stellar laboratory, and in addition to the magnetic field much of our atomic data is based on solar measurements. Initial observations of the Sun led to the conclusion that the Sun has periodic variations on a timescale of 11 years (Schwabe 1843). Later observations by Hale et al. (1919) showed that in fact the periodicity was on a timescale of 22 years, consisting of two 11-year cycles varying only based on the polarity of the magnetic field, something Schwabe (1843) was unable to measure. This variability is good evidence for a dynamic magnetic field resulting from an ongoing dynamo process and not a static fossil field.
The dynamo origin of the magnetic field in the Sun is thought to be the result of a magnetohydrodynamical process in the inner layers, at the interface between the radiative inner region of the star and the outer convective zones, the tachocline (Spiegel & Zahn 1992). At the tachocline the ionised plasma is subjected to shearing forces as a result of the differential rotation of the convective layer. These shearing forces produce a dynamo which in turn generates a magnetic field.

A large survey of solar-type stars found 67 out of 170 stars observed had magnetic fields (Marsden et al. 2014). It has also been possible to map the magnetic field of the surface of these stars (Donati et al. 1992; Carter et al. 1996). The polarity of the magnetic field changes frequently across the stellar surface in these stars, which means the disc-integrated field is likely to be weak even if the field of the star is much higher. Therefore measurements of the magnetic field of solar type stars using circularly polarised light may significantly underestimate the actually field strength.

Low mass stars between $1\,M_\odot$ and $0.1\,M_\odot$ generally show two types of magnetic field. The rapidly rotating stars are typically poloidal and symmetric, where the mag-

netic field lines emerge from the poles of the star (Gregory et al. 2012). The slow rotating stars show evidence of non-axisymmetric toroidal fields, where the field lines are perpendicular to the rotational axis (Gregory et al. 2012). Tens of stars have been detected with this magnetic field geometry and field maps have been produced by, for example, Donati & Landstreet (2009).

At the limit where stars become fully convective, $M \lesssim 0.35\,\mathrm{M}_{\odot}$ (Chabrier & Baraffe 1997), magnetic fields are observed (e.g., Donati & Collier Cameron (1997) and Morin et al. (2010)). There is much discussion about the formation of the fields in these stars. The fact that they are fully convective means that there is no boundary between different energy transport zones to produce the tachocline theorised in the formation of the solar dynamo. Brown et al. (2010) suggest, with the use of magnetohydrodynamical simulations, the possibility of a dynamo action within the convective zone resulting in "magnetic wreaths" which are not disrupted by the processes within the zone itself.

The magnetic fields of pre-main sequence T Tauri stars have been shown to be relatively strong in the several kG range (e.g., Johns-Krull 2007; Hussain et al. 2009; Hussain 2012; Donati et al. 2012). The magnetic fields are thought to cause an effect called *magnetospheric accretion* which influences how inflowing material falls onto the photosphere (Muzerolle, Calvet & Hartmann 1998).

In giant and super giant stars the fields are, in general, found to be around only a few G (Aurière et al. 2009; Konstantinova-Antova et al. 2012; Grunhut et al. 2010). This is very weak in comparison to the majority of observed stellar magnetic fields and intuitively it would appear to be too small for detection with existing instrumentation. The reliability of the measurements, however, is supported by multiple detections in the same stars and no detections in others.

The red giant star EK Eridani is of particular interest since it has a field strength of $\sim$100 G, which is larger than other similar stars. It is thought that EK Eri has evolved from a main-sequence A star with a magnetic field, however its present activity level is too high and thus not consistent with its rotation rate. This presents tantalising evidence for the transition between fossil fields and dynamo fields (Aurière et al. 2008; Konstantinova-Antova et al. 2010).

1.1.2 Fossil field origin magnetic field

An alternative origin of magnetic fields in stars, where the physics of the star does not support a dynamo origin, is the fossil field origin. These fields are thought to be the remnant of field generated earlier in the star's evolution or a field captured from the ISM during formation. We detect these fields in a variety of stars.

1.1.2.1 Main sequence O and B stars

The Of?p stars commonly show magnetic fields (Grunhut, Wade & MiMeS Collaboration 2012). They show signs of trapped magnetospheres where the magnetic field has stopped radiative stellar wind escaping. This is thought to lead to the trapped gas rotating about the star. The spectra of Of?p stars show strong emission lines of C III, and the spectral classification was introduced by Walborn (1972). These stars are, at this time, the only O stars for which fields have been detected.

There are a number of massive helium rich stars which show evidence of a trapped magnetosphere and large $\sim 5\,\mathrm{kG}$ magnetic fields. The first such star was discovered by Landstreet & Borra (1978). A number of B stars have been observed to have magnetic fields (Hubrig et al. 2006; Hubrig et al. 2009; Hubrig et al. 2011) using the FORS instrument. The work by Bagnulo et al. (2012) and Bagnulo et al. (2013) show that these results are likely spurious due to signals produced with the instrument. Of the 6 stars re-analysed by Shultz et al. (2012), for which Hubrig et al. (2011) have calculated models of the magnetic fields, only 2 were shown to have magnetic fields.

1.1.2.2 Pre-main sequence Herbig Ae/Be stars

Only a few per-cent of pre-main sequence A- and B-type stars are detected to have magnetic fields (Wade et al. 2005; Wade et al. 2007; Alecian et al. 2013), with dipolar morphology. The study of these stars could lead to vital clues about the presence of magnetic fields in Ap and Bp stars, since Herbig Ae/Be stars (HAeBe) are pre-main

sequence A- and B-type stars. The observational characteristics of the class HAeBe are described in Vieira et al. (2003); including the requirement to show emission lines in the spectra, and an infrared excess, which point to the presence of a circumstellar disc showing that the star is still in the pre-main sequence. There is also the requirement that there is "fairly bright nebulosity in its immediate vicinity" (Vieira et al. 2003), this is to differentiate between post- and pre-main sequence stars. The survey by Alecian et al. (2007) found four out of a total of 55 HAeBe stars with the signatures of large-scale ordered magnetic fields. These stars were also slow rotators which suggests the effects of some sort of magnetic braking since the stars are also young and are expected to be fast rotators as a result of conservation of angular momentum. There are a number of questions still to be answered in terms on magnetic Herbig Ae/Be stars. How do the magnetic fields in HAeBe relate to those found in Ap and Bp stars? How do the magnetic fields observed in HAeBe affect the accretion of material from the circumstellar disc? Vink et al. (2002) observed evidence to suggest that Herbig Ae stars undergo magnetic accretion, similar to that seen in T Tauri stars; Herbig Be stars on the other hand show evidence of disc accretion. Measurements of the Hα line of four HBe stars by Mendigutía et al. (2011) has provided additional evidence to support this. They show that there is no evidence of gas on Keplerian orbits which is required for magnetic accretion to take place.

1.1.2.3 White dwarfs

White dwarf stars (WDs) are the final evolutionary state of most stars. The analysis of the magnetic fields in WDs is important as they likely contain clues to the evolution of magnetism throughout stellar life. Surveys of WDs in the range of MG to hundreds of MG have been undertaken (Kepler et al. 2013). Far less information is known about WDs with fields below $\sim$ 10 kG, a survey by Aznar Cuadrado et al. (2004) suggested that a substantial fraction of white dwarfs have a weak magnetic field and Landstreet et al. (2012b) suggested a 10 % frequency, a survey by Kawka & Vennes (2012) concluded that the probability of field detection is of the order of 1-2 % per

decade of field strength.

Recently a survey of white dwarf stars (by J. Landstreet, S. Bagnulo, **A. Martin** and G. Valyavin), has aimed to detect weak magnetic fields below $\sim 10\,\mathrm{kG}$. As part of the survey the star 40 Eridani B was observed and no magnetic field was measured with an upper limit of 85 G (Landstreet et al. 2015). As part of the same survey a field of 57 kG was was detected in LTT 16093 = WD2047+372 (Landstreet et al. 2016), an important result since it is the third weakest field to be detected unambiguously in a white dwarf.

1.1.2.4 Ap and Bp Stars

In terms of magnetic stars, the main focus of this thesis is on chemically peculiar A- and B-type stars which comprise ∼10% of the total population of A- and B-type stars (e.g., Donati & Landstreet 2009). Ap and Bp stars range in temperature from 7000 K to 20000 K and are slow rotators (Catalano & Renson 1997). The spectra of Ap and Bp stars show strong peculiarities of a variety of elements especially iron-peak elements and rare-earths. This makes the modelling of these stars a particular challenge, since we can no longer rely on a close to solar abundance for the elements in the photosphere. Blends of rare-earths and iron-peak elements makes it difficult to disentangle the correct abundance for each element. When classifying these stars, if only the metal lines are considered the determination of spectral type can be far from the correct value. To illustrate this, Fig. 1.2 shows the difference between the Ap stars HD137909, HD24712 and a synthetic stellar spectrum. Each star has a similar temperature however there is extreme differences between the three spectra. In addition to the difference in strength and number of lines observed in the spectrum, there are also wavelength shifts of the line center of individual lines. This potentially indicates the presence of stellar spots, because, if a stellar spot with an enhanced abundance of a certain element is at the limb of a star, the line depth will increase only at those wavelengths consistent with the doppler shift resulting from the projected rotational velocity at the point on the star where the spot is located.

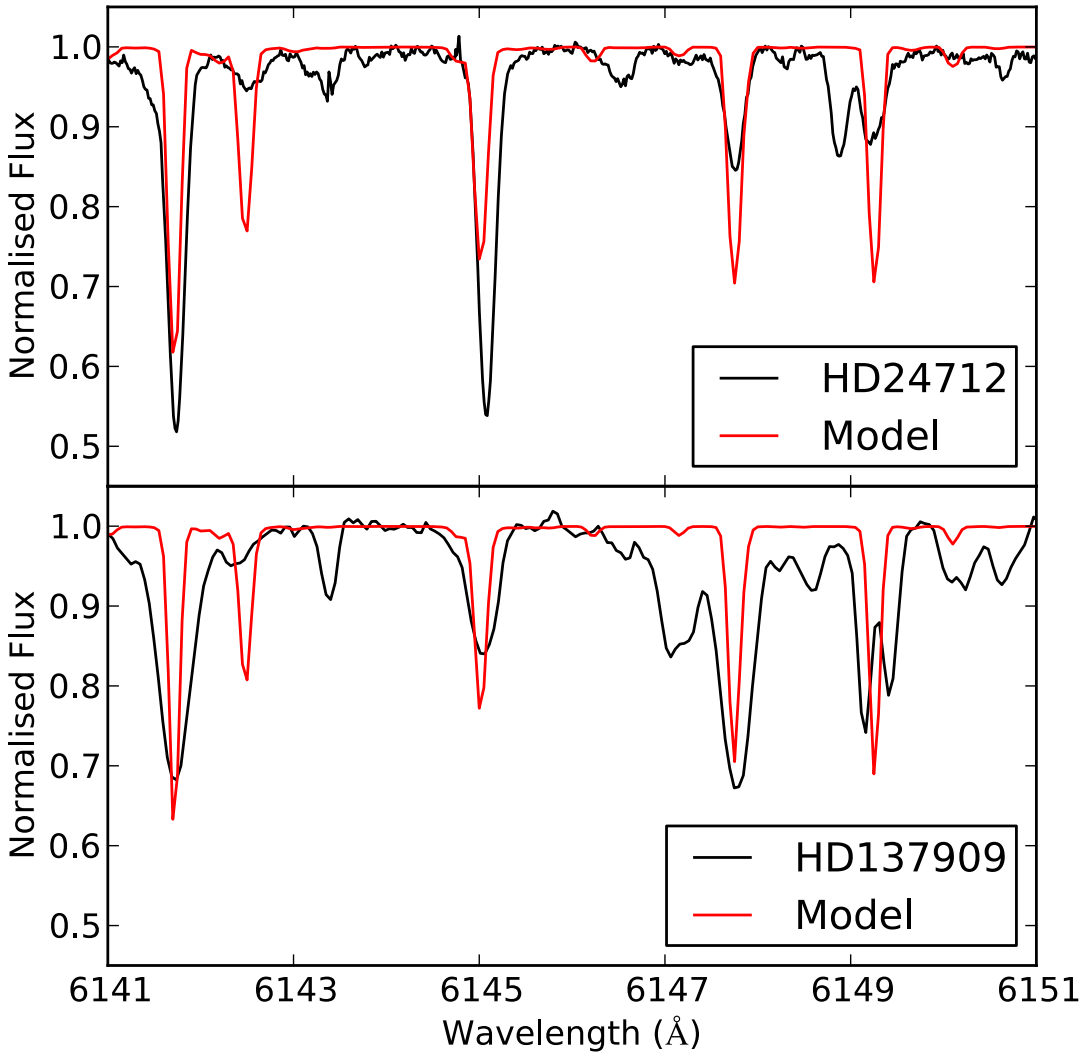

Figure 1.2: Top panel: The spectrum of HD24712 (black solid line) observed with HARPSpol, plotted with a synthetic spectrum calculated using the spectral synthesis code Cossam (red solid line) with $T_{\rm eff} = 7250$K, $\log g = 4.10$, solar abundances from Asplund et al. (2009) and convolved with an instrument response of HARPSpol (R = 120000). Bottom panel: The spectrum of HD137909 (black solid line) observed with CAOS, plotted with a synthetic spectrum calculated using the spectral synthesis code Cossam (red solid line) with $T_{\rm eff} = 7800$K, $\log g = 4.20$, solar abundances from Asplund et al. (2009) and convolved with an instrument response of CAOS (R = 60000).

In Ap stars, the interior of the star consists of a convective core wrapped within a radiative envelope. The hot matter rises in the convective zone and the cool matter drops. As the matter reaches the boundary between the convective layer and the radiative layer, energy is transferred by EM radiation to the stellar photosphere. Theory does not predict a dynamo in A- or B-type stars, the transition between the radiative and convective zones is inverted with respect to the solar case and it is far too deep in the star for it to reach the surface in time to explain the large-scale magnetic field structures seen in the pre-main sequence Ap stars (MacGregor & Cassinelli 2003). This means that any dynamo effect must occur very early on in the stars evolution, if it is the reason behind the large scale magnetic fields. This leads to the fossil field origin of the stellar magnetic field, either a remnant of an ISM field or a dynamo effect during pre-main sequence evolution. This is plausible as the ohmic decay timescale is 10^{10} yr (Cowling 1945) and the main-sequence lifetime of an A-type star is $<10^{9}$ yr (Bressan et al. 2012).

The magnetic fields observed in Ap and Bp stars range in strength from 300 G to 30 kG (Aurière et al. 2007), with weaker fields more common than stronger ones. The magnetic axis of Ap and Bp stars are in general offset from the rotation axis of the star. Often the *Oblique Rotator Model* (ORM; Stibbs 1950) is the model of choice for such stars with the mean longitudinal field varying periodically.

1.2 Detection and modelling of stellar magnetic fields

The simplest method of detecting magnetic fields in stars is to measure the splitting of spectral lines as a result of the Zeeman effect (Zeeman 1897). The first observation of the Zeeman effect in a star was detected in sunspots by Hale (1908). In other stars a mean value of the magnetic field strength over the entire stellar disk is measured, the "mean magnetic field modulus". The first star to have a magnetic field detected in this way was the Ap star HD215441 (Babcock 1960). This technique has since been applied to a number of stars and 40 stars with magnetic fields were found in surveys by Mathys

& Lanz (1992) and Mathys et al. (1997). The Fe line at 6149 Å is commonly used for the detection of magnetic fields in Ap stars (Mathys et al. 1997). The Zeeman effect, however, is easily hidden by the instrument response or the Doppler broadening of spectral lines as a result of the rotation velocity of the star. Only very strong magnetic fields can be detected in this way. As a rough guide the limit at which the Zeeman effect is detectable is 1 kG for every 1 $\mathrm{km\,s^{-1}}$ of $v \sin i$ (Bagnulo et al. 2001a).
As a result the measurement of the Zeeman splitting of spectral lines is not the most practical tool for the detection and characterisation of magnetic fields. We must therefore turn to a different technique which provides more information about the star. This technique is spectropolarimetry which allows us to observe the polarisation of the electromagnetic radiation emitted by the star, while still observing the intensity spectrum as previously from spectroscopy. The polarisation of the incoming radiation is dependent on the direction of the magnetic field vector with respect to the observer (see Section 2.2). By measuring the degree of linear and circular polarisation we are able to gain a more detailed understanding of the structure of the magnetic field in terms of the strength, orientation and geometry. Before we are able to make full use of spectropolarimetry we must first define parameters to allow us to consistently define the direction of the polarisation.

1.2.1 Stokes Parameters

The Stokes parameters are used as a means to define the amount of linear and circular polarised light emitted by a source and were developed by Stokes (1852). By convention the magnetic field vector of the electromagnetic wave is ignored and only the electric field vector is used to calculate the degree of polarisation. There are four Stokes parameters I, Q, U and V. With the exception of Stokes I an explanation of how to calculate the Stokes parameters is shown in Fig. 1.3.

Stokes I is the total intensity of light measured and is the same quantity as that measured by photometry in the case of no grating and spectroscopy where a grating is present. Stokes Q and U are both measures of linear polarisations with difference

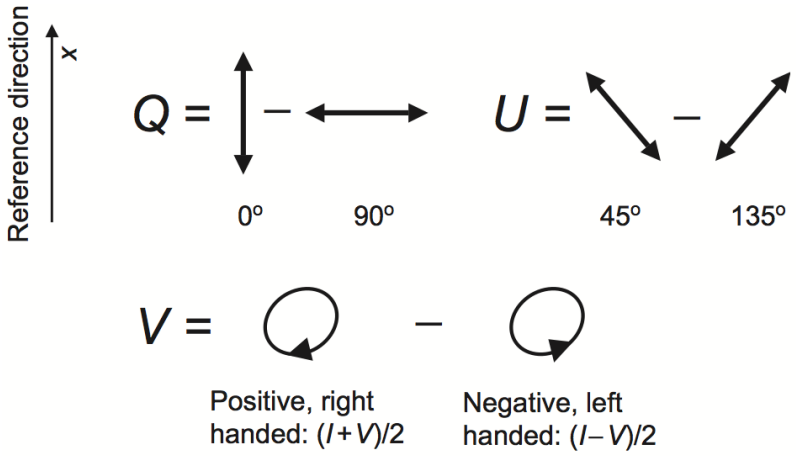

Figure 1.3: A visualisation of the determination of the Stokes Parameters. The double headed arrows show the direction of oscillation of the electric field vector with respect to the reference direction x. Each arrow represents the total flux in each direction and the Stokes parameters are calculated based on the difference between the two (Landi Degl'Innocenti, Bagnulo & Fossati 2007)[2].

[2]Figure 1 in *Polarimetric Standardization*, E. Landi Degl'Innocenti, S. Bagnulo, L. Fossati, 2007, ASP Conference Series, Vol. 364, page 495, eds. C. Sterken. Permission to reproduce granted by ASPCS.

orientations with respect to the chosen reference direction. Stokes V is the degree of circular polarisation. Stokes Q is measured by taking the difference between light polarised so that the electric field vector is parallel to a reference direction and light polarised so that the electric field vector is perpendicular to a reference direction. Stokes U is measured in the same way as Stokes Q however the measurement is made between electric vectors which in each case are offset by 45° compared with those used to measure Stokes Q. Stokes V is calculated as the difference between the right handed and left handed circularly polarised light. Circularly polarised light is light for which the electric field vector is rotating about the direction of travel.

This reference system is consistent with Landi Degl'Innocenti, Bagnulo & Fossati (2007) and with the majority of the measurements in the optical regime. However it is important to check the reference system used for the Stokes parameters of published results since in some cases the signs of the Stokes parameters given are different to those which would be calculated from the above definitions.

1.2.2 Mean longitudinal field measurements

The first use of Stokes profiles to observe the magnetic field in a star other than our Sun was carried out by Babcock (1947), measuring the "mean longitudinal" field of 78 Vir using Stokes I and V. Under the weak field approximation (B $<\sim$100 G), the Stokes V signal is proportional to the "mean longitudinal magnetic field", $\langle B_z \rangle$ (e.g., Babcock 1947; Mathys 1989), which is the component of the magnetic field vector parallel to the line of sight averaged over the visible stellar surface. As a result of this it is possible to use the Stokes V signal to measure $\langle B_z \rangle$, which is proportional to the wavelength difference between the right and left σ-components (see Section 2.2) of the Stokes V profile (e.g., Mathys 1989). Therefore by observing the Stokes V profile of individual spectral lines with high SNR it is possible to measure the $\langle B_z \rangle$ of the star so long as $\langle B_z \rangle <\sim$100 G. Commonly however multiple lines are used, $\langle B_z \rangle$ is calculated for each line and the average taken. This has two key advantages, first the SNR is increased, but, also, theoretical calculations by Semel (1967) have shown that the average of the

field strength measurements of all the lines is equal to the true field strength even for ($B \gg 100\,G$). An explanation of how to calculate $\langle B_z \rangle$ is given by Mathys (1989) and its uncertainties by Mathys (1994). The first attempts to model stellar magnetic fields were based on the mean longitudinal field by Babcock (1947) and later by Landstreet & Mathys (2000) and Bagnulo et al. (2002). Examples of large surveys which have found values of $\langle B_z \rangle$ in this way are Babcock (1958), Mathys (1991), Mathys (1994) and Kudryavtsev et al. (2006).

1.2.2.1 Least-squares deconvolution

A technique which builds on the mean longitudinal magnetic field method is "Least-Squares Deconvolution" (LSD) by Donati & Brown (1997) and its predecessor "Simple Line Addition" (SLA) by Semel (1989) and Semel & Li (1996). Both techniques combine multiple lines to form one average line profile, boosting the SNR of the observations. The difference between SLA and LSD is, LSD takes advantage of the proportionality between Stokes V and the derivative of Stokes I. LSD is not only used for the measurement of $\langle B_z \rangle$ but has also been applied to the modelling of the global magnetic field. An examination of the limitations of LSD was performed by Kochukhov, Makaganiuk & Piskunov (2010) and tests by Paletou (2012) led to the conclusion that LSD does not perform substantially better than the SLA. LSD has been used to measure the magnetic field of the vast majority of high-resolution spectropolarimetric data and examples of surveys which have used it are those by Wade et al. (2000b) studying Ap stars and by Shorlin et al. (2002) studying F, A and B type stars.

1.2.3 Modelling time series of Stokes profiles

With the advancement of spectropolarimetric instruments such as the Echelle Spectropolarimetric Device for the Observation of Stars (ESPaDOnS) and HARPSPol at the Canada France Hawaii Telescope and ESO's 3.6-metre telescope, respectively, we are able to observe high resolution and high SNR Stokes $IQUV$ profiles at multiple

points during a star's rotation period. By attempting to model the observed profiles using inversion algorithms based on polarised radiative transfer code, it is possible to gain an understanding of the entire stellar magnetic field. It is possible to determine the orientation of the star's rotation axis with respect to the observer and the equatorial rotational velocity and magnetic field strength. Landstreet (1988) and Landstreet et al. (1989) were the first to model stellar magnetic fields by comparing time series observations of Stokes I with synthetic spectra.

As the measurement of Stokes $IQUV$ has advanced so have modelling techniques. One approach to modelling the magnetic fields of stars is to start with a parameterised magnetic model and use a least-squares technique to minimise the difference between a set of synthetic spectra and time series observations of the Stokes $IQUV$ profiles. This has the advantage that the solution is physical and that solutions are easily compared, but it can be slow, and the magnetic field may have a structure more complex than the parameterised function allows. Another technique is to fit individual surface elements independently over the entire surface disk. This technique has the advantage that the little or no constraint is imposed on the complexity of the magnetic field, however the solution must be regularised to guarantee a physical and stable solution. This leads to a potential source of error within this technique, since the choice of regularisation has the potential to affect the results (Stift, Leone & Cowley 2012). The application of these techniques is commonly referred to as "Zeeman-Doppler Imaging" (ZDI; Donati 2001). Examples of the analysis of stellar magnetic fields by ZDI are those by Petit et al. (2005) modelling G-type stars and Petit et al. (2010) modelling Vega.

The latest technique is MDI which performs full radiative transfer to calculate the abundance structure horizontally over the stellar surface and the entire magnetic field structure (Piskunov & Kochukhov 2002 and Kochukhov & Piskunov 2002). This technique does not use a parameterised model to describe the magnetic field or abundance distribution, instead the modelling fits individual surface elements and regularises the solution to aim for a stable and physical solution, which does not violate physical laws such as conservation of magnetic flux. Currently their code has been mostly used to model Ap stars (e.g., Kochukhov et al. 2004 and Kochukhov & Wade 2010). How-

ever, there is a debate between Stift, Leone & Cowley (2012) and Kochukhov, Wade & Shulyak (2012) on the results of MDI, whether the results produced by Kochukhov, Wade & Shulyak (2012) are unique and accurate.

1.3 Diffusion

The magnetic fields of Ap and Bp stars has been shown to directly affect the normal diffusion of chemical elements within the photosphere (Michaud, Charland & Megessier 1981). As a result, the stellar magnetic field is thought to be strongly linked to the presence of the non-homogeneous distributions of chemical elements in the photosphere of Ap and Bp stars. It is worth noting however, that stars such as Am and HgMn chemically peculiar stars do not show evidence of magnetic fields (Aurière et al. 2010 and Kochukhov et al. 2013) and so increasing the observational data available to constrain diffusion theory is important.

The movement of elements through the stellar photosphere determines the abundance distribution of the elements in the photosphere. Diffusion is commonly ignored when modelling the photospheres of stars however it has been shown that it is a significant and important process (Michaud, Alecian & Richer 2015).

Diffusion describes the movement of elements in stellar photospheres. Largely it is controlled by radiative levitation as a result of the photons emitted from the core of a star balancing with gravitational settling of atoms (Michaud 1970). Ions for which the radiative levitation is stronger than the gravitational settling are pushed up in the atmosphere and potentially ejected. Where gravitational settling is strongest the opposite is true. If the two forces balance then the layers of ions can form in cloud-like structures creating areas of overabundance. Equally if the force of radiative levitation is too strong at a certain layer the majority of ions may be driven away created regions of under-abundance.

It is likely that the photospheric inhomogeneities we observe in Ap and Bp stars are the result of the magnetic field's effect on stellar atomic diffusion (Michaud, Char-

land & Megessier 1981). It has been shown that ions will diffuse along magnetic field lines (Michaud, Charland & Megessier 1981; Alecian & Stift 2007) which may result in horizontal as well as vertical abundance inhomogeneities in the stellar photosphere. These inhomogeneities present a problem for the modelling of stellar spectra.

1.3.1 Vertical stratification of chemical elements in Ap and Bp stars

Observational evidence for the presence of abundance stratification in stellar photospheres comes from the apparent difference in abundance necessary to fit weak and strong spectral lines of the same element and ionisation state as shown by Fig. 1.4. Strong and weak lines are formed at different depths in the stellar photosphere, so we can infer that the distribution of the elements which produce these lines is non-homogenous throughout the photosphere. Vertical stratification must be considered when modelling the magnetic field of stars and so it adds an additional complication.

The vertical stratification of elements has been both modelled by fitting observational data (Kochukhov et al. 2006) and by theoretical time evolution simulations of diffusion theory in magnetic stars of varying field strength (Stift & Alecian 2012). Currently, however, the theoretical results and those derived from observations do not agree. The difference between the two is shown in Fig. 1.5. To move further in the study of the abundance distributions of chemically peculiar stars we must consider three things. Firstly, we must understand whether current modelling provides unique and reliable solutions. It is common that a solution has been determined from separate points on the stellar surface and then regularised to ensure the result is physical. We must understand whether this regularisation affects the final model. This can be tested using a parameterised model, this however has its own problem, the solution is constrained by the model which is chosen and so it is important to allow sufficient degrees of freedom within the parameterisation.

The second and perhaps more difficult problem to address, is not enough lines are sampled from the stellar spectrum during analysis. There are two main limiting

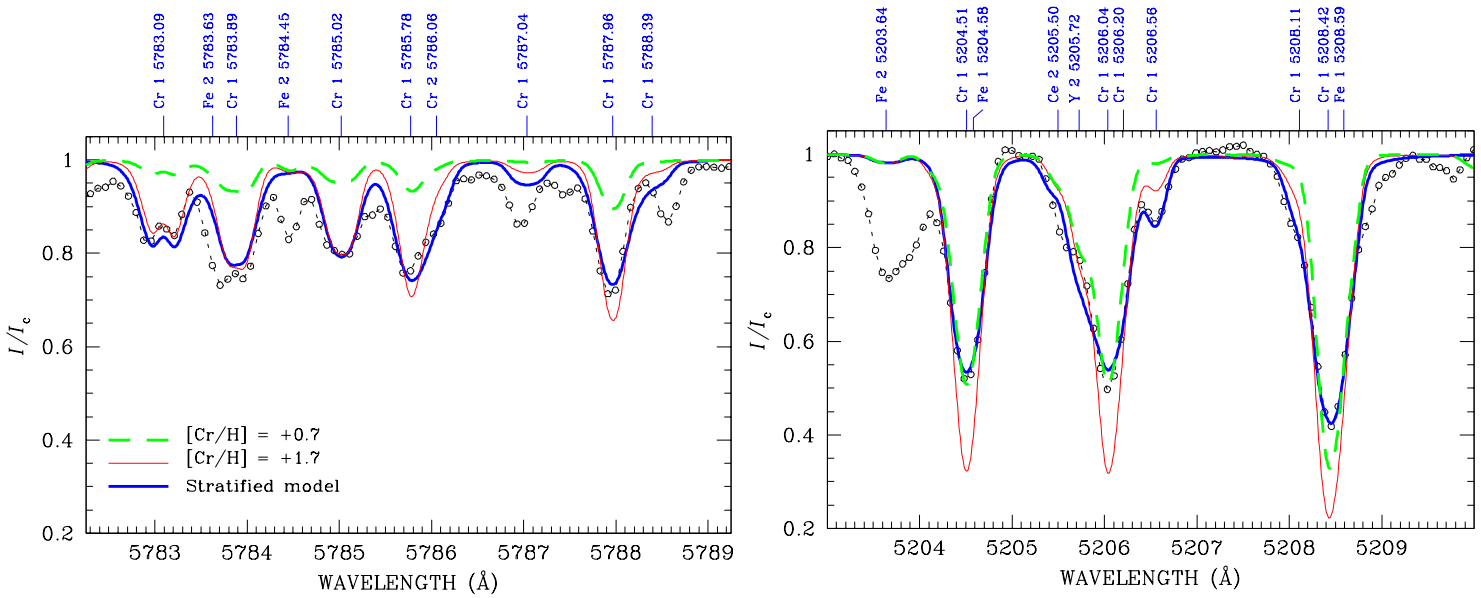

Figure 1.4: The difference between weak and strong Cr lines in the spectrum of β CrB. A stratified model is the only way to reproduce the observed spectrum with a 1 dex abundance difference between the lower and upper regions of the atmosphere (Bagnulo et al. 2001b)[3].

[3]Figure 2 in *A study of polarized spectra of magnetic CP stars: Predicted vs. observed Stokes IQUV profiles for* β *CrB and 53 Cam*, S. Bagnulo, G. A. Wade, J. F. Donati, J. D. Landstreet, F. Leone, D. N. Monin and M. J. Stift, 2001, A&A, Vol. 369, Num. 3, page 889 reproduced with permission © ESO. `http://dx.doi.org/10.1051/0004-6361:20010101`

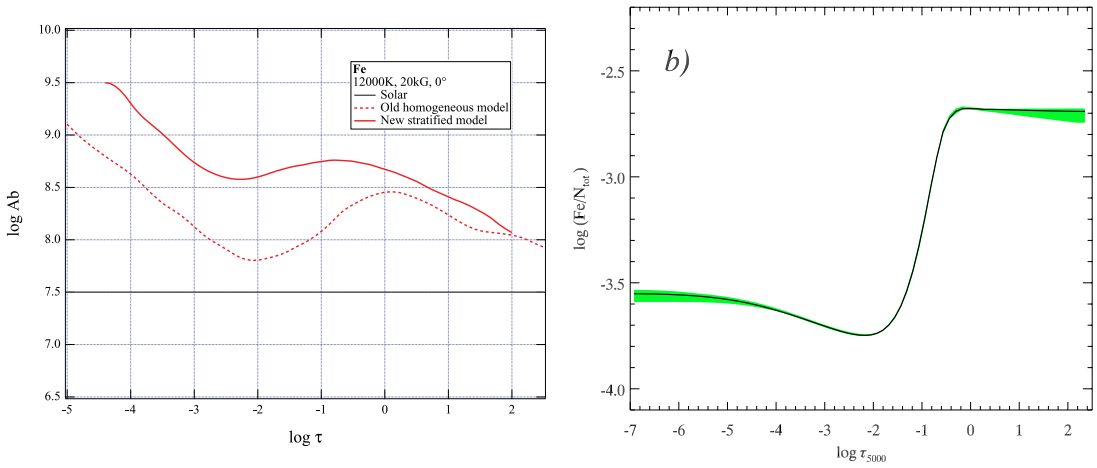

Figure 1.5: Left panel: Stratification model produced using theoretical time evolution simulations of diffusion theory in a star with $T_{\rm eff} = 12000$K and magnetic field strength 20 kG (Stift & Alecian 2012)[4]. Right panel: Stratification derived from observations of HD 133792 (Kochukhov et al. 2006)[5].

factors, first computer performance limits the number of lines which can be used in the analysis simultaneously and obtain a solution in a reasonable amount of time. Also, it is very difficult, if not impossible, to choose a line list for which there is complete coverage of the entire photosphere for each element. This is essential if we hope to reproduce the theoretical results, if we do not have line formation in a certain region of the photosphere, we are completely unable to fit that region.

[4]Figure 2 in *Modelling ApBp star atmospheres with stratified abundances consistent with atomic diffusion*, M. J. Stift and G. Alecian, 2012, MNRAS, Vol. 425, page 2715. Permission to reproduce is granted on the MNRAS website.

[5]Figure 3b in *Chemical stratification in the atmosphere of Ap star HD 133792, Regularized solution of the vertical inversion problem*, O. Kochukhov, V. Tsymbal, T. Ryabchikova, V. Makaganyk, and S. Bagnulo, 2006, A&A, Vol. 460, Num. 3, page 831, reproduced with permission © ESO.
`http://dx.doi.org/10.1051/0004-6361:20065607`

Third, and finally, as I have mentioned before, we see chemical peculiarities in magnetic and non-magnetic stars. Therefore we must obtain a large amount of data covering a large range of ages and temperatures to be able to add constraints to the theory of atomic diffusion in stellar photospheres.

1.4 ADA Programming Language

The programming language Ada is relatively unheard for the development of programs for the analysis of astronomical data, for which the majority of people use Fortran, IDL and Python. Ada however is extremely powerful and for this reason and because it is used to write Cossam (see Chapter 3), it is the language with which I have chosen to write Sparti and Sparti Simple (see Chapter 4).

Originally Ada was developed to be the exclusive programming language used by the United States Department of Defence, replacing a large number of codes which had been designed for individual applications. It is for this very reason that Ada is such a powerful language. It was essential that Ada was able to handle mission critical software, controlling any number of things including aircraft. As a result the language has robust error-checking, and parallelisation routines which use "tasks" to give commands to any number of CPUs. These "tasks" are able to complete a sequence of commands concurrently on each processor in the same program without interfering with each other. Additional safety features include the use of protected objects, these prevent multiple CPUs from accessing and simultaneously changing the same variable.

Ada further benefits from a well maintained compiler which is free to members of academic institutions (**http://libre.adacore.com/**).

1.5 Thesis Overview

The main aim of this thesis is the writing and testing of a new spectral inversion code Sparti (Spectro-Polarimetric Analysis by Radiative Transfer Inversion) for the

analysis of main-sequence stars with magnetic fields. SPARTI can also be used for the analysis of intensity spectra of non-magnetic stars, however this is inefficient because it must still calculate QUV which have no signal. Therefore as part of this thesis I also present the code SPARTI SIMPLE which takes advantage of the symmetries present when analysing non-magnetic stars, and so is considerably faster.

The results of the modelling of observed Stokes $IQUV$ profiles do not agree with the theoretical results as predicted by diffusion theory. As a result there are two key questions: are current magnetic maps and abundance distributions unique and reliable? How can we best add observational constraints to the theory of stellar atomic diffusion? Answering these questions requires careful analysis of a large sample of the spectra of non-magnetic and magnetic stars, with a large spread in stellar age. This analysis will give strong observational constraints for how stellar processes evolve with time.

To provide the tools necessary to answer the first question and to analyse the magnetic stars necessary to answer the second question, I have written the code SPARTI, which I use to determine the magnetic field structure of an observed star and the abundance distribution both vertically and horizontally throughout its photosphere. The benefit of SPARTI compared with previous inversion codes, is that no prior assumptions must be made about the inclination of the star's rotation axis. Furthermore I approach the problem in a different way, by using parameterised geometries and three-dimensional abundance distributions, which means I do not need to force the result to be physical. In this thesis, I test the convergence of SPARTI using model data and apply SPARTI to the analysis of the stars HD24712 and HD137909. Starting from a large number of different starting parameters allows me to determine whether all converged solutions for the two stars are identical within the error bars and so unique or whether several minima are found.

With the aim to answer the second question, I have analysed the open cluster NGC6250 as part of a large collaborative effort to understand how stellar processes vary as a function of stellar age. This analysis continues the work by Kılıçoğlu et al. (2016) (NGC6405); and Fossati et al. (2007), Fossati et al. (2008a), Fossati et al. (2010) and Fossati et al. (2011a) (Praesape cluster and NGC 5460). Kılıçoğlu et al. (2016) found

NGC 6405 to have an age of $\log t \sim 7.88$, a distance of 400 pc $\pm$ 50 pc and a [Fe/H] metallicity of 0.07 $\pm$ 0.03. The Praesape cluster has an age of $\log t \sim 8.85 \pm 0.15$ (González-García et al. 2006) and it is at a distance of 180 pc $\pm$ 10 pc (Robichon et al. 1999). Fossati et al. (2011a) found NGC 5460 to have an age of $\log t \sim 8.2 \pm 0.1$, a distance of 720 pc $\pm$ 50 pc and a near solar metallicity.

With an age of $\log t \sim 7.42$ yr and a distance of 865 pc (Kharchenko et al. 2013), NGC 6250 is both the youngest and most distant cluster analysed as part of this project so far. My analysis therefore substantially increases the range of stellar ages from which it is possible to draw conclusions. It is important for this study that the stars have known ages so I perform the cluster membership analysis to confirm which stars are members of the cluster, using the kinematics and photometry of the stars. To efficiently perform the chemical abundance analysis I wrote the code Sparti Simple, which is a fast version of Sparti designed to model the intensity spectra of main sequence stars. I apply Sparti Simple to the analysis of the 19 F-, A- and B-type stars which I determine to be members of the cluster NGC6250. I derive the masses and radii of the stars, I discuss the correlation between the stellar parameters and the chemical abundances and I look for patterns between my results and those of the previous studies.

2 Radiative Transfer

Radiative transfer describes the transfer of energy by photons. A photon can be emitted when an electron in an atom drops from an energy level to a lower energy level. The wavelength, λ, of this photon is related to the energy difference between the two levels (ΔE), following the Planck–Einstein relation (e.g. Hubeny & Mihalas 2014)

$$\lambda = \frac{hc}{\Delta E} \tag{2.1}$$

where h is Planck's constant and c is the speed of light in a vacuum. If the emitted photon passes through a vacuum it will not lose any energy. The problem of radiative transfer is simple in this case, the energy the photon initially has when it is emitted is the same as when it reaches an observer. The problem becomes complex when the photon travels through a medium, for example a cold gas with a temperature much less than the source of photons. As the photon passes through this gas, there is the chance of absorption, re-emission and scattering.

Radiative transfer in a star's photosphere is analogous to photons travelling through a cold gas. The core of the star is a source of EM radiation, and the photosphere is the cold gas through which the photons travel. As the photons travel through the photosphere of the star they interact with the elements (and molecules) in the star. These interactions lead to the formation of absorption lines at wavelengths corresponding to the energy levels in each atom present as given by Eq. 2.1.

2.1 Non-Magnetic Line Broadening

Calculating a synthetic spectrum based solely on the above definition would produce a spectrum with spectral lines of zero width, δ functions. However, in reality the spectral lines we observe in stars have been broadened or split by a number of processes. With the exception of natural broadening (which is a broadening intrinsically associated with quantum mechanics of an atom) all of these broadening and splitting effects are

directly related to the properties of the star (e.g. Gray 2005). Based on the shape of the spectral lines we can therefore infer a large number of stellar parameters for instance, temperature ($T_{\rm eff}$), surface gravity ($\log g$) and rotation velocity ($v \sin i$).

Natural Broadening is an effect observed independently of any properties of the star. It is related to Heisenberg's uncertainty principle (Heisenberg 1927) and occurs because of the relationship between the measurement of time and energy. Since we know the average time an electron will remain in an upper level (e.g., Degl'Innocenti 2014), there is an uncertainty in the energy of the upper level. This uncertainty in the energy results in a photon which can be have a number of different frequencies following Eq. 2.1.

Pressure broadening is an effect caused by the proximity of nearby particles to the atom absorbing the incoming radiation. These nearby particles affect energy levels within the atom. The upper level is more strongly affected by the perturber since it is closer (e.g. Gray 2005). The pressure broadening effects which must be considered as part of the analysis of stellar spectra are the linear and quadratic Stark effect, and the Van der Waals broadening. The linear and quadratic Stark effects are the result of perturbations caused by charged particles. Protons and electrons cause the linear Stark effect which particularly affects the hydrogen lines, causing the very broad lines (Struve 1929). For the quadratic Stark effect the perturbers are ions and electrons and effects most lines. Van der Waals broadening is caused by neutral particles, it is most common in stars with temperatures less than $\sim$10000K, where the main cause of the broadening is neutral hydrogen (e.g. Gray 2005).

The random movement of atoms in the photosphere also has an effect on the spectral lines. Atoms in a star do not all move with the same velocity, the differences in the velocities of the atoms leads to a doppler shifting of their spectral lines. The most significant cause is the thermal motion of the atoms, which is directly related to the temperature of the star (e.g. Degl'Innocenti 2014).

The microturbulence in stellar photospheres is the motions of material at scales smaller than the mean free path of the photons through the material. That is to say the average distance a photon will travel before interacting with an atom or molecule.

The microturbulence velocity, $v_{\rm mic}$, describes the magnitude of this overall small-scale motion. This motion is modelled in much the same way as thermal broadening, and the only difference is the mechanism, in thermal broadening the velocity is as a result of the temperature of the photosphere, where as, $v_{\rm mic}$ is the result of convective currents. The difference in strength between the strong and weak lines is used to measure the microturbulence (e.g. Hubeny & Mihalas 2014).

Rotational broadening is the result of the stars global rotation. As a star rotates one limb is traveling towards the observer and one limb is travelling away from the observer. This leads to a redshift of the light received from the limb moving away and a blueshift of the light received from the limb moving toward the observer. This broadening is used to determine the rotational velocity of the star. In the case of non-magnetic stars for which we have no information about the inclination of the star we measure $v \sin i$, which is the velocity with respect to the inclination of the star.

2.2 Zeeman Effect

Stars with magnetic fields show the signatures of each of the effects described in Section 2.1, with the addition of the Zeeman effect (Zeeman 1897). The Zeeman effect is a direct result of the magnetic field and measurement of line splitting allows us to determine the magnetic field strength. The Zeeman effect can be described both classically and quantum mechanically.

2.2.1 Classical Interpretation

The Zeeman Effect can be thought of classically as analogous to a harmonic electric oscillator (e.g. Degl'Innocenti 2014), with the electron oscillating in a magnetic field illustrated in Fig. 2.1. If the line of sight is perpendicular to the magnetic field a linear polarisation will be observed, this is as a result of viewing the electron orbiting side on, it will appear as if the electron is oscillating from left to right or top to bottom along

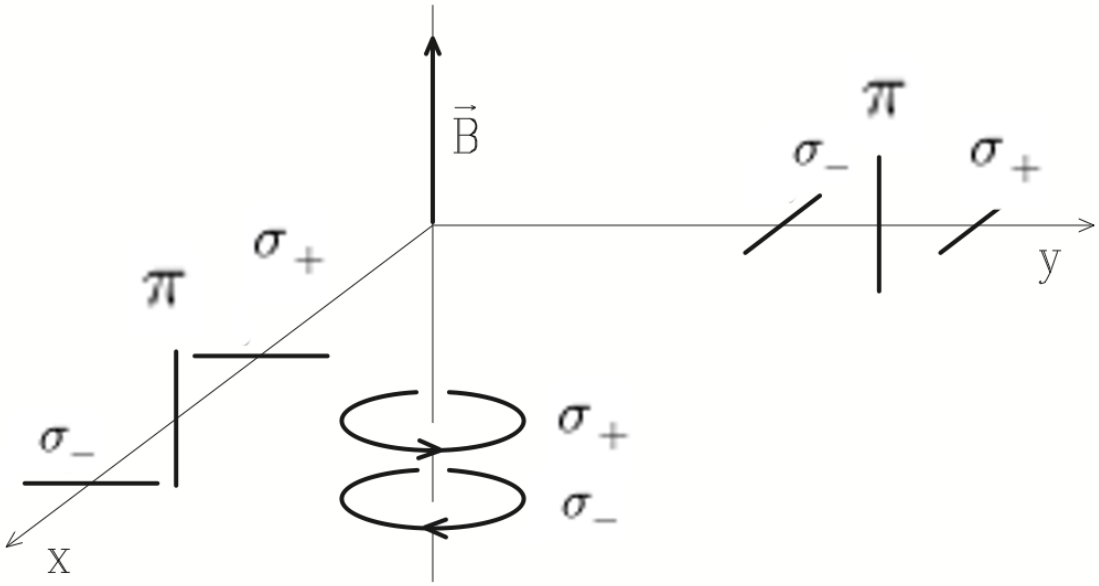

Figure 2.1: A visualisation based on the classical explanation of the polarisation features caused by the Zeeman effect. Where π is the line component with $\nu = \nu_0$ and σ_+ and σ_- are the split components with $\nu = \nu_0 + \nu_L$ and $\nu = \nu_0 - \nu_L$ respectively. $\vec{B}$ is the magnetic field vector (Landi Degl'Innocenti & Landolfi 2004)[1].

[1]Figure 3.1 in *Polarization in Spectral Lines*, E. Landi Degl'innocenti and M. Landolfi, 2004, Astrophysics and Space Science Library, Vol. 307 © 2005 Springer Science + Business Media, Inc. With permission of Springer. http://dx.doi.org/10.1007/1-4020-2415-0

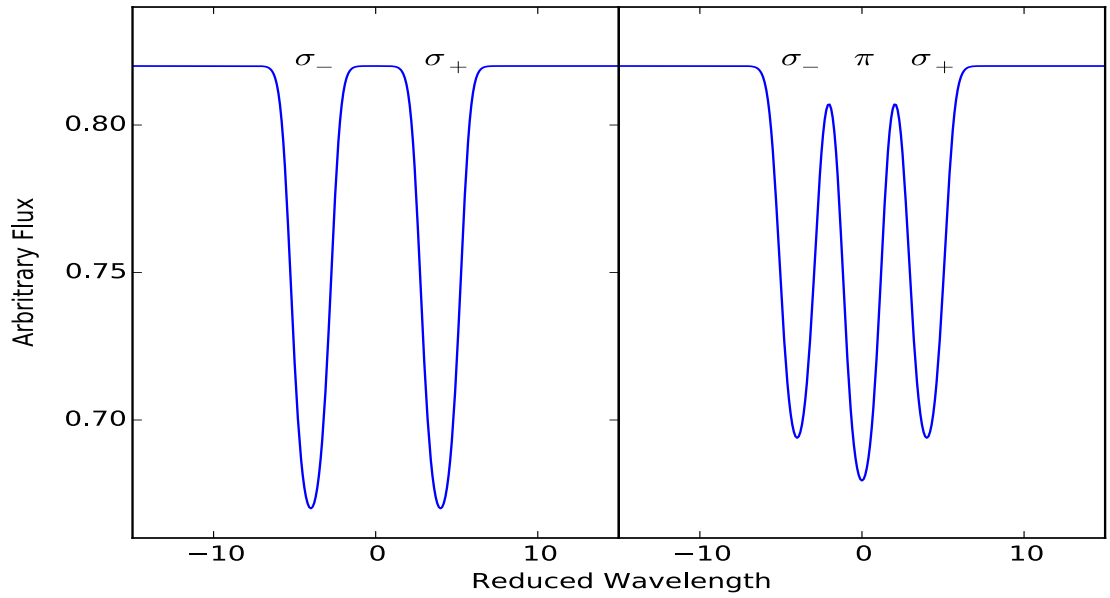

Figure 2.2: Left figure: line formed with the observers line of sight parallel to the magnetic field. Right figure: line formed with the observers line of sight perpendicular to the magnetic field.

a straight trajectory. In this case, as shown in the right side of Fig. 2.2, the spectral line will split into 3 components. If the line of sight is parallel to the magnetic field a circular polarisation will be observed, this is as a result of viewing the electron orbit face on making it possible to see the full orbit. The central component of the spectral line in the previous case is not observed as seen in Fig. 2.2. This is because the oscillations occurs in the plane of the observer. The frequency of each of the components is given by

$$\begin{aligned} \sigma_- &= \nu_0 - \nu_L \\ \pi &= \nu_0 \\ \sigma_+ &= \nu_0 + \nu_L \end{aligned} \tag{2.2}$$

where ν_L is the Larmor frequency given by

$$\nu_L = \frac{eB}{4\pi mc} = 1.3996 \times 10^6 Bs^{-1} \tag{2.3}$$

where B is the magnetic field strength in gauss, e is the electron charge, m is the electron mass and c is the speed of light in a vacuum.

The classical interpretation of the Zeeman effect is useful for an intuitive understanding of simple spectral lines in the presence of a magnetic field. However, to model the behaviour of spectral lines the classical approach is not sufficient, since the spin of the electron becomes important.

2.2.2 Quantum Mechanics Interpretation

Under the quantum mechanics interpretation of the Zeeman effect it is possible to recover the same solution as shown in Section 2.2.1. We start by considering the magnetic potential energy, E,

$$E = -\vec{\mu} \cdot \vec{B} = -\mu_z B \tag{2.4}$$

where B is the external magnetic field aligned to the z direction, and the magnetic moment about the z direction, μ_z is

$$\mu_z = -m_l \mu_B = -m_l \left(\frac{e\hbar}{2m_e} \right) \tag{2.5}$$

where m_L is the *magnetic quantum number* which can take values in the range $-l < \Delta m_l < l$ where l is the *azimuthal angular momentum quantum number* (e.g. Rae 2008). The energy difference between two levels is then given by

$$\Delta E = \Delta m_l \left(\frac{e\hbar}{2m_e} \right) B. \tag{2.6}$$

If we consider a transition between the levels $l = 1$ and $l = 0$, this means there is the potential for transitions at $\Delta m_l = -1, 0$ or $+1$. This results in energy differences of

$$\Delta E = -\left(\frac{e\hbar}{2m_e} \right) B, \quad \Delta E = 0 \quad \text{and} \quad \Delta E = -\left(\frac{e\hbar}{2m_e} \right) B. \tag{2.7}$$

We can re-write these energies in terms of frequency, using $E = h\nu$,

$$\Delta \nu = -\left(\frac{eB}{2m_e} \right) = -\nu_L, \quad \Delta \nu = 0 \quad \text{and} \quad \Delta \nu = +\left(\frac{eB}{2m_e} \right) = \nu_L \tag{2.8}$$

these match the frequencies shown in Section 2.2.1.

In reality, however, we must take into account the spin of each electron in the atom in addition to the magnetic moment. This is the *anomalous Zeeman effect* (Preston 1898). In this case, instead of only the orbital angular momentum we must also take in to account *spin* $\mathbf{S}$ which leads to the *total angular momentum*, $\mathbf{J}$, given by

$$\mathbf{J} = \mathbf{L} + \mathbf{S} \tag{2.9}$$

where L is the azimuthal angular momentum. The magnetic moment then becomes

$$\mu = -g_l \mu_B \frac{\mathbf{L}}{\hbar} - g_s \mu_B \frac{\mathbf{S}}{\hbar} \tag{2.10}$$

where g_l and g_s are the gyromagnetic ratios, giving the ratio between the angular momentum and the magnetic momentum for azimuthal momentum and spin respectively. Laboratory measurements have shown $g_l = 1$ and $g_s = 2$ (e.g. Tipler & Llewellyn 2003) which leads to

$$\mu = -\frac{\mu_B}{\hbar}(\mathbf{L} + 2\mathbf{S}). \tag{2.11}$$

In this case the energy difference is given by

$$\Delta E = g m_j \left(\frac{e\hbar B}{2m_e} \right) = g m_j \mu_B B \tag{2.12}$$

where g is the landé factor (e.g. Tipler & Llewellyn 2003)

$$g = 1 + \frac{j(j+1) + s(s+1) - l(l+1)}{2j(j+1)} \tag{2.13}$$

where j is the *total angular momentum quantum number* and s is the *spin quantum number*. If in Eq. 2.12 we set s = 0 and j = 1, and g = 1 we obtain the normal Zeeman effect result as should be expected with zero spin.

2.3 Radiative Transfer (unpolarised light)

To consider the passage of a beam of photons from the bottom of the stellar photosphere to the point where it emerges from the star, we must consider two processes which affect the intensity of this light, namely emission and absorption. In this thesis I do not consider electron scattering because it only becomes significant in hotter B- and O-type stars in which there is an abundance of ionised hydrogen (e.g. Gray 2005), and is not considered in COSSAM (see Chapter 3).

2.3.1 Emission

Spontaneous emission occurs when a photon is emitted from an atom as a result of an electron falling from an excited state to a lower state. To determine the increase in intensity of a beam of EM radiation due to emission, we use

$$dI_\nu = j_\nu ds \tag{2.14}$$

where ν is the frequency of the photon, dI_ν is the increase in the intensity of light from emission. The distance the beam travels is ds and

$$j_\nu = \frac{\epsilon_\nu \rho}{4\pi} \tag{2.15}$$

where ϵ_ν is the emissivity and ρ is the mass density of the photosphere.

2.3.2 Absorption

Absorption occurs when a photon, which has the energy required to promote an electron to an excited state, is absorbed by an atom. To determine the change in intensity of a beam of EM radiation due to absorption, dI_ν, we use

$$dI_\nu = -\alpha_\nu I_\nu ds \tag{2.16}$$

where the distance the beam travels is ds and

$$\alpha_\nu = \rho\kappa_\nu \tag{2.17}$$

where ρ is the mass density of the photosphere and κ_ν is the *mass absorption coefficient.*

2.3.3 Optical Depth and the Source Function

After determining how absorption and emission effect the intensity of light as it passes through a stellar atmosphere we can combine the two effects to find the combined effects of the two. This is given by

$$dI_\nu(\nu) = -\alpha_\nu I_\nu ds + j_\nu ds. \tag{2.18}$$

Instead of defining the change in flux per distance travelled, it is possible to define the quantities *optical depth* (τ) and the *source function* (S)

$$d\tau_\nu = \alpha_\nu ds \tag{2.19}$$

and

$$S_\nu = \frac{j_\nu}{\kappa_\nu}. \tag{2.20}$$

The optical depth defines the opaqueness of the stellar photosphere for a particular wavelength. A photosphere is optically thick if $\tau > 1$ and is optically thin if $\tau \leq 1$. An optically thick medium is one for which an average photon cannot pass through without being absorbed. The source function as shown in Eq. 2.20 is the ratio of emission to

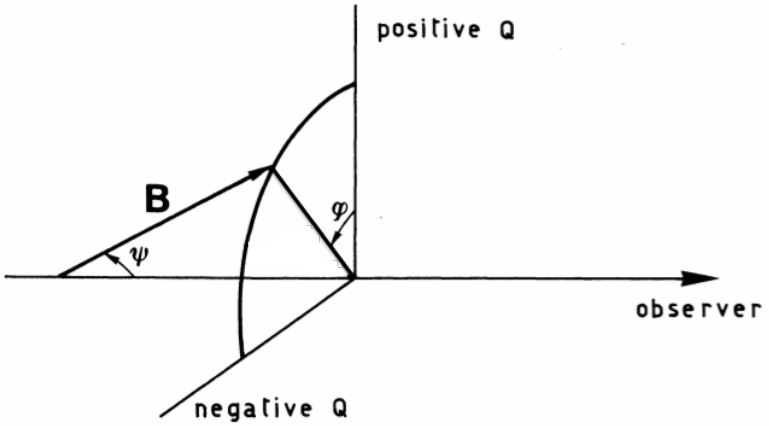

Figure 2.3: The geometry used by the Stokes profiles Analyser program. ψ gives the inclination of the magnetic field, with respect to the observer, and ϕ rotates the magnetic field. Image credit Landolfi & Landi Degl'Innocenti (1982)[2].

absorption and so describes the number of photons absorbed and emitted as a beam of radiation traverses a medium. In the case of local thermodynamic equilibrium it is possible to make the assumption

$$S_\nu(T) = B_\nu(T) = \frac{2h\nu^2}{c^2\left[e^{(h\nu/k_BT)} - 1\right]} \tag{2.21}$$

where $B_\nu(T)$ is the Planck function. Including these quantities into Eq. 2.18 gives

$$\frac{dI_\nu}{d\tau_\nu} = -I_\nu + B_\nu(T). \tag{2.22}$$

[2]Figure 1 in *Magneto-optical effects and the determination of vector magnetic fields from stokes profiles*, M. Landolfi and E. Landi DeglInnocenti, 1982, Solar Physics, Vol. 78, Issue 2, page 355, http://dx.doi.org/10.1007/BF00151615

2.4 Radiative Transfer (polarised light)

In the presence of a large scale ordered magnetic field, the light observed from a star will be polarised as a result of the Zeeman effect (Section 2.2). The degree of polarisation is related to the orientation, strength and structure of the magnetic field. Taking advantage of this additional polarisation requires the use of the coupled radiative transfer equations (given in Rees, Durrant & Murphy (1989))

$$\frac{d\boldsymbol{I}}{dz} = -\boldsymbol{K}\boldsymbol{I} + \boldsymbol{j} \tag{2.23}$$

where $\boldsymbol{I} = (I, Q, U, V)$, $\boldsymbol{K}$ is the *total absorption matrix* given by

$$\boldsymbol{K} = \kappa_c \boldsymbol{i} + \kappa_0 \boldsymbol{\alpha} \tag{2.24}$$

where $\boldsymbol{i}$ is a unit matrix and $\boldsymbol{j}$ is the *total emission vector* given by

$$\boldsymbol{j} = \kappa_c S_c \boldsymbol{e}_0 + \kappa_0 S_l \boldsymbol{\alpha} \boldsymbol{e}_0. \tag{2.25}$$

where κ_c is the continuum opacity and κ_0 is the line center opacity. In the case of local thermodynamic equilibrium, $S_c = S_l = B_\nu(T)$ and

$$\boldsymbol{\alpha} = \begin{pmatrix} \alpha_I & \alpha_Q & \alpha_U & \alpha_V \\ \alpha_Q & \alpha_I & \alpha'_V & -\alpha'_U \\ \alpha_U & -\alpha'_V & \alpha_I & \alpha'_Q \\ \alpha_V & \alpha'_V & -\alpha'_Q & \alpha_I \end{pmatrix} \tag{2.26}$$

where the absorption and anomalous dispersion profiles are given by

$$\begin{aligned}
\alpha_I &= \frac{1}{2}\alpha_p \sin^2\psi + \frac{1}{4}(\alpha_r + \alpha_b)(1 + \cos^2\psi), \\
\alpha_Q &= \frac{1}{2}[\alpha_p - \frac{1}{2}(\alpha_r + \alpha_b)] \sin^2\psi \cos 2\phi, \\
\alpha_U &= \frac{1}{2}[\alpha_p - \frac{1}{2}(\alpha_r + \alpha_b)] \sin^2\psi \sin 2\phi, \\
\alpha_V &= \frac{1}{2}(\alpha_r - \alpha_b) \cos\psi, \\
\alpha'_Q &= \frac{1}{2}[\alpha'_p - \frac{1}{2}(\alpha'_r + \alpha'_b)] \sin^2\psi \cos 2\phi, \\
\alpha'_U &= \frac{1}{2}[\alpha'_p - \frac{1}{2}(\alpha'_r + \alpha'_b)] \sin^2\psi \sin 2\phi, \\
\alpha'_V &= \frac{1}{2}(\alpha'_r - \alpha'_b) \cos\psi,
\end{aligned} \tag{2.27}$$

where, in the case of a normal Zeeman triplet, p is the π component of the Zeeman split line and b and r are the σ components of the Zeeman split line. The orientation of the magnetic field is given by ψ and ϕ as shown in Fig. 2.3.

2.4.1 Analytical solution

The radiative transfer equations (Eq. 2.23) are solved numerically within COSSAM (Chapter 3) using the Zeeman Feautrier method (Rees, Durrant & Murphy 1989). To solve the equations analytically, Unno (1956) presented a solution based on four simplifications (Landolfi & Landi Degl'Innocenti 1982):

- The atmosphere is plane-parallel and unidimensional
- The source function is linear with optical depth
- The ratio of line and continuous absorption coefficients is constant
- Magneto-optical effects are neglected.

However, it was shown by Wittmann (1971), Calamai, Landi Degl'Innocenti & Landi Degl'Innocenti (1975) and Landi Degl'Innocenti (1979) that it is important to consider magneto-optical effects. Magneto-optical effects occur as the result of the application of an external magnetic field to a medium which causes a change in the optical properties of the medium (e.g. Pershan 1967). Landolfi & Landi Degl'Innocenti (1982) present the polarised transfer equations including the simplifications above with the exception that they include the magneto-optical effects. This results in the following equations

$$\begin{aligned}
I &= B_0 + \mu B_1 \Delta^{-1}[(1+\eta_I)((1+\eta_I)^2 + \rho_Q^2 + \rho_U^2 + \rho_V^2)] \\
Q &= -\mu B_1 \Delta^{-1}[(1+\eta_I)^2\eta_Q + (1+\eta_I)(\eta_V\rho_U - \eta_U\rho_V) + \rho_Q(\eta_Q\rho_Q + \eta_U\rho_U + \eta_V\rho_V)] \\
U &= -\mu B_1 \Delta^{-1}[(1+\eta_I)^2\eta_U + (1+\eta_I)(\eta_Q\rho_V - \eta_V\rho_Q) + \rho_U(\eta_Q\rho_Q + \eta_U\rho_U + \eta_V\rho_V)] \\
V &= -\mu B_1 \Delta^{-1}[(1+\eta_I)^2\eta_V + \rho_V(\eta_Q\rho_Q + \eta_U\rho_U + \eta_V\rho_V)]
\end{aligned} \tag{2.28}$$

where μ is the electromagnetic permeability, B_0 and B_1 are used to define the source function versus optical depth and

$$\Delta = (1+\eta_I)^2[(1+\eta_I)^2 - \eta_Q^2 - \eta_U^2 - \eta_V^2 + \rho_Q^2 + \rho_U^2 + \rho_V^2] - (\eta_Q\rho_Q + \eta_U\rho_U + \eta_V\rho_V)^2 \quad (2.29)$$

where

$$\begin{aligned}
\eta_I &= \frac{1}{2}[\eta_p \sin^2\psi + \frac{1}{2}(\eta_r + \eta_b)(1+\cos^2\psi)] \\
\eta_Q &= \frac{1}{2}[\eta_p - \frac{1}{2}(\eta_r + \eta_b)]\sin^2\psi\cos 2\phi \\
\eta_U &= \frac{1}{2}[\eta_p - \frac{1}{2}(\eta_r + \eta_b)]\sin^2\psi\sin 2\phi \\
\eta_V &= \frac{1}{2}(\eta_r - \eta_b)\cos\psi \\
\rho_Q &= \frac{1}{2}[\rho_p - \frac{1}{2}(\rho_r + \rho_b)]\sin^2\psi\cos 2\phi \\
\rho_U &= \frac{1}{2}[\rho_p - \frac{1}{2}(\rho_r + \rho_b)]\sin^2\psi\sin 2\phi \\
\rho_V &= \frac{1}{2}(\rho_r - \rho_b)\cos\psi
\end{aligned} \quad (2.30)$$

where

$$\begin{aligned}
\eta_p &= \eta_0 H(a,\nu) \\
\eta_{b,r} &= \eta_0 H(a,\nu \pm \nu_H) \\
\rho_p &= 2\eta_0 F(a,\nu) \\
\rho_{b,r} &= 2\eta_0 F(a,\nu \pm \nu_H)
\end{aligned} \quad (2.31)$$

where η_0 is strength of the absorption line and ν_H is the Zeeman splitting normalised to the Doppler broadening, a is a damping constant and ν is the wavelength at which the profile is to be calculated. H and F are the Voigt and Voigt-Faraday functions (e.g. Landolfi & Landi Degl'Innocenti 1982) which describe the magneto-optical effects of the star. Since the purpose of this analysis is simply to understand in a simple way the effects of modifying ψ, ϕ, η_0 and ν_h, I consider constant values of B_0 and B_1.

I have used the above equations to produce, Figs. 2.4, 2.5, 2.6, & 2.7, to show how varying the orientation and strength of the magnetic field and the strength of the absorption line affects the Stokes $IQUV$ profiles.

As discussed in Section 2.2, under the classical interpretation of the Zeeman effect the electron's motion is analogous to a harmonic oscillator, with the electron

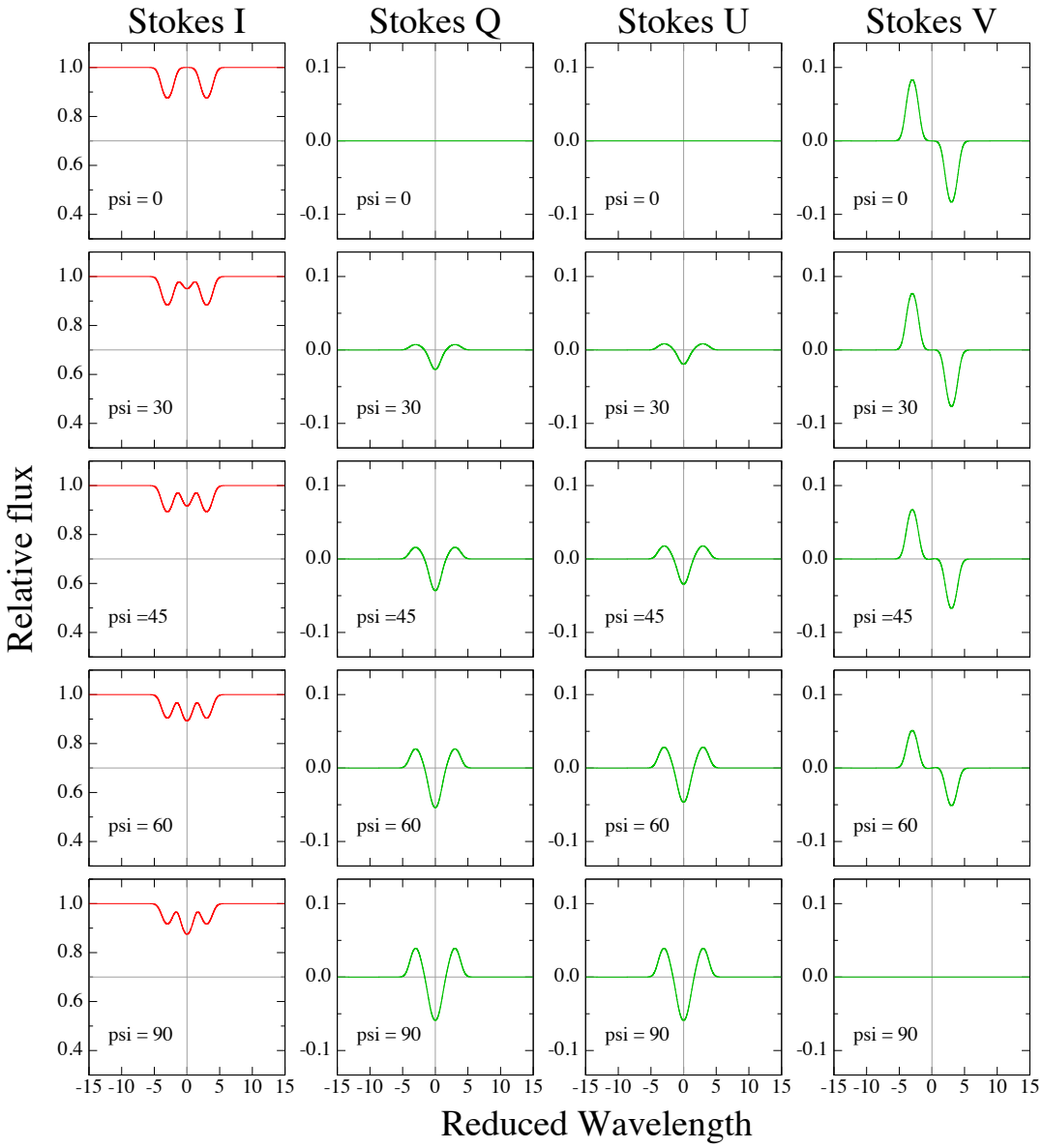

Figure 2.4: The effect of the inclination (ψ) of the magnetic field vector with respect to the observer on Stokes $IQUV$. The sequence of Stokes profiles were generated using equations from Landolfi & Landi Degl'Innocenti (1982), with ψ varying between 0° and 90°. The other input parameters, ν_H, η_0 and ϕ (see text for more information), are set to: 3, 1 and 22.5°, respectively.

orbiting about the magnetic field vector. At $\psi = 0°$ the observer's line of sight is parallel to the magnetic field and so the circular motion of the electron, as a result of the magnetic field, will be seen face on. The electron can either orbit clockwise or anti-clockwise, this leads to two spectral lines being seen in Stokes I and both left and right-handed polarisations being seen in Stokes V; shown by Fig. 2.4. In the case of $\psi = 90°$, the observer's line of sight is perpendicular to the magnetic field and so the circular motion is viewed edge on. As a result, the observer will see both the clockwise and anti-clockwise orbits as linear oscillations in opposite directions. In addition, the observer will be able to see a linear oscillation parallel to the magnetic field vector, this was not visible at $\psi = 0°$ because it is not oscillating in that line of sight. As ψ varies, away from the two extremes at 0° and 90°, contributions from Q, U and V can be seen simultaneously.

It can clearly be seen from Fig. 2.5 that ϕ has no effect on the circular polarisation Stokes V or intensity Stokes I. Once again under the classical picture of the Zeeman effect, no matter to what value ϕ is set, Stokes V will simply rotate with respect to the electron orbit and so produce unchanged left and right-handed polarisation, as a result Stokes V is unchanged by ϕ. However, changing ϕ strongly affects Stokes Q and U, the linear polarisation changes from vertical to horizontal. This leads to a change in Stokes Q and U going from + Q to + U to - Q as ϕ changes from 0° to 90°.

The strength of the Zeeman splitting is modified with the parameter ν_H, the effect of increasing this is shown by Fig. 2.6. With $\nu_H = 0$, there is no effect on Stokes I and the remaining Stokes profiles are zero, this is because without a magnetic field, in this particular model, there is nothing to cause polarisation. As the value increases, Stokes I splits into a triplet with the separation increasing with increasing ν_H. The remaining Stokes profiles also appear and broaden relative to Stokes I.

In Fig. 2.7, it can be seen that for $\eta_0 = 0$ there is no drop in intensity, this is because there are no atoms to absorb the EM radiation and so there is no drop in intensity; all of the light passes through unaffected. As η_0 increases, the strength of the Stokes profiles increases, as shown by Fig. 2.7. This is as a result of the number

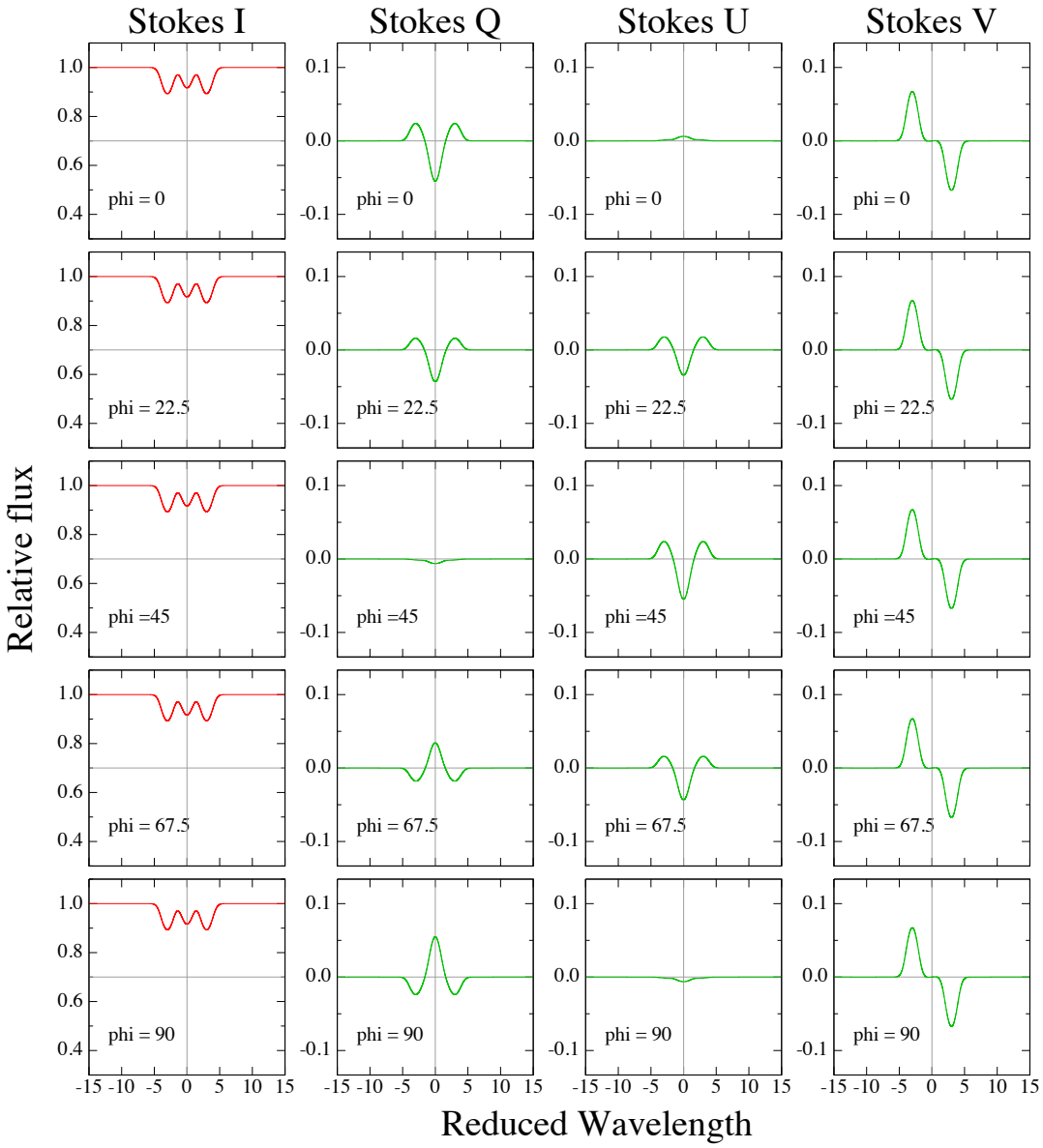

Figure 2.5: The effect of the orientation (ϕ) of the magnetic field vector with respect to the observer on Stokes $IQUV$. The sequence of Stokes profiles were generated using equations from Landolfi & Landi Degl'Innocenti (1982), with ϕ varying between 0° and 90°. The other input parameters, ν_H, η_0 and ψ (see text for more information), are set to: 3, 1, 45°, respectively.

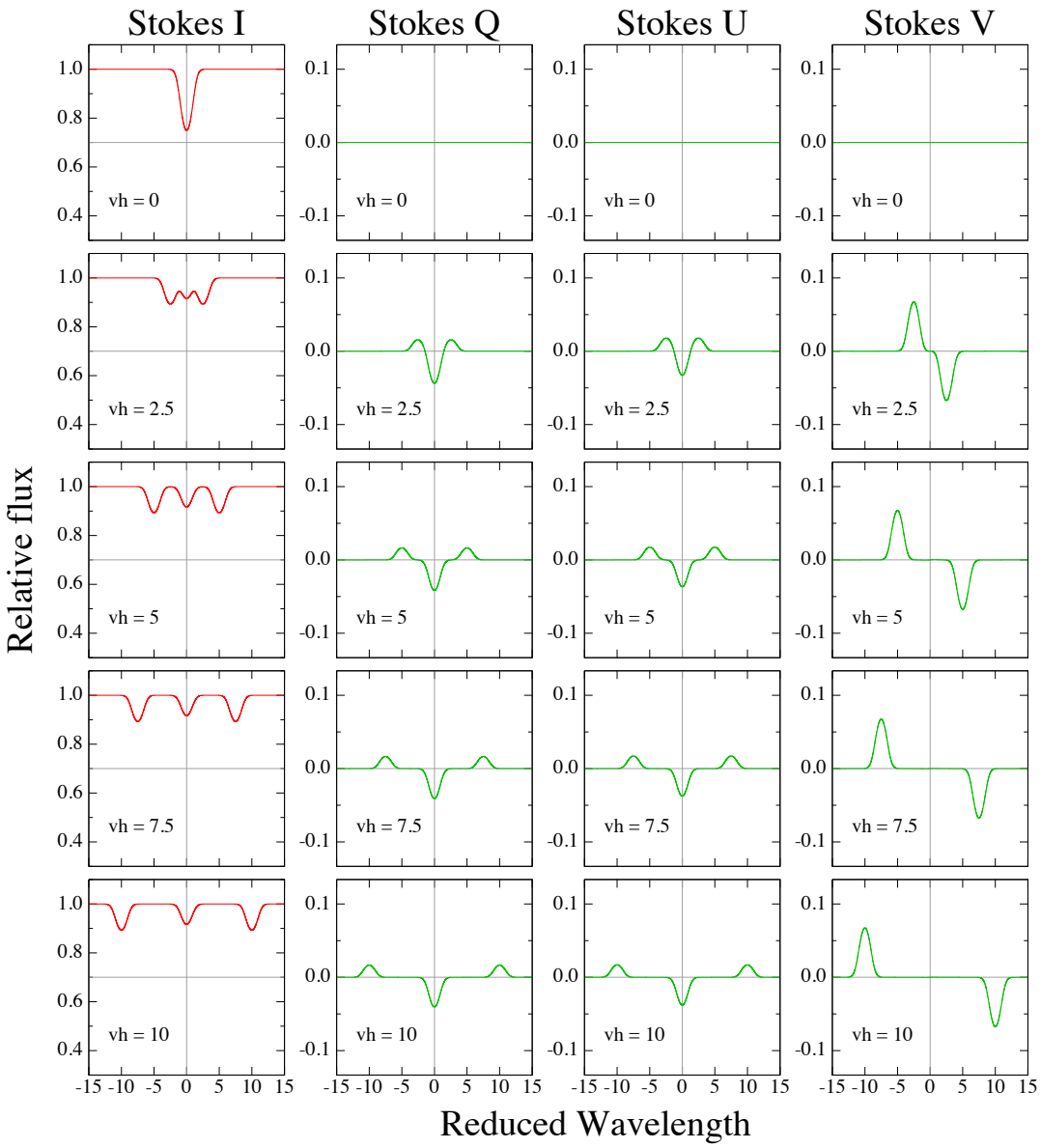

Figure 2.6: The effect of the magnetic field strength (ν_H) on Stokes $IQUV$. The sequence of Stokes profiles were generated using equations from Landolfi & Landi Degl'Innocenti (1982), with ν_H varying between 0 and 10. The other input parameters, η_0, ψ, ϕ (see text for more information), are set to: 1, 45°, 22.5°, respectively.

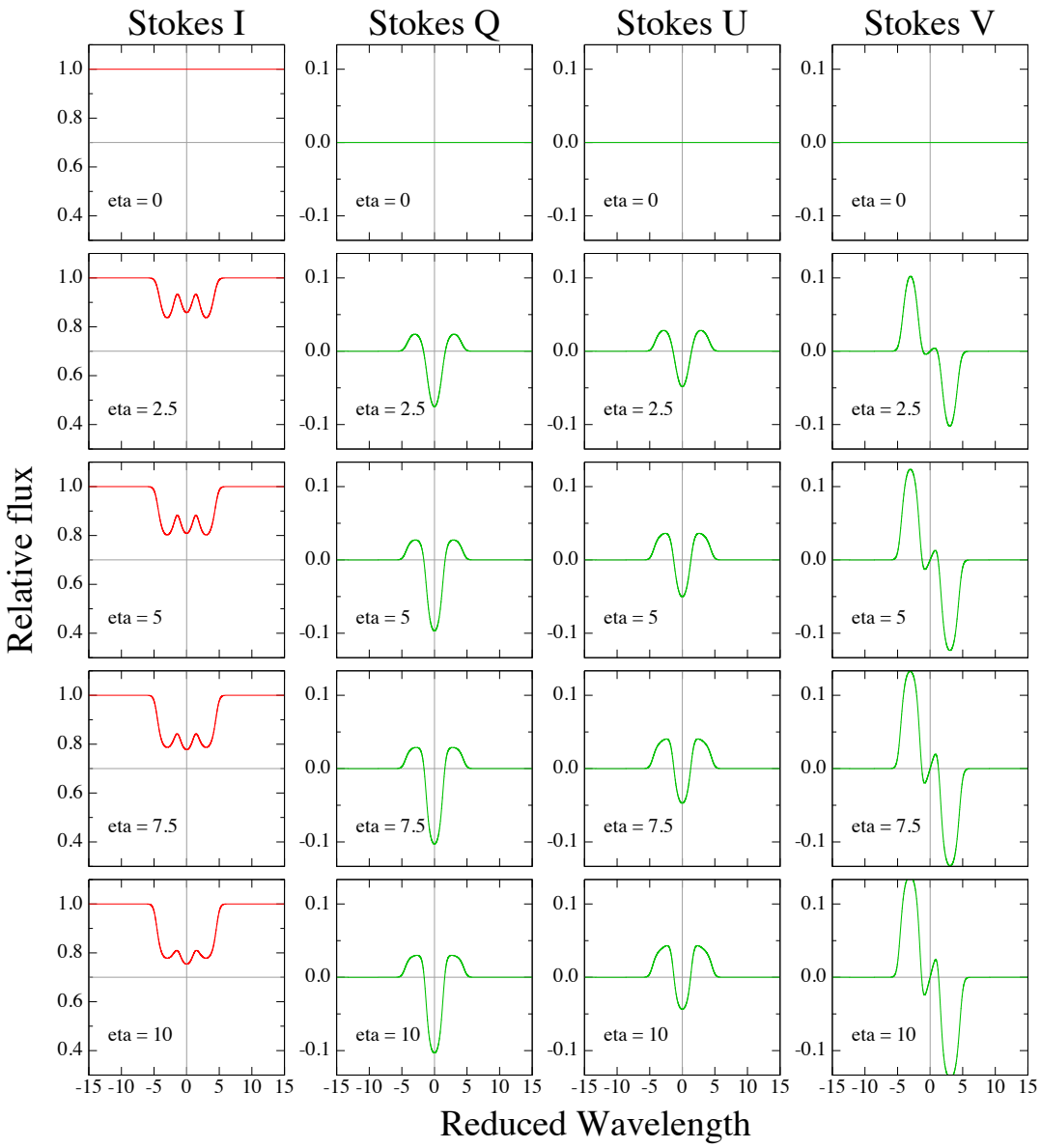

Figure 2.7: The effect of the chemical abundance of a single element (η_0) on Stokes $IQUV$. The sequence of Stokes profiles were generated using equations from Landolfi & Landi Degl'Innocenti (1982), with η_0 varying between 0 and 10. The other input parameters, ν_H, ψ, ϕ (see text for more information), are set to: 3, 45°, 22.5°.

of atoms increasing with larger η_0, leading to the observer seeing increasingly higher, cooler and consequently lower intensity regions of the atmosphere.

2.5 Summary of radiative transfer

To solve the radiative transfer problem in a stellar photosphere requires knowledge of a number of processes within the stellar photosphere. The stellar properties have a large impact on the formation of spectral lines in the atmosphere this, however, is beneficial since we are able to measure a multitude of properties as a result. The magnetic field of a star further complicates the radiative transfer problem by introducing further considerations into the radiative transfer equations. However, it also allows us to exploit the polarisation of light caused by the Zeeman effect, which adds additional data, in the form of the Stokes $IQUV$ profiles, for analysis.

3 COSSAM

COSSAM stands for "**Co**dice per la **s**intesi **s**pettrale nelle **a**tmosfere **m**agnetiche" and is a polarised line synthesis code written by M.J. Stift. It has been described and its performance compared to that of other spectral synthesis codes by Wade et al. (2001). Further details on COSSAM can be found in Stift, Leone & Cowley (2012). The code is available to the astronomical community under GNU copyleft (Stift 2000). With present versions of COSSAM it is possible to calculate detailed Stokes $IQUV$ spectra of stars with a simple dipole field (Landolfi, Bagnulo & Landi Degl'Innocenti 1998), a dipole plus quadrupole field (Landolfi, Bagnulo & Landi Degl'Innocenti 1998) or a non-axisymmetric decentred dipole field (Stift 1975). Vertical and/or horizontal ("spots" or "rings") abundance distributions can also be treated. The lineage of COSSAM can be traced back to the ALGOL 60 code ANALYSE 65 by Baschek, Holweger & Traving (1966) and to the Fortran code ADRS3 by Chmielewski (1979). COSSAM is written entirely in Ada (section 1.4) which makes it possible to take full advantage of the unique parallel constructs of the Ada programming language on multi-core architectures.

To calculate a synthetic spectrum, it is first necessary to establish either an ATLAS9 or an ATLAS12 model atmosphere (see Kurucz 2005 and Castelli 2005). ATLAS12_ADA, also written entirely in Ada, provides the atmospheric input file in the format required by COSSAM (see section 3.1) and by the LINES code. LINES, taking atomic transition data from the VALD database (Piskunov et al. 1995), selects the transitions with a central opacity at least 10^{-3} times the local continuum opacity (see section 3.2), determines the Zeeman splitting and stores these line data in intermediary files for use with COSSAM. Having created a spatial grid covering the visible hemisphere of the star, and having determined the magnetic field direction and field strength at each quadrature point, COSSAM carries out detailed opacity sampling and solves the coupled polarised radiative transfer equations (Eq. 2.23) by means of the Zeeman Feautrier method (Rees, Durrant & Murphy 1989). A two-dimensional integration of the Doppler shifted local Stokes profiles leads to the final synthetic spectrum. A simpli-

fied version, CossamSimple, has been developed by M.J. Stift for non-magnetic stars, where local spectra solely depend on $\mu = \cos\theta$, and yields only the intensity spectrum (Stokes I). I chose to use Cossam as the backend for my spectral analysis code for several reasons. Most importantly, Cossam offers a fair amount of freedom in terms of describing the magnetic morphology and abundance distributions (both vertically and horizontally) in the stellar photosphere. Cossam is also fully parallelised with the inverse execution time scaling almost linearly with the number of available CPU cores. Cossam has the additional benefit of being free software (under copyleft protection as mentioned previously), making my inversion code independent of proprietary programs. Finding that the results obtained with the help of my inversion code are consistent with those found by other authors indicates reproducibility, reliability and possibly uniqueness. Importantly, the spectral synthesis parts of the codes have to be tested to confirm that they yield identical spectra for the same model parameters, to make sure that differences in the results originate from the inversion algorithms. This has been done in the past by Wade et al. (2001) who extensively compared the respective performances of Cossam, Invers10 (Piskunov 1998) and Zeeman2 (Landstreet 1988).

In this chapter I describe the process of calculating a synthetic spectrum with Cossam, introduce the different kinds of spatial grids and magnetic geometries provided by Cossam, and list the vertical and horizontal abundance inhomogeneities which can be modelled. I shall also introduce the new code Cossam Simple used for the modelling of non-magnetic spectra.

3.1 Modelling Stellar Atmospheres

The first step when calculating a synthetic spectrum with Cossam or Cossam Simple is the calculation of a model stellar atmosphere. A model atmosphere specifies the temperature, gas pressure, electron pressure and standard continuous opacity in relation to optical depth for a given $T_{\rm eff}$, $\log g$ and chemical composition. Cossam calculates syn-

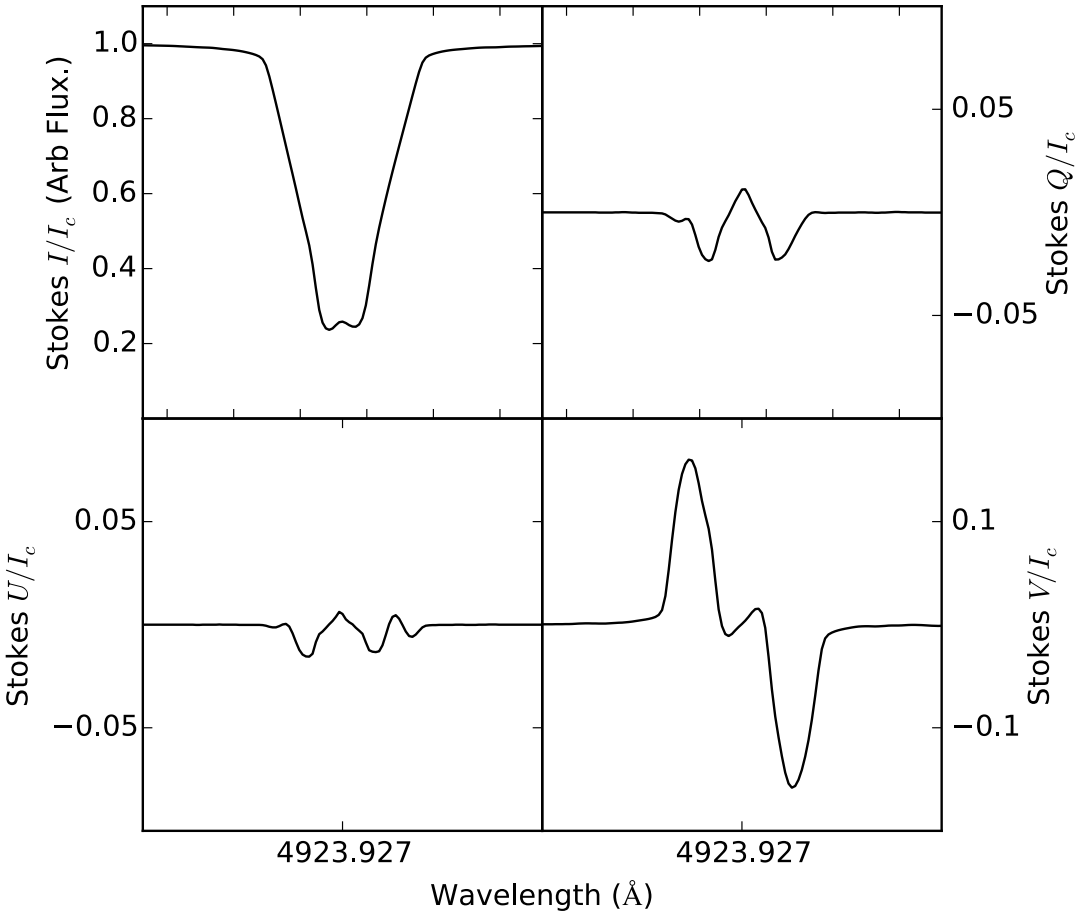

Figure 3.1: The Fe II 4923.927Å line synthesised by COSSAM, using a dipole + quadrupole field geometry and parameters: $i = 45.00°$, $\beta = 50.00°$, $\beta_1 = 10.00°$, $\beta_2 = 140.00°$, $\gamma_1 = 350.00°$, $\gamma_2 = 6.00°$, $B_\mathrm{d} = 5000.00\,\mathrm{G}$, $B_\mathrm{q} = 3000.00\,\mathrm{G}$, $v \sin i = 1.00\,\mathrm{kms}^{-1}$.

thetic spectra under the assumption of local thermodynamic equilibrium (LTE), and so it makes sense to either use ATLAS9 (Kurucz 2005) or ATLAS12 (see Kurucz 2005 and Castelli 2005). LTE implies that the excitation and de-excitation of atomic levels is dominated by collisions rather than by radiative transitions, it also means that the typical distance travelled by particles and photons between collisions - their mean free path - is small compared to the scale over which the temperature changes significantly. In LTE the energy levels are populated according to the Boltzmann distribution and the ionisation equilibrium can be determined with the help of the Saha equation. For both, the atomic partition functions are required and are provided by a routine taken from ATLAS12. Originally written in Fortran, ATLAS12 has been translated to Ada by Bischof (2005) who added a subprogram that creates an atmospheric file in the particular format required by COSSAM. COSSAM needs the monochromatic opacity at 5000 Å whereas the ATLAS codes output column density ρ_x and Rosseland mean opacity $\tau_{\rm Ross}$ (here the wavelength-dependent opacity is harmonically weighted over the temperature derivative of the Planck curve).

As I have already mentioned, the vertical structure of a model atmosphere is determined by the fundamental parameters ($T_{\rm eff}$ and $\log g$) and by the elemental abundances. When analysing a star, it is necessary to first adopt reasonable starting estimates of these parameters. $T_{\rm eff}$ and $\log g$ are determined from the Balmer lines and photometry and, in general, abundances are assumed to be solar. With better estimates for the parameters, the model atmosphere has to be recomputed, iterating until the model does not change anymore. It is important to carry out this iterative procedure since an increased number of spectral lines and increased opacity affecting the atmospheric structure by steepening the temperature gradient (Chandrasekhar 1935).

ATLAS9 uses pre-calculated opacity distribution functions which approximate the line opacity in a certain wavelength interval by some simple function. Instead of having to perform detailed opacity sampling in a highly complex distribution of line opacity with wavelength, line blanketing is taken into account in an efficient but less accurate way than ATLAS12. Non-magnetic stars featuring more or less solar abundances are quite well handled by ATLAS9 but if a star exhibits significant individual over-

abundances that do not scale with solar abundances as is the case with many Ap and Bp stars, it becomes necessary to revert to ATLAS12 model atmospheres. ATLAS12 relies entirely on opacity sampling of 10^8 or more spectral lines; in the Ada version of this code (ATLAS12_ADA) abundances are allowed to freely vary with optical depth. ATLAS12_ADA is slower than ATLAS9 but thanks to the parallel execution of the opacity sampling routine on multi-processor architectures this remains within acceptable limits. Whenever vertically stratified abundances are encountered in stars and when individual elemental abundances do not scale with solar abundances, ATLAS12_ADA has to be the code of choice.

3.2 Modelling Stellar Spectra

Once the model atmosphere has been established, it is necessary to determine the lines which contribute to the spectrum in the wavelength interval chosen, and to store them in intermediate line data files for use by COSSAM. This is handled by the code LINES which has been designed to work separately from COSSAM, making it possible to calculate spectra for many different magnetic geometries, stellar inclinations and rotational velocities with the same set of line data.

Both LINES and COSSAM work under the assumption of LTE and a plane-parallel atmosphere, which usually constitutes a reasonable approximation to the physical conditions in Ap and Bp stellar atmospheres. From the VALD line database (Piskunov et al. 1995), LINES extracts the full set of atomic transition data (including the radiation damping, Stark broadening and van der Waals broadening constants), the Landé factors and the J-values of the lower and the upper energy levels. Radiation damping determines the natural broadening of a line and is a consequence of the uncertainty principle described in Section 2.1 as applied to the finite lifetimes of the atomic levels. Stark broadening results from level splitting in the electric micro-fields of nearby charged particles, ions and electrons; it is described in Section 2.1. In F-, A- and B-type stars it is most prominently observable in the hydrogen Balmer lines (linear

Stark effect) whereas the quadratic Stark effect found in most other lines is far less conspicuous. Van der Waals broadening in the atmospheres of cooler stars can mainly be ascribed to collisions of metal ions with neutral hydrogen (see Section 2.1).

In the case of a model star hosting a magnetic field each spectral line is split into a number of Zeeman components, that can be linearly and circularly polarised (see Section 2.2). The Landé factors and J-values provided by VALD (see Section 2.2.2) make it possible to determine splitting and strengths of the individual components; where Landé factors are not given in the line database, LINES assumes a classical Zeeman triplet. The opacity profiles of the metal lines are calculated with the help of the approximation to the Voigt and Faraday functions given by Hui, Armstrong & Wray (1978). Routines taken from the TLUSTY code (Hubeny & Lanz 1995) give the hydrogen opacity profiles, the higher Balmer series members are treated according to the recipe found in Hubeny, Hummer & Lanz (1994) and based on the occupation probability formalism (Dappen, Anderson & Mihalas 1987, Hummer & Mihalas 1988, Seaton 1990).

Temperature and electron pressure at a given layer in the atmosphere, together with the Boltzmann distribution, the Saha equation, the broadening parameters of a given spectral line and the abundance of the corresponding chemical element yield the central line opacity. This line opacity must be related to the continuous opacity, κ_{c}, at this wavelength which is due to a variety of bound-free and free-free transitions. Again, routines taken from ATLAS12 provide κ_{c}. LINES selects only those atomic transitions that exhibit a central line opacity exceeding 10^{-3} times the local continuous opacity at any depth in the atmosphere and stores the data in intermediary files.

COSSAM uses the line data established by LINES for the calculation of the Stokes $IQUV$ profiles. At a given wavelength, the total line opacity matrix – resulting in general from a multitude of blended lines – is determined by detailed opacity sampling of the σ_-, σ_+, and π components separately. To solve the polarised radiative transfer equations COSSAM relies by default on the Zeeman Feautrier method (Auer, Heasley & House 1977) as reformulated for blends by Alecian & Stift (2004). Opacity sampling (taking into account macroscopic velocity fields and Zeeman splitting) and solving the

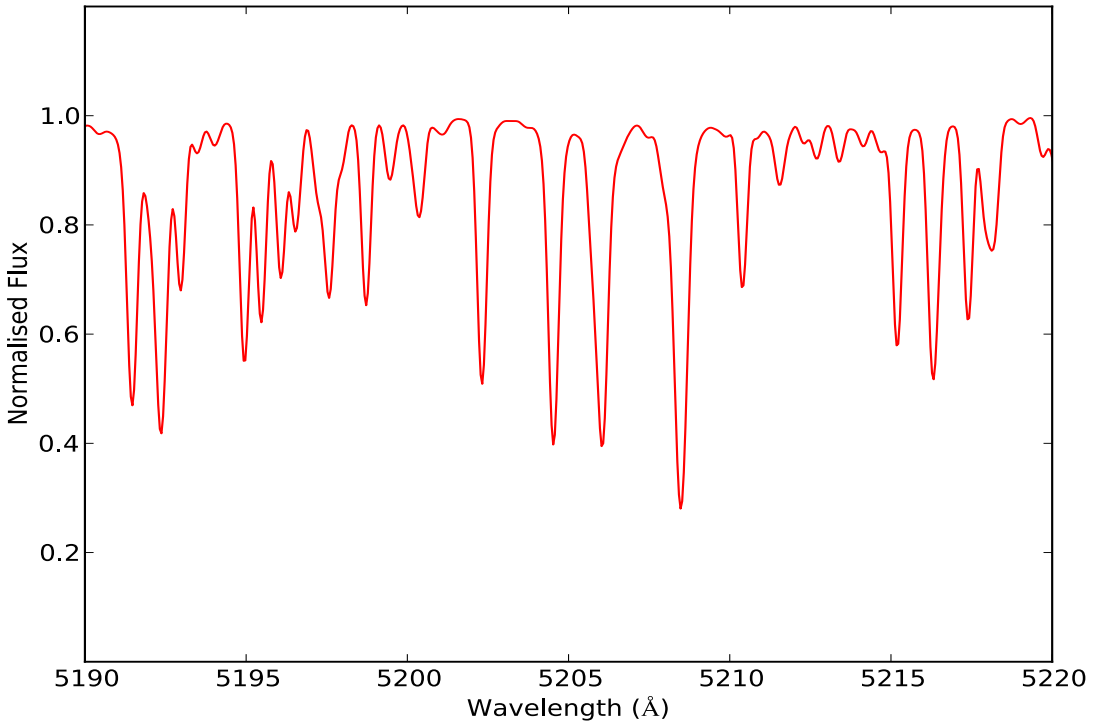

Figure 3.2: A section of a stellar spectrum synthesised by CossamSimple with stellar parameters: $T_{\rm eff} = 5800$ and $\log g = 4.49$. The abundances are those given by Asplund et al. (2009).

radiative transfer equations is done for each quadrature point of the spatial grid (section 3.3). Finally the local spectra are integrated over the entire visible stellar hemisphere to deliver the resulting global spectrum. Fig. 3.1 shows the Stokes $IQUV$ profiles obtained from Cossam of an iron line in a strong dipole + quadrupole magnetic field.

3.2.1 Cossam Simple

Cossam Simple belongs to the Cossam family of codes and has been optimised for the fast and efficient modelling of the spectra of non-magnetic stars. In the magnetic

case featuring a complex magnetic geometry, local spectra have to be calculated for every grid point over the visible hemisphere. In the non-magnetic case however it is not only possible to take advantage of certain symmetries, but also replace the Zeeman Feautrier solver with the much faster classical Feautrier solver (Feautrier 1964). Local spectra are calculated at a number of positions in $\mu = \cos\theta$ from the centre of the disc to the limb. These are then integrated – appropriately shifted according to the line-of-sight component of the rotational velocity – over the entire disc. This simple procedure reduces the number of local spectra to be calculated from hundreds or thousands to a few tens at most. COSSAM SIMPLE also caters for vertical stratifications.

3.3 Cossam spatial grids

The spatial grids provided by COSSAM define the points over the stellar surface where local Stokes profiles are calculated. Three different grid types are found in COSSAM: *observer-centred*, *adaptive* and *co-rotating*.

Observer-centred grids are simply determined by the observer's choice of the number of rings and sectors into which the visible hemisphere is divided. Neither magnetic field nor stellar rotation have an impact on the distribution of the quadrature points. The *observer-centred* grid is the only one available for COSSAMSIMPLE .

An *adaptive* grid makes it possible to reduce the number of quadrature points and is discussed in Stift (1985) and Fensl (1995). A special algorithm determines the optimum 2D-integration over the visible hemisphere by ensuring that the change in the monochromatic opacity matrix between two adjacent quadrature points does not exceed a certain percentage. Depending on the rotation in conjunction with the magnetic geometry, the distribution of quadrature points can be highly asymmetric as shown in Fig. 3.3. For a given accuracy of the resulting integrated profiles, adaptive grids can considerably reduce the overall number of quadrature points compared to fixed grids.

The *co-rotating* grid, extensively used in Doppler mapping (see for example Vogt,

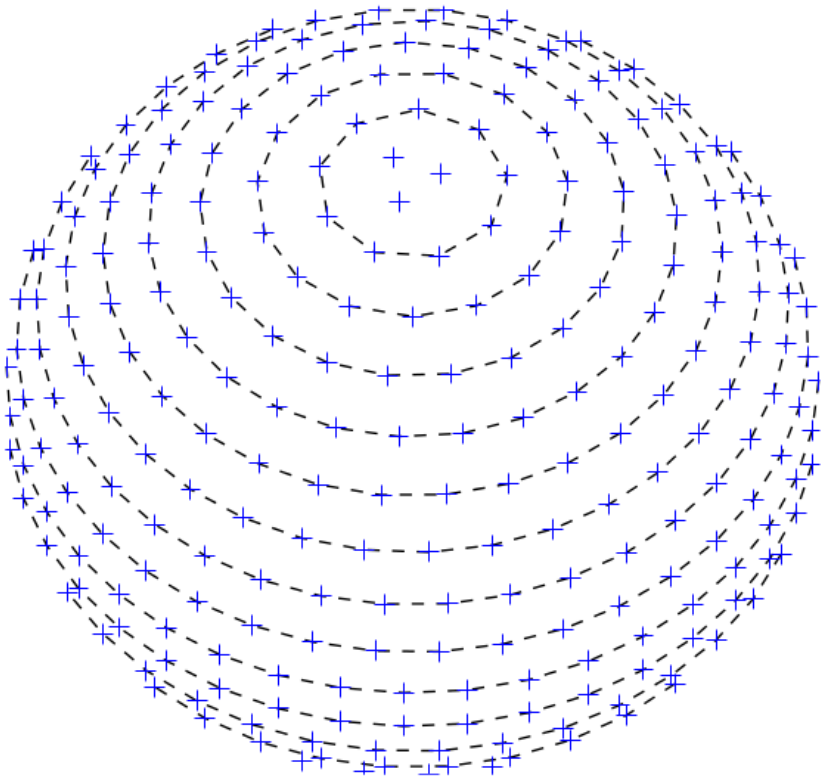

Figure 3.3: An example of the *co-rotating* grid provided by COSSAM. The blue crosses indicate the points over the visible stellar surface where COSSAM establishes local Stokes profiles, carrying out opacity sampling and solving the coupled equations of polarised radiative transfer. The dashed black lines connect points of equal latitude. The rotation axis of the star is inclined by 20° with respect to the line of sight.

Penrod & Hatzes 1987), splits the entire stellar surface into elements of approximately equal size. Such a grid type is at the basis of the modelling of chemical and magnetic spots. An example of a *co-rotating* grid is shown in Fig. 3.3; the fact that in this example the rotation axis of the star is inclined by 20° with respect to the line-of-sight leads to a concentration of points in the lower part of the plot.

3.4 Magnetic Field Parameterisation

In magnetic Ap stars, typically the field vector is not aligned with the rotation axis. This so called Oblique Rotator model is shown schematically in Fig. 3.4. Within this framework it is possible to specify a simple dipole or a dipole + quadrupole magnetic morphology. The publicly available version of COSSAM offers a tilted eccentric dipole geometry which I shall also describe below.

3.4.1 Dipole Field

The dipole field is the simplest magnetic field possible. To create a dipole, two poles are separated by a distance which is considerably smaller than the distance at which the field will be measured. To parametrise this field we need to define some quantities which are shown in Fig. 3.4. The x-axis in the figure is aligned with the North celestial pole, the y-axis is aligned with the celestial meridian and the z-axis is aligned with the observer's line of sight. The vector joining C and R is one half of the rotation axis of the star, C is the center of the star, and R is the point at which the rotation axis emerges in the northern hemisphere. The northern rotation pole is defined so that an observer standing at the pole sees the star rotating counterclockwise. The magnetic axis of the star, $\boldsymbol{u}$, is at an angle β from the rotation axis of the star and M is the positive magnetic pole. The inclination, i, of the star is the angle between R and the z-axis. The azimuthal angle, θ, is the angle between the x-axis and the projection of the rotation axis on the $x-y$ plane. The angle f is the azimuth of dipole axis with

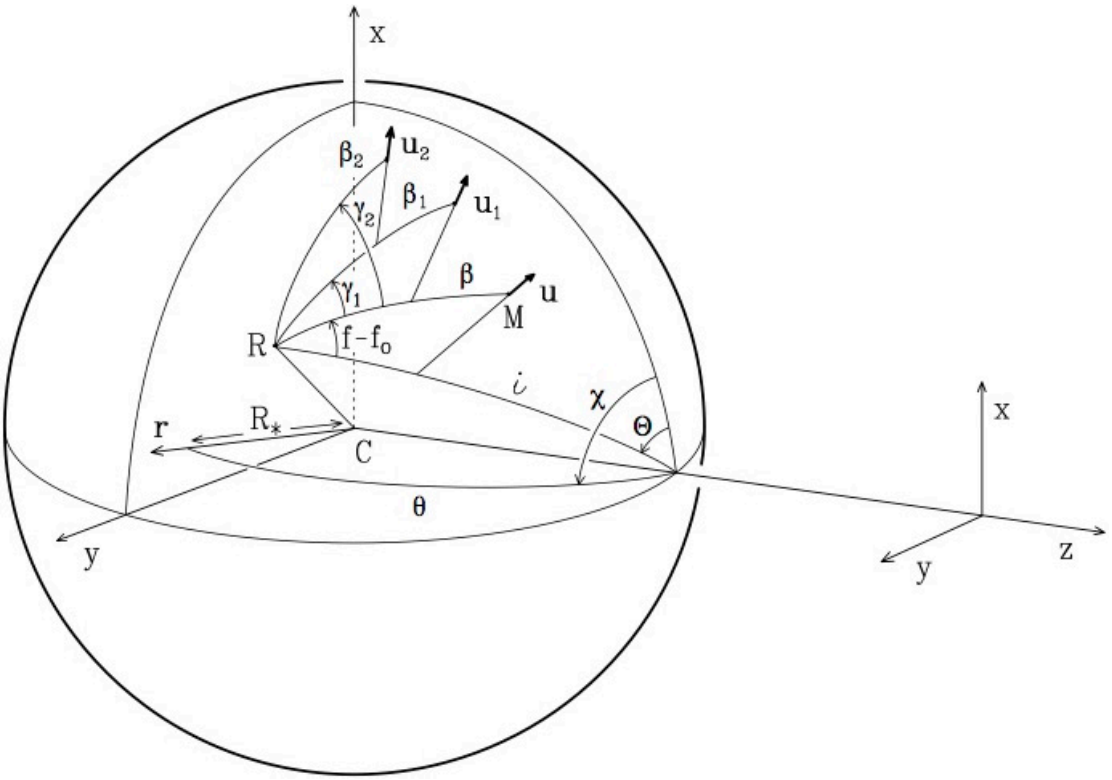

Figure 3.4: The geometry of the dipole + quadrupole magnetic field configuration (Landolfi, Bagnulo & Landi Degl'Innocenti 1998)[1].

[1]Figure 1 in *Modelling of magnetic fields of CP stars I. A diagnostic method for dipole and quadrupole fields from Stokes I and V observations*, 1998, M. Landolfi , S. Bagnulo, and M. Landi Degl'Innocenti, A&A, Vol. 338, page 111, reproduced with permission © ESO.

respect to the star's rotation axis and at the point where $f = f_0$ the angle between the z-axis and $\boldsymbol{u}$ is at its minimum. The magnetic field vector at any point in the star, $\mathbf{B}_d(\mathbf{r})$, is given by Landolfi, Bagnulo & Landi Degl'Innocenti (1998) as

$$\mathbf{B}_d(\mathbf{r}) = -\frac{B_d}{2}\left[\mathbf{u} - 3\frac{\mathbf{u}\cdot\mathbf{r}}{R_*^2}\mathbf{r}\right] \tag{3.1}$$

where R_* is the radius of the star and B_d is the magnetic dipole field modulus at the pole of the star.

3.4.2 Quadrupole field

A quadrupole field is generated by two dipoles, with opposite sign, separated by a distance, which as before, is much smaller than the distance at which the field is to be measured.

The addition of two extra dipole moments, increases the complexity of magnetic fields which can be modelled. The definitions of the parameters in Fig. 3.4 are the same as Section 3.4.1, with the addition of the vectors which describe the position of the additional dipole moments with respect to the rotation axis CR and dipolar axis $\boldsymbol{u}$. The angles β_1 and β_2 are the angles between the rotation axis CR and the unit vectors $\boldsymbol{u}_1$ and $\boldsymbol{u}_2$ respectively. The angles γ_1 and γ_2 are the azimuth angles between the unit vectors $\boldsymbol{u}_1$ and $\boldsymbol{u}_2$ respectively, and the dipole vector $\boldsymbol{u}$. In the case of a quadrupole the magnetic field vector at any point in the star, $\mathbf{B}_q(\mathbf{r})$, is given by Landolfi, Bagnulo & Landi Degl'Innocenti (1998) as

$$\mathbf{B}_q(\mathbf{r}) = -\frac{B_q}{2}\left[\frac{\mathbf{u_2}\cdot\mathbf{r}}{R_*}\mathbf{u_1} + \frac{\mathbf{u_1}\cdot\mathbf{r}}{R_*}\mathbf{u_2} + \left(\frac{\mathbf{u_1}\cdot\mathbf{u_2}}{R_*} - 5\frac{(\mathbf{u_1}\cdot\mathbf{r})(\mathbf{u_2}\cdot\mathbf{r})}{R_*^3}\right)\mathbf{r}\right] \tag{3.2}$$

where B_q is the field strength at the pole if all unit vectors were aligned.

3.4.3 Non-axisymmetric decentred dipole

The standard version of COSSAM uses a non-axisymmetric tilted eccentric dipole morphology (Stift 1975) to model the magnetic field of magnetic stars. In this parametrisation the dipole need not pass directly through the centre of the star, the dipole axis may

intersect the stellar surface at any angle. A combination of rotation matrices define the position of the dipole axis and of the magnetic field with respect to the rotational axis and to the observer. The transformation matrix, S, which represents a rotation about the x-axis, S_α, a rotation about the z-axis, S_β, and another rotation about the new x-axis, S_γ, is given by

$$S = \begin{pmatrix} \cos\beta & \cos\alpha\sin\beta & \sin\alpha\sin\beta \\ -\sin\beta\cos\gamma & \cos\alpha\cos\beta\cos\gamma - \sin\alpha\sin\gamma & \sin\alpha\cos\beta\cos\gamma + \cos\alpha\sin\gamma \\ \sin\beta\sin\gamma & -\cos\alpha\cos\beta\sin\gamma - \sin\alpha\cos\gamma & -\sin\alpha\cos\beta\sin\gamma + \cos\alpha\cos\gamma \end{pmatrix} \tag{3.3}$$

The matrix S generates the transformation from the rotational system of the star to the dipole system, the rotation of the dipole around the rotation axis is generated by the matrix S_ϕ

$$S_\phi = \begin{pmatrix} \cos\phi & \sin\phi & 0 \\ -\sin\phi & \cos\phi & 0 \\ 0 & 0 & 1 \end{pmatrix} \tag{3.4}$$

where ϕ is is the azimuth of dipole axis with respect to the star's rotation axis. The move from the observer's reference system to the rotational system of the star is given by the matrix

$$S_i = \begin{pmatrix} 1 & 0 & 0 \\ 0 & \cos i & \sin i \\ 0 & -\sin i & \cos i \end{pmatrix} \tag{3.5}$$

where i is the inclination of the star. With the help of these matrices we obtain the coordinates $\boldsymbol{r}$ (in the dipole system) of a surface point $\boldsymbol{z}$ on the visible hemisphere (in the observer's system) relative to the dipole position $\boldsymbol{x}$ (in the rotational system)

$$\mathbf{r} = S\left(S_\phi S_i \mathbf{z} - \mathbf{x}\right) \tag{3.6}$$

where it is possible to set $\boldsymbol{x} = \{0, x_2, x_3\}$ without loss of generality. The magnetic field vector at the surface point $\boldsymbol{z}$ is given by

$$\mathbf{h} = \nabla\left(\frac{\mathbf{m}\cdot\mathbf{r}}{r^3}\right) \tag{3.7}$$

where $\boldsymbol{m}$ denotes the dipole moment. This field vector in the dipole system can then be transformed to the field vector in the observer's system, taking advantage of the orthonormality of the matrices in question.

3.5 Abundance inhomogeneities

As mentioned previously, there is evidence for non-homogeneous abundance distributions in the photospheres of chemically peculiar Ap and Bp stars. As a result it is important that this be taken into account when modelling their spectra. COSSAM allows for both vertical and horizontal non-homogeneous abundance distributions.

For each layer and associated optical depth of the stellar model atmosphere, it is possible to specify individual abundances for each chemical element. An abundance file with a single column is all that is needed.

COSSAM allows for complex spot distributions over the stellar surface but also for the presence of (warped) abundance rings about the magnetic equator. Keep in mind that the number of quadrature points of the spatial grid has to be large enough to resolve the specified features. Examples of both these abundance configurations are shown in Fig. 3.5. Each spot is defined by latitude and longitude of its centre and by its radius; the atmosphere can differ from the surrounding atmosphere and so can the (stratified) abundances. Multiple spots of different sizes can be placed on top of each other or offset by some small amount to provide smoother gradients in abundance but also asymmetries. Rings are defined by lower and upper limits to the field angle with respect to the surface normal, they can also feature arbitrary (stratified) abundances.

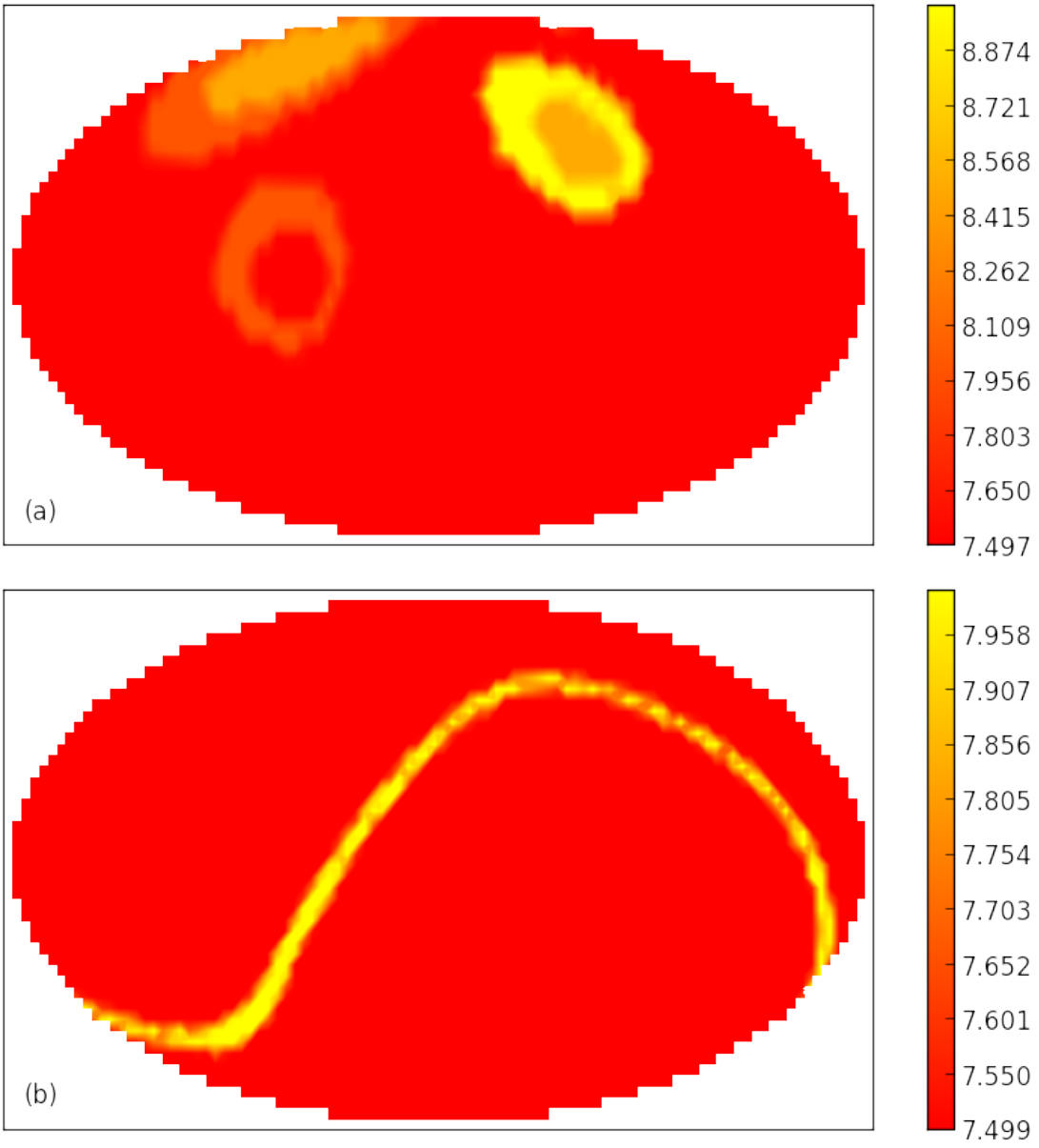

Figure 3.5: An example of the surface abundance inhomogeneities which can be modelled using COSSAM. The upper panel shows abundance spots and the lower panel shows an abundance ring. The vertical bars to the right of each image show the variation of log(Fe/H) with colour.

4 SPARTI

This Chapter describes the core of my PhD work, which consisted of creating the new inversion algorithm, SPARTI (Spectral Polarimetric Analysis by Radiative Transfer Inversion), for the modelling of the magnetic field structure and the abundance distribution of the chemical elements in the photospheres of upper main sequence stars. Using SPARTI I am able to model Stokes $IQUV$ profiles formed in main sequence F-, A- or B-type stellar atmospheres in the presence of magnetic fields. This allows me to plot magnetic field and chemical abundance distribution maps of entire stellar surfaces. SPARTI is based around the spectral synthesis code COSSAM (see Chapter 3).

The task of modelling polarised spectra of magnetic stars is extremely challenging because spectral lines are affected by a variety of phenomena including the Zeeman effect due to a magnetic field of unknown morphology, vertical stratification, non-homogeneous horizontal distribution of chemical elements and overabundances of rare-earth elements. The overabundances of rare-earth elements are particularly difficult to model since often they have not been studied to the same level of detail as elements such as Fe, this means some lines do not appear in the line databases. Increasing the abundance of any rare-earth element in a model causes a large number of spectral lines to appear in the synthetic spectrum. This, in combination with many blended lines as a result of a strong magnetic field, makes it very difficult to disentangle which lines have an important contribution in the stellar spectra. Furthermore, not just for rare-earth elements but for the lines of all chemical elements, the $\log gf$ and other line parameters may be inaccurate.

In addition to the properties of the stellar photosphere, complications appear during the observation of Stokes $IQUV$ profiles. The resolution of the instrument used to observe the profiles is important since if it is too low the fine detail in the profiles is lost and the magnetic field may appear simpler than it is in reality. The photon-noise is a particular problem for the observation of Stokes Q and U because the signal is typically considerably lower than for Stokes I and V. The crosstalk of the instrument

is also a concern. This is usually caused by an anomaly within the optical set-up of the instrument, some of the Stokes V can contaminate Stokes Q and U and vice versa. As a result of this, in Section 5.4 I describe the tests I use to determine how these three effects affect the ability of Sparti to recover the magnetic field structure and chemical abundance distribution in the stellar photosphere.

To accomplish the task of modelling polarised spectra of magnetic stars, I first considered the simpler case of the inversion of the Stokes I profiles of non-magnetic stars. There are already a number of spectral synthesis codes for the modelling of non-magnetic stellar atmospheres for example, Spectral Investigation Utility (SIU; Reetz 1991) and Spectroscopy Made Easy (SME; Valenti & Piskunov 1996). As a result it may seem redundant to write another code, but there were two reasons for this. First, the inversion of non-magnetic and magnetic spectra follow similar procedures, and the non-linear regression algorithm is the same in both. This means I am able to test the majority of the functions in Sparti using the faster and simpler case of non-magnetic atmospheres. The second reason is that writing a new code enabled me to check that the output of Sparti is fully consistent/correct in the case of non-magnetic stars.

To calculate a synthetic spectrum in the non-magnetic case using Cossam, I must set the magnetic field strength to zero and then only consider the Stokes I profile. This however is slow and inefficient since Cossam is not able to take advantage of the symmetries which are present in the non-magnetic case because of the symmetrical stellar surface. I therefore asked Prof. Martin Stift (the author of Cossam), to create a version of Cossam designed specifically for the fast and efficient synthesis of non-magnetic stellar spectra. As a result of this request Prof. Stift created Cossam Simple (see Section 3.2.1), which I used as the spectral synthesis code in my inversion code Sparti Simple.

While developing and using Sparti Simple I had to think about and solve various problems, common also to the analysis of magnetic stars: how to normalise stellar spectra; how to take into account instrument resolution; how to determine $\log g$ and effective temperature $T_{\rm eff}$; how to identify spectral lines; how to correct for radial velocity; and how to select spectral lines for the analysis (e.g., eliminating those formed

in non-local thermodynamic equilibrium). However the first consideration was which non-linear regression algorithm to adopt for the inversion (the Genetic algorithm or the Levenberg-Marquardt algorithm). After the selection of the algorithm, I then had to consider the conditions of convergence to determine when the algorithm should finish.

While working on determining $T_{\rm eff}$ and $\log g$ of stars, I made a modification to Cossam and Cossam Simple. When calculating $T_{\rm eff}$ and $\log g$ I first fit synthetic spectra to the Balmer lines using my tool described in Section 6.5.2. The Balmer lines, however, are not always sensitive to changes in $\log g$ and, furthermore, by increasing $T_{\rm eff}$ and $\log g$ together it is possible to still obtain a perfectly consistent fit. Therefore, to check the reliability of $\log g$ I compared the ionisation balance of Fe I and Fe II. To do this it was necessary for me to modify Cossam Simple to make it possible to allow different abundances for the different ionisation stages of each element.

The next step was to include the presence of a magnetic field. This involved creating Sparti using the spectral synthesis code Cossam to calculate synthetic spectra. The original version of Cossam uses only the de-centered dipole (Stift 1975) as the magnetic field parameterisation. I modified Cossam to include the dipole + quadrupole morphology given in Landolfi, Bagnulo & Landi Degl'Innocenti (1998). The first reason for this was that parameter consistency and indistinguishable solutions are also given in Landolfi, Bagnulo & Landi Degl'Innocenti (1998) which means it is very easy to compare the output to previous outputs to check the uniqueness of results. This has not yet been completed for the de-centered dipole model, however the model is still very useful to use, since it is possible to compare magnetic maps. The second reason for including the dipole + quadrupole morphology is that it makes it significantly easier to add a multipolar expansion in the future to allow for any greater freedom when modelling the magnetic field. These magnetic field parameterisations are described in Section 3.4. The inclusion of a magnetic field complicates the process of inversion by adding extra free parameters and the Stokes $IQUV$ profiles, but also because the ApBp stars show evidence of abundance inhomogeneities which must be modelled. Furthermore, to account for the non-homogeneous nature of the stellar surface, it is necessary to include spectra of multiple rotational phases simultaneously so

as to gain a full picture of the entire stellar surface.

In this chapter I explain the function of SPARTI. In Section 4.1 I describe and justify my use of a non-linear fitting routine. In Section 4.2 I describe the important considerations when comparing observed and synthetic spectrum, and how I handle these within SPARTI. In Section 4.3 I describe the input file used in SPARTI and the free parameters for each parameterisation. In section 4.4 I explain how I check for the convergence of the solution, i.e. when SPARTI has reached the best possible solution for the particular run. In Section 4.5 I describe the various output files created by SPARTI, including the error calculation, output spectra and element identification. In Section 4.6 & 4.7 I describe how I make sure that the free parameters in the magnetic case are consistent and how I handle indistinguishable solutions. Finally, in Section 4.8 I describe how I have parameterised the vertical stratification of the elements in the photosphere.

4.1 Non-linear regression

I use SPARTI to calculate the array of free parameters ($\boldsymbol{x}$), used in the spectral synthesis, which minimise the expression

$$\chi^2 = \sum_{i=1}^{n} \frac{\left[\boldsymbol{F}_{\rm mod}\left(\lambda_i, \boldsymbol{x}\right) - \boldsymbol{F}_{\rm obs}\left(\lambda_i\right)\right]^2}{\sigma_i^2} \tag{4.1}$$

where $\boldsymbol{F}_{\rm obs}$ is a vector containing the observed Stokes profiles $IQUV$, σ_i is the error associated to each spectral bin i, $\boldsymbol{F}_{\rm mod}$ is a vector containing the synthetic Stokes profiles $IQUV$, λ is the wavelength grid and n is the number of spectral points.

SPARTI SIMPLE has the same code structure and uses the same fitting algorithms as SPARTI. In SPARTI SIMPLE $\boldsymbol{F}_{\rm obs}$ is the observed flux spectrum normalised to unity and $\boldsymbol{F}_{\rm mod}$ is the synthetic flux spectrum normalised to unity, further differences between the two codes are made clear throughout this chapter.

To minimise Eq. 4.1 I use a non-linear regression algorithm, since the the radiative transfer equation Eq. 2.23 is non-linear. I investigated the suitability of the Levenberg-

Marquardt Algorithm (Levenberg 1944 and Marquardt 1963) and the genetic algorithm (Holland 1975) for use in my code SPARTI. Both algorithms are widely used to solve non-linear regression problems and have different strengths and weaknesses which I considered in my choice of algorithm.

4.1.1 Genetic Algorithm

In its current form the genetic algorithm was first described by Holland (1975) and works on the principles of natural selection "survival of the fittest". This algorithm is incredibly powerful because no initial guesses have to be provided for the parameters which are being calculated (VanderNoot & Abrahams 1998). The only constraint is that imposed by the laws of physics or the symmetry arguments given in Section 4.6.

For the purpose of spectral synthesis the set of parameters used in COSSAM to determine the synthetic spectrum constitute each set analogous to genes. The number of sets which the program calculates determines the initial gene pool, from which new generations of parameter sets can be produced. At each stage the two parameter sets which define the two synthetic spectra that are the best fit to the observed spectrum remain in the gene pool. This means that the χ^2 of the best solution, is always the same or better than previous generations. The remaining parameter sets are combined with the parameters set with the lowest χ^2. There are several methods of combination and I chose to use two different combination methods in my algorithm. Each parameter set also has the potential for a random mutation to occur in any number of its parameters.

An initial population of parameters is created using random number generation, the fitness of each member of the population is determined and then each member is ranked from best fitting to worst. When running the inversion routine with COSSAM using the genetic algorithm, χ^2 is used to estimate the quality of the fit. Once the population has been ranked the parameter sets must be mated together. For this code two different mating procedures are used. The primary alpha parameter set (which has the lowest χ^2) mates by way of averaging its parameters with each parameter set in

turn. The secondary alpha parameter set (which has the second lowest χ^2) interchanges a random number of its parameters with each parameter set in turn (Swets & Punch 1995). Once this has been carried out there is a chance of mutation in any of the parameters and then the sets are ranked from best to worst again and the process continues, until the desired χ^2 is reached.

I chose to investigate the potential of the genetic algorithm, because it was likely that I would have a large number of parameters as part of my inversion code. Unfortunately the speed of COSSAM limits the usefulness of this algorithm. After testing the genetic algorithm with ∼15 variables, I found it would consistently take several days to achieve a low χ^2. This is due to each call to COSSAM, from the algorithm, taking several seconds and the genetic algorithm must call COSSAM a large number of times, since I found that the initial gene pool had to consist of between 100 and 500 sets for convergence.

4.1.2 Levenberg-Marquardt Algorithm

The Levenberg-Marquardt Algorithm (LMA) is a non-linear fitting routine which uses a combination of the steepest descent and Gauss-Newton methods. It was developed by Levenberg (1944) and Marquardt (1963). An initial set of starting parameters is chosen or randomly generated depending on prior knowledge of the solution. If the problem is complex and multiple minima exist, it may be necessary to start the algorithm multiple times using several different parameter sets as some will not converge. The algorithm is used to iteratively search for the minimum χ^2, and at each iteration it calculates the new parameter set, $\boldsymbol{x}'$,

$$\boldsymbol{x}' = \boldsymbol{x} + \left(\Delta\boldsymbol{F}\Delta\boldsymbol{F}^T + \mathrm{diag}(\Delta\boldsymbol{F}\Delta\boldsymbol{F}^T)\Lambda\right)^{-1}\Delta\boldsymbol{F}\boldsymbol{F} \tag{4.2}$$

where $\boldsymbol{x}$ is the previous parameter set, $\boldsymbol{F}$ is the difference between the observed and synthetic spectra, given by

$$\boldsymbol{F} = \sum_{i=1}^{n} \frac{\boldsymbol{F}_{\mathrm{mod}}\left(\lambda_i, \boldsymbol{x}\right) - \boldsymbol{F}_{\mathrm{obs}}\left(\lambda_i\right)}{\sigma_i}, \tag{4.3}$$

$\Delta \boldsymbol{F}$ is the Jacobian matrix (evaluated numerically)

$$\Delta \boldsymbol{F} = \begin{pmatrix} \frac{\delta F_1}{\delta x_1} & \cdots & \frac{\delta F_1}{\delta x_m} \\ \vdots & \ddots & \vdots \\ \frac{\delta F_n}{\delta x_1} & \cdots & \frac{\delta F_n}{\delta x_m} \end{pmatrix} \tag{4.4}$$

where m is the number of parameters, $\Delta \boldsymbol{F}^T$ is its transpose, and Λ is a scalar constant used to determine whether the LMA will follow a gradient search or Gauss-Newton approach. After calculating $\boldsymbol{x}'$ the χ^2 of the new model is calculated. If the χ^2 is lower than the previous value of χ^2, Λ is decreased by a factor of ten, this moves the algorithm towards the Gauss-Newton method, and the process repeats. If however the χ^2 is equal or higher, the parameters are set to their previous values and Λ is increased by a factor of ten, this forces a gradient descent search which aims to force the parameters to the minima of the function being fit (Press et al. 1992).

After testing the effectiveness of the LMA using my Milne-Eddington approximation code and COSSAM, I found it to consistently out-perform the genetic algorithm and so chose it as the algorithm used within SPARTI. It is also a commonly used algorithm for MDI problems (e.g., Piskunov & Kochukhov 2002 and Kochukhov & Piskunov 2002). In addition, Aster, Borchers & Thurber (2013) states 'The LMA is usually the method of choice for small- to medium-sized nonlinear least squares problems' this is because of the Gauss Newton performance in combination with 'robust convergence properties'.

4.1.2.1 Numerical Differentiation

The radiative transfer equation, Eq. 2.23, does not have an analytical solution, and so to calculate the matrix of values which corresponding to the partial differentials which make up the matrix $\Delta \mathbf{F}$, Eq. 4.4 , I use

$$\frac{\delta F_n}{\delta x_m} = \frac{\boldsymbol{F}_{\text{mod}}\left(\lambda_n, x_m + h_m\right) - \boldsymbol{F}_{\text{mod}}\left(\lambda_n, x_m - h_m\right)}{2h} \tag{4.5}$$

where

$$h = x_m \epsilon_m \tag{4.6}$$

where ϵ_i in the ideal case is the smallest floating point number which can be stored before there is a rounding error. In reality however, this number is determined based on the signal-to-noise-ratio of the data, and also on a parameter by parameter basis.

4.2 Comparing observed and synthetic spectra

Before I am able to directly compare $\boldsymbol{F}_{\rm mod}$ and $\boldsymbol{F}_{\rm obs}$, I must first correct for a number of instrumental and observational effects. The first challenge, which is critical and must be performed with care, is the normalisation of the observed spectrum. The method of normalisation I use is described in Section 6.3 and I perform this before my analysis with SPARTI.

4.2.1 Radial Velocity

As a star moves towards or away from an observer, for all wavelengths, the light is blue or red-shifted respectively. This means the spectral lines of $\boldsymbol{F}_{\rm obs}$ will not be at the same wavelength as those in $\boldsymbol{F}_{\rm mod}$. As a result it is necessary to calculate and correct for the radial velocity ($v_{\rm rad}$) shift. Before correcting for the star's $v_{\rm rad}$ it is first necessary to correct for the heliocentric radial velocity, which is an addition or subtraction from the star's true radial velocity as a result of our orbit around the Sun. To calculate the $v_{\rm rad}$ corrected wavelength value, λ_0', I use

$$\lambda_0' = \lambda_0 \left[1 + \frac{v_{\rm rad}}{c}\right] \tag{4.7}$$

where λ_0 is the observed wavelength, and c is the speed of light. To calculate the star's $v_{\rm rad}$ it is included as a free parameter in SPARTI. I shift the wavelength grid of $F_{\rm mod}$ to coincide with the wavelength grid of $F_{\rm obs}$.

4.2.2 Instrument Resolution

The instrument resolution determines the smallest resolvable wavelength difference in a spectrum. Before comparing the synthetic spectrum with the observed spectrum it is convolved with the instrumental profile given by a Gaussian. Each convolved point of the model spectrum $\boldsymbol{F}_{\rm mod}(\lambda_0)$ is given by,

$$\boldsymbol{F}_{\rm mod}(\lambda_0) = \sum_{i=-L}^{L} \frac{\boldsymbol{F}'_{\rm mod}(\lambda_i)}{\sigma\sqrt{(2\pi)}} \exp\left(\frac{-(\lambda_i - \lambda_0)^2}{2\sigma^2}\right)\Delta\lambda \tag{4.8}$$

where L=INT[$3\sigma\Delta\lambda$]+10, $\Delta\lambda$ is the wavelength step-size of the synthetic spectrum and λ_0 is the wavelength value for the new convolved point. The unconvolved spectrum is $\boldsymbol{F}'_{\rm mod}$ and the standard deviation of the Gaussian is given by

$$\sigma = \frac{\lambda_0}{4R\ln(2)} \tag{4.9}$$

where R is the resolving power of the instrument given by

$$R = \frac{\lambda_0}{\delta\lambda} \tag{4.10}$$

where $\delta\lambda$ is the smallest difference in wavelength which can be resolved by the instrument at the wavelength λ_0.

4.2.3 Linear Interpolation

When comparing the synthetic and observed spectra using the LMA, it is essentially that they both have the same wavelength grid. The wavelength step-size I use to calculate the synthetic spectrum is closely spaced, and so I am able to perform a simple linear interpolation to match the synthetic spectrum to the observed wavelength grid[1]. Each new synthetic flux point, $\boldsymbol{F}_{\rm mod}(\lambda_{\rm obs})$, is given by

$$\boldsymbol{F}_{\rm mod}(\lambda_{\rm obs}) = \boldsymbol{F}_{\rm mod}(\lambda_1) + \left[(\boldsymbol{F}_{\rm mod}(\lambda_1) - \boldsymbol{F}_{\rm mod}(\lambda_0))\,\frac{\lambda_{\rm obs} - \lambda_0}{\lambda_1 - \lambda_0}\right] \tag{4.11}$$

[1]This would not, however, be suitable for poorly sampled spectra

where λ_{obs} is a wavelength value in the observed spectrum, λ_0 is the closest wavelength in the synthetic spectrum which is less than λ_{obs} and λ_1 is the closest wavelength in the synthetic spectrum which is greater than λ_{obs}.

4.2.4 Rejected spectral lines

If a spectral line is formed in a region of the atmosphere for which it is not possible to assume LTE, then it is not possible for COSSAM to calculate the line profile since COSSAM calculates spectra based on LTE. There are a small number of lines which appear in either the synthetic or observed spectrum but not in the other. This could be due to incorrect atomic data or contamination by interstellar sources. I do not consider these lines in the spectrum because they will affect the parameters. I keep all rejected lines in a database which SPARTI accesses to determine whether to use each line.

4.3 SPARTI interface

I put a lot of work into developing an input file which allows the user enough freedom to model magnetic stellar spectra without too much complication. While this section is not intended to be a user manual, it is useful for illustrative purposes to describe an example of an input file used by SPARTI. The following is an example input to SPARTI:

```
-------Data start at line 3, col 32-----------------------------
-----------------------------------------------------------------
Number of Lines                 : 2
Number of Variables             : 21
Number of Phases                : 5
Number of Rings on Disc         : 10
Number of Spots or Rings        : 1
Number of Processors            : 32
```

In the magnetic case, it is convenient to consider lines rather than spectral ranges due to the difference in CPU time. Therefore here, I define the "Number of Lines",

which is simply the number of spectral lines to analyse in the code[2]. The "Number of Variables" is the total free parameters for the magnetic field parametrisation of choice, each abundance parameter, and the rotation and radial velocities. To fully model the stellar magnetic field it is important to include a number of spectra observed at well spaced rotational phases of the star as viewed from Earth. The "Number of Phases" is simply the number of distinct phases to be modelled. The "Number of Rings on Disc", defines how refined the stellar surface grid is, this has an impact on the runtime of the code, but also the ability to detect small scale surface features. In the case of Sparti, the "Number of Spots" on the stellar surface can be specified. Currently spot 1 is the entire stellar surface. Each spot, including spot 1, can be assigned an individual abundance file, which means it is possible to create a different abundance profile for each spot and the stellar disc. The "Number of Processors" is the number of CPU cores available to Cossam.

```
Interval per Processor          : 0.34
Lower Wavelength Limit (A)      : 5216.49
Upper Wavelength Limit (A)      : 5852.44
Delta Lambda (A)                : 0.020
Width of Regions (A)            : 0.9
Resolution                      : 120000
```

The "Interval per Processor" is the wavelength range calculated by each processor. The "Lower Wavelength Limit (A)" and "Upper Wavelength Limit (A)" are the minimum and maximum wavelength which are considered during the analysis, this defines the size of the arrays used within Sparti and Cossam. "Delta Lambda (A)" is the resolution of the synthetic spectrum. The "Width of Regions (A)" is the radius of each line from the line center. "Resolution" is the Spectral resolving power of the instrument used for observation of the profiles and is used in Eq. 4.9.

```
Run Type                        : Invert
Ring or Spot                    : spotquad
Star Name                       : HD24712_HARPS
```

[2]Note that in fact these are the number of dominant lines the user wishes to consider. If a single line profile is made up of many blends this still counts as one line

```
Rotational phases [0<=phi<=1]: 0.004 0.200 0.443 0.521 0.924
```

The "Run Type" determines whether SPARTI fits a synthetic spectrum to an observed spectrum in the case of "Invert" or simply calculates a synthetic spectrum in the case of "Direct". The input "Ring or Spot" determines which parameterisation SPARTI uses whether de-centered dipole or dipole + quadrupole and also whether it considers rings or spots as the surface abundance inhomogeneities. The "Star Name" is the name of the input file and also forms part of the output file names. The "Rotational phases" are calculated from the rotational period of the star. Phase zero is set to a certain arbitrary date and the phase at each observation, ϕ is calculated using

$$\phi = \frac{t_{\rm obs} - t_0}{P_{\rm rot}} - \mathrm{INT}\left[\frac{t_{\rm obs} - t_0}{P_{\rm rot}}\right] \tag{4.12}$$

where $t_{\rm obs}$ is the Julian date of the observation, t_0 is an arbitrary Julian date before the date of observation (used consistently for the calculation of all phases in a set) and $P_{\rm rot}$ is the rotation period of the star.

```
------------------------------------------------------------------------
-------INVERSION REGIONS------------------------------------------------
------------------------------------------------------------------------
Central Wave  1                 : 5217.39 1 1 1 1
Central Wave  2                 : 5383.37 1 1 1 1
```

The "Central Wave" is the line center in Ångströms for each line considered in the inversion. It is also possible to consider all Stokes profiles or any combination of the Stokes $IQUV$ by changing the four numbers following the wavelength value.

```
------------------------------------------------------------------------
-------ELEMENT FILES----------------------------------------------------
------------------------------------------------------------------------
Element file 1                  : spots_abund1.dat
------------------------------------------------------------------------
-------ATMOSPHERE FILES-------------------------------------------------
------------------------------------------------------------------------
Atmospheric model 1             : t7250_410_00.fil
------------------------------------------------------------------------
-------LINES VERSIONS---------------------------------------------------
------------------------------------------------------------------------
```

```
Lines Version 1                    : 0725041000
```

Each spot has an individual atmosphere model, and vertical element distribution defined in "Atmospheric model" and "Element file" respectively where the number determines which spot the files refer to. As a result of the individual atmosphere models each spot must have an a separate "Lines Version". It is possible to use the same atmosphere model for each spot but they must still be given separately for each spot.

```
-------------------------------------------------------------------
--------INPUT VARIABLES--------------------------------------------
-------------------------------------------------------------------
1   Incl                       :    78.0     360.0     0.0
2   b                          :   173.0     360.0     0.0
3   b21                        :     9.0     360.0     0.0
4   b22                        :   129.0     360.0     0.0
5   g21                        :   262.0     360.0     0.0
6   g22                        :   321.0     360.0     0.0
7   D_Strength                 :  2183.0   20000.0     0.0
8   Q_Strength                 :   147.0   20000.0     0.0
9   vr                         :     1.0      20.0     0.0
10  F0                         :     1.0       1.0     0.0
11  Strat(Fe 1) Star       A   :     7.5      10.0     0.0
12                         B   :    45.0      72.0     1.0
13                         C   :     8.0      10.0     0.0
17  vrad                       :    0.01      10.0   -10.0
18  vrad                       :    0.01      10.0   -10.0
19  vrad                       :    0.01      10.0   -10.0
20  vrad                       :    0.01      10.0   -10.0
21  vrad                       :    0.01      10.0   -10.0
```

This portion defines the input variables which vary based on the parameterisation and the different free parameters are given in section 4.3.2. The first column after the colon is the initial estimate for the free parameter, the second column is the maximum value that parameter can have and the third column is the minimum value.

Since there are a large number of input parameters and if a large number of spots are chosen, writing this input file can quickly become complicated and prone to error. Therefore I have written a PYTHON routine which is able to generate this input file and

each abundance file required, with a smaller number of inputs. This PYTHON routine has the added benefit of being able to generate pseudo-random numbers as starting values for the magnetic field parameters and abundance distributions.

In the case of SPARTI SIMPLE, it is not possible to add spots[3] and instead of the number of lines entire spectral ranges are given as input. For the free parameters only initial values for $v \sin i$, $v_{\rm mic}$ and $v_{\rm rad}$ need to be specified. The initial values of the abundances are set as the solar values from Asplund et al. (2009). In the case of cluster analysis it is useful to model a number of stars sequentially therefore I have written a PYTHON routine which is able to generate a SPARTI SIMPLE input file given the $T_{\rm eff}$, $\log g$ of a star and initial estimates of $v \sin i$ and $v_{\rm rad}$.

4.3.1 Sparti Simple Free Parameters

In the non-magnetic case, the $v \sin i$, $v_{\rm mic}$, $v_{\rm rad}$ and the abundance of the elements (relative to H) with atomic number 2 through to 92 can be set as a free parameters. This includes the abundance of each ionisation stage and the abundance of the element can be stratified throughout the photosphere. The stratification is described by a simple step function (see Section 4.8) and each ionisation state of each element can have an independent stratification.

It is possible to determine the abundance of all of the elements and their ionisation stages simultaneously. However, due to computer performance limitations it is often useful to consider, prior to analysis, which elements are visible in the spectrum as a result of the wavelength range of the data, the stellar $T_{\rm eff}$ and the instrument resolving power.

[3]To model a non-magnetic spotted star it would be necessary to use SPARTI since, in the case of a spotted star, it is no longer possible to take advantage of the symmetries on the stellar surface.

4.3.2 SPARTI Free Parameters

In the magnetic case, $v \sin i$ and $v_{\rm rad}$ (for each phase) are set as free parameters. The value of $v_{\rm mic}$ is set to $0\,{\rm km\,s^{-1}}$ because it is found to be zero in Ap stars (e.g. Donati & Landstreet 2009 and Ryabchikova et al. 1997). The free parameters for the three magnetic models are

- Dipole (Landolfi, Bagnulo & Landi Degl'Innocenti 1998)
  i, β, $B_{\rm d}$, f_0, θ
- De-centred Dipole (Stift 1975)
  i, α, β, γ, y_2, y_3, $B_{\rm d}$, f_0, θ
- Quadrupole (Landolfi, Bagnulo & Landi Degl'Innocenti 1998)
  i, β, β_1, β_2, γ_1, γ_2, $B_{\rm d}$, $B_{\rm q}$, f_0, θ

and are described in Section 3.4. As in the non-magnetic case, the abundance of the elements can be set as free parameters including stratification and different ionisation stages. However, it is often convenient to model only a small number of lines of one particular element at a time. It is important to consider the abundances of the elements which blend with the central line even those which are weak lines as this can effect the determination of the magnetic field. In addition it is possible to choose the number of spots for a particular inversion, with free parameters defining the latitude, longitude and radius of each spot.

4.4 Checking for Convergence

An important consideration when performing an iterative least-squares minimisation is when to stop and take the current values as the best achievable. During testing, I simply selected a large number of iterations between 20–50, depending on the test. In general the algorithm would find the correct solution within this number of iterations but, if not, it was possible to increase this number. However for real world

problems, where the correct solution is usually unknown, a better method is required. In the current version of my code, there are four stop conditions. At the end of each iteration if the χ^2 is an improvement on the previous iteration, SPARTI or SPARTI SIMPLE will check the following four conditions given in Aster, Borchers & Thurber (2013).

1. The gradient of f(m) is approximately 0

$$\sum_{i=1}^{n}[\nabla\chi^2]^2 < \sqrt{\epsilon}\sum_{i=1}^{n}[1+\boldsymbol{f}(i)] \tag{4.13}$$

2. That the value of each parameter is not changing significantly.

$$\sum_{i=1}^{n}\left[\boldsymbol{x}(i)-\boldsymbol{x}_0(i)\right]^2 < \sqrt{\epsilon}\sum_{i=1}^{n}\left[1+\boldsymbol{x}(i)^2\right] \tag{4.14}$$

3. The values in the synthetic spectrum are not changing significantly

$$\sum_{i=1}^{n}\left[\boldsymbol{F}(x)-\boldsymbol{F}_0(x)\right]^2 < \epsilon\sum_{i=1}^{n}\left[1+\boldsymbol{F}(x)^2\right] \tag{4.15}$$

4. Maximum number of iterations

If the algorithm does not converge then it is likely these tests will always fail, it is important to have a maximum number of iterations allowed and if this number is reached the program outputs which test/s have failed so that the user can determine the problem.

4.5 Output Files

The output of SPARTI includes: a file containing the observed wavelength grid, the observed spectrum and the calculated synthetic spectrum; a logfile which shows the

best-fit parameters calculated during each iteration; and a file containing the parameters required to plot magnetic and abundance distribution maps. Fig. 4.5 shows an example of the synthetic spectrum output by SPARTI.

The output of SPARTI SIMPLE is similar with the exception of the abundance distribution maps, and the addition of a file containing the errors of each parameter. Fig. 4.5 shows an example of the synthetic spectrum output by SPARTI SIMPLE.

4.5.1 Error Calculation

I estimate the uncertainties of the best-fit parameters, including $v_{\rm mic}$ and $v \sin i$ by taking the square root of the diagonal values of the covariance matrix

$$\mathrm{cov}(\widehat{\boldsymbol{x}}) = s^2 \boldsymbol{\Delta F} \boldsymbol{\Delta F}^T, \tag{4.16}$$

where $\widehat{\boldsymbol{x}}$ is the vector of best fit parameters and s is

$$s = \sqrt{\frac{\sum_{i=0}^{n} \left[\boldsymbol{F}_{\rm mod}\left(\lambda_i\right) - \boldsymbol{F}_{\rm obs}\left(\lambda_i\right)\right]^2}{n-m}} \tag{4.17}$$

where n is the number of wavelength points in the spectrum and m is the number of best-fit parameters.

This error is only a lower limit since $T_{\rm eff}$ and $\log g$ are not free parameters within SPARTI or SPARTI SIMPLE and their effects on the calculation of $\widehat{\boldsymbol{x}}$ are not present in the covariance matrix. To calculate an error which encompasses all variables I calculate the best-fit parameters using a total of five model atmospheres for each star:

1. $T_{\rm eff} = T^0_{\rm eff}$, $\log g = \log g^0$;
2. $T_{\rm eff} = T^0_{\rm eff} + \Delta T_{\rm eff}$, $\log g = \log g^0$;
3. $T_{\rm eff} = T^0_{\rm eff} - \Delta T_{\rm eff}$, $\log g = \log g^0$;
4. $T_{\rm eff} = T^0_{\rm eff}$, $\log g = \log g^0 + \Delta \log g$;
5. $T_{\rm eff} = T^0_{\rm eff}$, $\log g = \log g^0 - \Delta \log g$;

where $T^0_{\rm eff}$ and $\log g^0$ are the best estimates of $T_{\rm eff}$ and $\log g$, respectively. $\Delta T_{\rm eff}$ and

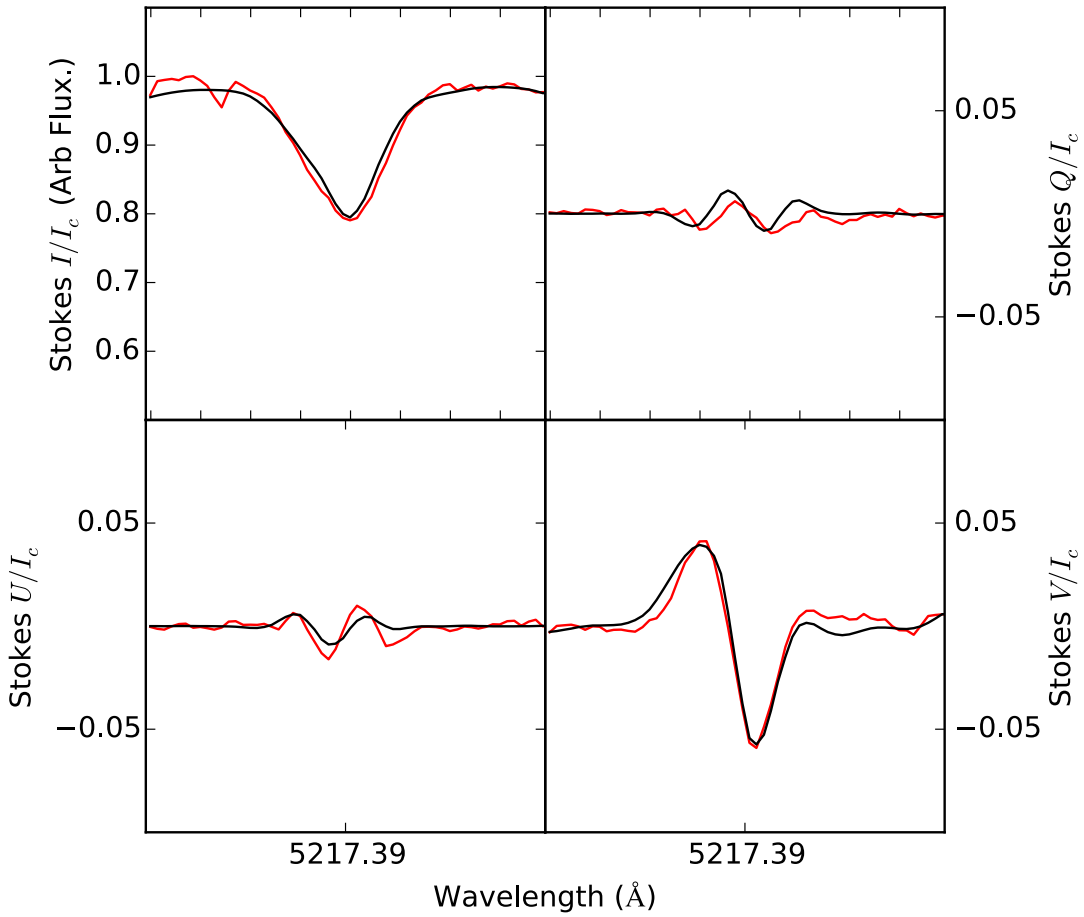

Figure 4.1: The spectrum of HD24712 observed with the HARPSpol instrument (solid red line), plotted with the synthetic spectrum calculated using SPARTI (solid black line)

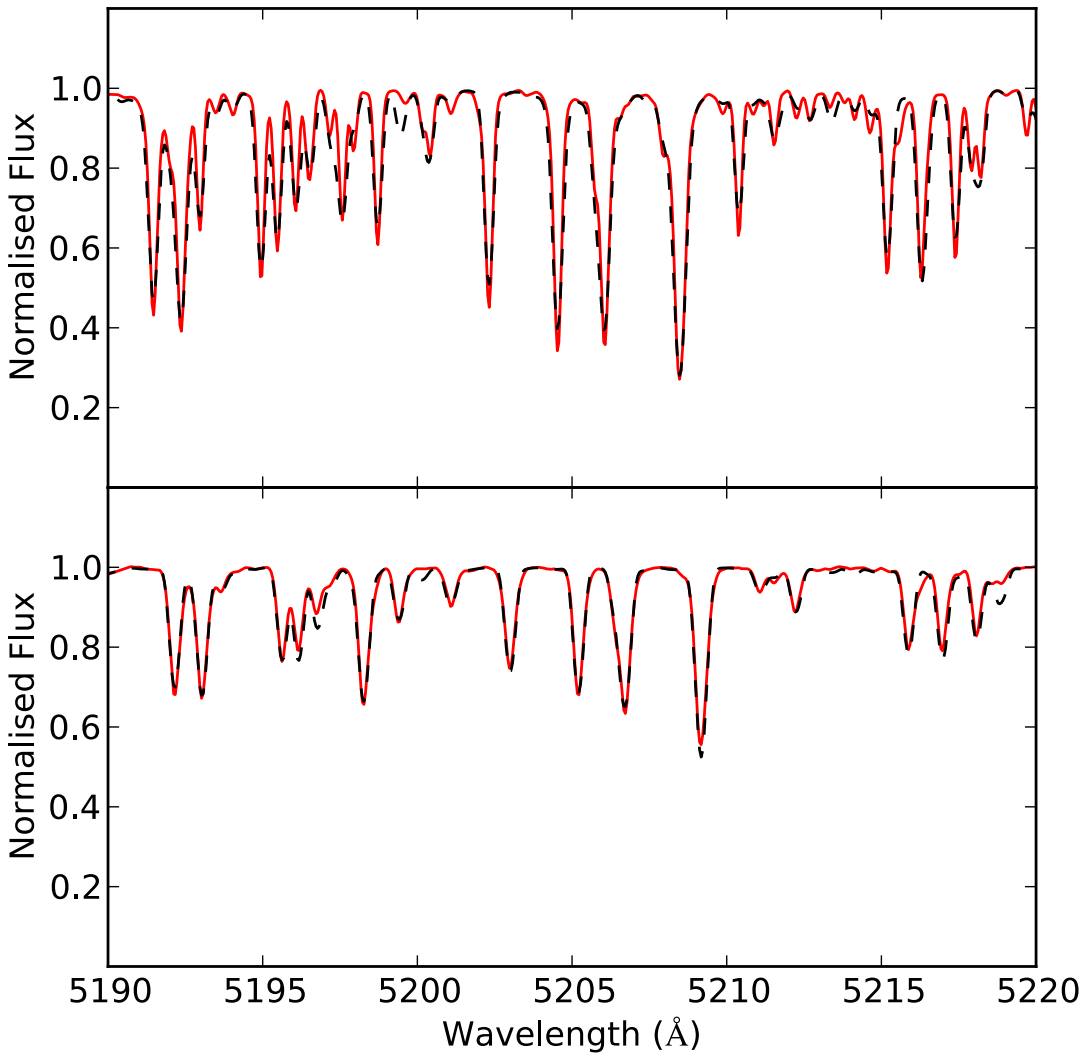

Figure 4.2: Upper Panel: The spectrum of the Sun (solid red line), plotted with the synthetic spectrum calculated using SPARTI SIMPLE (solid black line). Lower Panel: The spectrum HD32115 observed with the 2.7-m telescope at McDonald Observatory (Fossati et al. 2011b) (solid red line), plotted with the synthetic spectrum calculated using SPARTI (solid black line)

$\Delta \log g$ are the uncertainties of $T_{\rm eff}$ and $\log g$ respectively. I am then able to calculate the maximum error, $\boldsymbol{\sigma_{\rm max}}$, using

$$\boldsymbol{\sigma_{\rm max}} = \sqrt{\boldsymbol{\sigma^2_{\rm cov}} + \boldsymbol{\sigma^2_{\rm T_{eff}}} + \boldsymbol{\sigma^2_{\rm log\, g}}} \tag{4.18}$$

where $\boldsymbol{\sigma_{\rm cov}}$ is the error calculated using Eq. 4.16, $\boldsymbol{\sigma_{\rm T_{eff}}}$ is half of the difference between the best-fit values obtained using $T_{\rm eff} = T^0_{\rm eff} + \Delta T_{\rm eff}$ and $T_{\rm eff} = T^0_{\rm eff} - \Delta T_{\rm eff}$ and $\boldsymbol{\sigma_{\rm log\, g}}$ is half of the difference between the best-fit values for the abundances obtained assuming $\log g = \log g^0 + \Delta \log g$ and $\log g = \log g^0 - \Delta \log g$.

4.5.2 Semi-automatic element identification

The list of lines contained in the file named 'sysom_line.[EXTENSION]' (an output of LINES) contains those which may not be visible or do not have an effect on the shape of the observed spectrum. This can be as a result of the instrument resolving power, or because the $v \sin i$ blends the line with stronger lines. If all of the lines of a particular element are not seen and do not have an effect on the shape of the synthetic or observed spectrum, then the abundance calculated for that element will be meaningless. A solution I have developed for this problem, is to calculate a number of synthetic spectra, each is calculated setting the abundance of a difference element to zero each time. The reduced χ^2 of these spectra are compared with observed spectrum. If the reduced χ^2 has not changed within the signal-to-noise threshold then it is not possible to calculate the abundance of that element. If the reduced χ^2 does change I check the spectrum to confirm the lines corresponding to that element are visible.

4.6 Parameter Consistency Dipole (+ Quadrupole)

The dipole + quadrupole parameterisation of the magnetic field, discussed in Section 3.4, allows me to maintain positive values for each of the parameters with the following conditions

- $\sin(i) < 0 \rightarrow i \Rightarrow -i$ and $f_0 \Rightarrow 0.5 + f_0$;
- $\sin(\beta) < 0 \rightarrow \beta \Rightarrow -\beta$ and $f_0 \Rightarrow 0.5 + f_0$;
- $\sin(\beta_1) < 0 \rightarrow \beta_1 \Rightarrow -\beta_1$ and $\gamma_1 \Rightarrow \pi + \gamma_1$;
- $\sin(\beta_2) < 0 \rightarrow \beta_2 \Rightarrow -\beta_2$ and $\gamma_2 \Rightarrow \pi + \gamma_2$;
- $B_{\rm dip} < 0 \rightarrow B_{\rm dip} \Rightarrow -B_{\rm dip}$, $\beta \Rightarrow \pi - \beta$, $f_0 \Rightarrow 0.5 + f_0$, $\gamma_1 \Rightarrow \pi + \gamma_1$ and $\gamma_2 \Rightarrow \pi + \gamma_2$;
- $B_{\rm quad} < 0 \rightarrow B_{\rm quad} \Rightarrow -B_{\rm quad}$ and $\beta_1 \Rightarrow \pi + \beta_1$.

This leads to a consistency between parameters making it significantly easier to check for unique solutions. These conditions were calculated by Landolfi, Bagnulo & Landi Degl'Innocenti (1998) so that they do not modify the magnetic model when applied which means they do not effect the LMA.

4.7 Indistinguishable solutions

There are a number of solutions, which have different sets of parameters but produce the same Stokes $IQUV$ profiles. In the case of the de-centered dipole model a characterisation of these solutions has not been performed. It is a complex task to complete and would take a considerable amount of time to finish. However, in the dipole and dipole + quadrupole case the indistinguishable solutions have been calculated by Landolfi, Bagnulo & Landi Degl'Innocenti (1998) as

1. i, β, f_0
2. $\pi - i, \pi - \beta, f_0$
3. β, i, f_0
4. $\pi - \beta, \pi - i, f_0$

and

5. $i, \beta, \beta_1, \beta_2, \gamma_1, \gamma_2, f_0$
6. $i, \beta, \pi - \beta_1, \pi - \beta_2, \pi + \gamma_1, \pi + \gamma_2, f_0$
7. $i, \beta, \beta_2, \beta_1, \gamma_2, \gamma_1, f_0$
8. $i, \beta, \pi - \beta_2, \pi - \beta_1, \pi + \gamma_2, \pi + \gamma_1, f_0$
9. $\pi - i, \pi - \beta, \pi - \beta_1, \pi - \beta_2, \gamma_1, \gamma_2, f_0$
10. $\pi - i, \pi - \beta, \beta_1, \beta_2, \pi + \gamma_1, \pi + \gamma_2, f_0$
11. $\pi - i, \pi - \beta, \pi - \beta_2, \pi - \beta_1, \gamma_2, \gamma_1, f_0$
12. $\pi - i, \pi - \beta, \beta_2, \beta_1, \pi + \gamma_2, \pi + \gamma_1, f_0$

respectively where all the variables are defined in Section 3.4. In the dipole case, solutions 1 and 2 describe identical stars which are rotating in opposite directions. Similarly 3 and 4 describe identical stars rotating in opposite directions but which are different to 1 and 2. In the case of dipole+quadrupole morphology solutions 5–8 describe the same magnetic field and solutions 9–12 all describe the same magnetic field which is different from 5–8. In principle because I use all Stokes $IQUV$ profiles at multiple phases it should be possible for Sparti to discriminate between these solutions. However, it is useful to consider them during the analysis, in the case my results do not match those found previously.

4.8 Abundance Inhomogeneities

I have described the original method of stratification used in Cossam in Section 3.5. For use in Sparti it was necessary for me to make some modifications to the vertical stratification which I describe below. Currently when I determine the distribution of chemical spots, I set the number of spots prior to running Sparti. This limits the number of free parameters the code must find and so constrains the total runtime.

4.8.1 Vertical Stratification

In the inversion case it is important to have a parameterised model of the stratification. Using the original COSSAM method of defining the abundance of each element for each layer, would lead to an extra 72 free parameters for each element. In addition, with my modification, which allows individual abundances for each ionisation stage of each element, the number of free parameters would quickly become computational too expensive. An additional problem is that of regularisation which would be necessary to prevent unphysical abundance distributions. A further and potentially more serious problem, which will likely prevent the complete recovery of the vertical stratification, is that the depths at which spectral lines form are limited. It has not been possible for me to find spectral lines which span the entire range of optical depths. Therefore any solution to the stratification is unlikely to be unique, except at the optical depths which correspond to the formation regions of the spectral lines.

I have investigated a number of functions to determine the vertical stratification, my initial thought was to use a function which can be used to to fit the abundance distribution calculated by Stift, Leone & Cowley (2012). For this I tested a range of polynomial functions, Fig. 4.3 demonstrates the ability of a polynomial functions to recreate the abundance distribution. The 6th order polynomial is the lowest function which still fits the distribution. After testing the polynomial in SPARTI, I determined that it was not a viable solution. It was very difficult to constrain the parameters so that the function stayed below the maximum abundance value set in LINES. As a result I started from the simplest abundance distribution, a step function, and then tested more distributions to determine how easy their free parameters were to constrain.

4.8.1.1 Step function

I first tested a step function where the abundance stratification was described by

$$y(\tau) = \begin{cases} A, & \text{if } \tau < B \\ C, & \text{if } \tau \geq B \end{cases} \tag{4.19}$$

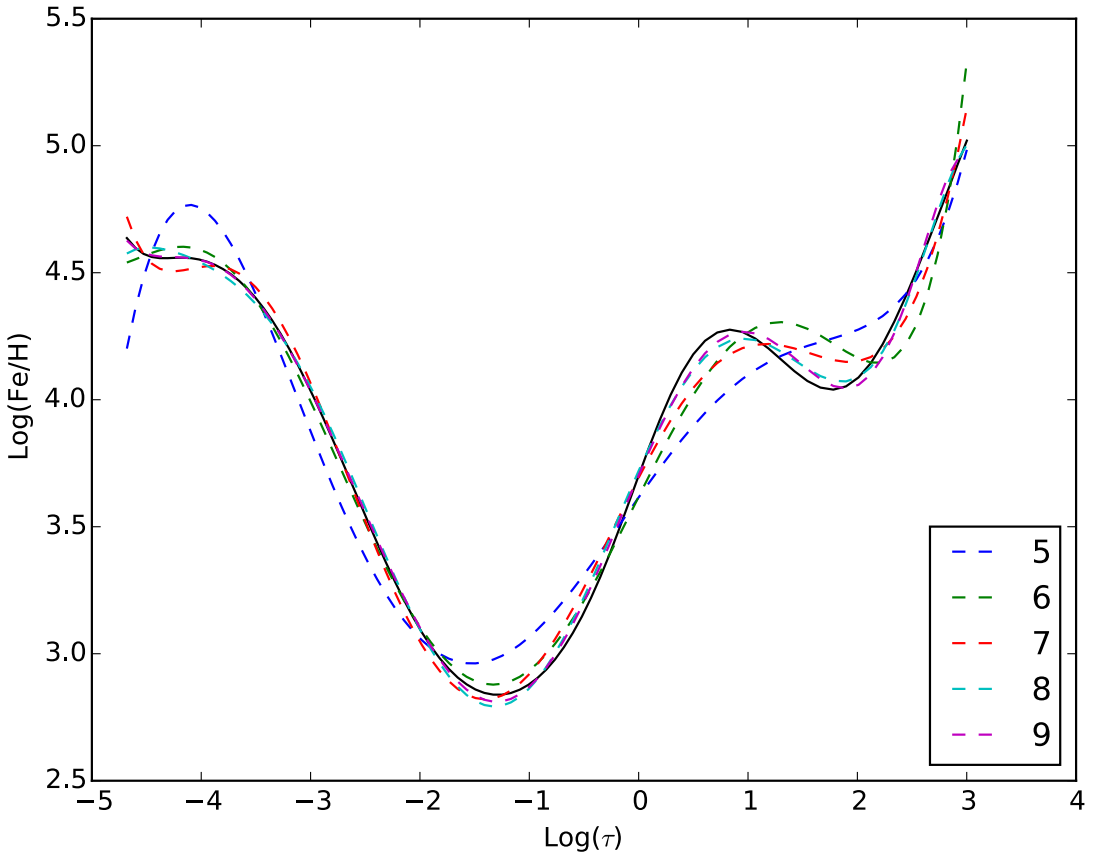

Figure 4.3: Fits to the stratification profile predicted by Stift, Leone & Cowley (2012) shown by the solid black line for polynomials of different orders.

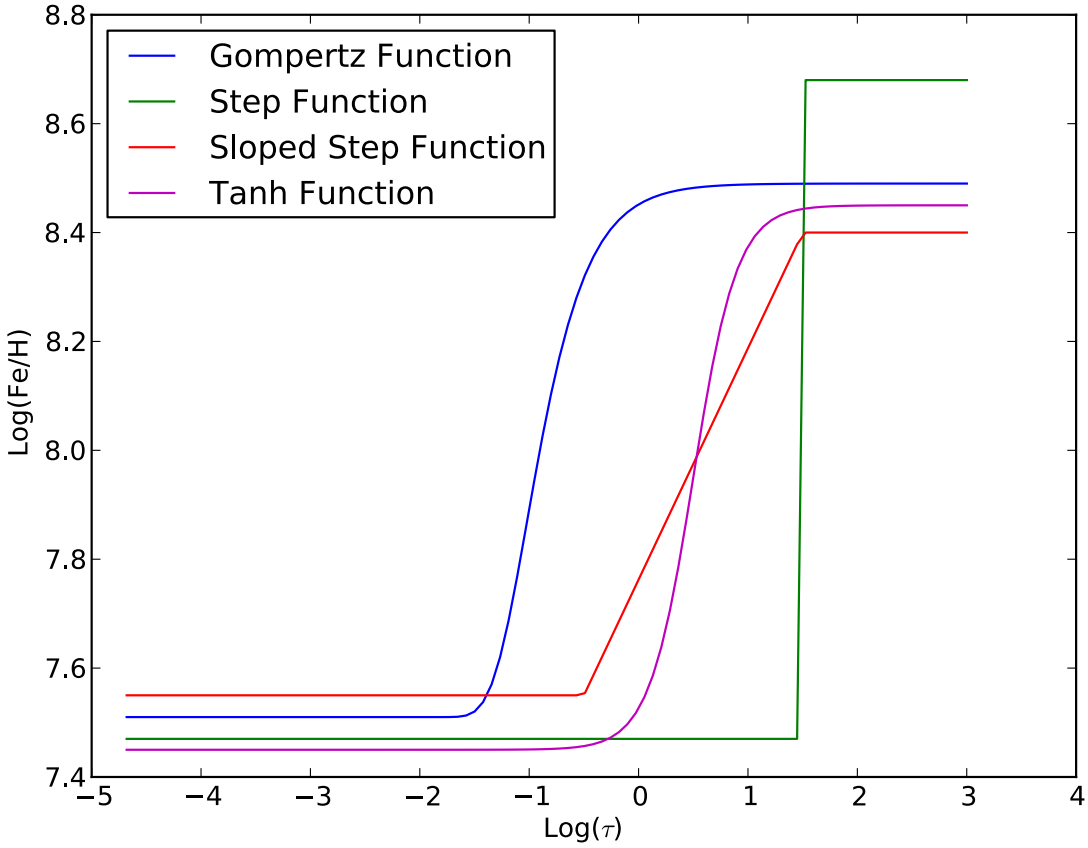

Figure 4.4: Examples of the functions tested for the parameterisation of the vertical stratification. The functions shown are, a simple step function (solid green line), a sloped step function (solid red line), a Gompertz function (solid blue line) and a tanh function (solid magenta line)

where A is the abundance below layer B and C is the abundance at level B and above. To add extra degrees of freedom I made it possible for the step to have a slant

$$y(\tau) = \begin{cases} A, & \text{if } \tau < B \\ D + \left[(D-A)\,\frac{\tau - B}{C-B}\right], & \text{if } B \leq \tau < C \\ D, & \text{if } \tau \geq C \end{cases} \tag{4.20}$$

where A is the abundance below layer B and D is the abundance at level C and above.

In both cases the parameters are easy to constrain, since it is clear what the maximum and minimum value of the abundance is. Also the layers at which the transition occurs are easily constrained.

4.8.1.2 Gompertz Function

The Gompertz function (Gompertz 1832) is still a step function but there is a smooth transition between the flat abundance distribution and the step. An example of this function is shown in Fig. 4.8.1. The equation which describes this function is

$$y(\tau) = A \exp\left(-B \exp\left[-C \log \tau\right]\right) + D, \tag{4.21}$$

where A is the height of the step, B determines the position of the step horizontally, C determines the gradient of the slope and D is the value before the step. When inverting the data, all four of the Gompertz function constants are free parameters. The Gompertz function was an interesting function to test, however constraining the parameters proved unmanageable since they behave in a non-linear fashion.

4.8.1.3 The tanh function

The tanh function is very similar to the shape of the Gompertz function. The advantage of tanh is the minimum and maximum values are easier to constrain than the Gompertz function. An example of this function is shown in Fig. 4.8.1. To determine the abundance distribution with tanh I use

$$y(\tau) = \frac{C}{2}\left[1 + \tanh\left(\frac{\tau - B}{2D}\right)\right] + A, \tag{4.22}$$

where A is the initial abundance value before the step, C is the height of the function and B and D determine the position of the step. While the maximum and minimum values of the function are easily definable, the position of the step is not and so this function did not provide a solution to the problem of parameterisation.

I have chosen to use the simple step function as the parameterisation for the vertical stratification of chemical abundances in the stellar photosphere. It does not allow a large degree of freedom, however it does allow me to model the observed difference in abundance between weak and strong lines.

5 Testing the inversion codes

Before applying Sparti and Sparti Simple to observed data, I had to be sure that the codes work correctly with numerical simulations. Following this I tested the ability of Sparti to converge to the correct model solution starting from random starting values. To do this I created a grid of model spectra and attempted to fit each one starting from a set of random initial parameters. Since the uniqueness and reliability of previously published magnetic models have been questioned I further tested the algorithm by adding artificial noise and instrumental effects to synthetic spectra calculated using Express written by Dr. Stefano Bagnulo. Express is a fast spectral synthesis code which calculates Stokes $IQUV$ for an arbitrary dipole + quadrupole magnetic configuration, under the Milne-Eddington atmosphere approximation (see Section 2.4.1) but without the ability to model non-homogeneous abundance distributions. Finally I applied Sparti Simple to the test cases of the Sun, HD32115 and 21 Peg.

5.1 Testing the modifications of Cossam

As part of the process of writing Sparti, I made significant alterations to Cossam, both adding the dipole + quadrupole morphology and modifying and moving large code structures. The result of this, is the inherent risk that I have modified the output of Cossam such that it no longer calculates the correct synthetic spectra. There are a number of checks which I used throughout the code development to ensure the consistency of synthetic spectra. First I checked the output spectra using an an un-altered version of Cossam. This is the simplest and most effective check in the majority of cases. I take the output of Sparti and generate a synthetic spectrum with an unaltered version of Cossam with the same output parameters calculated using Sparti and then compare the two. When adding the dipole + quadrupole morphology into Cossam I did not have an un-altered version of Cossam to compare the output with, however, I was able to use the output of Express to check that the shape of the synthetic spectra

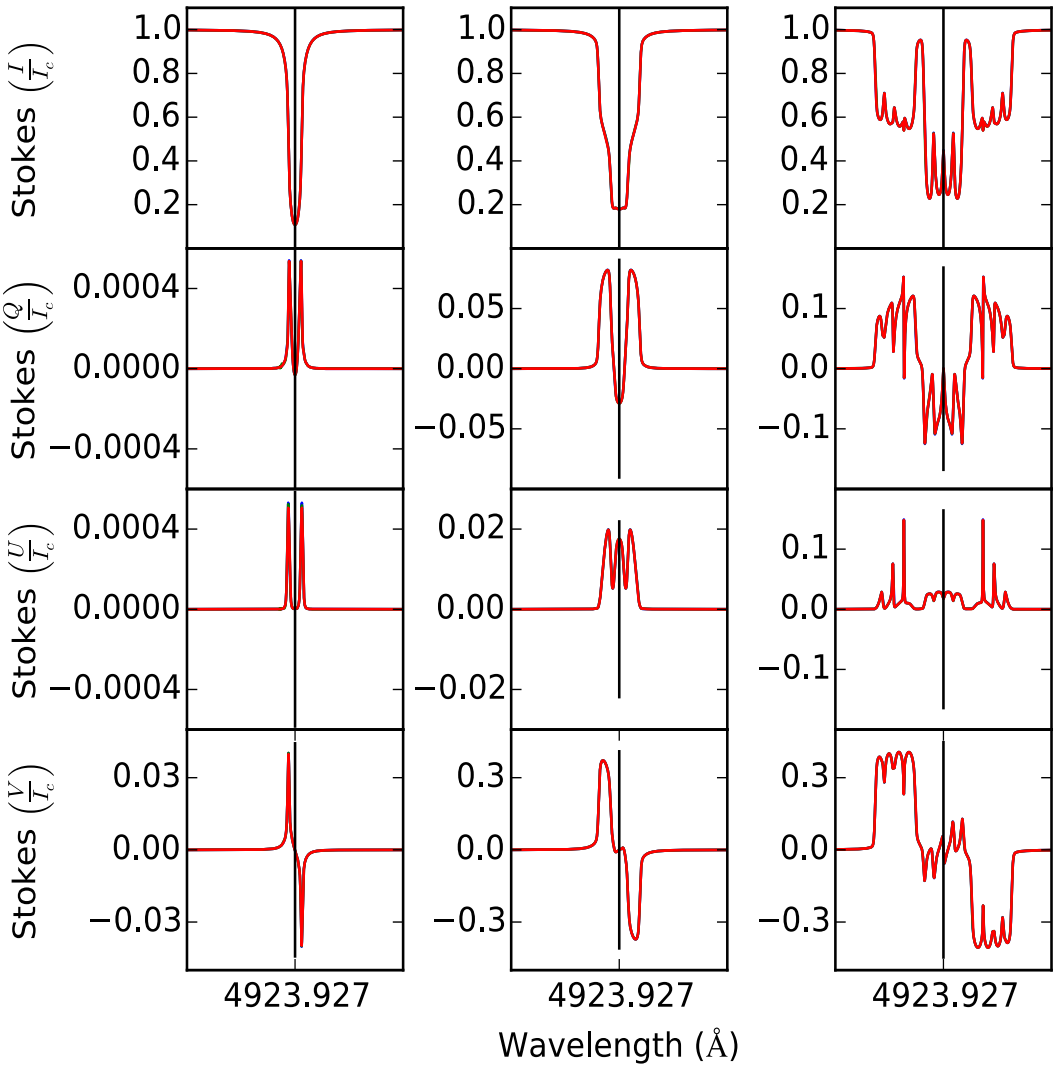

Figure 5.1: A portion of the data used by Wade et al. (2001) to check the accuracy of COSSAM, INVERS10 and ZEEMAN2. Each column contains the Stokes profiles $IQUV$ each calculated, using COSSAM, for a star of $T_{\rm eff} = 7500\,{\rm K}$ and $\log g = 4.0$, with magnetic field strengths from left to right of; 1. $B_{\rm d} = 0.1\,{\rm kG}$; 2. $B_{\rm d} = 5\,{\rm kG}$; 3. $B_{\rm d} = 10\,{\rm kG}$.

matches for the same input parameters. Finally to check the consistency of COSSAM I use the data from Wade et al. (2001). These data were previously used to compare the output of the three spectral synthesis codes COSSAM, INVERS10 and ZEEMAN2. An example of this data is shown in Fig. 5.1.

5.2 Testing Convolution

A potential source of errors in my code is my implementation of the convolution, therefore it was important for me to test the output. To a first-order approximation the behaviour of $v \sin i$ and instrument response is similar. As a result of this, I compared the output of my convolution with a synthetic spectrum calculated with $v \sin i$ corresponding to

$$v \sin i = \frac{c}{R} \tag{5.1}$$

where R is the spectral resolving power of the instrument and c is the speed of light. The results are shown in Fig.5.2, it can be seen that the convolved spectra agree well, at least to a first-order, with the synthetic spectra calculated with the corresponding $v \sin i$ values. The differences between each of the profiles results from the fact that $v \sin i$ is calculated within COSSAM as part of the spectral synthesis, and so treats blended lines differently to the convolution.

5.3 SPARTI Convergence

To test the ability of SPARTI to recover a model magnetic morphology, I calculated a grid of model spectra using random parameters and then attempted to fit each one starting from a random set of initial parameters. I did this for the three magnetic morphologies, dipole (Table 5.1), de-centered dipole (Table 5.2) and dipole + quadrupole (Table 5.3). In some cases, it appears that the best fit parameters do not match the initial model, however by referring to Section 4.7 it can be seen that in all dipole and

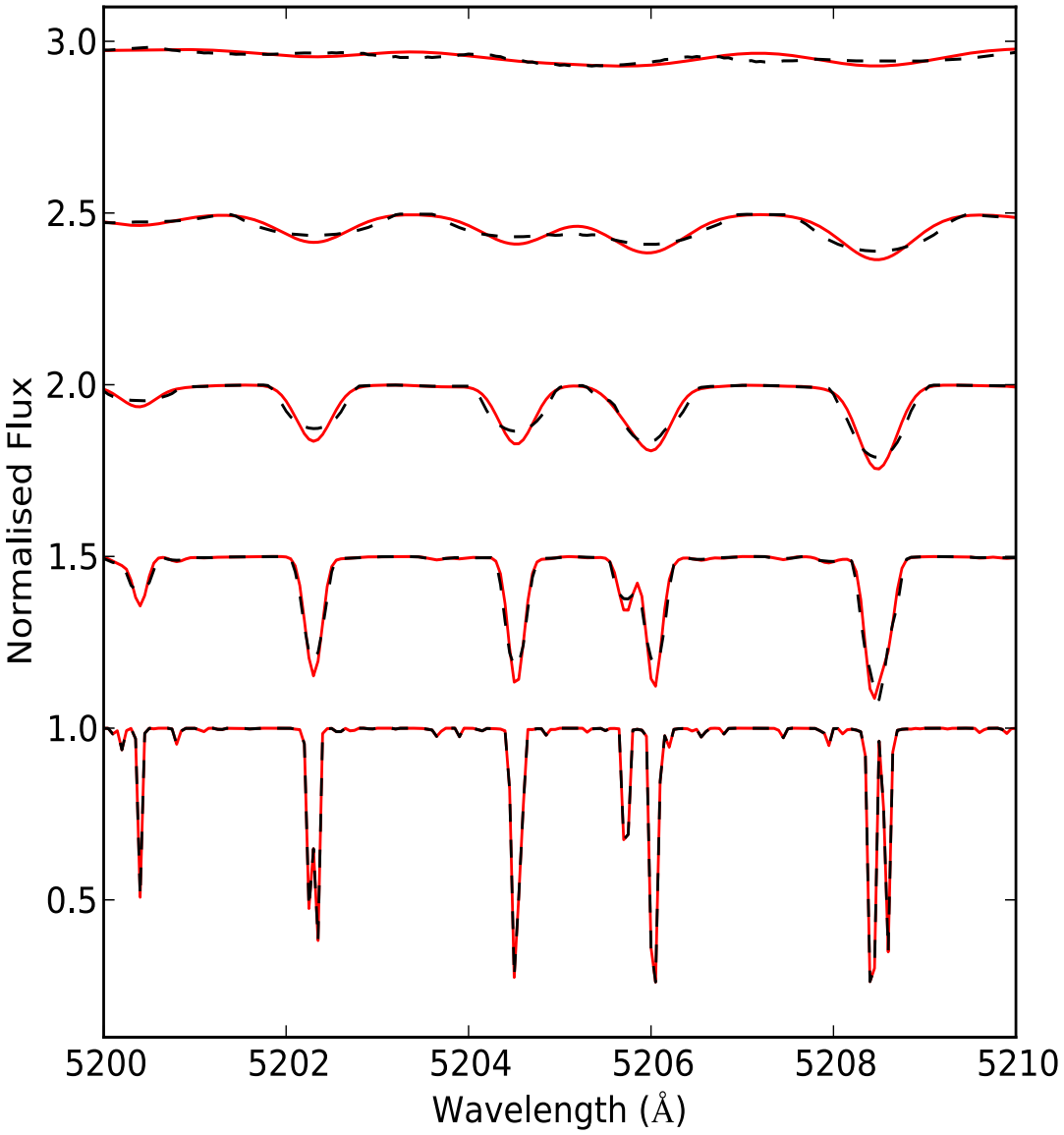

Figure 5.2: Comparison between COSSAM spectra convolved with instrument response using my function (solid red line) and spectra calculated using COSSAM for various values of $v \sin i$. Each spectrum has $T_{\rm eff} = 7500$K and $\log g = 4.2$, from top to bottom; 1. Resolving power = 3000, $v \sin i = 100\,{\rm kms}^{-1}$; 2. Resolving power = 6000, $v \sin i = 50\,{\rm kms}^{-1}$; 3. Resolving power = 12000, $v \sin i = 25\,{\rm kms}^{-1}$; 4. Resolving power = 30000, $v \sin i = 10\,{\rm kms}^{-1}$; 5. Resolving power = ∞, $v \sin i = 0\,{\rm kms}^{-1}$;

dipole + quadrupole cases they are indistinguishable solutions. Currently I have run 20 such tests for each morphology. Tables 5.1, 5.2 & 5.3 show a sample of each of these tests which reflect the total convergence rate. This test is intended to determine how far the initial parameters can be from the correct solution before SPARTI is unable to converge on the model parameters.

In the dipole case SPARTI converged to the correct solution in the majority of cases. This is likely because the model is very simple and so there are a small number of local minima. In one case the initial values where very close to the model parameters, but the code was unable to converge which suggests a local minimum.

In the de-centered dipole case SPARTI converged less frequently than in the dipole case. However, even when the starting parameters, for the algorithm, were far from the correct solution convergence was still achieved. The disadvantage of the de-centered dipole morphology is that the indistinguishable solutions have not yet been determined and so it is not clear whether the converged solutions are the same or whether they are different.

In the dipole+quadrupole case SPARTI converged less than in both the dipole and de-centred dipole case. This is expected since the number of local minima are expected to be greater. When it did converge however the solution matched the model case, even when the initial parameters were far from the correct solution, this points to a uniqueness in the solution.

In all cases SPARTI was able to converge even when the initial values were far from the model parameters and in the dipole and dipole + quadrupole case when the solution converged each solution matched the model parameters. This analysis shows that is necessary to start from a number of initial parameters because some will not converge, sometimes even if the values are close to the correct solution. In the cases where SPARTI did not converge, by starting from a different set of parameters the model parameters could be recovered.

Table 5.1: A sample of the tests performed to check convergence to a model spectrum starting from random initial conditions, in the dipole case. For each test number the three rows are, the parameters used to generate the model spectrum, the starting parameters used by Sparti and finally the best-fit parameters calculated using Sparti. The tests in bold are those which reached convergence.

Test Number	i (°)	β (°)	B_d (G)	$v \sin i$ ($\mathrm{km\,s^{-1}}$)	f_0 (°)
1	109	41	15478	4.00	288.00
	6	145	16104	1.00	288.00
	41	108	15494	3.54	289.58
2	**149**	**40**	**6366**	**8.00**	**36.00**
	32	**52**	**14645**	**1.00**	**216.00**
	31	**140**	**6356**	**8.00**	**35.71**
3	**41**	**121**	**12483**	**2.00**	**108.00**
	52	**59**	**4730**	**1.00**	**216.00**
	41	**121**	**12483**	**2.00**	**108.00**
4	**93**	**67**	**8193**	**9.00**	**108.00**
	103	**120**	**14164**	**1.00**	**252.00**
	87	**113**	**8183**	**8.99**	**108.04**
5	**62**	**33**	**14069**	**10.00**	**216.00**
	93	**109**	**1913**	**1.00**	**324.00**
	62	**33**	**14069**	**10.00**	**216.00**
6	**178**	**25**	**18376**	**9.00**	**180.00**
	157	**67**	**9187**	**1.00**	**360.00**
	178	**25**	**18376**	**9.00**	**180.00**
7	161	138	6160	1.00	288.00
	82	114	1129	1.00	36.00
	136	180	5504	1.99	7.38
8	**18**	**116**	**11794**	**2.00**	**324.00**
	31	**59**	**8936**	**1.00**	**144.00**
	18	**116**	**11794**	**2.00**	**324.00**
9	**137**	**31**	**14788**	**10.00**	**72.00**
	10	**59**	**9154**	**1.00**	**216.00**
	43	**149**	**14782**	**10.02**	**71.96**
10	**51**	**121**	**11427**	**10.00**	**252.00**
	131	**158**	**15985**	**1.00**	**144.00**
	51	**121**	**11427**	**10.00**	**252.00**

Table 5.2: A sample of the tests performed to check convergence to a model spectrum starting from random initial conditions, in the de-centered dipole case. For each test number the three rows are, the parameters used to generate the model spectrum, the starting parameters used by SPARTI and finally the best-fit parameters calculated using SPARTI. The tests in bold are those which reached convergence.

Test Number	i (°)	α (°)	β (°)	γ (°)	y_2	y_3	B_d (G)	$v \sin i$ ($\mathrm{km\,s^{-1}}$)	f_0 (°)
1	**10**	**135**	**5**	**142**	**0.01**	**0.01**	**9234**	**8.00**	**36.00**
	28	**67**	**156**	**20**	**0.00**	**0.01**	**6641**	**1.00**	**216.00**
	10	**84**	**76**	**356**	**-0.01**	**-0.01**	**9617**	**7.95**	**217.26**
2	**78**	**108**	**82**	**145**	**0.01**	**0.01**	**9086**	**9.00**	**36.00**
	95	**86**	**42**	**7**	**0.01**	**0.00**	**3859**	**1.00**	**36.00**
	282	**196**	**218**	**113**	**-0.01**	**0.00**	**9089**	**-8.99**	**36.22**
3	**16**	**41**	**18**	**37**	**0.01**	**0.01**	**8850**	**6.00**	**288.00**
	115	**48**	**155**	**151**	**0.01**	**0.00**	**10534**	**1.00**	**324.00**
	196	**39**	**163**	**141**	**-0.01**	**-0.01**	**8856**	**-5.96**	**310.43**
4	172	13	171	98	0.01	0.00	9065	6.00	108.00
	134	31	132	136	0.01	0.00	16678	1.00	324.00
	144	27	133	126	0.01	-0.03	17607	9.85	322.38
5	**166**	**150**	**59**	**38**	**0.01**	**0.01**	**588**	**7.00**	**288.00**
	141	**41**	**2**	**47**	**0.00**	**0.01**	**1067**	**1.00**	**216.00**
	166	**114**	**216**	**117**	**0.01**	**0.01**	**-588**	**7.00**	**287.96**
6	50	29	10	153	0.00	0.00	2776	2.00	72.00
	84	103	91	51	0.00	0.01	14796	1.00	288.00
	79	129	130	58	0.04	0.04	13706	-0.37	269.68
7	**23**	**164**	**5**	**136**	**0.01**	**0.01**	**8662**	**9.00**	**36.00**
	58	**178**	**140**	**172**	**0.00**	**0.00**	**2717**	**1.00**	**144.00**
	23	**58**	**356**	**2**	**-0.01**	**0.01**	**8661**	**8.98**	**212.62**
8	40	66	134	28	0.01	0.01	15100	7.00	324.00
	8	9	67	177	0.00	0.01	8285	1.00	144.00
	81	45	170	41	0.04	0.04	12429	12.20	344.45
9	96	88	59	134	0.01	0.01	12215	3.00	180.00
	54	106	73	30	0.00	0.00	12696	1.00	144.00
	0	112	42	337	-0.03	0.04	3595	18.19	154.69
10	**78**	**178**	**53**	**41**	**0.00**	**0.00**	**7899**	**2.00**	**324.00**
	60	**29**	**155**	**75**	**0.01**	**0.01**	**12155**	**1.00**	**216.00**
	102	**95**	**142**	**83**	**0.00**	**-0.00**	**7908**	**1.96**	**16.49**

Table 5.3: A sample of the tests performed to check convergence to a model spectrum starting from random initial conditions, in the dipole + quadrupole case. For each test number the three rows are, the parameters used to generate the model spectrum, the starting parameters used by SPARTI and finally the best-fit parameters calculated using SPARTI. The tests in bold are those which reached convergence.

Test Number	i (°)	β (°)	β_1 (°)	β_2 (°)	γ_1 (°)	γ_2 (°)	B_d (G)	B_q (G)	$v \sin i$ (km s^{-1})	f_0 (°)
1	134	46	120	167	191	57	112	8761	7.00	288.00
	45	5	122	75	91	253	5390	3451	1.00	180.00
	80	17	139	125	191	43	5914	3238	6.83	103.90
2	127	169	3	50	60	156	19803	13229	7.00	36.00
	86	66	43	108	223	211	3631	5017	1.00	360.00
	172	125	48	103	182	167	13218	19159	8.22	121.68
3	103	98	88	135	311	149	5717	13415	8.00	144.00
	42	96	134	137	183	196	10721	16288	1.00	324.00
	58	101	85	141	119	301	4626	13999	8.26	164.56
4	**121**	**20**	**120**	**7**	**289**	**222**	**19221**	**15749**	**7.00**	**108.00**
	29	**125**	**104**	**27**	**65**	**5**	**10173**	**13502**	**1.00**	**108.00**
	59	**160**	**120**	**7**	**108**	**41**	**19301**	**15701**	**6.94**	**108.97**
5	**118**	**176**	**73**	**83**	**82**	**92**	**15993**	**7103**	**3.00**	**288.00**
	74	**118**	**78**	**82**	**62**	**67**	**16179**	**2726**	**1.00**	**36.00**
	118	**176**	**98**	**107**	**261**	**248**	**15956**	**7178**	**3.01**	**300.56**
6	**133**	**21**	**44**	**36**	**55**	**350**	**11268**	**13697**	**8.00**	**108.00**
	159	**45**	**78**	**89**	**90**	**272**	**6377**	**4206**	**1.00**	**324.00**
	133	**21**	**44**	**36**	**55**	**350**	**11268**	**13697**	**8.00**	**108.00**
7	**82**	**103**	**114**	**37**	**188**	**137**	**1761**	**786**	**6.00**	**252.00**
	93	**50**	**66**	**119**	**67**	**302**	**6082**	**12527**	**1.00**	**72.00**
	98	**78**	**112**	**38**	**359**	**327**	**1744**	**757**	**6.01**	**251.89**
8	117	169	100	82	257	108	688	19995	3.00	252.00
	160	21	121	52	20	127	11402	17211	1.00	324.00
	169	138	137	51	269	110	1353	19955	2.17	210.46
9	62	168	135	175	184	191	9409	6834	7.00	108.00
	131	55	112	70	69	330	3690	11689	1.00	216.00
	161	9	126	94	56	312	5005	12418	1.08	174.28
10	118	57	64	102	186	11	16488	811	4.00	36.00
	79	166	122	24	81	185	1378	13078	1.00	108.00
	79	108	91	20	138	282	9066	19344	1.75	45.47

5.4 Simulating instrument effects

After confirming that the code achieves the correct parameters in the model case, it is important to test how the code functions in a more realistic scenario. This involves artificially adding sources of noise to model spectra, allowing me to simulate real spectra while still knowing the parameters which define each model. In this way I am able to test the limits at which point Sparti is no longer able to regain the parameters describing the model magnetic field, neglecting variations in abundances.

5.4.1 Photon-noise

The effects of photon-noise are shown in Fig. 5.3. The signals of I and V are not as strongly affected as Q and U, because the amplitude of the former are several times larger than the latter. At a signal-to-noise ratio (SNR) of 50 the shape of Q and U is lost in the noise and the result will not be accurate. As a result of this constraint, when observing full Stokes $IQUV$ profiles, it is important to achieve a SNR of at least 200. To model the photon-noise the σ of Stokes QUV is (1/SNR) and the σ of Stokes I is $(1/\sqrt{3}\mathrm{SNR})$. The synthetic spectra with artificial noise, $\boldsymbol{F}'_I$, $\boldsymbol{F}'_Q$, $\boldsymbol{F}'_U$ and $\boldsymbol{F}'_V$ are calculated using

$$\begin{aligned}
\boldsymbol{F}'_I(\lambda_0) &= \boldsymbol{F}_I(\lambda_0) + \frac{P}{\sqrt{3}\mathrm{SNR}} \\
\boldsymbol{F}'_Q(\lambda_0) &= \boldsymbol{F}_Q(\lambda_0) + \frac{P}{\mathrm{SNR}} \\
\boldsymbol{F}'_U(\lambda_0) &= \boldsymbol{F}_U(\lambda_0) + \frac{P}{\mathrm{SNR}} \\
\boldsymbol{F}'_V(\lambda_0) &= \boldsymbol{F}_V(\lambda_0) + \frac{P}{\mathrm{SNR}}
\end{aligned} \tag{5.2}$$

where F is the synthetic flux at a particular point λ_0,

$$P = t - \frac{2.515517 + 0.802853t + 0.010328t^2}{1.0 + 1.432788t + 0.189269t^2 + 0.001308t^3} \tag{5.3}$$

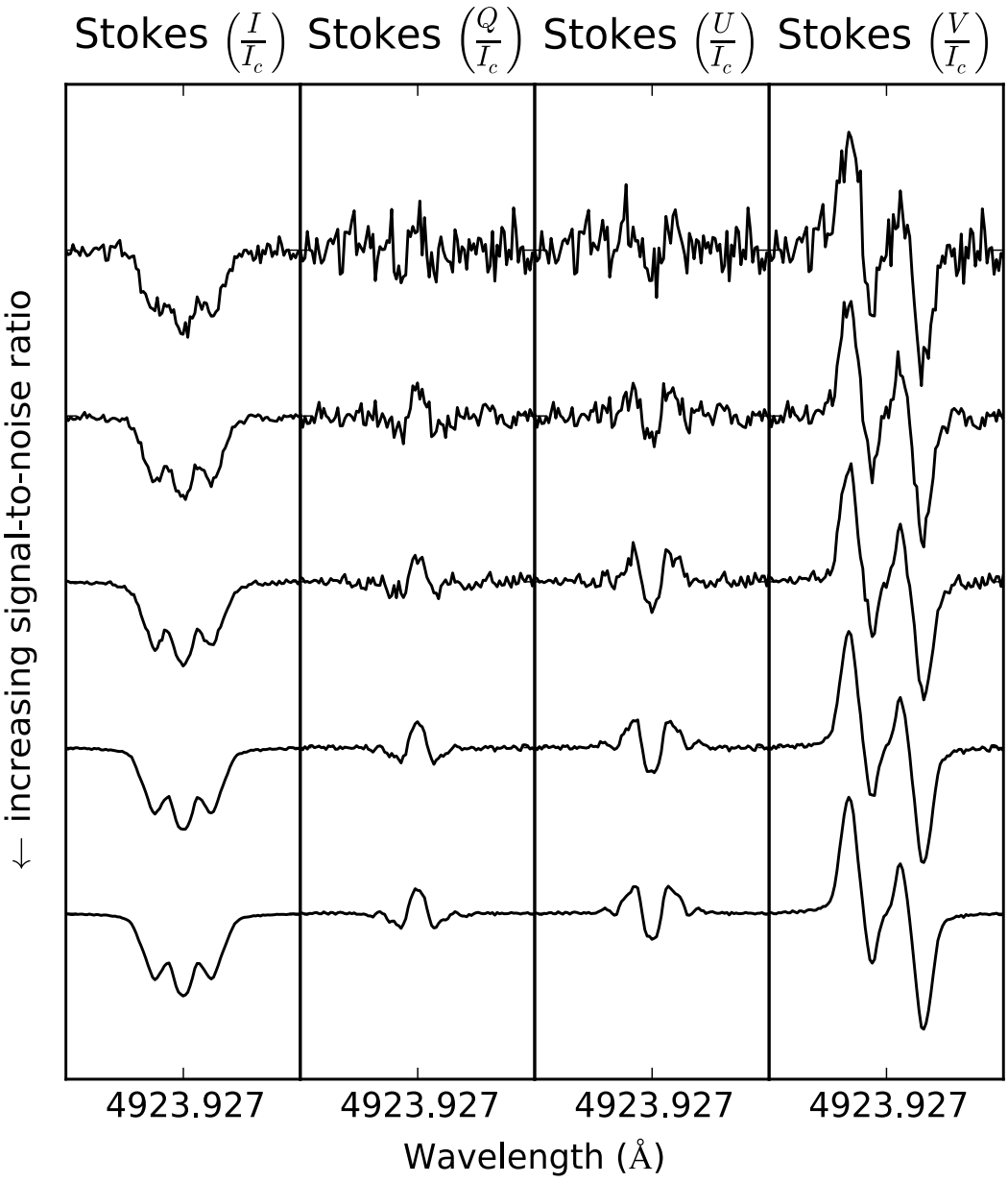

Figure 5.3: Signal degradation of Stokes $IQUV$ in percentage units as a result of photon noise. From top to bottom 1. SNR = 50; 2. SNR = 100; 3. SNR = 200; 4. SNR = 500; 5. No Instrumental effects

where P is the result of the calculation of the inverse of the normal cumulative density function (e.g. Abramowitz & Stegun 1965) and

$$t = \sqrt{\log\left(\frac{1}{D^2}\right)} \tag{5.4}$$

where D is a random floating point number between 0.0 and 1.0.

I tested the convergence of SPARTI using the EXPRESS code with SNR = 1000, 300, 100, 30 and 10. The lowest SNR for which SPARTI was still able to calculate the correct solution was 100.

5.4.2 Instrument Resolving Power

The effects of the resolution of the instrument used to measure stellar spectra are shown in Fig. 5.4. The resolving power of the instrument acts on an observed spectrum in a similar way to $v \sin i$. In the figure, it can be seen that at a resolving power (R) of $\lesssim 30000$ the Zeeman splitting of the spectral lines cannot be observed. If only Stokes I was observed it would not be possible to determine whether the broadening was a result of $v \sin i$ or the magnetic field. The Stokes Q, U and V signals are still observed and so with spectropolarimetry it is possible to still detect a magnetic field. At an instrument resolving power of 10000 there is an overall lack of signal, however the detection of a magnetic field is still possible using the signal of Stokes V.

I tested the convergence of SPARTI using the EXPRESS code with R = 200000, 50000, 25000, 10000, 5000, 2500, 1000. The lowest R for which SPARTI was still able to calculate the correct solution was 5000. However, this was for only for very simple magnetic morphologies, in the case of a more complicated geometry the lowest instrument resolution for which SPARTI was still able to calculate the correct solution was 25000.

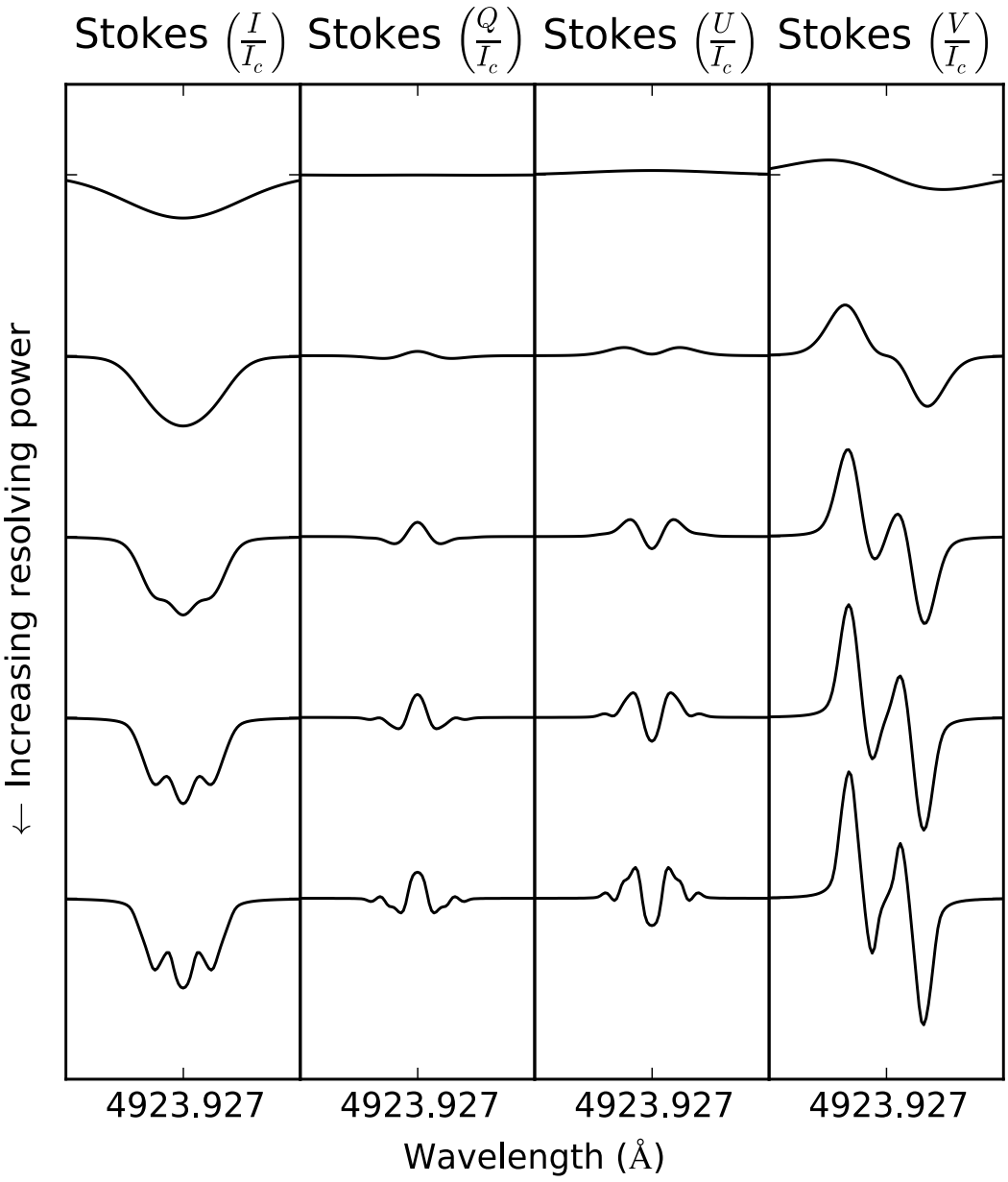

Figure 5.4: Signal degradation of Stokes $IQUV$ in percentage units as a result of instrument resolving power (R). From top to bottom 1. R = 10000; 2. R = 30000; 3. R = 60000; 4. R = 120000; 5. No Instrumental effects

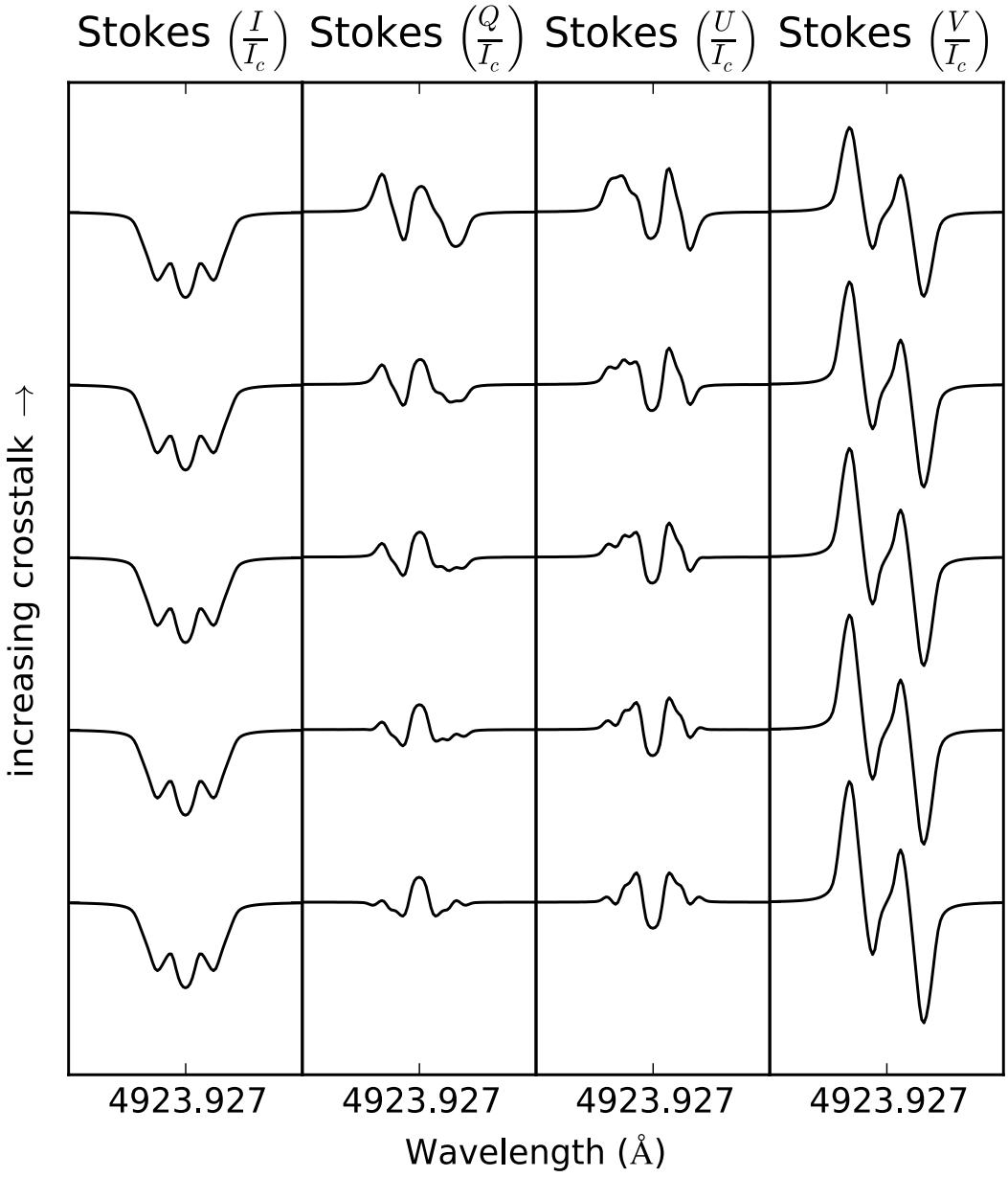

Figure 5.5: Signal degradation of Stokes $IQUV$ in percentage units as a result of crosstalk between Stokes V and Stokes Q and U. From top to bottom 1. crosstalk = 30%; 2. crosstalk = 15%; 3. crosstalk = 10%; crosstalk = 5%; 5. No Instrumental effects

5.4.3 Crosstalk

An important consideration in terms of instrumental effects is the crosstalk between different Stokes parameters. This effect occurs, for example, when a small percentage of Stokes I is measured by the instrument as Stokes Q or V. Cross-talk from Stokes I is generally well seen as an offset in the continuum and may be removed by rectifying the continuum of Stokes V to zero. More difficult to deal with is crosstalk from linear to circular polarisation, i.e., when a signal of circular polarisation is seen by the instrument as a signal of linear polarisation. This effect is generally due to the birefringent properties of the optical elements that precede the polarimetric optics, e.g., the instrument collimator. The crosstalk phenomenon has been described in detail by Bagnulo et al. (2009) and its effects are illustrated in Fig. 5.5, where it can be seen that a crosstalk of 10% has a serious impact on the observed Stokes Q and U profiles. Testing for the effects of crosstalk is important because it has been discovered in spectropolarimeters such as ESPaDOnS (Silvester et al. 2012). When first commissioned ESPaDOnS was found to have 10–15% of Stokes V contaminating Stokes Q and U. The triplet lens was replaced twice along with the atmospheric dispersion corrector and currently the crosstalk is below 1%. The NARVAL spectropolarimeter, which is a copy of ESPaDOnS, has not been as thoroughly tested for cross-talk as ESPaDOnS but results show a cross-talk of 3.1% (Silvester et al. 2012). To simulate the effects of crosstalk I use

$$\begin{aligned} F_{I+\Upsilon}(\lambda) &= F'_I(\lambda) \\ F_{Q+\Upsilon}(\lambda) &= F'_Q(\lambda) + \Upsilon F'_V(\lambda) \\ F_{U+\Upsilon}(\lambda) &= F'_U(\lambda) + \Upsilon F'_V(\lambda) \\ F_{V+\Upsilon}(\lambda) &= (1-\Upsilon) F'_V(\lambda) \end{aligned} \tag{5.5}$$

where Υ is the fractional crosstalk.

I tested the convergence of Sparti using the Express code with crosstalk of 0%, 10% and 15%. In the majority of cases Sparti was able to recover the model parameters with a crosstalk of 10%, however when the tested magnetic field was weak or when the Stokes V signal was particularly strong, 5% was the maximum crosstalk

over which SPARTI would not converge to the original model.

5.4.4 Testing Convergence with all instrument effects

Considering the effects of both SNR and the resolving power of the instrument SPARTI was successfully able to recover the model solution to a resolving power of 60000 and a SNR of 100. If a crosstalk of 10% is added to the spectrum, SPARTI can recover the model solution for a spectral resolution of 60000 and an SNR between 1000 and 200.

5.5 SPARTI Simple

This section has been published in MNRAS (Martin et al. 2017) [1]*, I completed all work in this section.*

Since I plan to use SPARTI not only to recover the magnetic configuration of stars, but also for a full spectral analysis. It is important to check also whether my inversion algorithms are able to recover the abundance of the chemical elements, as well as the fundamental parameters of the stars. I therefore analysed the Sun (G2V), HD32115 (A9V) and 21 Peg (B9.5V). These stars were chosen since they cover a range of temperature with Balmer lines sensitive to different fundamental parameters of the star. For the Sun the Balmer lines are mostly sensitive to temperature, for HD32115 the Balmer lines are sensitive to temperature and surface gravity and for 21 Peg the Balmer lines are more sensitive to surface gravity.

I have calculated the fundamental parameters based on the methods in Section 6.5.1 and 6.5.2 and the results are shown in Tables 5.4, 5.5 & 5.6. My results are within the errors of those previously published. In Fig. 5.6 & 5.7 I show the fit of the observed Balmer lines with the synthetic spectrum I calculated for 21Peg and HD32115

[1] *A spectroscopic study of the open cluster NGC 6250*, A. J. Martin, M. J. Stift, L. Fossati, S. Bagnulo, C. Scalia, F. Leone, and B. Smalley, 2017, MNRAS, Volume 466, Page 613, Oxford University Press. Permission to reproduce is granted on the Oxford Journals website.
http://dx.doi.org/10.1093/mnras/stw3052

Table 5.4: The fundamental parameters associated with the Sun. Given both by Prsa et al. (2016) and by the method used in this work.

Fundamental Parameters	Prsa et al. (2016)	This work
$T_{\rm eff}$ [K]	5772	5800 ± 200
$\log g$ [cgs]	4.438	4.49 ± 0.1
$v \sin i$ [km s^{-1}]	1.2	2.64 ± 0.13
$v_{\rm mic}$ [km s^{-1}]	0.875	1.0 ± 0.03

respectively. I used the Balmer lines to determine $T_{\rm eff}$ and $\log g$ for HD32115 because Fossati et al. (2011b) showed that the ionisation balance does not provide an accurate value of $\log g$.

To determine the abundances of the elements in the solar photosphere I convolved the solar spectrum with an instrument resolution of 25900 to simulate the analysis of a GIRAFFE spectrum. My analysis of the chemical abundances of the Sun shows good agreement with the results of Asplund et al. (2009) within the errorbars as shown in Table 5.7.

The next step was to determine the abundances for 21 Peg and compare them to those determined by Fossati et al. (2009). For the analysis I chose the same lines, atomic parameters and ATLAS12 model atmosphere as Fossati et al. (2009) and removed any lines which show non-local thermodynamic equilibrium effects and/or have evidence of hyperfine structure. My analysis of the chemical abundances of 21 Peg, shows good agreement with the results of Fossati et al. (2009) within the errorbars as shown in Table 5.8[2].

[2]The errors calculated by Fossati et al. (2009) are based on the standard deviation of the measured chemical abundances for each line. Only one line was measured for Sr and so no standard deviation could be calculated.

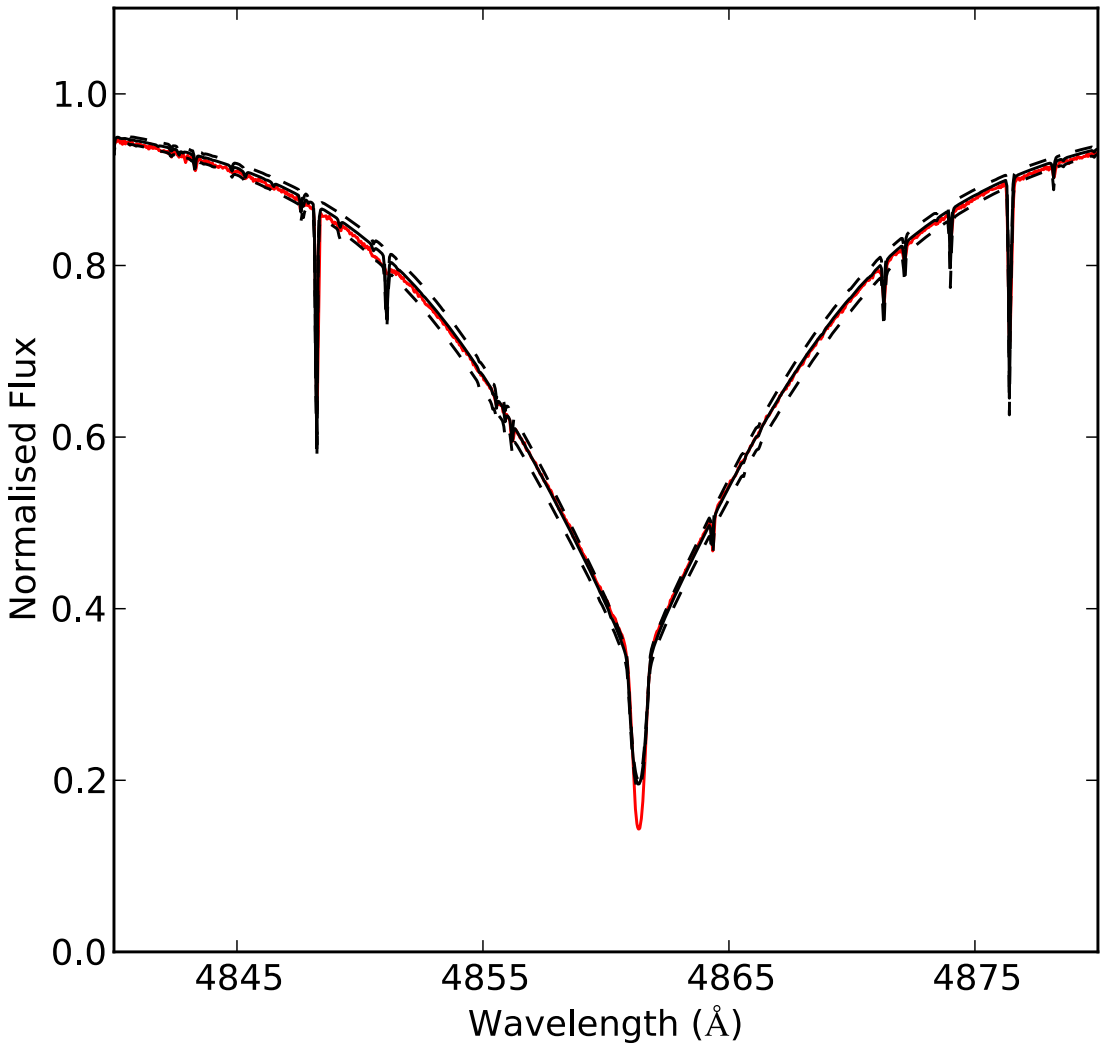

Figure 5.6: The fit to the Hβ line in the spectrum of 21 Peg. The solid red line is the observed spectrum. The dashed black line is the synthetic spectrum calculated using $T_{\rm eff} = 10400\,{\rm K}$ and $\log g = 3.55$. The two dashed blue lines are ± 200K

Table 5.5: The fundamental parameters associated with HD32115.

Fundamental Parameters	Fossati et al. (2011b)	This work
$T_{\rm eff}$ [K]	7250 ± 100	7300 ± 200
$\log g$ [cgs]	4.2 ± 0.1	4.2 ± 0.1
$v_{\rm mic}$ [km s^{-1}]	2.5 ± 0.2	2.5 ± 0.02

Table 5.6: The fundamental parameters associated with 21 Peg.

Fundamental Parameters	Fossati et al. (2009)	This work
$T_{\rm eff}$ [K]	10400 ± 200	10400 ± 200
$\log g$ [cgs]	3.55 ± 0.1	3.5 ± 0.1
$v \sin i$ [km s^{-1}]	3.76 ± 0.35	4.2 ± 0.1
$v_{\rm rad}$ [km s^{-1}]	0.5 ± 0.5	0.40 ± 0.04
$v_{\rm mic}$ [km s^{-1}]	0.5 ± 0.5	0.40 ± 0.2

Table 5.7: A comparison between the chemical abundances of the Sun calculated by Asplund et al. 2009 and those calculated by SPARTI SIMPLE. Δ is the difference between the chemical abundances presented by Asplund et al. (2009) and those calculated by SPARTI SIMPLE.

	$\log [N/H]$		
Element	Asplund et al. (2009)	SPARTI ABUND	Δ
Mg	7.60 ± 0.04	7.63 ± 0.02	−0.03
Ti	4.95 ± 0.05	4.96 ± 0.01	−0.01
V	3.93 ± 0.08	3.97 ± 0.01	−0.04
Cr	5.64 ± 0.04	5.60 ± 0.01	0.04
Fe	7.50 ± 0.04	7.49 ± 0.01	0.01
Ni	6.22 ± 0.04	6.21 ± 0.01	0.01

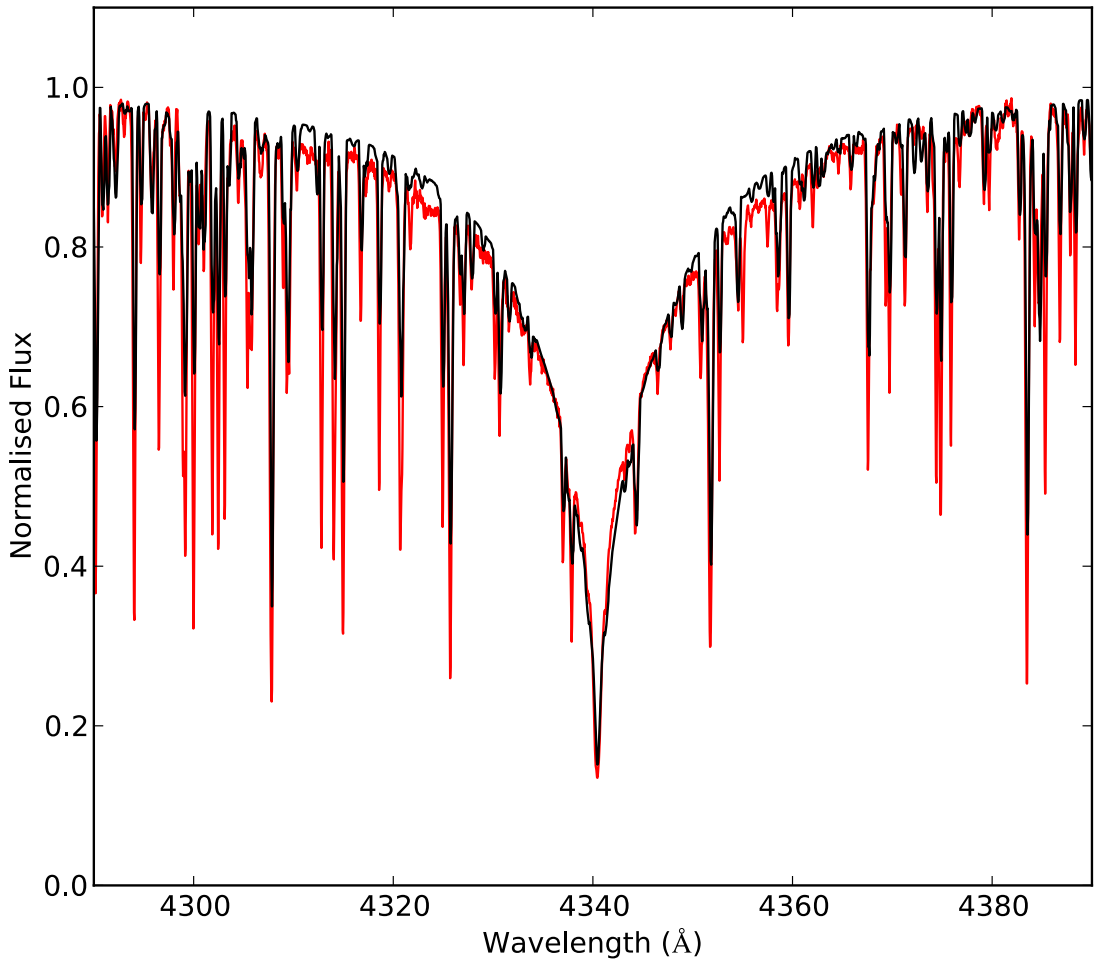

Figure 5.7: The fit to the Hγ line in the spectrum of HD32115. The solid red line is the observed spectrum. The black line is the synthetic spectrum calculated using $T_{\rm eff}$=7250 and $\log g$ =4.2 and solar abundances (Asplund et al. 2009).

Table 5.8: A comparison between the chemical abundances of 21 Peg calculated by Fossati et al. (2009) and those calculated by SPARTI SIMPLE, along with the Solar abundances from Asplund et al. (2009). Δ is the difference between the chemical abundances presented by Fossati et al. (2009) and those calculated by SPARTI SIMPLE.

	$\log[N/H]$			
Element	Fossati et al. (2009)	SPARTI ABUND	Δ	Solar
O I	8.76 ± 0.11	8.80 ± 0.06	−0.04	8.69
Al II	6.34 ± 0.10	6.37 ± 0.16	−0.03	6.45
Si II	7.55 ± 0.13	7.51 ± 0.07	0.04	7.51
S II	7.18 ± 0.13	7.24 ± 0.34	−0.06	7.12
Sc II	2.67 ± 0.10	2.59 ± 0.23	0.08	3.15
Ti II	4.81 ± 0.09	4.78 ± 0.03	0.03	4.95
V II	4.06 ± 0.06	3.96 ± 0.05	0.10	3.93
Cr II	5.84 ± 0.10	5.79 ± 0.02	0.05	5.64
Fe II	7.54 ± 0.12	7.52 ± 0.01	0.02	7.50
Ni II	6.43 ± 0.09	6.38 ± 0.03	0.05	6.22
Sr II	2.94 ± -	2.91 ± 0.04	0.03	2.87
Ba II	2.85 ± 0.06	2.81 ± 0.24	0.04	2.18

5.6 Summary of Testing

In this chapter both Sparti Simple and Sparti were tested confirming that my modifications to Cossam have not introduced errors in the output. I have shown that the convolution works as expected and that my method for determining the fundamental parameters of the stars is accurate. Sparti was able to recover the parameters of a model spectrum, even when the initial values are considerably different from the model. My tests have, however, highlighted the need in the magnetic case to repeat the inversion from a number of different starting values as some will not converge. Sparti was able to accurately recover the model parameters even with the addition of photon noise, instrument response and crosstalk. My analysis shows that a resolving power of at least 60000 and a signal-to-noise ratio of at least 200 are required to recover the magnetic morphology of the star. Finally, using Sparti Simple, I was able to show that the recovered abundances of elements in the photospheres of observed stars agree with previously published results within the error-bars.

6 Abundance Analysis of NGC6250

This chapter has been published in MNRAS (Martin et al. 2017) [1]*. I completed all of the work in the chapter except for the K-means clustering analysis which was performed by C. Scalia. The reduced un-normalised spectra were provided by L. Fossati.*

Using Sparti Simple I am able to efficiently perform the chemical abundance analysis of the photospheres of multiple stars. In this thesis I have considered the low and mid resolution spectra of 32 stars observed with the Fibre Large Array Multi Element Spectrograph (FLAMES) instrument of the European Southern Observatory's (ESO) Very Large Telescope (VLT) in the field of view of the open cluster NGC 6250 and I have performed a detailed chemical abundance analysis of the 19 member stars. These observations are part of a data set containing the spectra of approximately 1000 stars observed as part of a larger effort to explore how various physical effects change as a function of stellar age, in particular to set observational constraints to the theory of atomic diffusion in stellar photospheres (Michaud 1970), both in case of magnetic and non-magnetic atmospheres. The overall project includes data for potential members of various open clusters, covering ages from $\log t = 6.8$ to 8.9 years and distance moduli from 6.4 to 11.8. The full list of observed open clusters is given by Fossati et al. (2008b).

The analysis of three of these clusters has been performed by Kılıçoğlu et al. (2016) (NGC6405); Fossati et al. (2007), Fossati et al. (2008a), Fossati et al. (2010) and Fossati et al. (2011a) (Praesape cluster and NGC 5460). Kılıçoğlu et al. (2016) found NGC 6405 to have an age of $\log t \sim 7.88$, a distance of 400 pc $\pm$ 50 pc and a [Fe/H] metallicity of 0.07 ± 0.03. The Praesape cluster has an age of $\log t \sim 8.85 \pm 0.15$ (González-García et al. 2006) and it is at a distance of 180 pc $\pm$ 10 pc (Robichon et al. 1999). Fossati et al. (2011a) found NGC 5460 to have an age of $\log t \sim 8.2 \pm 0.1$, a distance of 720 pc $\pm$ 50 pc and a near solar metallicity.

[1] *A spectroscopic study of the open cluster NGC 6250*, A. J. Martin, M. J. Stift, L. Fossati, S. Bagnulo, C. Scalia, F. Leone, and B. Smalley, 2017, MNRAS, Volume 466, Page 613, Oxford University Press. Permission to reproduce is granted on the Oxford Journals website.
http://dx.doi.org/10.1093/mnras/stw3052

With an age of $\log t \sim 7.42$ years and a distance of 865 pc (Kharchenko et al. 2013), NGC 6250 is both the youngest and most distant cluster analysed as part of this project so far. As a result my work adds important data for younger stars.

Further studies completed by different groups, with data which can be used as part of this study include those by Gebran & Monier (2008) and Gebran, Monier & Richard (2008, Gebran et al. (2010) (Coma Berenices, $\log t = 8.65$; the Pleiades, $\log t = 8.13$; and Hyades, $\log t = 8.9$); Folsom et al. (2007) and Villanova, Carraro & Saviane (2009) (NGC 6475, $\log t = 8.48$); and Stütz et al. (2006) (IC 2391, $\log t = 7.66$).

The study by Bailey, Landstreet & Bagnulo (2014) searched for trends between chemical abundance and stellar parameters of chemically peculiar Ap stars, to determine whether chemical peculiarities change as a star evolves. This data allows me to compare the behaviour of chemically peculiar magnetic stars with the sample of chemically normal stars.

6.1 NGC6250

The open cluster NGC 6250 is the southern constellation of Ara. The age of the cluster and distance from the Sun to the cluster have been determined to be $\log t \sim 7.42$ years and 865 pc by Kharchenko et al. (2013) using proper motions and photometry from PPMXL (Roeser, Demleitner & Schilbach 2010) and 2MASS JHK photometric data (Skrutskie et al. 2006). Kharchenko et al. (2013) determined the cluster proper motion as $0.74 \pm 0.4\,\mathrm{mas\,yr^{-1}}$ in right ascension (RA) and $-4.14 \pm 0.4\,\mathrm{mas\,yr^{-1}}$ in declination (DEC) with a cluster radial velocity of $-8.0 \pm 0.81\,\mathrm{km\,s^{-1}}$. Previously, Herbst (1977) estimated $\log t \sim 7.146$ yr and distance (d) 1025 pc. Moffat & Vogt (1975) estimated $d = 950$ pc. NGC 6250 is located in a dust-rich region of space, with $E(B-V) = 0.385$ and $E(J-H) = 0.123$ (Kharchenko et al. 2013). My review of the literature revealed that the cluster has not been spectroscopically studied in detail. The previous studies are limited to a small number of classification spectra and radial velocity measurements.

Table 6.1: Instrument settings information with the useful spectral lines given for stellar $T_{\rm eff}$ between ~ 6000 K and ~ 25000 K (e.g. Fossati et al. 2011a)

Instrument Setting	Resolving Power	Spectral Region (Å)	Important Spectral Lines
LR3	7500	4500-5077	Hβ
HR9B	25900	5139-5355	Fe-peak (inc. Fe,Ti and Cr) Mg triplet at 5167, 5172 and 5183 Å
HR11	24200	5592-5838	Fe, Na and Sc
LR6	8600	6438-6822	Hα
UVES	47000	4140-6210	Hβ, Hγ Fe-peak (inc. Fe,Ti and Cr) Mg triplet at 5167, 5172 and 5183 Å

6.2 Observations with FLAMES

The observations of NGC 6250 were obtained in service mode on 2007 May 27th and 2007 May 30th using FLAMES, the multi-object spectrograph attached to UT2 (Kueyen) of the ESO/VLT. The FLAMES instrument (Pasquini & etal. 2002) has a field of view covering 25 arcmin. A total of 138 fibres feed the two spectrographs, GIRAFFE and the Ultraviolet and Visual Echelle Spectrograph (UVES). Of these fibres 130 are linked to GIRAFFE using MEDUSA fibres and the remaining eight are linked to UVES using UVES fibres. FLAMES-GIRAFFE can obtain low- or medium-resolution spectra ($R = 7500 - 30000$), within the spectral range $3700 - 9000$ Å. Low-resolution spectra may be obtained within wavelength intervals 500 to 1200 Å, medium-resolution spectra are obtained in wavelength intervals 170 to 500 Å. FLAMES-UVES can obtain high-resolution spectra (R = 47 000), with central wavelengths of 5200, 5800, or 8600 Å each covering a wavelength range ~ 2000 Å.

The instrument set-ups were strategically chosen to allow for the observation of two Balmer lines (Hβ & Hα for GIRAFFE and Hβ & Hγ for UVES), which are es-

sential to the determination of $T_{\rm eff}$ and $\log g$. Another key consideration for choosing the set-up of the instrument is the wavelength range which maximises the number of metal lines observed and consequently the number of chemical elements available for spectral analysis. The wavelength used for the telescope guiding was set as 5200 Å and, to avoid light losses due to atmospheric differential refraction, the GIRAFFE settings were chosen to be as close to this value as possible. The spectral resolution of UVES is significantly higher than GIRAFFE and so to achieve a high enough signal-to-noise ratio for the UVES spectra it was necessary to have an exposure time generally 3-4 times longer than that of GIRAFFE. As a result of this, during one UVES observation, observations with three GIRAFFE settings could be completed. The settings used for the observations are shown in Table 6.1. The HR9B and HR11 settings were observed both observing nights and one L- setting was observed each night. To prevent saturation of the observations each UVES observation was divided into four sub-exposures and each GIRAFFE setting was divided into two sub-exposures.

The data were obtained in service mode, and the package released included the products reduced by ESO with the instrument dedicated pipelines. For each setting of UVES and GIRAFFE, all stars were observed simultaneously. Tables 6.2 & 6.3 include all stars observed for which the S/N was high enough to allow for the determination of $T_{\rm eff}$, $\log g$, $v \sin i$ and $v_{\rm rad}$.

6.3 Normalisation of stellar spectra

To compare the observed spectrum of a star with a model spectrum, it must first be normalised to unity. This is because there are a number of factors which can affect the continuum shape of the observed spectrum, including the stellar properties, atmospheric conditions and the instrument response.

There are already normalisation routines available. However, in an effort to create a suite of programs which allows me to efficiently perform the abundance analysis of cluster and non-cluster stars, I wrote a normalisation program to semi-automatically

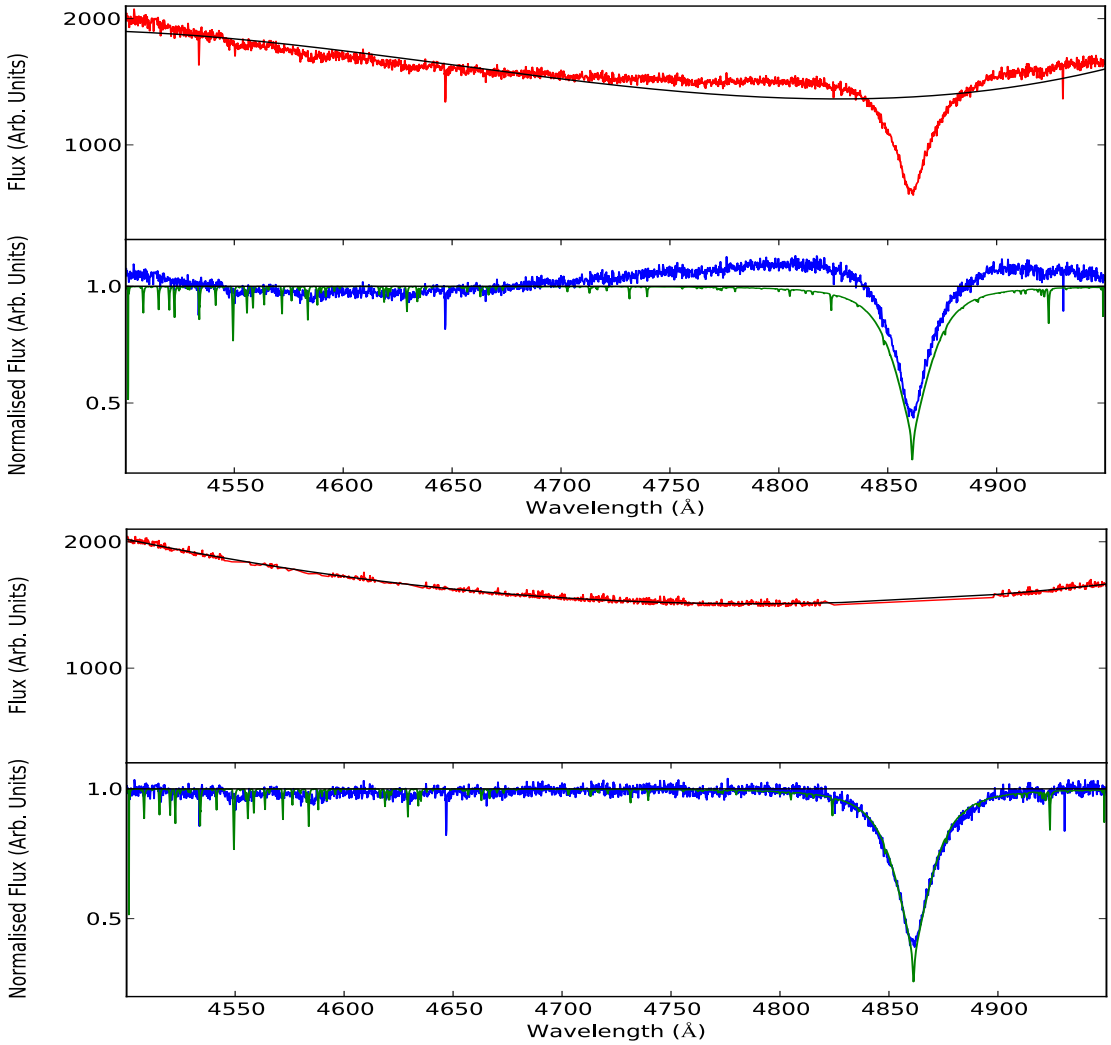

Figure 6.1: From top to bottom: 1. The observed spectrum of UCAC12284645 (red solid line) and a polynomial fit (black solid line); 2. The observed spectrum of UCAC12284645 normalised using the fit in 1 (blue solid line) and a synthetic spectrum at $T_{\rm eff} = 11000$ and $\log g = 4.3$ (green solid line); 3. The observed spectrum of UCAC12284645 after the σ-clipping routine (red solid line) and a polynomial fit (black solid line); 3. The observed spectrum of UCAC12284645 normalised using the fit in 3 (blue solid line) and a synthetic spectrum at $T_{\rm eff} = 11000$ and $\log g = 4.3$ (green solid line).

normalise stellar spectra. An example of a spectrum before and after normalisation is shown in Fig. 6.1.

I begin by fitting the observed stellar spectrum with a third-order polynomial in the case of the low-resolution GIRAFFE settings LR3 and LR6 and a cubic spline in the case of the medium-resolution GIRAFFE settings HR9B and HR11 and the UVES spectra. Experience has shown these are the most effective functions for the wavelength ranges in this analysis. An example of the normalisation which would result if I used this initial fit to normalise an observed spectrum is shown in the second panel of Fig. 6.1. To improve the quality of the normalisation I iteratively σ-clip about the function I have fitted to the observed spectrum, calculating a new function after each iteration. The number of iterations and the number of σ above and below to be clipped are free parameters and can be tuned for each individual setting. Typically I will clip all points $3\,\sigma$ above and $1\,\sigma$ below the spectrum. This asymmetry is present since, in this work, I am normalising absorption spectra for which the majority of the signal will be below the continuum as a result of the absorption lines. At each iteration, I compare the normalised spectrum with a synthetic spectrum generated with Cossam at a $T_{\rm eff}$ approximately equal to the observed spectrum. When I am confident that the two continua match I stop the iterations. There is however still the potential for the continuum to be too high or too low, for this reason Sparti Simple is able to independently move the spectrum up and down to obtain the best possible fit.

6.4 Cluster Membership

The studies by Bayer et al. (2000), Dias et al. (2006) and Feinstein et al. (2008) provide cluster membership probabilities for the stars in the field of NGC 6250. Of these the most complete study is that by Dias et al. (2006) who base their analysis on the method from Sanders (1971). This method calculates the probability of a star being part of a cluster by using a *maximum likelihood procedure* to fit a model based on *overlapping normal bivariate frequency functions*. The proper motions of each of the stars are used

as inputs to the model.

Dias et al. (2006) calculate a cluster mean proper motion consistent with that found by Kharchenko et al. 2013, however some of their cluster membership probabilities show inconsistencies. Three stars (UCAC 12065057, UCAC 12284608 and UCAC 12284626) are calculated to have a 100 % likelihood of being members despite their proper motion values being far from the cluster mean. Additionally the star UCAC 12065064 has proper motion values and photometry which match well to the cluster, but it has only been given a 3 % likelihood of being a member.

The initial target selection for observation was based on these cluster membership studies. My analysis of the new spectroscopic data allows me to refine the cluster membership because the determination of member stars is of vital importance for this study.

6.4.1 Kinematics

The proper motions and radial velocities of the observed stars are shown in Table 6.2 and are plotted in Fig. 6.2. My membership analysis consists of the following two methods.

I first identify all stars whose proper motion and radial velocity values are within $1\,\sigma$ of the mean proper motion and radial velocity values for the observed sample. Using this method I identified 19 stars to be members of the cluster with cluster mean proper motions of, $0.1 \pm 2.9\,\mathrm{mas\,yr^{-1}}$ in RA, $-6.1 \pm 4.4\,\mathrm{mas\,yr^{-1}}$ in DEC and a cluster radial velocity of $-10 \pm 11\,\mathrm{km\,s^{-1}}$.

Secondly, as a cross-check, a partitional clustering technique, K-means clustering[2] (MacQueen 1967), was also used. This is a technique used to determine common data points based on the analysis of the variables which define the data. In general, the method is to set a predicted number of data clusters and give an initial guess for the centers of these clusters. The algorithm then assigns points to the closest cluster center

[2]The K-means clustering was completed by C. Scalia

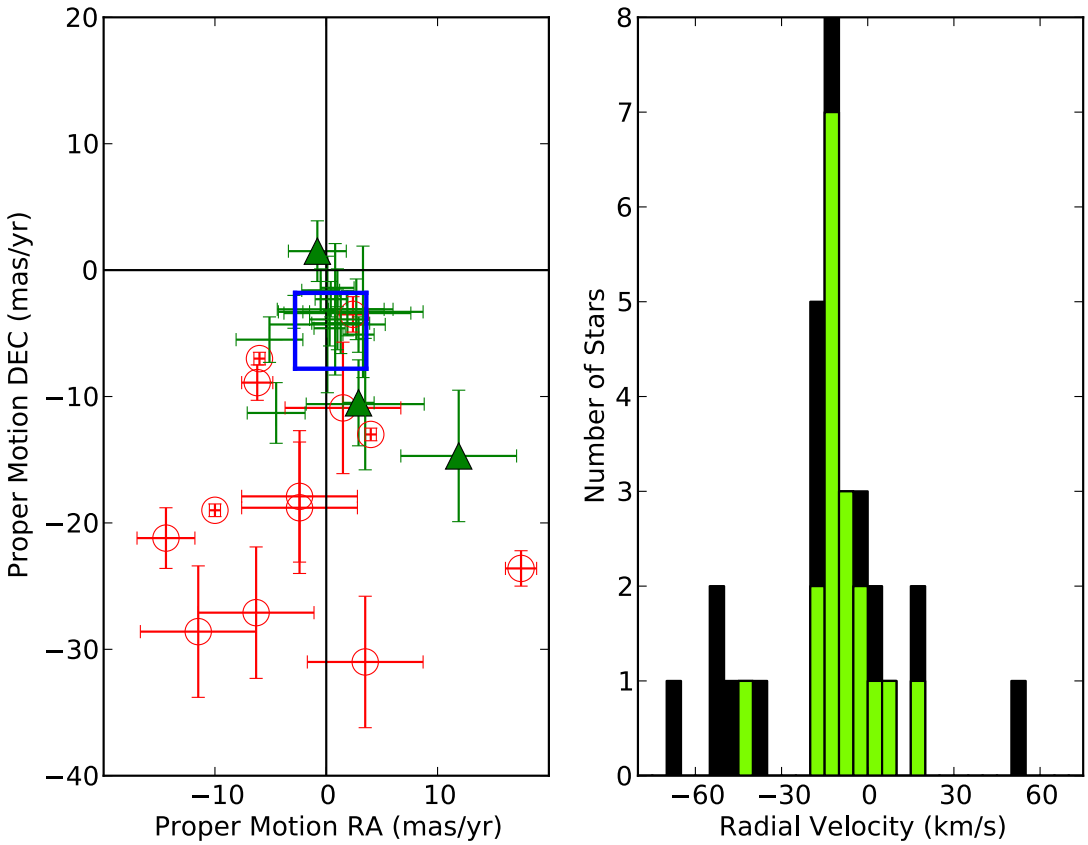

Figure 6.2: Left Panel: The proper motion of the observed stars from the UCAC2 catalogue (Zacharias et al. 2005). Green plus-signs are stars I consider to be members and red circles are stars I do not consider to be members. Triangles are the stars for which membership is considered based solely on photometry. The remaining points are stars for which membership is considered based on the kinematics and photometry. The blue box is centered at the cluster mean proper motions and represents the uncertainty of these values in each direction. Right Panel: Histogram of the the radial velocity measurements calculated using the method described in Section 6.5.1 for non-member stars and for the member stars using SPARTI SIMPLE. The green histogram highlights the radial velocity of the cluster members.

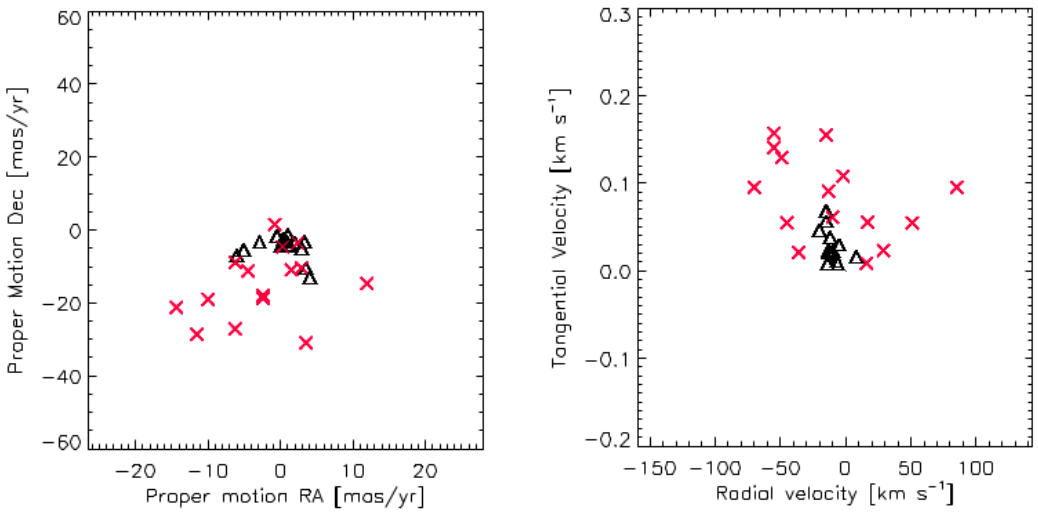

Figure 6.3: K-means clustering result for the membership analysis of NGC6250 the black triangles are member stars and the red crosses are non-members. The left panel shows the sample distribution in proper motion. The right panel shows the sample distribution in velocity. The tangential velocity was computed considering the distance 940pc given by Kharchenko et al. (2013)

Table 6.2: Proper motions and radial velocities for the stars in the field of NGC 6250. For each UCAC designated star the proper motions are taken from the UCAC2 catalogue (Zacharias et al. 2005), and for the other stars they are taken from the TYCHO-2 catalogue (Hog et al. 2000). The radial velocities (v_r) are calculated using the method in Section 6.5.1 and for the member stars using SPARTI SIMPLE. Δ is the number of standard deviations the proper motions and radial velocity are away from the cluster mean.

Star Name	μ_{RA} (mas yr^{-1})	$\Delta\mu_{RA}$	μ_{DEC} (mas yr^{-1})	$\Delta\mu_{DEC}$	v_r (km s^{-1})	Δv_r	Member
CD-4511088	2.4 ± 1.4	0.6	-3.5 ± 1.4	0.4	-36.0 ± 0.5	2.6	n
HD152706	-2.9 ± 1.4	1.0	-3.3 ± 1.3	0.5	-4.6 ± 0.4	0.5	y
HD152743	0.3 ± 1.4	0.0	-4.6 ± 1.4	0.1	0.4 ± 52.4	1.0	y
HD329261	-10.0 ± 0.5	3.3	-19.0 ± 0.5	4.7	-3.1 ± 0.5	0.7	n
HD329268	-6.0 ± 0.5	2.0	-7.0 ± 0.5	0.7	-20 ± 3.0	1.0	n
HD329269	4.0 ± 0.5	1.1	-13.0 ± 0.5	2.7	-16 ± 3.0	0.6	n
NGC6250-11	17.5 ± 1.4	5.3	-23.6 ± 1.4	6.3	1 ± 3.0	1.1	n
NGC6250-13	2.7 ± 2.5	0.7	-3.1 ± 2.4	0.6	-14 ± 3.0	0.4	n
TYC8327-565-1	-0.5 ± 1.7	0.3	-1.6 ± 1.7	1.1	-9.4 ± 0.2	0.1	y
UCAC12065030	-2.4 ± 5.2	0.9	-17.9 ± 5.2	4.4	-20 ± 3.0	1.0	n
UCAC12065057	-14.4 ± 2.6	4.6	-21.2 ± 2.4	5.5	-49 ± 3.0	3.9	n
UCAC12065058	11.9 ± 5.2	3.6	-14.7 ± 5.2	3.3	85.0 ± 0.2	9.5	y*
UCAC12065064	1.3 ± 2.6	0.3	-4.2 ± 2.4	0.2	-14.5 ± 0.6	0.5	y
UCAC12065075	-0.8 ± 2.6	0.4	1.5 ± 2.4	2.1	18.4 ± 0.1	2.8	y*
UCAC12284480	1.5 ± 5.2	0.3	-10.9 ± 5.2	2.0	17 ± 3.0	2.7	n
UCAC12284506	-4.5 ± 2.6	1.5	-11.3 ± 2.4	2.2	-10 ± 3.0	0.0	n
UCAC12284534	-2.4 ± 5.2	0.9	-18.8 ± 5.2	4.7	-70 ± 3.0	6.0	n
UCAC12284536	1.0 ± 2.5	0.2	-3.9 ± 2.4	0.3	-12.5 ± 6.7	0.2	y
UCAC12284546	1.9 ± 5.7	0.5	-3.4 ± 1.8	0.5	-16.1 ± 2.3	0.6	y
UCAC12284585	-6.2 ± 1.4	2.1	-8.9 ± 1.4	1.4	51 ± 3.0	6.1	n
UCAC12284589	-5.1 ± 3.0	1.7	-5.5 ± 1.8	0.2	-12 ± 3.0	0.2	y
UCAC12284594	0.8 ± 5.2	0.1	-3.1 ± 5.2	0.6	9.7 ± 0.3	2.0	y
UCAC12284608	3.5 ± 5.2	1.0	-31.0 ± 5.2	8.7	-55 ± 3.0	4.5	n
UCAC12284620	-6.3 ± 5.2	2.1	-27.1 ± 5.2	7.4	-55 ± 3.0	4.5	n
UCAC12284626	-11.5 ± 5.2	3.7	-28.6 ± 5.2	7.9	-15 ± 3.0	0.5	n
UCAC12284628	2.9 ± 1.4	0.8	-10.5 ± 3.4	1.9	-45.0 ± 0.5	3.5	y*
UCAC12284631	2.9 ± 1.4	0.8	-5.1 ± 1.4	0.1	-0.9 ± 0.2	0.9	y
UCAC12284638	1.0 ± 1.5	0.2	-1.4 ± 1.5	1.1	-6 ± 3.0	0.4	y
UCAC12284645	0.4 ± 1.4	0.0	-2.3 ± 1.4	0.8	-19.0 ± 9.2	0.9	y
UCAC12284653	3.3 ± 5.4	0.9	-3.3 ± 5.2	0.5	-13.4 ± 0.6	0.3	y
UCAC12284662	3.5 ± 5.3	1.0	-10.6 ± 5.2	1.9	-14.9 ± 0.9	0.5	y
UCAC12284746	0.1 ± 5.2	0.1	-4.3 ± 5.4	0.2	-10.9 ± 0.2	0.1	y

* Star considered as members based only on photometry.

and recalculates until the cluster center values do not change. Cluster membership analysis is simplified by the fact it is possible to define one cluster center close to the literature value of cluster proper motion and radial velocity. For this analysis, the number of clusters was set to 5: one initially centered in the literature values (μ_0, v_{r_0}) and the other four initially centered respectively at $(\mu_0 + 1.5\,\sigma_\mu, v_{r_0})$,$(\mu_0 - 1.5\,\sigma_\mu, v_{r_0})$, $(\mu_0, v_{r_0} + 1.5\,\sigma_{v_r})$ and $(\mu_0, v_{r_0} + 1.5\,\sigma_{v_r})$. Where σ_{v_r} and σ_μ are the standard deviation in the sample. The computation was completed using the CLUSTER function in IDL® 8.5 (Exelis Visual Information Solutions, Boulder, Colorado).

Figure 6.3 shows the results of the cluster analysis. Fifteen stars are found to be members and the cluster mean proper motions were calculated to be, $0.4 \pm 3.0\,\mathrm{mas\,yr^{-1}}$ in RA, $-4.8 \pm 3.2\,\mathrm{mas\,yr^{-1}}$ in DEC and the radial velocity was calculated to be $-10 \pm 6\,\mathrm{km\,s^{-1}}$. Both methods give the same results apart from four stars. The discrepancy between the two methods is likely because the spread of radial velocity is large and asymmetric, and the K-means clustering is able to deal with this more effectively.

6.4.2 Photometry

The magnitude and colour of the sample of stars are good indicators of cluster membership. Using the B and V magnitudes from Henden et al. (2016) and the J and K magnitudes from Zacharias et al. (2005), I have produced two colour magnitude diagrams, displayed in Fig. 6.4. Each diagram shows the photometry and a theoretical isochrone calculated with CMD 2.7 (Bressan et al. 2012; Chen et al. 2014; Tang et al. 2014; Chen et al. 2015) for an age of $\log t = 7.42$. The photometry has been corrected for the extinction (Kharchenko et al. 2013) and distance to the cluster (850 pc; Kharchenko et al. 2013).

In general, I see very good agreement between the member stars determined using the kinematics approach and those that fit the isochrones. Notable exceptions are UCAC 12065058, UCAC 12065075 and UCAC 12284628, which do not agree with the kinematics of the cluster mean, but agree very well with the photometry. This may be the result of binary interactions with much fainter stars which cannot be observed

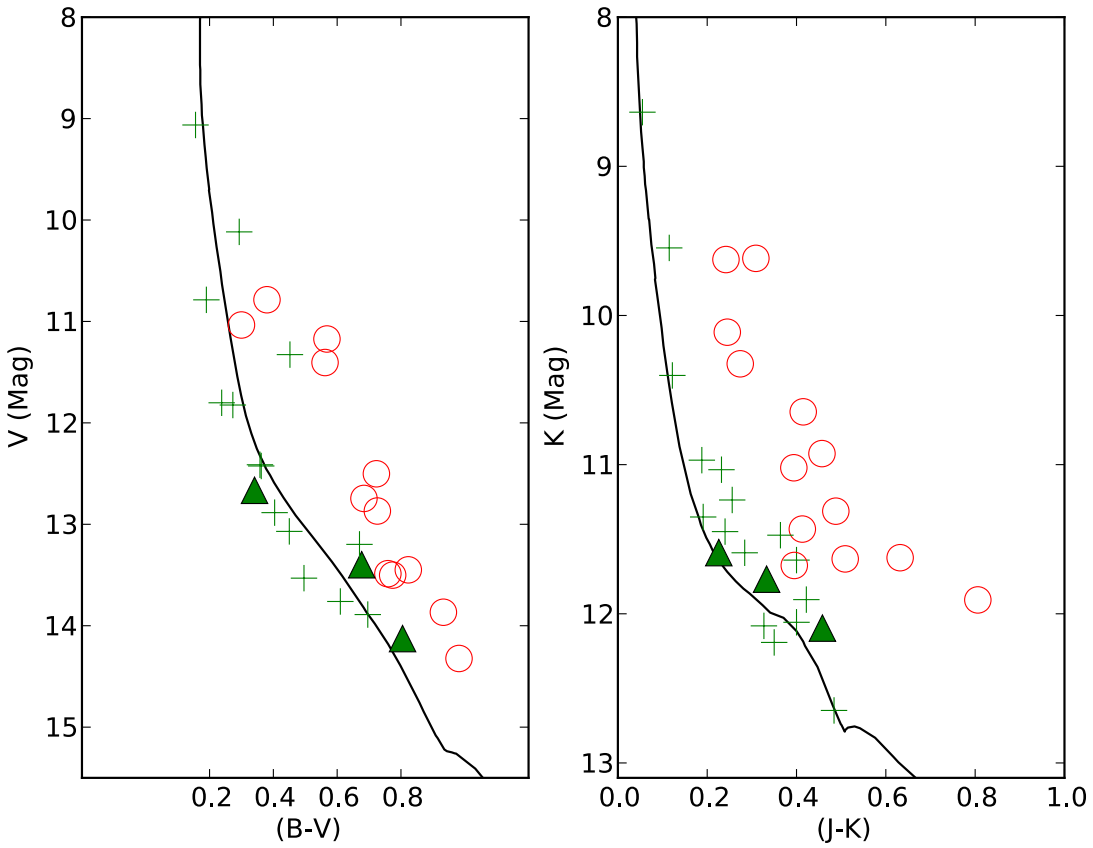

Figure 6.4: In both panels, green plus-signs are stars I consider members and red circles are stars I do not consider to be members. Triangles are the stars for which membership is considered based solely on photometry. The remaining points are stars for which membership is considered based on the kinematics and photometry. Left Panel: Optical colour-magnitude diagram of the observed stars. The BV photometry is taken from the APASS catalogue (Henden et al. 2016), plotted with the isochrone at ($\log t \sim 7.42$ years) corrected for E(B-V) = 0.385 (black solid line; Kharchenko et al. 2013). Right Panel: Infrared colour-magnitude diagram of the observed stars. The JK photometry is taken from the UCAC2 catalogue (Zacharias et al. 2005), plotted with the isochrone at ($\log t \sim 7.42$ years) corrected for E(J-K) = 0.200 (black solid line; Kharchenko et al. 2013).

Table 6.3: Photometry of the stars of NGC6250

	Magnitude (mag)				
Star	B	V	J	K	Member
CD-4511088	11.4	11.0	10.4	10.1	n
HD152706	10.4	10.1	9.7	9.5	y
HD152743	9.2	9.1	8.7	8.6	y
HD329261	11.2	10.8	9.9	9.6	n
HD329268	12.0	11.4	10.6	10.3	n
HD329269	11.7	11.2	9.9	9.6	n
NGC6250-11	13.4	12.7	11.4	11.0	n
NGC6250-13	13.5	13.1	12.0	11.6	n
TYC8327-565-1	11.0	10.8	10.5	10.4	y
UCAC12065030	14.2	13.5	11.8	11.4	n
UCAC12065057	13.6	12.9	11.4	10.9	n
UCAC12065058	14.9	14.1	12.6	12.1	y*
UCAC12065064	14.0	13.5	12.4	12.1	y
UCAC12065075	14.1	13.4	12.1	11.8	y*
UCAC12284480			12.7	11.9	n
UCAC12284506	13.9	13.2	11.8	11.5	n
UCAC12284534	14.8	13.9	12.1	11.6	n
UCAC12284536	12.8	12.4	11.5	11.4	y
UCAC12284546	13.3	12.9	11.9	11.6	y
UCAC12284585	13.2	12.5	11.1	10.6	n
UCAC12284589	12.1	11.8	11.2	11.0	y
UCAC12284594	14.6	13.9	12.5	12.1	y
UCAC12284608	15.3	14.3	12.3	11.6	n
UCAC12284620	14.3	13.4	11.8	11.3	n
UCAC12284626	14.3	13.5	12.1	11.7	n
UCAC12284628	13.0	12.7	11.8	11.6	y*
UCAC12284631	11.8	11.3	11.3	11.0	y
UCAC12284638	12.0	11.8	11.7	11.4	y
UCAC12284645	12.8	12.4	11.5	11.2	y
UCAC12284653			13.1	12.6	y
UCAC12284662	14.4	13.8	12.3	11.9	y
UCAC12284746			12.5	12.2	y

* Star considered as members based only on photometry.

in the spectra and so I consider these stars as members.

6.5 Fundamental Parameters

6.5.1 Radial velocity and rotational velocity

Using Sparti Simple I am able to calculate the radial velocity ($v_{\rm rad}$) and $v \sin i$ of each stellar spectrum. However, to use Sparti Simple I must first know the $T_{\rm eff}$ and $\log g$, which requires knowledge of $v_{\rm rad}$ and $v \sin i$. To determine initial values for $v_{\rm rad}$ and $v \sin i$ I begin by performing a least-square deconvolution (LSD; Kochukhov, Makaganiuk & Piskunov 2010) of the spectra in the wavelength range $5150 - 5350$ Å, which is the highest resolution setting HR9B for the FLAMES instrument. The lines were selected from the VALD list (Piskunov et al. 1995) and the LSD program calculates an average line profile in velocity space. Selecting the lines from the VALD list requires an estimate of the temperature and so I use a combination of Balmer lines and photometry for this.

The value of $v_{\rm rad}$ is determined by the center of the LSD profile in velocity space. To measure $v \sin i$ I first shift the LSD profile to the rest frame and then calculate a fast Fourier transform (FFT). An example of the FFT is shown in Fig. 6.6. Gray (2005) shows that the first minimum of the FFT corresponds to the stellar $v \sin i$ value. Glazunova et al. 2008 showed that it is possible to use the LSD profile, in place of the more noisy profiles of single lines, to derive the $v \sin i$ value using the FFT method described by Gray (2005).

6.5.2 $T_{\rm eff}$ and $\log g$ from Balmer lines

To obtain the $T_{\rm eff}$ and $\log g$ of the member stars of NGC6250 I have written a program to fit the Balmer lines. The interface of the program is shown in Fig. 6.7. For the UVES spectra I fit the observed H_β and H_γ lines with synthetic profiles, while for the GIRAFFE spectra I use H_α and H_β lines. I have calculated a grid of stellar spectra

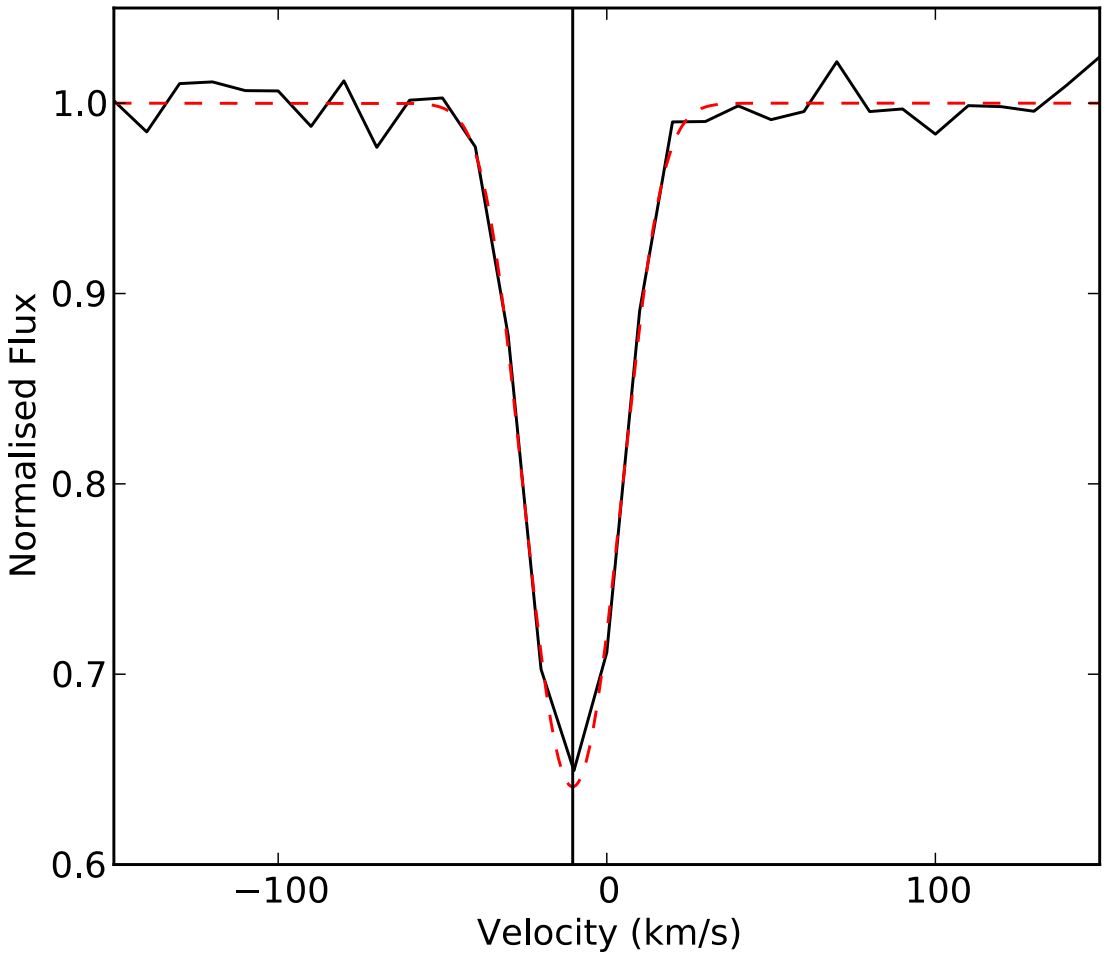

Figure 6.5: The least-square deconvolution of the spectrum of UCAC 12284653 ($T_{\rm eff}$ = 6500 K) (solid line), plotted against the Gaussian fit (red dashed line). The radial velocity is given by the position of the centre of the Gaussian, and it is indicated by a solid vertical line.

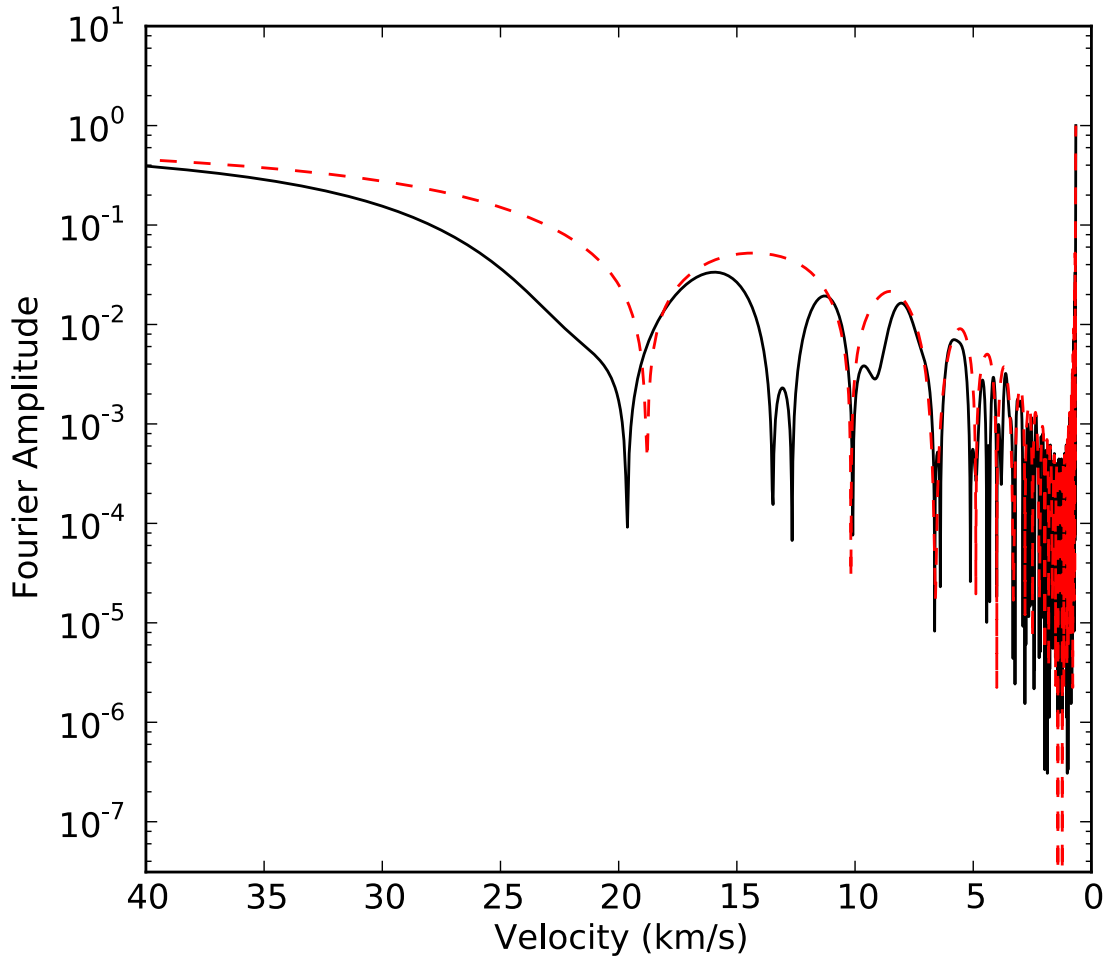

Figure 6.6: The fast Fourier transform of the LSD profile of Fig. 6.5 (black solid line), plotted with the FTT of a model LSD profile with $T_{\rm eff} = 6500\,{\rm K}$, $\log g = 3.75$ and $v \sin i = 20\ {\rm km\,s^{-1}}$ (red dashed lines)

covering a $T_{\rm eff}$ range from 5500K to 20000K and a $\log g$ range of 3.5 to 4.5. This allows me to move freely in both $T_{\rm eff}$ and $\log g$ until the synthetic and observed spectra agree. The addition of a panel showing the spectral range of the HR9B GIRAFFE setting allows me to confirm the quality of my fit with a range metal lines.

Hydrogen lines are very useful indicators for $T_{\rm eff}$ and $\log g$. For $T_{\rm eff} < 8000\,{\rm K}$ they are sensitive to temperature. As the temperature increases they become sensitive to both temperature and gravity and for higher $T_{\rm eff}$ although they are more sensitive to gravity, temperature effects are still visible in the part of the line wing close to the core (Fossati et al. 2011b).

Since the hydrogen lines in stars $T_{\rm eff} < 8000\,{\rm K}$ are not sensitive to $\log g$, I required a different technique to calculate $\log g$ for these stars. I accomplished this by comparing the abundances between Fe I and Fe II and the $\log g$ for which they balance. To test this method I analysed the abundances of Fe I and Fe II in the Sun using $T_{\rm eff} = 5777$K and varying $\log g$ between 3.8 and 4.5 (Fig. 6.8). The value of $\log g$ at which the abundances of Fe I and Fe II are equal is 4.49 compared with 4.44 given by Prsa et al. (2016). In addition I analysed the abundances of Fe I and Fe II in 21 Peg using $T_{\rm eff} =$ 10400K and varying $\log g$ between 3.5 and 4.2 (Fig. 6.9). The value of $\log g$ at which the abundances of Fe I and Fe II are equal is 3.50 compared with 3.55 given by Fossati et al. (2009).

After determining the $T_{\rm eff}$ and $\log g$ for each cluster member star, I applied SPARTI to determine the chemical abundances of the elements in their photospheres.

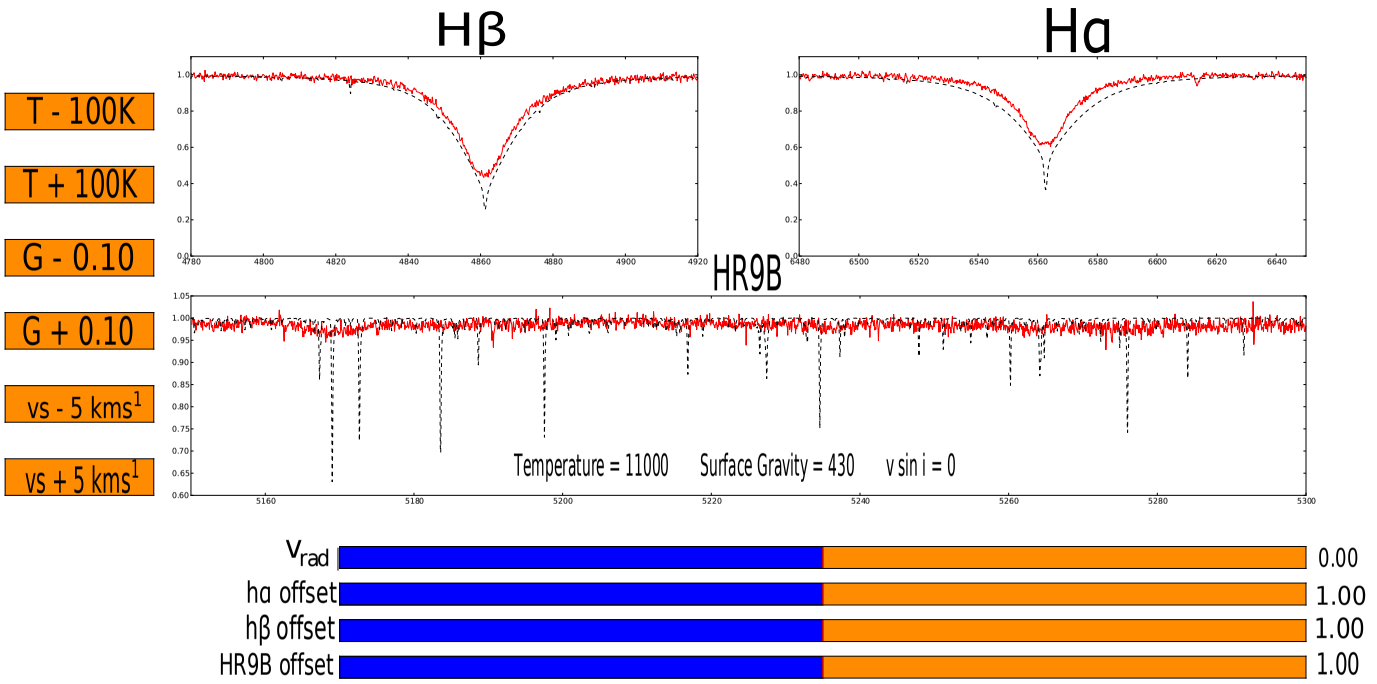

Figure 6.7: The interface of the program I wrote to determine the $T_{\rm eff}$ and $\log g$ from the Balmer lines. Depending on the wavelength coverage of the spectrum it is possible to change the Balmer lines used. The higher resolution of the HR9B setting also allows me to check the metal lines.

Table 6.4: Fundamental parameters for the sample of stars from NGC 6250.

Star	$T_{\rm eff}$ (K)	$\log g$ (CGS)	$v_{\rm mic}$ ($\mathrm{km\,s^{-1}}$)	$v \sin i$ ($\mathrm{km\,s^{-1}}$)
HD 152706	9900 ± 200	4.2 ± 0.1	1.9 ± 0.1	151.6 ± 0.2
HD 152743	19 800 ± 200	4.1 ± 0.1	2.1 ± 2.5	198.9 ± 12.7
NGC 6250-13	8200 ± 200	4.2 ± 0.1	2.0 ± 0.1	70.1 ± 0.8
TYC 8327-565-1	14 200 ± 500	4.2 ± 0.3	–	–
UCAC 12065058	6000 ± 200	4.4 ± 0.1	0.9 ± 0.2	4.8 ± 0.9
UCAC 12065064	7600 ± 200	4.2 ± 0.1	0.3 ± 0.4	54.1 ± 0.7
UCAC 12065075	6300 ± 200	4.4 ± 0.1	1.0 ± 0.1	15.2 ± 0.2
UCAC 12284506	6100 ± 200	4.4 ± 0.1	0.6 ± 0.1	10.6 ± 0.2
UCAC 12284536	10 000 ± 200	4.4 ± 0.1	2.0 ± 0.2	170.2 ± 3.6
UCAC 12284546	8400 ± 200	4.2 ± 0.1	0.3 ± 0.5	146.0 ± 1.5
UCAC 12284589	12 600 ± 200	4.2 ± 0.1	0.5 ± 0.7	215.5 ± 2.7
UCAC 12284594	6100 ± 200	4.4 ± 0.1	0.3 ± 0.2	50.3 ± 0.5
UCAC 12284628	10 000 ± 200	4.3 ± 0.1	0.3 ± 0.5	22.9 ± 0.8
UCAC 12284631	9800 ± 200	4.2 ± 0.1	0.7 ± 0.2	17.8 ± 0.4
UCAC 12284638	10 800 ± 400	4.2 ± 0.3	–	–
UCAC 12284645	11 000 ± 200	4.3 ± 0.1	2.0 ± 0.4	270.0 ± 3.0
UCAC 12284653	6200 ± 200	4.4 ± 0.1	1.5 ± 0.2	49.5 ± 1.0
UCAC 12284662	7400 ± 200	4.4 ± 0.1	2.0 ± 0.1	81.4 ± 0.9
UCAC 12284746	7200 ± 200	4.3 ± 0.1	1.8 ± 0.2	24.5 ± 0.4

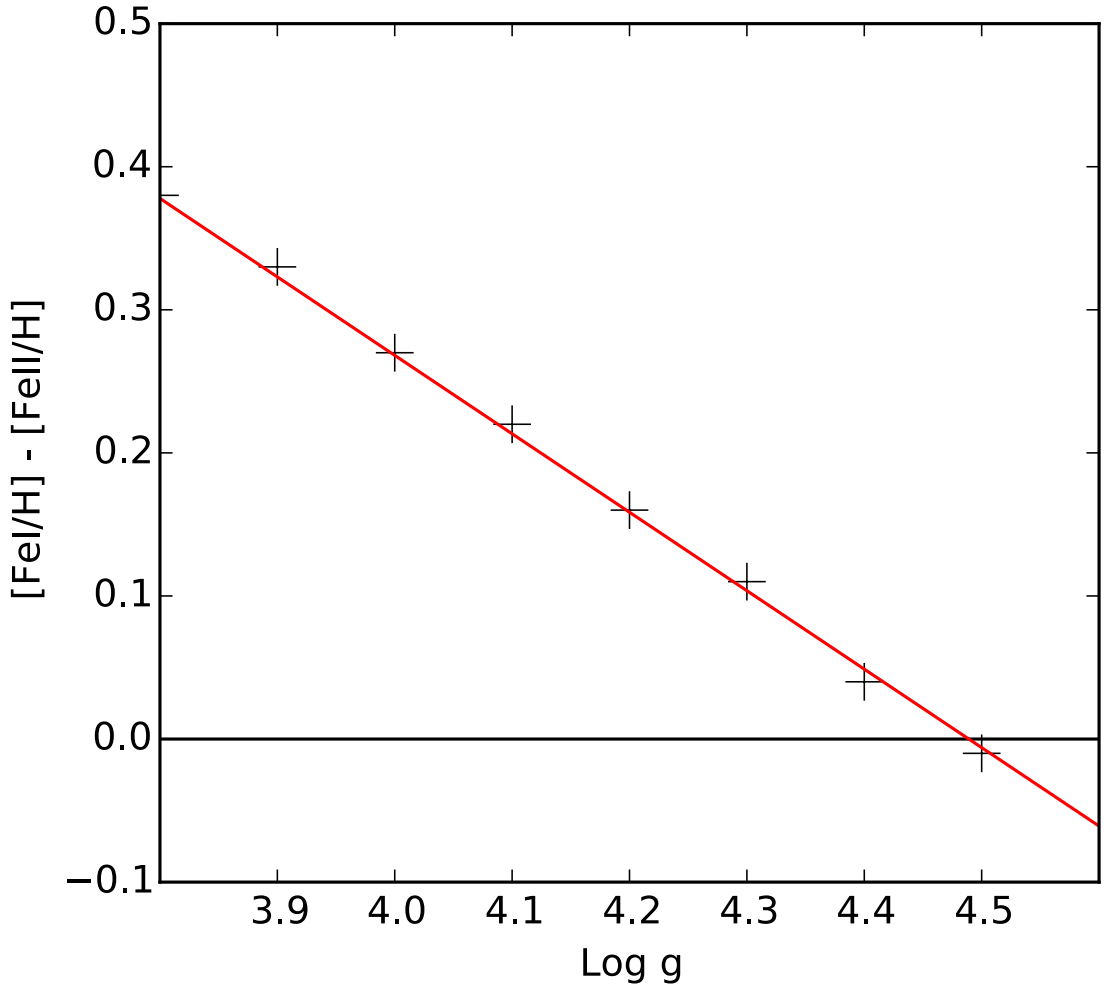

Figure 6.8: The difference between the abundance of Fe I and Fe II plotted as a function of surface gravity for the Sun determined using SPARTI ABUND by varying the $\log g$ of the model atmosphere at $T_{\rm eff} = 5800$K.

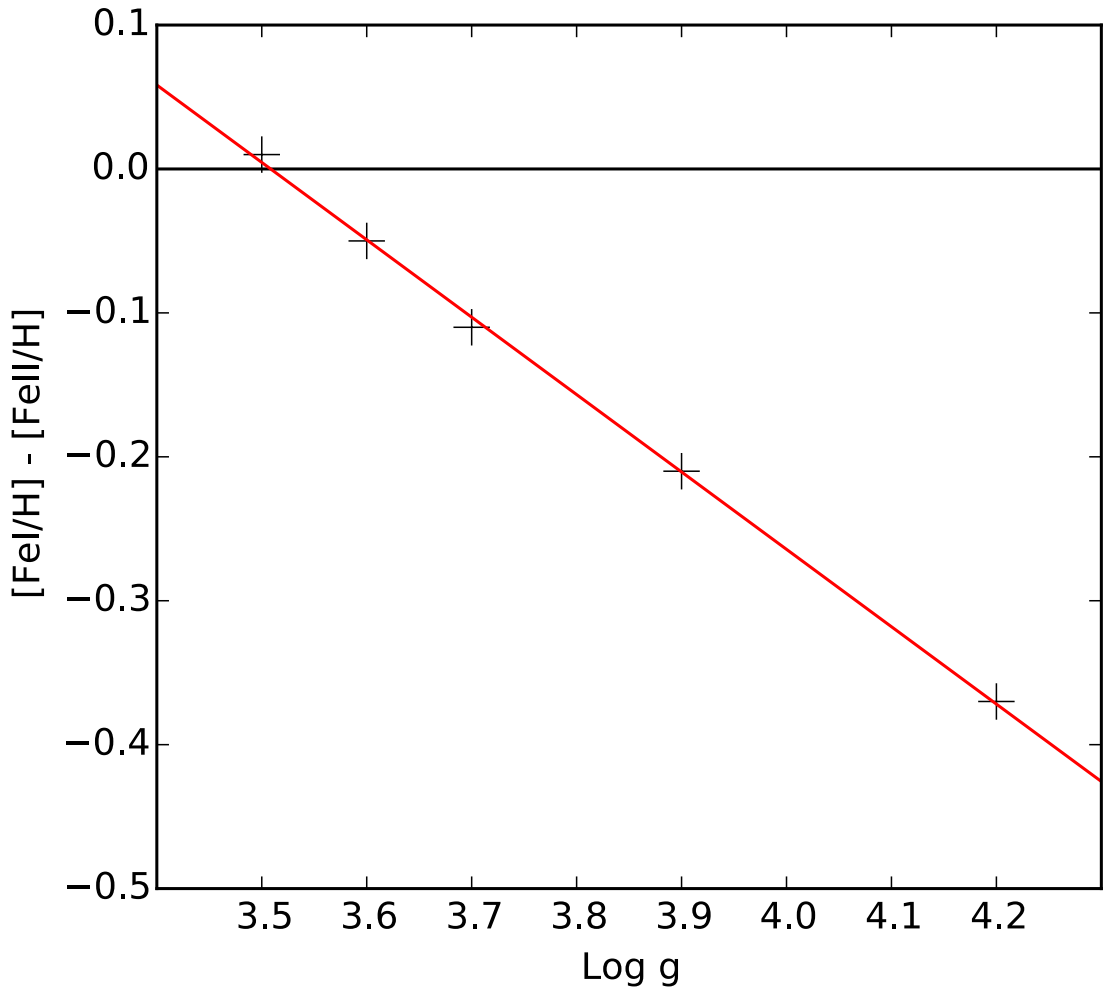

Figure 6.9: The difference between the abundance of Fe I and Fe II plotted as a function of surface gravity for the star 21Peg determined using SPARTI ABUND by varying the $\log g$ of the model atmosphere at $T_{\rm eff} = 10400$K.

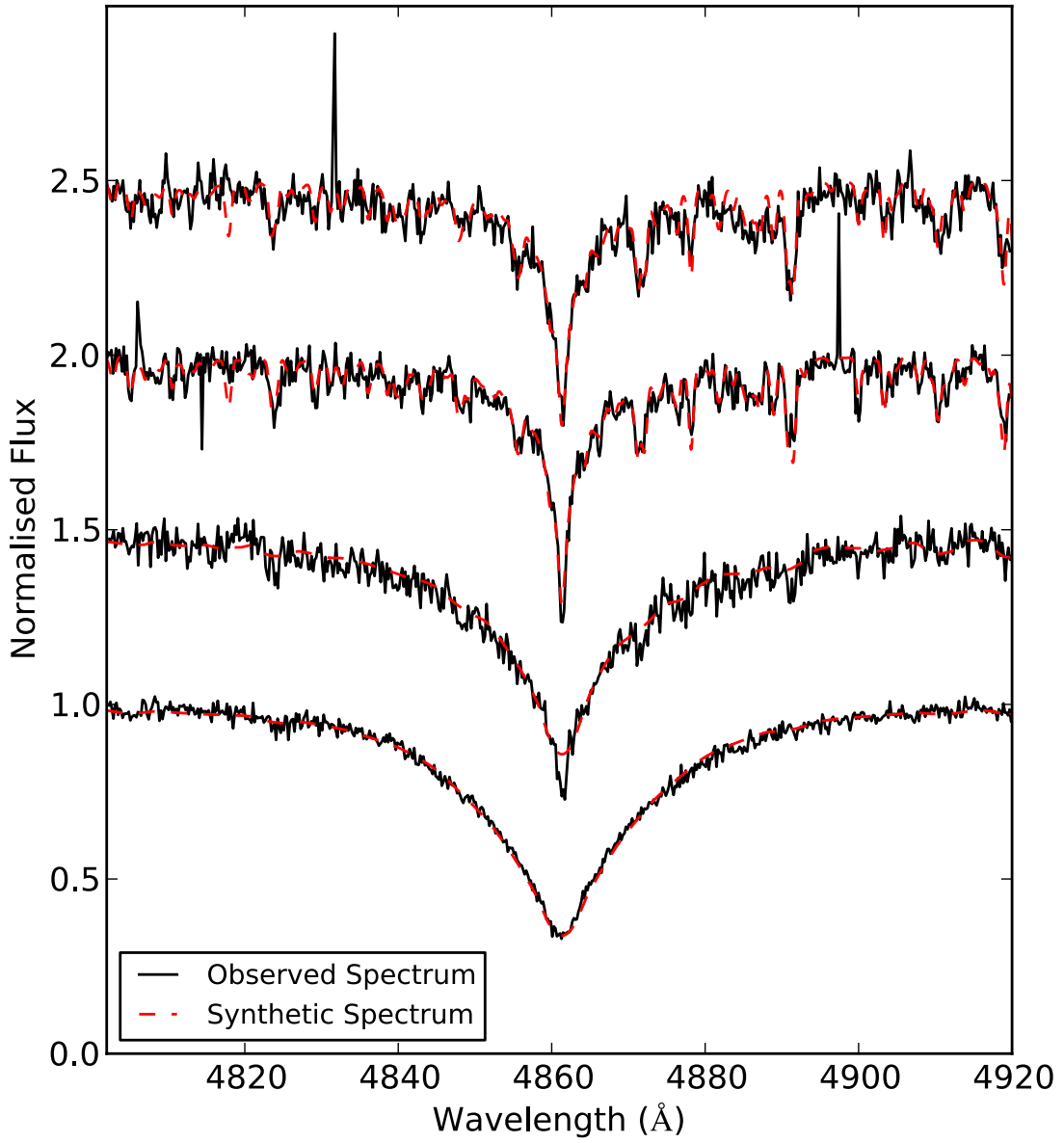

Figure 6.10: A sample of the observed Hβ lines (black solid lines) fitted with the model spectra (red dashed line). From top to bottom the stars are: NGC6250-11 ($T_{\rm eff}$ = 6100 K), HD 329269 ($T_{\rm eff}$ = 7400 K), NGC6250-13 ($T_{\rm eff}$ = 7900 K), UCAC12284536 ($T_{\rm eff}$ = 9800 K), UCAC12284589 ($T_{\rm eff}$ = 11000 K). Each profile is calculated with $v \sin i$ as shown in Table 6.4.

Table 6.5: The abundance of elements for the analysed stars of NGC6250, given in $\log(N/\mathrm{H})$ where H = 12.00. In parentheses the first number is the error calculated using Eq. 4.16 and the second in the error calculating using Eq. 4.18. Both errors are in units of 0.01 dex. The last row of each set gives the solar abundances from Asplund et al. (2009)

Star	T_{eff} [K]	$v \sin i$ [km s^{-1}]	C	O	Na	Mg	Si	S
HD152743	19800	198.9 ± 12.7					8.07 (95;102)	
UCAC12284589	12600	215.5 ± 2.7						
UCAC12284645	11000	270.0 ± 3.0						
UCAC12284628	10000	22.9 ± 0.8				6.41 (06;12)		
UCAC12284536	10000	170.2 ± 3.5				7.58 (25;27)		
HD152706	9900	151.6 ± 0.2	8.91 (02;34)	8.68 (02;04)		7.99 (02;28)	7.83 (02;27)	
UCAC12284631	9800	17.8 ± 0.4	8.84 (13;16)			6.61 (04;12)	7.98 (11;27)	
NGC6250-13	8200	70.1 ± 0.8				7.74 (06;14)		
UCAC12065064	7600	54.1 ± 0.7	8.63 (11;15)			7.29 (08;13)	7.39 (08;15)	7.92 (11;59)
UCAC12284662	7400	81.4 ± 0.9	8.50 (19;37)		6.24 (17;20)	7.59 (09;13)	7.51 (10;10)	
UCAC12284746	7200	24.5 ± 0.4	8.92 (13;14)		6.25 (13;15)	7.68 (10;15)	7.26 (10;11)	
UCAC12065075	6300	15.2 ± 0.2			6.49 (07;22)	7.64 (04;22)	7.34 (04;19)	
UCAC12284653	6200	49.5 ± 1.0			6.37 (21;26)	7.58 (11;19)	7.50 (13;14)	
UCAC12284594	6100	50.3 ± 0.5			6.24 (09;10)	7.45 (03;12)	7.11 (06;07)	
UCAC12284506	6100	10.6 ± 0.2	8.91 (08;26)		6.05 (05;07)	7.28 (01;10)	6.94 (03;04)	7.81 (28;46)
UCAC12065058	6000	4.8 ± 0.9			6.08 (17;17)	7.70 (08;12)	6.91 (12;12)	
Solar	**5777**	**1.2**	**8.43**	**8.69**	**6.24**	**7.60**	**7.51**	**7.12**

Table 6.5: Continued.

Star	$T_{\rm eff}$ [K]	$v \sin i$ [km s^{-1}]	Ca	Sc	Ti	V	Cr	Mn
HD152743	19800	198.9 ± 12.7						
UCAC12284589	12600	215.5 ± 2.7					6.25 (14;18)	
UCAC12284645	11000	270.0 ± 3.0			4.96 (28;35)		5.64 (23;32)	
UCAC12284628	10000	22.9 ± 0.8			4.94 (11;16)		5.57 (09;10)	
UCAC12284536	10000	170.2 ± 3.5			5.02 (23;23)		5.73 (21;23)	
HD152706	9900	151.6 ± 0.2	6.92 (02;46)		4.95 (02;04)		5.78 (02;16)	
UCAC12284631	9800	17.8 ± 0.4			4.75 (06;08)		5.49 (07;08)	
NGC6250-13	8200	70.1 ± 0.8	6.22 (08;14)		4.83 (05;08)		5.75 (06;09)	5.51 (13;17)
UCAC12065064	7600	54.1 ± 0.7	6.63 (17;24)		5.24 (02;08)		5.95 (07;12)	5.63 (23;35)
UCAC12284662	7400	81.4 ± 0.9	6.32 (12;21)	3.13 (14;23)	4.97 (06;14)		5.69 (08;23)	5.45 (16;21)
UCAC12284746	7200	24.5 ± 0.4	6.19 (13;16)	3.11 (11;12)	5.23 (06;10)		5.92 (07;10)	5.46 (16;18)
UCAC12065075	6300	15.2 ± 0.2	6.55 (07;21)	3.41 (05;11)	5.12 (03;13)	4.44 (07;18)	5.92 (03;17)	5.27 (10;15)
UCAC12284653	6200	49.5 ± 1.0	6.40 (23;28)	2.95 (24;26)	5.19 (09;42)	3.99 (34;55)	6.06 (09;25)	5.62 (23;47)
UCAC12284594	6100	50.3 ± 0.5	6.33 (09;11)	2.90 (13;14)	5.00 (04;05)	4.78 (07;09)	5.92 (03;08)	5.18 (15;17)
UCAC12284506	6100	10.6 ± 0.2	6.22 (06;08)	3.16 (05;06)	4.93 (02;05)	3.81 (07;11)	5.53 (02;07)	5.30 (07;09)
UCAC12065058	6000	4.8 ± 0.9	6.42 (16;16)	3.01 (15;16)	4.92 (08;10)	4.05 (18;20)	5.62 (07;10)	5.25 (22;23)
Solar	**5777**	**1.2**	**6.34**	**3.15**	**4.95**	**3.93**	**5.64**	**5.43**

Table 6.5: Continued.

Star	$T_{\rm eff}$ [K]	$v \sin i$ [km s^{-1}]	Fe	Ni	Zn	Y	Ba	Nd
HD152743	19800	198.9 ± 12.7	7.67 (47;49)					
UCAC12284589	12600	215.5 ± 2.7	7.77 (04;04)					
UCAC12284645	11000	270.0 ± 3.0	7.50 (12;23)					
UCAC12284628	10000	22.9 ± 0.8	7.43 (06;10)					
UCAC12284536	10000	170.2 ± 3.5	7.56 (16;17)					
HD152706	9900	151.6 ± 0.2	7.61 (01;12)					
UCAC12284631	9800	17.8 ± 0.4	7.41 (03;06)					
NGC6250-13	8200	70.1 ± 0.8	7.54 (04;08)	6.33 (08;13)			2.09 (42;45)	
UCAC12065064	7600	54.1 ± 0.7	7.74 (05;14)	6.16 (11;13)				
UCAC12284662	7400	81.4 ± 0.9	7.51 (07;10)	6.27 (10;28)			2.34 (36;38)	
UCAC12284746	7200	24.5 ± 0.4	7.73 (07;11)	6.30 (08;12)	4.71 (44;46)	2.54 (13;14)	2.18 (49;49)	
UCAC12065075	6300	15.2 ± 0.2	7.65 (03;19)	6.28 (04;14)	4.06 (33;34)	2.38 (11;14)	2.18 (17;17)	1.76 (09;12)
UCAC12284653	6200	49.5 ± 1.0	7.70 (09;20)	6.44 (11;27)	4.62 (88;88)		2.20 (41;43)	
UCAC12284594	6100	50.3 ± 0.5	7.54 (02;09)	6.15 (06;07)			2.41 (13;14)	1.98 (14;17)
UCAC12284506	6100	10.6 ± 0.2	7.28 (01;07)	5.99 (03;05)	4.69 (28;28)	2.07 (09;11)	2.42 (09;09)	1.61 (07;13)
UCAC12065058	6000	4.8 ± 0.9	7.39 (06;09)	6.02 (10;11)			2.18 (39;41)	1.63 (25;25)
Solar	**5777**	**1.2**	**7.50**	**6.22**	**4.56**	**2.21**	**2.18**	**1.42**

6.6 Results and Discussion

The results of the abundance analysis are given in Table 6.5. Since this is a young cluster there is the potential for some of the stars to still have disks. If disks were present I would expect to see the presence of emission lines, particularly in the core of Hα and Hβ. I do not see any evidence of emission lines in any of the stars.

6.6.1 UCAC 12284546

UCAC 12284546 shows an overabundance of C, Ca, Cr, Fe, and Ni and an underabundance of Mg. However, this abundance pattern does not match any standard chemically peculiar star in this temperature range. To better understand this star it would be necessary to collect and analyse a higher resolution spectrum with higher S/N. As a result of the abundance anomalies, I observe in this star, I do not consider this star in the global analysis of the results.

6.6.2 Stellar Metallicity

For the evolutionary tracks and isochrones I adopted the metallicity calculated as

$$Z_{\rm cluster} = 10^{[{\rm Fe/H}]_{\rm stars} - [{\rm Fe/H}]_\odot} Z_\odot, \tag{6.1}$$

where $Z_{\rm cluster}$ and $[{\rm Fe/H}]_{\rm stars}$ are respectively the clusters metallicity and average Fe abundance. This formulation does not follow the definition of Z, which is

$$Z = \sum_{i=1}^{n} m_i X_i, \tag{6.2}$$

where n is the number of elements, m_i is the atomic mass of each element, and X_i the abundance of each element. In Eq. (6.2), Z is driven mostly by the abundance of C and O, which are the most abundant elements following H and He, but in stellar evolutionary calculations the relevant factor is the Fe opacity. This is why for the

cluster metallicity I adopt the expression given by Eq. (6.1). When using Eq. (6.1) to infer the metallicity, it is important to use as $Z_\odot$ the value adopted by the considered stellar evolution tracks. In this work I use the stellar evolutionary tracks by Bressan et al. 2012, which adopt $Z_\odot = 0.0152$. Using the average Fe abundance obtained from the non-chemically peculiar stars, I obtain $Z_{\rm cluster} = 0.018 \pm 0.005$, which is consistent with the solar value within the uncertainty.

6.6.3 Spectroscopic H-R Diagram

Following Langer & Kudritzki (2014) I have plotted a spectroscopic H-R Diagram (Fig. 6.11) using the $T_{\rm eff}$ and $\log g$ values calculated for each star. I calculate the flux-weighted gravity–luminosity relationship, $\log \mathcal{L}/\mathcal{L}_\odot$, following Langer & Kudritzki (2014) with

$$\log \mathcal{L}/\mathcal{L}_\odot = \log\left(\frac{T_{\rm eff}^4}{g}\right) - \log\left(\frac{T_{\rm eff\odot}^4}{g_\odot}\right) \tag{6.3}$$

where $T_{\rm eff}$ and $\log g$ are taken from Table 6.4, $T_{\rm eff\odot}$ is the solar effective temperature and $g_\odot$ is the solar surface gravity. The isochrones are from Bressan et al. (2012). Based on the H-R diagram, I are not able to constrain the age of this cluster, however the age of $\log t = 7.42$ given by Kharchenko et al. (2013) fits the data well. As a result I use this age in the reminder of the paper. I also give $\log \mathcal{L}/\mathcal{L}_\odot$, the masses and the fraction of the stars' main sequence lifetime in Table 6.6 calculated by fitting evolutionary tracks (Bressan et al. 2012) to each star.

6.6.4 Analysis of chemical abundances

Figure 6.12 shows the mean abundance of each element obtained for the F-, A- and B-type stars. The errorbars are calculated as the standard deviation about the mean abundance. I consider only the measurements from Table 6.5 with maximum errors smaller than 0.5.

To determine whether there is any correlation with the stellar fundamental parameters I have compared each set of element abundances with $T_{\rm eff}$, $v \sin i$, $M/M_\odot$ and

Table 6.6: $\log \mathcal{L}/\mathcal{L}_{\odot}$, $\log T_{\rm eff}$, $M/M_{\odot}$ and fractional age (τ) with associated error bars for the stars of the NGC 6250 open cluster.

Star	$\log \mathcal{L}/\mathcal{L}_{\odot}$	$\log T_{\rm eff}$ ($\log K$)	$M/M_{\odot}$	τ
HD 152706	1.17 ± 0.10	4.00 ± 0.02	2.25 ± 1.00	0.02 ± 0.04
HD 152743	2.47 ± 0.06	4.30 ± 0.01	6.40 ± 0.60	0.44 ± 0.09
NGC 6250-13	0.84 ± 0.12	3.91 ± 0.02	1.75 ± 1.00	0.01 ± 0.03
TYC 8327-565-1	1.79 ± 0.21	4.15 ± 0.04	3.80 ± 0.20	0.12 ± 0.14
UCAC 12065058	0.10 ± 0.16	3.78 ± 0.03	1.05 ± 0.10	-0.02 ± 0.01
UCAC 12065064	0.71 ± 0.13	3.88 ± 0.03	1.60 ± 0.05	0.00 ± 0.02
UCAC 12065075	0.18 ± 0.15	3.80 ± 0.03	1.15 ± 0.05	-0.01 ± 0.02
UCAC 12284506	0.13 ± 0.15	3.79 ± 0.03	1.05 ± 0.10	-0.02 ± 0.01
UCAC 12284536	0.98 ± 0.10	4.00 ± 0.02	2.05 ± 0.10	0.02 ± 0.04
UCAC 12284546	0.88 ± 0.12	3.92 ± 0.02	1.80 ± 1.00	0.01 ± 0.03
UCAC 12284589	1.59 ± 0.09	4.10 ± 0.02	3.20 ± 1.00	0.07 ± 0.01
UCAC 12284594	0.13 ± 0.15	3.79 ± 0.03	1.05 ± 0.10	-0.02 ± 0.01
UCAC 12284628	1.08 ± 0.10	4.00 ± 0.02	2.20 ± 0.10	0.02 ± 0.04
UCAC 12284631	1.15 ± 0.11	3.99 ± 0.02	2.20 ± 1.00	0.02 ± 0.04
UCAC 12284638	1.32 ± 0.22	4.03 ± 0.04	2.60 ± 0.20	0.04 ± 0.06
UCAC 12284645	1.25 ± 0.10	4.04 ± 0.02	2.40 ± 0.20	0.03 ± 0.05
UCAC 12284653	0.15 ± 0.15	3.79 ± 0.03	1.10 ± 0.05	-0.02 ± 0.01
UCAC 12284662	0.46 ± 0.13	3.87 ± 0.03	1.40 ± 0.10	-0.00 ± 0.02
UCAC 12284746	0.51 ± 0.13	3.86 ± 0.03	1.45 ± 0.05	-0.00 ± 0.02

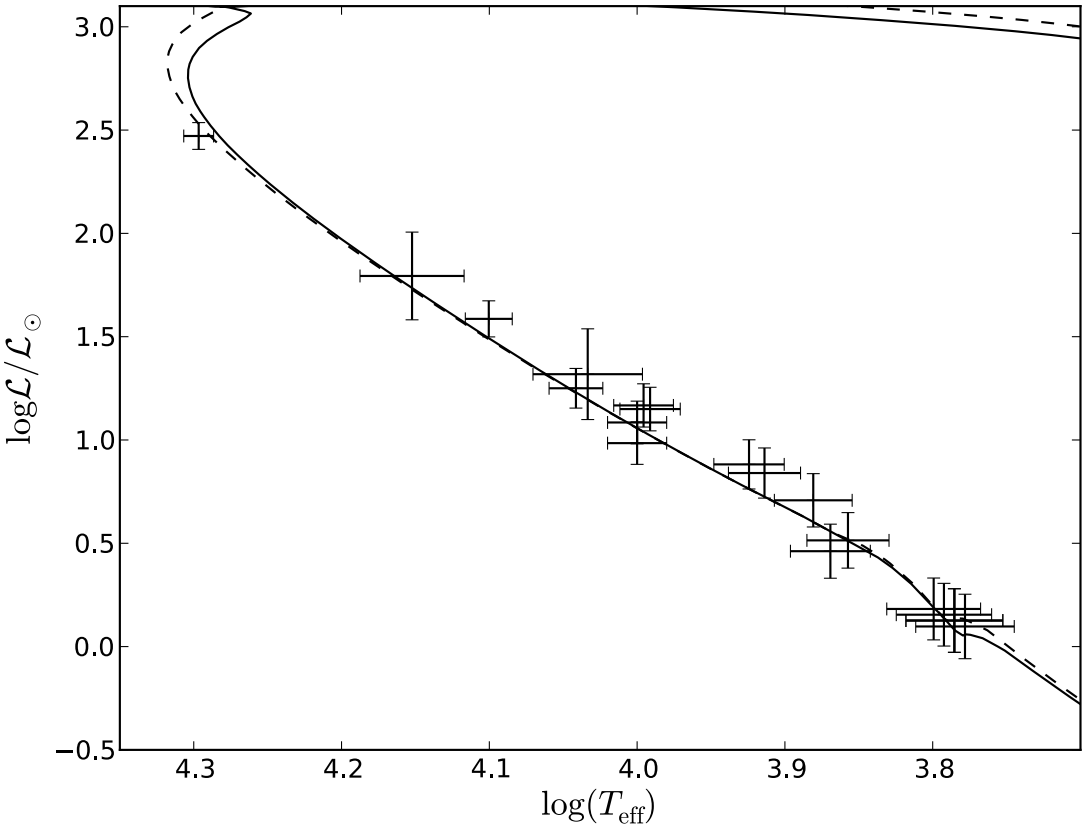

Figure 6.11: An H-R Diagram of NGC6250, the stars plotted (black plus-signs) with theoretical isochrones (Bressan et al. 2012) at $\log t = 7.40$ (dashed black line) and $\log t = 7.45$ (solid black line). Both isochrones have solar metallicity.

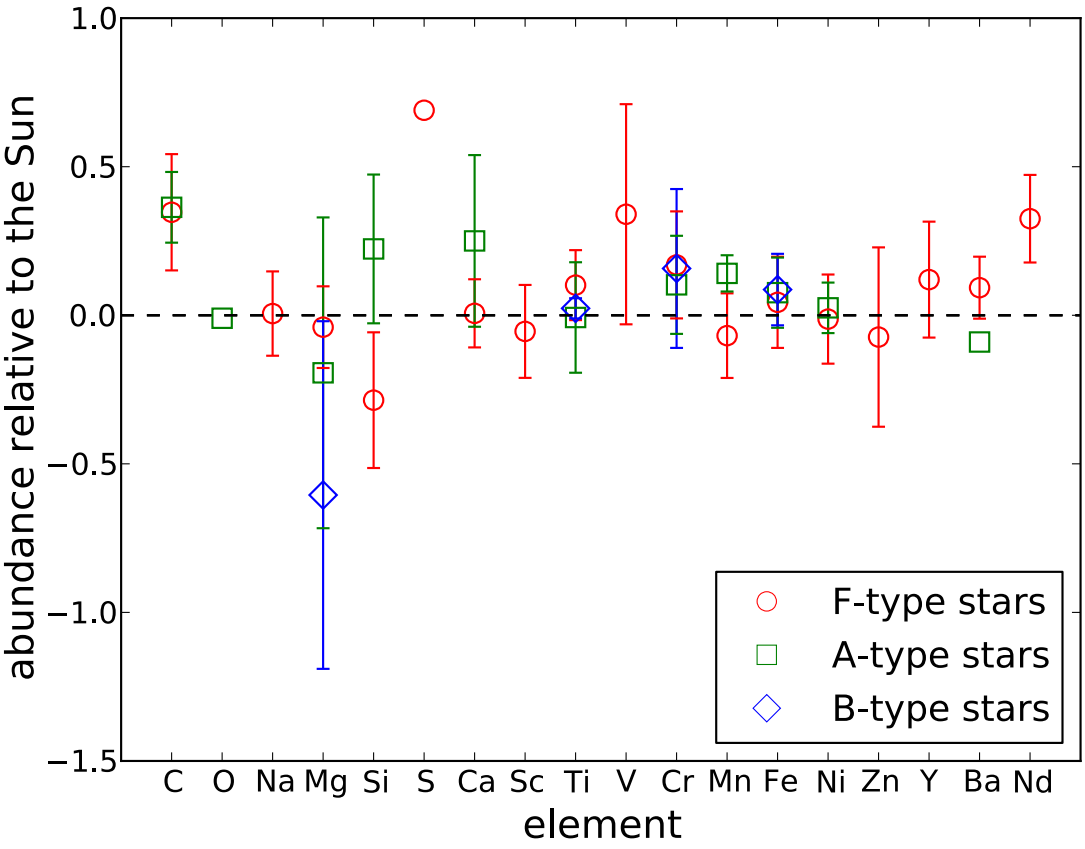

Figure 6.12: The mean abundances of each element relative to solar for F- (red circles), A-(green squares) and B- (blue diamonds) type stars. The error bars are calculated by taking the standard deviations of the calculated mean abundances.

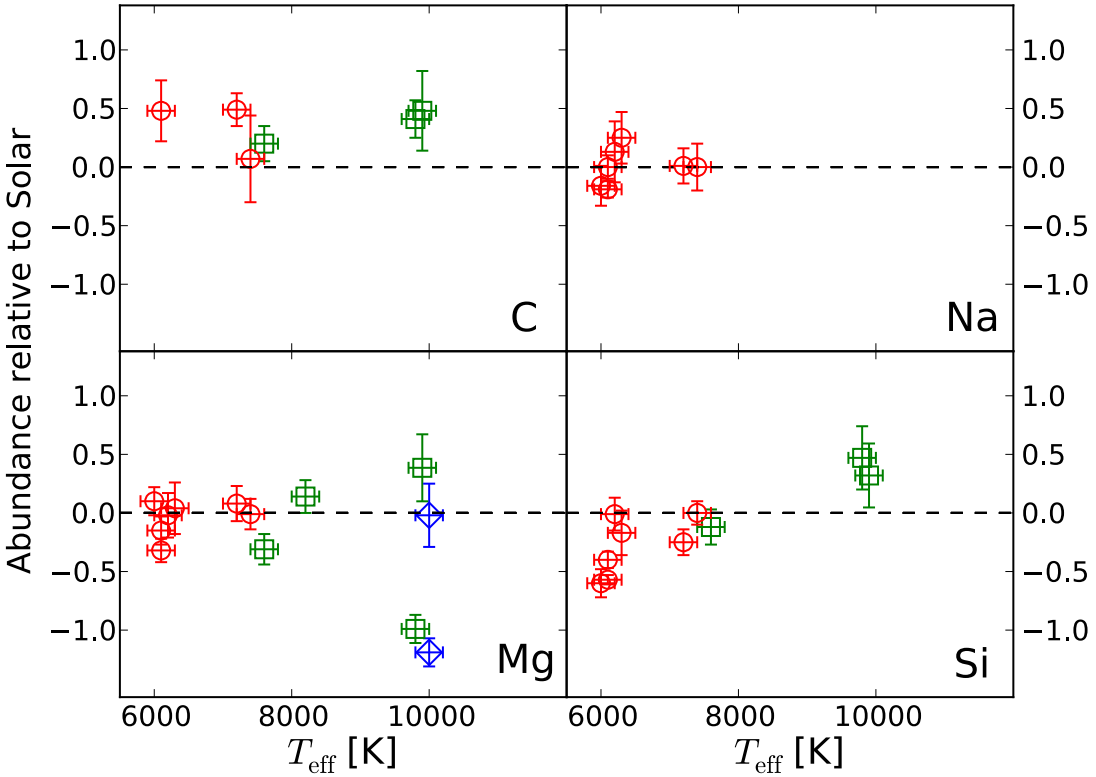

Figure 6.13: The abundances of C, Na, Mg, Si relative to the solar abundance (Asplund et al. 2009) against $T_{\rm eff}$, for F- (red circles), A-(green squares) and B- (blue diamonds) type stars

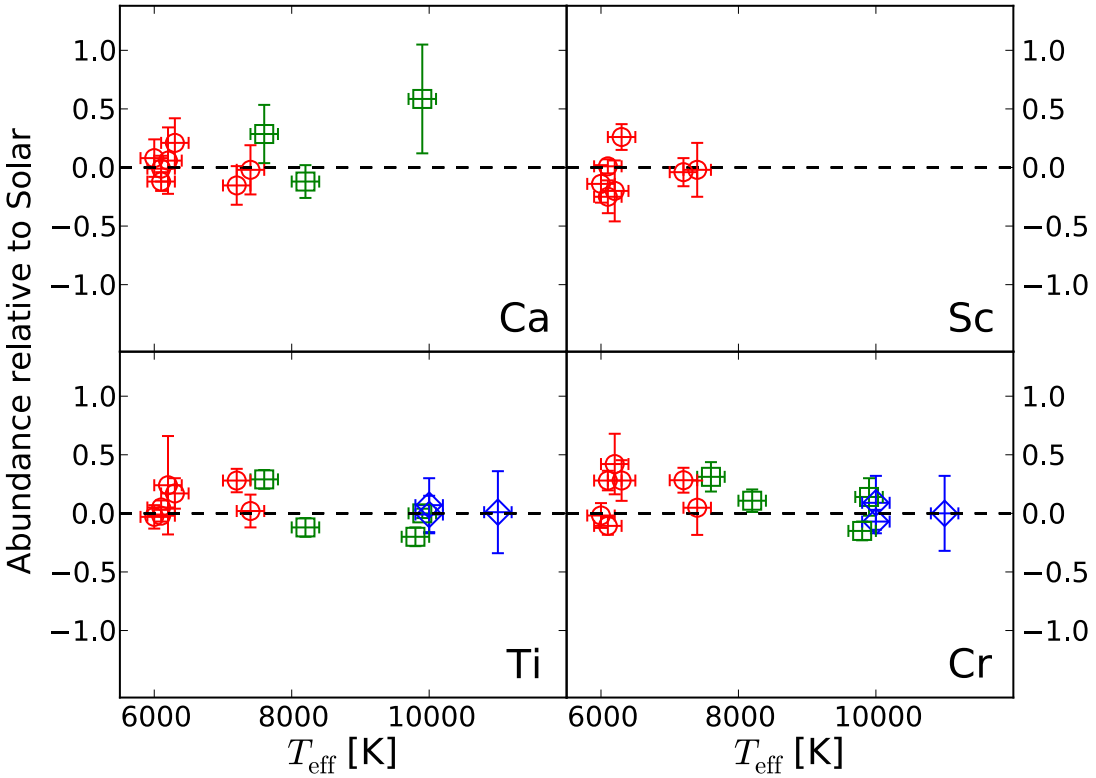

Figure 6.14: Same as Fig. 6.13, but for Ca, Sc, Ti and Cr.

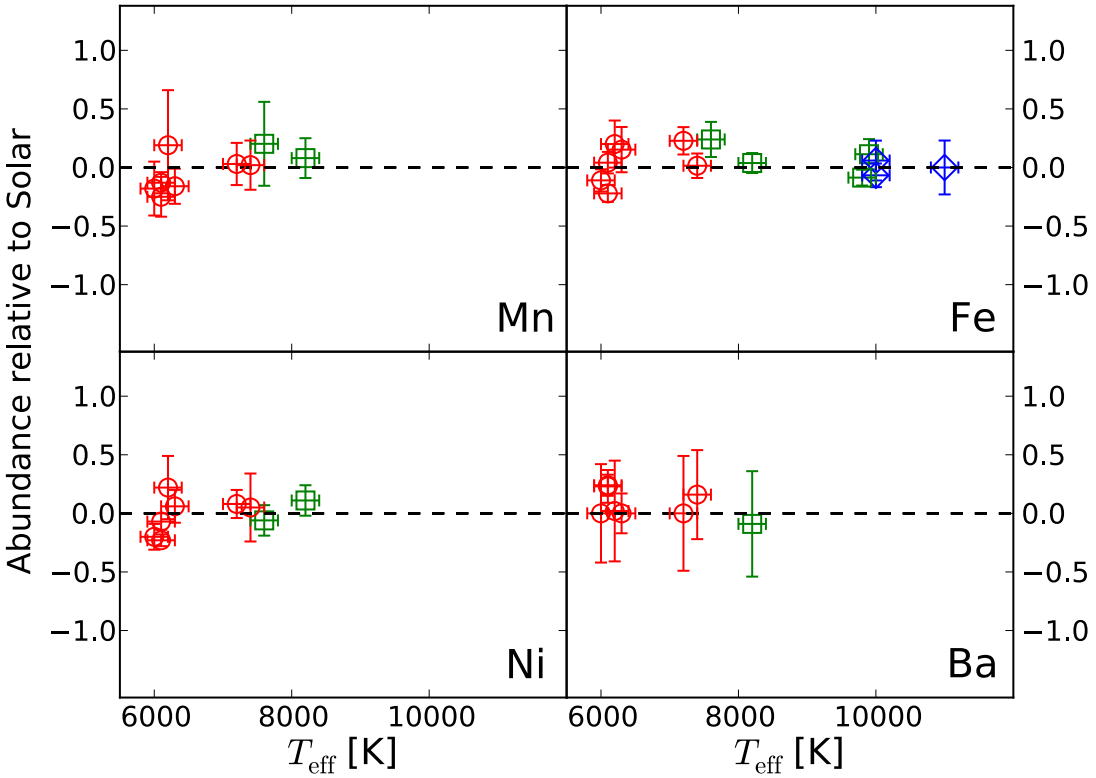

Figure 6.15: Same as Fig. 6.13, but for Mn, Fe, Ni and Ba.

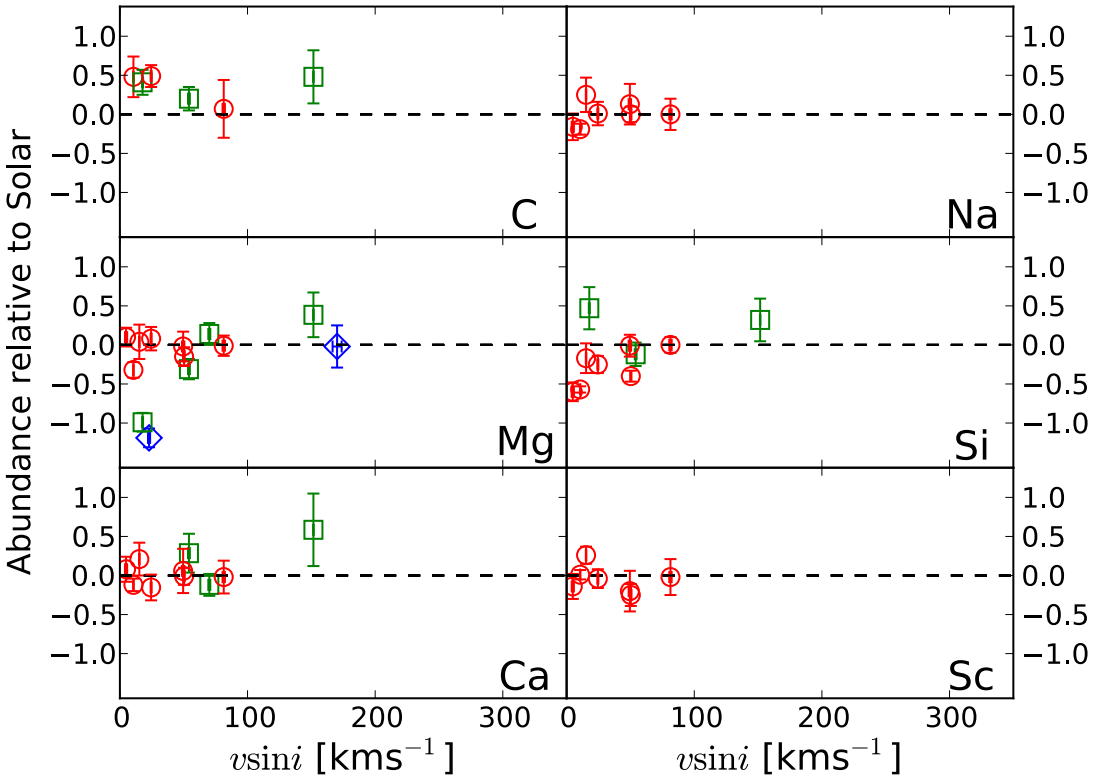

Figure 6.16: The abundances of C, Na, Mg, Si,Ca and Sc relative to the solar abundance (Asplund et al. 2009) against $v \sin i$, for F- (red circles), A-(green squares) and B- (blue diamonds) type stars.

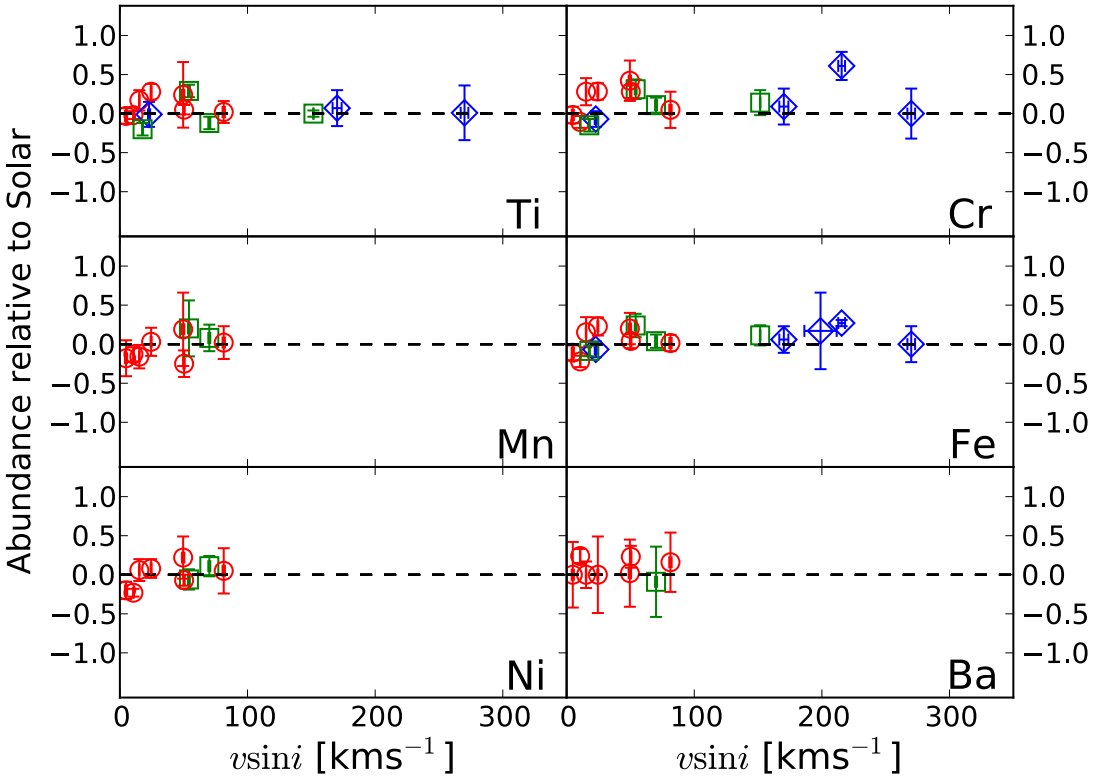

Figure 6.17: Same as Fig. 6.16, but for Ti, Cr, Mn, Fe, Ni and Ba.

fractional main sequence age. In Figs. 6.13-6.15 I show abundance as a function $T_{\rm eff}$ and in Figs. 6.16 & 6.17 I show abundance as a function of $v \sin i$. After comparison between abundance and each of the fundamental parameters I see no statistically significant patterns. This is consistent with the findings of Kılıçoğlu et al. (2016).

In addition, I have compared my results with the previous studies of the open clusters NGC6405, NGC5460 and Praesape performed by Kılıçoğlu et al. (2016), Fossati et al. (2011a) and Fossati et al. (2007), Fossati et al. (2008a), Fossati et al. (2010), respectively. This allows me to determine whether there is any evidence for correlation between cluster age and abundance. I compare my results with only these clusters since they have all been analysed within this project and the analysis has been either fully carried out (Praesape and NGC5460) or supervised by Luca Fossati (NGC6405 and NGC6250), to minimise the possibility of systematic differences between the results. To compare the results from each cluster analysis, I have offset the abundance values of the individual chemical elements according to the cluster metallicities as estimated from Fe abundances of the cluster F and later type stars, which should be less affected by diffusion than earlier type stars.

In NGC 6250 I found that O, Na, Sc, Ti, Cr, Mn, Ni, Zn and Y all have solar abundances within the uncertainties, while S and V are overabundant. These results are consistent with the findings of Fossati et al. (2008a), Fossati et al. (2011a) and Kılıçoğlu et al. (2016) for the Praesepe cluster, NGC 5460 and NGC 6405 respectively (see Figs. 6.18 & 6.19).

Similarly to what was found by Fossati et al. (2008a), Fossati et al. (2011a) and Kılıçoğlu et al. (2016) in the Praesepe cluster, NGC 5460 and NGC 6405, I have found an overabundance of C in the F- and A-type stars of NGC 6250. However, I do not see any trend with age (see Fig. 6.18).

For all of the F-type stars I find a solar abundance of Mg, for the A-type and B-type stars there is an underabundance of Mg, however there is a large spread in the results and all but two stars have approximately solar abundance, which matches with

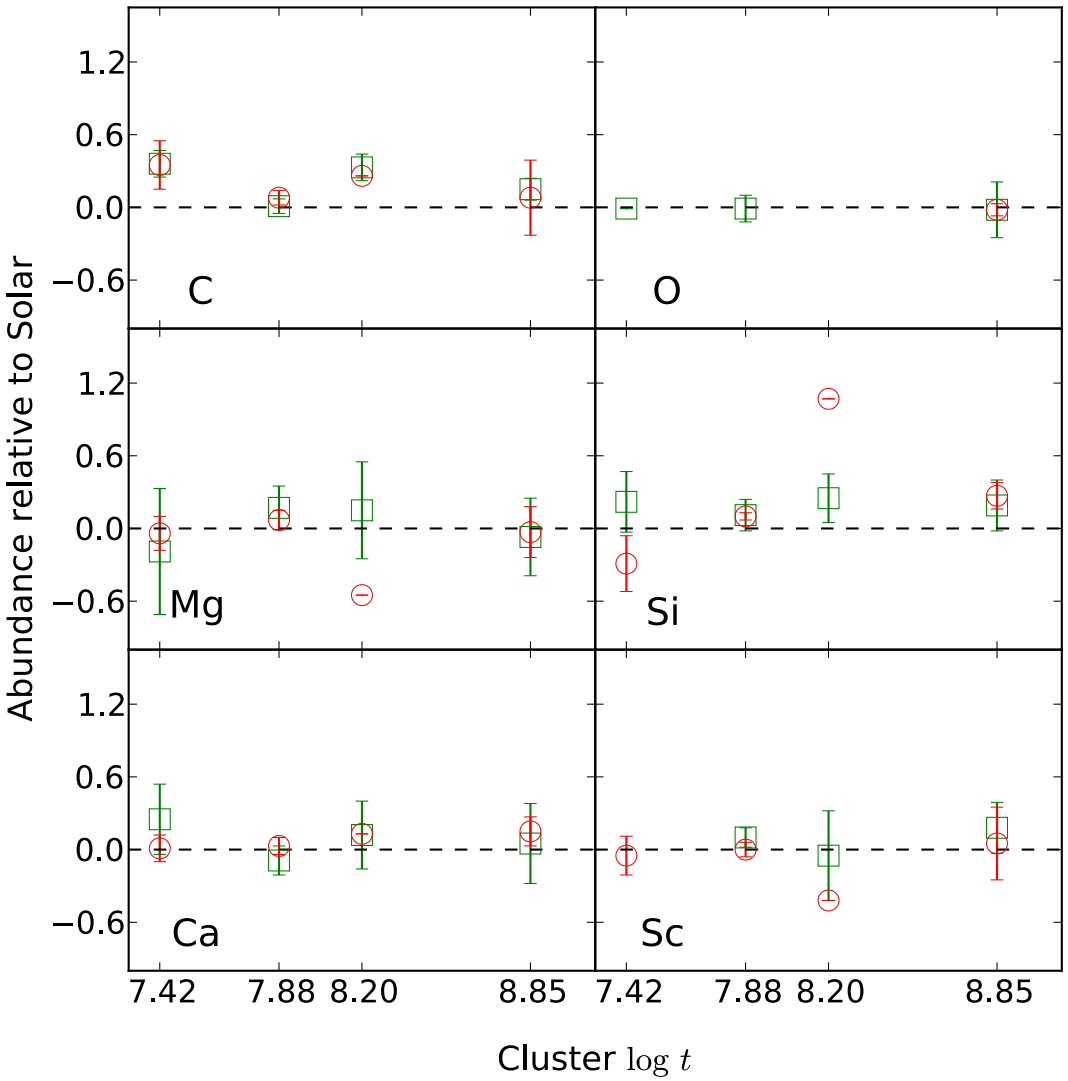

Figure 6.18: A comparison between the mean C, O, Mg, Si, Ca, and Sc abundances found for each of the previous studies and those found in this paper. Mean abundances for F- (red circles) and A-type (green squares) stars are plotted against cluster age ($\log t$ = 7.42 for NGC 6250; $\log t$ = 7.88 for NGC 6405; $\log t$ = 8.20 for NGC5460; and $\log t$ = 8.85 for Praesepe). The error is given by the standard deviation of all the measured abundances.

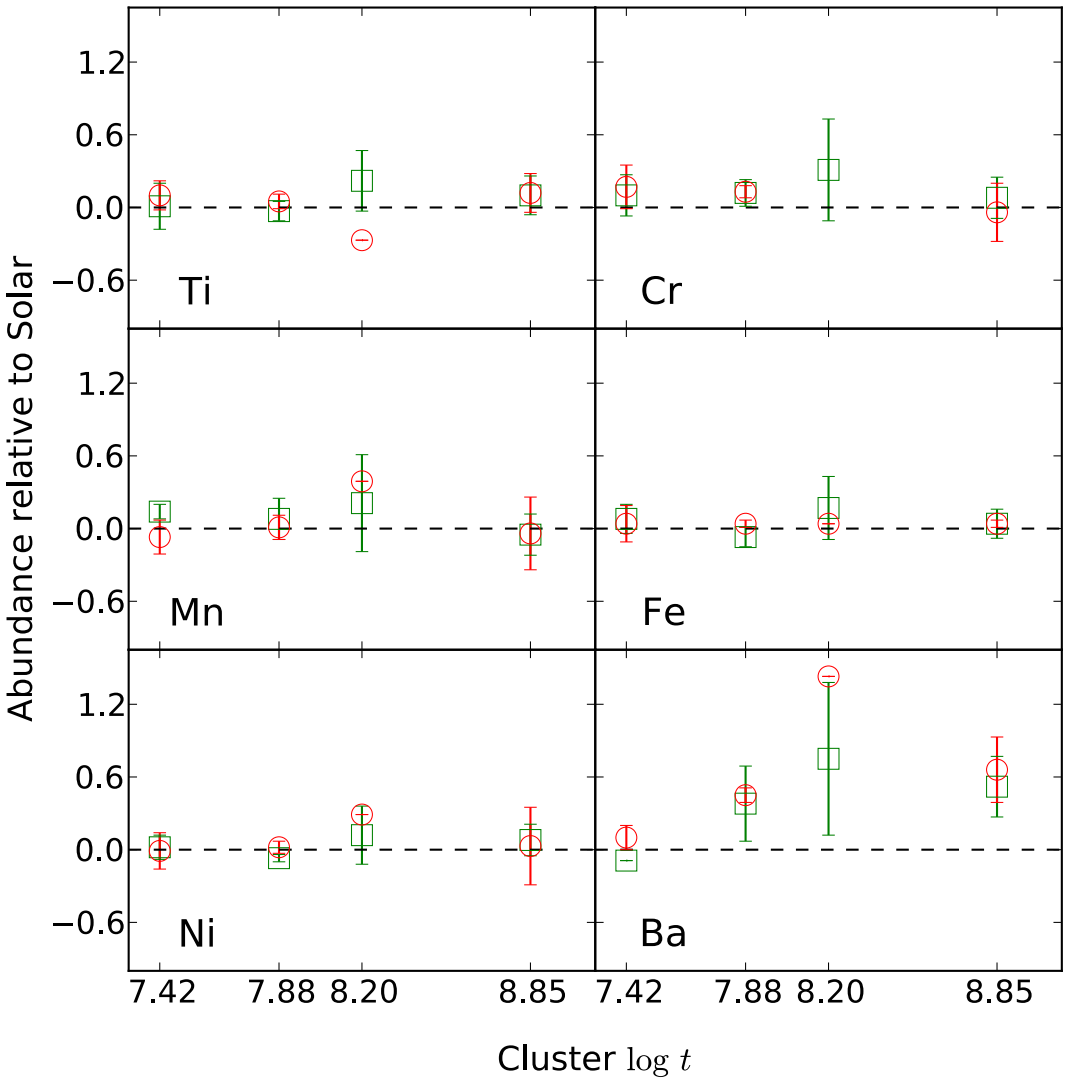

Figure 6.19: Same as Fig. 6.19 but for Ti, Cr, Mn, Fe, Ni and Ba.

Table 6.7: The statistical significance of the trends seen in Figs. 6.13, 6.14 & 6.15.

Element	Slope	χ^2	Degrees of Freedom	Reduced χ^2	p-value
C	$4\times10^{-6}\pm5\times10^{-5}$	3.02	4	0.75	0.55
C	0.0	3.02	5	0.60	0.70
Na	$1\times10^{-4}\pm1\times10^{-4}$	5.71	5	1.14	0.34
Na	0.0	6.75	6	1.12	0.34
Mg	$-2\times10^{-4}\pm7\times10^{-5}$	75.66	11	6.88	0.00
Mg	0.0	133.23	12	11.10	0.00
Si	$3\times10^{-4}\pm7\times10^{-5}$	21.46	8	2.68	0.01
Si	0.0	68.86	9	7.65	0.00
Ca	$2\times10^{-5}\pm6\times10^{-5}$	7.42	8	0.93	0.49
Ca	0.0	7.54	9	0.84	0.58
Sc	$1\times10^{-5}\pm1\times10^{-4}$	10.27	5	2.05	0.07
Sc	0.0	10.28	6	1.71	0.11
Ti	$-2\times10^{-5}\pm2\times10^{-5}$	29.48	12	2.46	0.00
Ti	0.0	31.85	13	2.45	0.00
Cr	$-1\times10^{-5}\pm3\times10^{-5}$	41.24	13	3.17	0.00
Cr	0.0	41.72	14	2.98	0.00
Mn	$1\times10^{-4}\pm3\times10^{-5}$	1.23	7	0.18	0.99
Mn	0.0	4.18	8	0.52	0.84
Fe	$1\times10^{-5}\pm2\times10^{-5}$	21.66	13	1.67	0.06
Fe	0.0	22.12	14	1.58	0.08
Ni	$1\times10^{-4}\pm6\times10^{-5}$	8.63	7	1.23	0.28
Ni	0.0	15.54	8	1.94	0.05
Ba	$-1\times10^{-4}\pm9\times10^{-5}$	1.82	6	0.30	0.94
Ba	0.0	2.51	7	0.36	0.93

Table 6.8: The statistical significance of the trends seen in Figs. 6.16 & 6.17.

Element	Slope	χ^2	Degrees of Freedom	Reduced χ^2	p-value
C	$-2\times10^{-3}\pm2\times10^{-3}$	2.61	4	0.65	0.63
C	0.0	3.02	5	0.60	0.70
Na	$3\times10^{-3}\pm2\times10^{-3}$	4.40	5	0.88	0.49
Na	0.0	6.75	6	1.12	0.34
Mg	$5\times10^{-3}\pm4\times10^{-3}$	115.65	11	10.51	0.00
Mg	0.0	133.23	12	11.10	0.00
Si	$7\times10^{-3}\pm2\times10^{-3}$	27.61	8	3.45	0.00
Si	0.0	68.86	9	7.65	0.00
Ca	$1\times10^{-3}\pm2\times10^{-3}$	6.88	8	0.86	0.55
Ca	0.0	7.54	9	0.84	0.58
Sc	$-3\times10^{-3}\pm3\times10^{-3}$	8.44	5	1.69	0.13
Sc	0.0	10.28	6	1.71	0.11
Ti	$-5\times10^{5}\pm6\times10^{-4}$	31.83	12	2.65	0.00
Ti	0.0	31.85	13	2.45	0.00
Cr	$2\times10^{-3}\pm9\times10^{-4}$	31.34	13	2.41	0.00
Cr	0.0	41.72	14	2.98	0.00
Mn	$2\times10^{-3}\pm1\times10^{-3}$	2.98	7	0.43	0.89
Mn	0.0	4.18	8	0.52	0.84
Fe	$1\times10^{-3}\pm7\times10^{-4}$	17.83	13	1.37	0.16
Fe	0.0	22.12	14	1.58	0.08
Ni	$4\times10^{-3}\pm2\times10^{-3}$	8.08	7	1.15	0.33
Ni	0.0	15.54	8	1.94	0.05
Ba	$-5\times10^{-4}\pm2\times10^{-3}$	2.49	6	0.41	0.87
Ba	0.0	2.51	7	0.36	0.93

Table 6.9: The statistical significance of the trends seen in Figs. 6.18, 6.19 for F-type stars.

Element	Slope	χ^2	Degrees of Freedom	Reduced χ^2	p-value
C	0.27±0.25	6.01	2	3.00	0.05
C	0.00	9.54	3	3.18	0.02
Mg	-0.77±0.64	45.84	2	22.92	0.00
Mg	0.00	79.46	3	26.49	0.00
Si	2.01±1.23	486.20	2	243.10	0.00
Si	0.00	1133.29	3	377.76	0.00
Ca	0.15±0.07	0.97	2	0.48	0.62
Ca	0.00	3.26	3	1.09	0.35
Sc	-0.79±0.43	20.88	2	10.44	0.00
Sc	0.00	56.80	3	18.93	0.00
Ti	-0.44±0.39	26.82	2	13.41	0.00
Ti	0.00	43.89	3	14.63	0.00
Cr	-0.15±0.04	0.03	1	0.03	0.86
Cr	0.00	0.54	2	0.27	0.76
Mn	0.60±0.35	11.01	2	5.50	0.00
Mn	0.00	27.29	3	9.10	0.00
Fe	0.00±0.00	0.00	2	0.00	1.00
Fe	0.00	0.00	3	0.00	1.00
Ni	0.60±0.23	7.81	2	3.91	0.02
Ni	0.00	33.82	3	11.27	0.00
Ba	1.94±0.71	95.78	2	47.89	0.00
Ba	0.00	451.80	3	150.60	0.00

Table 6.10: The statistical significance of the trends seen in Figs. 6.18, 6.19 for A-type stars.

Element	Slope	χ^2	Degrees of Freedom	Reduced χ^2	p-value
C	-0.02±0.22	11.66	2	5.83	0.00
C	0.00	11.69	3	3.90	0.01
O	-0.00±0.00	0.00	1	0.00	0.98
O	0.00	0.00	2	0.00	1.00
Mg	-0.11±0.19	0.65	2	0.33	0.72
Mg	0.00	0.76	3	0.25	0.86
Si	0.03±0.09	0.40	2	0.20	0.82
Si	0.00	0.42	3	0.14	0.94
Ca	-0.03±0.25	1.49	2	0.74	0.48
Ca	0.00	1.50	3	0.50	0.68
Sc	0.07±0.11	0.22	1	0.22	0.64
Sc	0.00	0.31	2	0.15	0.86
Ti	0.11±0.10	0.79	2	0.40	0.67
Ti	0.00	1.27	3	0.42	0.74
Cr	-0.01±0.06	0.26	2	0.13	0.88
Cr	0.00	0.27	3	0.09	0.97
Mn	-0.12±0.04	0.18	2	0.09	0.91
Mn	0.00	1.21	3	0.40	0.75
Fe	0.01±0.11	1.74	2	0.87	0.42
Fe	0.00	1.75	3	0.58	0.63
Ni	0.07±0.11	2.07	2	1.03	0.36
Ni	0.00	2.42	3	0.81	0.49
Ba	0.49±0.13	1.28	2	0.64	0.53
Ba	0.00	10.03	3	3.34	0.02

the results of the previous studies.

In agreement with previous studies, I found that in A-type stars Si is overabundant; however, at odds with previous studies, I found that in F-type stars Si is underabundant. Figure 6.13 indicates the presence of a possible correlation between Teff and the Si abundance, though a further analysis shown in Table 6.7 reveals that this apparent correlation is not statistically significant.

For all of the F-type stars I find a solar abundance of Ca which is consistent with the previous results. However for the A-type stars I find an overabundance, which is contrary to the findings of the previous studies; the origin of this is unclear.

I measure the abundance of Fe in all of the stars to be approximately solar. For both Mn and Fe, Fossati et al. (2011a) found an increase in abundance with $T_{\rm eff}$, which I do not, this therefore may be the result of an age effect. The narrow $T_{\rm eff}$ range of the stars analysed by Fossati et al. (2008a) for the Praesepe cluster means I are unable to provide any definite conclusions until the remaining clusters are analysed.

I measure an almost solar abundance for Ba, albeit with relatively large uncertainties. This is in contrast with the findings of Fossati et al. (2008a), Fossati et al. (2011a) and Kılıçoğlu et al. (2016) who all report overabundances. To understand each of the results together I plot the mean abundance of Ba measured for each cluster in Fig. 6.19. I did not consider the stars HD 122983 and HD 123182 from NGC5460 because of their apparent chemical peculiarities (Fossati et al. 2011a). From Fig. 6.19, I obtain a hint of a positive correlation of Ba abundance with age, however the abundance uncertainties are too large to draw any concrete conclusion. By analysing further clusters I will be able to determine whether this effect is the result of diffusion or the different chemistry of the star forming region for each cluster.

I measure Nd to be overabundant in four stars, however the data from previous papers is too sparse to provide any conclusion.

Finally I have compared my results with the study of chemically peculiar magnetic Ap stars by Bailey, Landstreet & Bagnulo (2014). This allows me to examine the differences and similarities between abundance trends of chemically normal and chemi-

cally peculiar stars. Bailey, Landstreet & Bagnulo (2014) found statistically significant trends between He, Ti, Cr, Fe, Pr and Nd and stellar age. They also found a strong trend between the abundances of Cr and Fe, and $T_{\rm eff}$. For Cr an underabundance was observed for stars with $T_{\rm eff} \lesssim 7000\,{\rm K}$, for stars with $T_{\rm eff} \gtrsim 7000\,{\rm K}$ the abundance of Cr sharply rises and peaks at $T_{\rm eff} \sim 10000\,{\rm K}$ before falling back to approximately solar. For Fe an underabundance was observed for stars with $T_{\rm eff} \lesssim 8000\,{\rm K}$ and an overabundance for the remaining stars. These results are in stark contrast with what I observed for NGC 6250. This suggests that the abundance of chemical elements in the photosphere of chemically normal F-, A- and B-type stars remains relatively constant during their main sequence lifetime except when influenced by a magnetic field.

6.7 Summary of results

In this chapter I have presented the analysis of NGC 6250 which represents the first use of SPARTI SIMPLE for determination of chemical abundances in the photosphere of non-magnetic stars. I have shown that the tools I have created allow for the efficient analysis of observed spectra from normalisation through to abundance determination. Based on the additional knowledge gained from the analysis of the spectra of the member stars, I have re-calculated the cluster proper motions as $0.4 \pm 3.0\,\mathrm{mas\,yr^{-1}}$ in RA, $-4.8 \pm 3.2\,\mathrm{mas\,yr^{-1}}$ in DEC, and the cluster mean radial velocity as $-10 \pm 6\,\mathrm{km\,s^{-1}}$, which agree well with Kharchenko et al. (2013). The age and distance given by Kharchenko et al. (2013) agree well with my photometric analysis of the cluster.

Finally, I have examined the chemical abundance measurements for each star and searched for any trend between abundance and the stellar fundamental parameters and between the abundance measured in this study and the abundance measured in the previous studies of older clusters by Kılıçoğlu et al. (2016), Fossati et al. (2011a) and Fossati et al. (2007), Fossati et al. (2008a),Fossati et al. (2010). My results for the abundance of O, Na, Sc, Ti, Cr, Mn, Ni, Zn and Y are solar within the uncertainties, while S and V are overabundant. These results are consistent with previous studies. I do not find evidence of the correlation between either the Fe or Mn abundance and $T_{\rm eff}$ found by Fossati et al. (2011a); however, this may be evidence of an age effect and more clusters need to be studied before being able to determine this. I find hints of an increase in mean Ba abundance with cluster age but more clusters should be analysed to confirm this trend. Comparing my results with those from Bailey, Landstreet & Bagnulo (2014), who searched for trends between chemical abundances and stellar parameters of chemically peculiar magnetic Ap stars, suggests that the abundance of chemical elements in the photosphere of chemically normal F-, A- and B- type stars remains relatively constant during their main-sequence lifetime except when influenced by a magnetic field.

7 Observations and modelling of magnetic stars

The application of Sparti to the analysis of observed Stokes $IQUV$ profiles of Ap stars adds extra challenges which were difficult to test with numerical simulations. I was able to determine the effects of photon-noise, instrument response and crosstalk, which give good constraints on the quality of data required for observation. The difficulty, however, comes as a result of the very real possibility that the observed star has a magnetic field geometry which is far more complex than can be modelled with a dipole+quadrupole morphology. In addition, with numerical simulations I consistently use the same line parameters both to generate the model and to recover the model. This means I am certain that all of the lines present in both cases are the same and have identical atomic data. This however is unlikely to be true in the case of an observed star. Errors in the calculation of atomic parameters, extreme overabundances and non-homogeneous abundance distributions all lead to a situation where it may be unclear which lines have an impact on the overall line profile without a very large amount of repeat analysis.

In this thesis I have chosen to analyse the stars HD24712 and HD137909 (β Coronae Borealis; βCrB) using Sparti. These stars both represent ideal test cases for Sparti. HD24712 appears to have a reasonably simple magnetic field geometry, but also shows evidence of a strong overabundance of Nd which varies significantly with the rotational phase of the star. This variation in abundance potentially suggests the presence of a large spot with considerable enhancement of Nd. This reasonably simple geometry coupled with a stellar spectrum dominated by unblended lines makes this star an ideal case study. By contrast, βCrB is a considerably more complicated star to analyse: in addition to the presence of a very strong magnetic field, there is evidence of a complex magnetic field geometry and abundance inhomogeneities. Furthermore, there are a large number of blends with multiple chemical elements determining the shape of the line profile, as result of the magnetic field broadening. For these reasons the modelling of βCrB is challenging. However, this is precisely why it is a good test

for Sparti since it allows me to test all aspects of the code. As part of the analysis of both stars I performed a large number of iterations starting from random initial parameters. This has allowed me to test the uniqueness of the solutions generated by Sparti.

In addition to being good test subjects for Sparti, the modelling of both these stars allows us to develop our understanding of how dynamo magnetic fields transition into fossil fields. In particular, determining the different complexities of magnetic field geometries which can occur in Ap stars. The analysis of chemical peculiarities in combination with detailed stellar magnetic field modelling will allow us to understand whether the strength and geometry of stellar magnetic fields have an impact on the chemical peculiarities observed.

As mentioned in Chapter 6, Bailey, Landstreet & Bagnulo (2014) found statistically significant trends between He, Ti, Cr, Fe, Pr and Nd and stellar age. They also found a strong trend between the abundances of Cr and Fe, and $T_{\rm eff}$. However, more importantly for this chapter they found statistically significant trends between abundance and the magnetic field strength for the same elements. These trends are directly opposite to those found for abundance vs age. This is expected since it has been shown that $\langle \mathrm{Bz} \rangle$ decreases with stellar age in Ap stars (Landstreet et al. 2007; Landstreet et al. 2008). Detailed modelling of these stars is necessary to understand whether stellar age or magnetic field strength is the main contributing factor to the observed correlations, and to determine whether geometry has an additional impact.

Furthermore the detailed study of Ap stars allows for the investigation of a variety of processes which can be observed simultaneously. As a result, these stars can act as "stellar laboratories" from which we can learn about processes in common with other stars. The only method currently available which makes it possible to study these stars in the detail required is Zeeman Doppler Mapping of a time series of Stokes $IQUV$ profiles. My code is the first to allow simultaneous modelling of 3D abundance distributions and a parameterised magnetic field.

During my thesis work I have had the opportunity to complete a long campaign of spectropolarimetric observations of magnetic stars at the Serra La Nave (SLN) ob-

servatory in Italy consisting of two periods; the first of 18 days and the second of six days. During this time I observed the Stokes $IQUV$ profiles of 14 stars and obtained observations at 11 different rotational phases of βCrB. In addition to this observational experience, I also observed at the William Herschel Telescope using the ISIS instrument in spectropolarimetric mode. In total my observational experience with ISIS consists of 13 nights. I have taken a variety of observations of white dwarf stars (WDs), asteroids, solar system objects and the interstellar medium. While these observations at the WHT are outside the scope of this thesis, the knowledge gained from taking the observations and by reducing the long-slit spectropolarimetric data has allowed me to understand the effects which can create spurious signals in the reduced data.

In this chapter I describe the way in which spectropolarimetric data is taken. Then, for each star, HD24712 and βCrB, I review previous results and analysis and give details of the observations I use for this thesis. Finally, I present the results of my analysis using Sparti for each star, attempting to model the Stokes $IQUV$ profiles using magnetic fields with dipole, de-centered dipole and dipole+quadrupole morphology for HD24712 and with a dipole+quadrupole morphology for βCrB.

7.1 Spectropolarimetric observations

The observations of Stokes profiles are undertaken using a spectropolarimeter. A simple schematic view of a polarimeter is shown in Fig. 7.1 consisting of a retarder, a polariser and a detector.

The retarder wave plate introduce a phase shift of an angle γ between the electric component of the electromagnetic wave parallel to the *fast axis* of the retarder and the electric component of the electromagnetic wave perpendicular to the fast axis. Retarder wave plates which introduce a phase shift of $\gamma = 180°$ are called half-wave plates and are used for the measurement of linear polarisation. Retarder wave plates which introduce a phase shift of $\gamma = 90°$ are called quarter-wave plates and are used

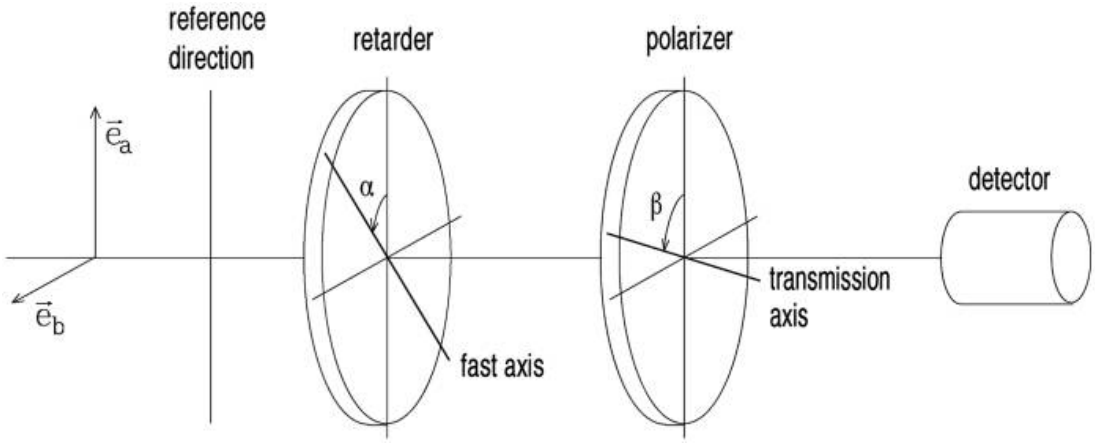

Figure 7.1: Schematic of an ideal polariser (Landi Degl'Innocenti & Landolfi 2004)[1], where α is the angle between the reference direction and the *fast axis* of the retarder. The *fast axis* is the direction for which the retarder has its lowest refractive index. β is the angle between the reference direction and the *transmission axis* of the polariser. The *transmission axis* is the direction which light is able to propagate.

for the measurement of circular polarisation.

Instead of a polariser, HARPSpol, CAOS and the majority of astronomical spectropolarimeters employ a beam splitter, which splits the incoming radiation into two beams, one polarised parallel to the principle plane of the beam splitter and one polarised perpendicular to it. These two beams, $f_{\parallel}$ and $f_{\perp}$ respectively, are fed to the spectrograph and then to the detector. In Fig. 7.1 $f_{\parallel}$ corresponds to the case of $\beta = 0°$ and $f_{\perp}$ the case of $\beta = 90°$. Since these beams are measured simultaneously sky conditions do not affect the differences in their fluxes.

The signal $S(\alpha, \beta, \gamma)$ measured by the detector in Fig. 7.1 is given by Landi

[1]Figure 1.9 in *Polarization in Spectral Lines*, E. Landi Degl'innocenti and M. Landolfi, 2004, Astrophysics and Space Science Library, Vol. 307 © 2005 Springer Science + Business Media, Inc. With permission of Springer. http://dx.doi.org/10.1007/1-4020-2415-0

Degl'Innocenti & Landolfi (2004)

$$\begin{aligned} S(\alpha,\beta,\gamma) \propto \frac{1}{2}\{I &+ [Q\cos 2\alpha + U\sin 2\alpha]\cos(2\beta - 2\alpha) \\ &- [Q\sin 2\alpha - U\cos 2\alpha]\sin(2\beta - 2\alpha)\cos\gamma \\ &+ V\sin(2\beta - 2\alpha)\sin\gamma\}. \end{aligned} \tag{7.1}$$

To illustrate the calculation of the Stokes QUV profiles, I will take the example of the measurement of Stokes Q. To measure Stokes Q we use a half-wave plate, therefore $\gamma = 180°$. If we set $\alpha = 0°$ and take $\beta = 0°$ we obtain

$$S(0°,\ 0°, 180°) \propto \frac{1}{2}\{I + [Q + 0] - [0 - U] \times 0 + 0\} = \frac{1}{2}\{I + Q\} = f^{\parallel} \tag{7.2}$$

and $\beta = 90°$ we obtain

$$S(0°, 90°, 180°) \propto \frac{1}{2}\{I + [Q + 0]\,(-1) - [0 - U] \times 0 + 0\} = \frac{1}{2}\{I - Q\} = f^{\perp}. \tag{7.3}$$

To obtain Stokes Q we take the difference between $f_\perp$ and $f_\parallel$

$$f_\parallel - f_\perp = \frac{1}{2}\{I + Q\} - \frac{1}{2}\{I - Q\} = Q. \tag{7.4}$$

We can also show that Stokes I may be calculated by

$$f_\parallel + f_\perp = \frac{1}{2}\{I + Q\} + \frac{1}{2}\{I - Q\} = I. \tag{7.5}$$

This is an important result because it shows that the intensity spectrum is a natural bi-product of the observation of Stokes profiles and so, in addition to the information about the polarisation of the incoming radiation, we also gain all of the information which would result from an ordinary spectroscopic measurement.

In general we are interested in the ratio between Stokes Q and Stokes I and so we calculate

$$\frac{f_\parallel - f_\perp}{f_\parallel + f_\perp} = \frac{\frac{1}{2}\{I + Q\} - \frac{1}{2}\{I - Q\}}{\frac{1}{2}\{I + Q\} + \frac{1}{2}\{I - Q\}} = \frac{Q}{I}. \tag{7.6}$$

This method for calculating the Stokes parameters works in the ideal case. However, in reality the difference between $f_\parallel$ and $f_\perp$ may be affected by instrumental effects. These may be due to the two beams passing through different optical pathways and

landing on different parts of the detector or to deviation of the polarimetric optics from their nominal behaviour, e.g., the angle γ may not be exactly 90° or 180° and can even vary with wavelength. These problems may be overcome by adopting the beam swapping technique. For instance the measurement of Q/I is accomplished by observing the source at the pair of angles[2] $\alpha = 0°$ and $\alpha = 45°$. In the following I will explain why the beam swapping technique mitigates the problem of imperfect detector flat-fielding. We consider the flux transmitted through two different optical pathways for which the various optical artefacts combine to give constants for each path, r_k and r_p, which leads to

$$\mathcal{G} = \frac{1}{2}\left(\frac{r_k f_\parallel - r_p f_\perp}{r_k f_\parallel + r_p f_\perp}_{\alpha=0°} - \frac{r_k f_\parallel - r_p f_\perp}{r_k f_\parallel + r_p f_\perp}_{\alpha=45°}\right) \tag{7.7}$$

substituting $f_\parallel$ and $f_\perp$ for $\{I+Q\}$ and $\{I-Q\}$ respectively for $\alpha = 0°$ and vice-versa for $\alpha = 45°$ leads to

$$\mathcal{G} = \frac{1}{2}\left(\frac{r_k\{I+Q\} - r_p\{I-Q\}}{r_k\{I+Q\} + r_p\{I-Q\}} - \frac{r_k\{I-Q\} - r_p\{I+Q\}}{r_k\{I-Q\} + r_p\{I+Q\}}\right). \tag{7.8}$$

This can be rewritten as

$$\mathcal{G} = \frac{1}{2}\left(\frac{(r_k - r_p)I + (r_k + r_p)Q}{(r_k - r_p)I + (r_k - r_p)Q} + \frac{-(r_k - r_p)I + (r_k + r_p)Q}{(r_k + r_p)I - (r_k - r_p)Q}\right) \tag{7.9}$$

which after cross-multiplying and simplifying yields

$$\mathcal{G} = \frac{IQ(r_k + r_p)^2 - IQ(r_k - r_p)^2}{I^2(r_k + r_p)^2 - Q^2(r_k - r_p)^2}. \tag{7.10}$$

The two beams, $f_\parallel$ and $f_\perp$, pass through essentially the same optical pathway as they travel through the instrument, therefore in most cases we can assume that $r_k \simeq r_p$ which means that $(r_k - r_p)^2$ is negligible in comparison to $(r_k + r_p)^2$, which results in

$$\mathcal{G} = \frac{IQ}{I^2} = \frac{Q}{I}. \tag{7.11}$$

The procedure for calculating Stokes U/I and V/I is the same as above however using different angles of α and γ. For the observation of Stokes U/I again we use a

[2]It is equally possible to use angle pairs of 90° and 135°; 180° and 225° and 270° and 315°. In fact the more pairs of angles used the better the removal of optical artefacts.

half-wave plate so $\gamma = 180°$. The pairs of α which can be used for the beam swapping technique are 22.5° and 67.5; 112.5° and 157.5°; 202.5° and 247.5° and 292.5° and 337.5°. For the observation of Stokes V/I we use a quarter-wave plate so $\gamma = 90°$. The pairs of α which can be used for the beam swapping technique are -45° and 45°; 135° and 225°; and 315° and 45°. Further details on the calculation of Stokes profiles are given in Bagnulo et al. (2009), which demonstrates how the beam swapping technique solves the problem of the deviation of the polarimetric optics from their nominal values.

7.2 HD24712

The first star which I analysed using Sparti was HD24712. This star has been shown to have a reasonably simple dipolar magnetic morphology and so was a good test to check the functionality of Sparti. This star is a rapidly oscillating Ap (roAp) star (Kurtz 1981). The class of roAp stars represent a subset of Ap stars and were discovered by Kurtz (1982). These stars show photometric variability on timescales between 5 and 20 minutes. They often shown a number of different pulsations within that range. In general, the pulsations are aligned with the magnetic axis of the star, which suggests an interplay between the magnetic field and the observed pulsations. Indeed, the modelling of the magnetic fields of roAp stars is important since they have been shown to strongly affect pulsations (e.g., Cunha 2007). It is also important to consider whether the pulsations have an effect on the magnetic field. Studies of the pulsations of HD24712 have been carried out by Kurtz et al. (2005) as part of the photometric study (Whole Earth Telescope campaign; WET). Measurements of the magnetic field taken at multiple time intervals by Kochukhov & Wade (2007) did not show any variability of the magnetic field consistent with the pulsations. For this reason and because I do not yet have the ability to consider pulsations within Sparti, I do not consider pulsations in my analysis.

For the purposes of this analysis I took the values of $T_{\rm eff}$ and $\log g$ to be 7250 ± 150K and 4.2 ± 0.1 (Ryabchikova et al. 1997 and Shulyak et al. 2009). These values

Table 7.1: The maximum and minimum values of the chemical abundance of sixteen elements over the surface of HD24712 from Lüftinger et al. (2010). The solar values are from Asplund et al. (2009)

Element	Min log(N/H)	Max log(N/H)	Solar log(N/H)
Mg	6.04	7.54	7.60
Ca	6.84	7.04	6.34
Sc	1.94	3.14	3.15
Ti	4.24	4.94	4.95
Cr	5.94	6.14	5.64
Fe	6.74	7.34	7.05
Co	5.64	6.24	4.99
Ni	4.44	5.74	6.22
Y	3.04	3.54	2.21
La	2.24	3.24	1.10
Ce	2.74	3.14	1.58
Pr	2.04	2.44	0.72
Pr	3.64	4.34	0.72
Nd	2.74	3.54	1.42
Nd	4.04	5.14	1.42
Gd	3.24	3.54	1.07
Tb	2.94	4.34	0.30
Dy	3.24	3.74	1.10

were calculated by detailed analysis of the spectra and the two references agree well. When I obtain a better fit to the Stokes $IQUV$ profiles with both the abundances and magnetic field it will be possible to further refine these value. The rotational period of the star is 12.45877(16) days as determined by Ryabchikova et al. (2005).

Modelling of the star has been carried out by a number of authors. The analysis completed by Bagnulo et al. (1995) of the circular polarisation and broadband linear polarisation gives magnetic field parameters

$$i = 137^\circ \pm 3^\circ,\ \beta = 150^\circ \pm 3^\circ,\ \theta = 4^\circ \pm 3^\circ \text{ and } B_\mathrm{d} = 3900\,G \pm 200\,G.$$

An analysis by Lüftinger et al. (2010) determined the surface abundance of sixteen elements and the results are shown in Table 7.1. Finally the latest results by Rusomarov et al. (2015), determined by modelling a time series of Stokes profiles, found the

Table 7.2: The date, time and rotational phase of each of the observations of HD24712 observed using HARPSPOL. Data from the ESO Science Archive Facility.

Julian Date	Gregorian Date	Observation Start Time (UT)	Rotational Phase
2455200.228	3rd January 2010	17:28	0.711
2455201.246	4th January 2010	17:54	0.793
2455202.176	5th January 2010	16:13	0.868
2455203.103	6th January 2010	14:28	0.942
2455204.178	7th January 2010	16:16	0.028
2455205.202	8th January 2010	16:50	0.110
2455206.177	9th January 2010	16:14	0.189
2455209.173	12th January 2010	16:09	0.429
2455210.190	13th January 2010	16:33	0.511
2455211.191	14th January 2010	16:35	0.591
2455212.191	15th January 2010	16:35	0.671
2455213.199	16th January 2010	16:46	0.752
2455607.071	14th February 2011	13:42	0.366

magnetic parameters

$$i = 120^\circ,\ \beta = 160^\circ \text{ and } B_\mathrm{d} = 3440\,G.$$

7.2.1 Observations

The data for HD24712 obtained with the HARPSpol instrument were taken from the ESO Science Archive Facility (202630 and 202633; Piskunov et al. 2011). The optical design of HARPSpol is described in Snik et al. (2008) and Snik et al. (2011). HARPSpol has a resolving power of 120 000 and so provides very detailed Stokes $IQUV$ spectra. The data consist of spectra obtained at 13 rotation phases. The Julian and Gregorian date of each observation is given in Table 7.2 along with the phase rotation of the star between 0.0 and 1.0 where the rotational phase is calculated using Eq. 4.12. Calculated starting from a zero phase at Julian date 2440577.23 which is consistent with the zero phase adopted by Kurtz & Marang (1987) and Mathys (1991).

7.2.2 Results

Using the Fe lines, 5217.39Å, 5383.37Åand 5410.91Å and the Nd lines 5677.17Å, 5802.53Å and 5851.54Å at 11 of the 13 phases observed, I have calculated the best fit parameters for the dipole, de-centered dipole and dipole + quadrupole magnetic field morphologies to the observed spectrum of HD24712. After approximately 30 consecutive modelling attempts using the dipole+quadrupole morphology with random starting parameters I found a number of models which were consistent with each other. Using these parameters as a guide I repeated the analysis once more for the dipole, de-centered dipole and dipole + quadrupole magnetic field morphology. Table 7.3 shows the best fit parameters for each of these morphologies. The difference between the observed and model Stokes $IQUV$ profiles are shown, for each of the magnetic field parameterisations, in Figs. 7.2, 7.3 & 7.4. The maps of the magnetic field strength over the entire stellar surface are shown in 7.5.

Table 7.3: The model parameters found during the analysis of HD24712, with SPARTI, for each of the magnetic morphologies. The uncertainty is calculated using Eq. 4.16. The final six rows of the table are the parameters used in the step function given in Section 4.8.1.1.

Parameter	Dipole	Decentered Dipole	Dipole + Quadrupole
$i(^\circ)$	145 ± 11	220 ± 30	145 ± 12
$\beta(^\circ)$	147 ± 2		148 ± 2
$\alpha_{\rm dipole}(^\circ)$		146 ± 6	
$\beta_{\rm dipole}(^\circ)$		76 ± 115	
$\gamma_{\rm dipole}(^\circ)$		356 ± 3	
y_2		0.05 ± 0.03	
y_3		0.06 ± 0.05	
$\beta_1(^\circ)$			15 ± 9
$\beta_2(^\circ)$			141 ± 7
$\gamma_1(^\circ)$			3196 ± 61
$\gamma_2(^\circ)$			2 ± 13
B_d (G)	3600 ± 100	2400 ± 200	4700 ± 250
B_q (G)			2500 ± 350
f_0		0.80 ± 0.05	0.77 ± 0.05
$v \sin i$ (km s^{-1})		-5.2 ± 0.2	5.7 ± 0.2
$\theta(^\circ)$	150 ± 5	76 ± 10	148 ± 4
Fe (A)	6.76 ± 0.04	6.52 ± 0.06	6.76 ± 0.03
Fe (B)	68 ± 85	53.5 ± 0.6	56.7 ± 0.3
Fe (C)	8.45 ± 0.01	8.1 ± 0.1	9.8 ± 0.2
Nd (A)	2 ± 151	4.4 ± 0.3	4.5 ± 0.9
Nd (B)	33 ± 32	49.7 ± 4.5	49 ± 54
Nd (C)	5.02 ± 0.53	6.6 ± 0.5	5 ± 5

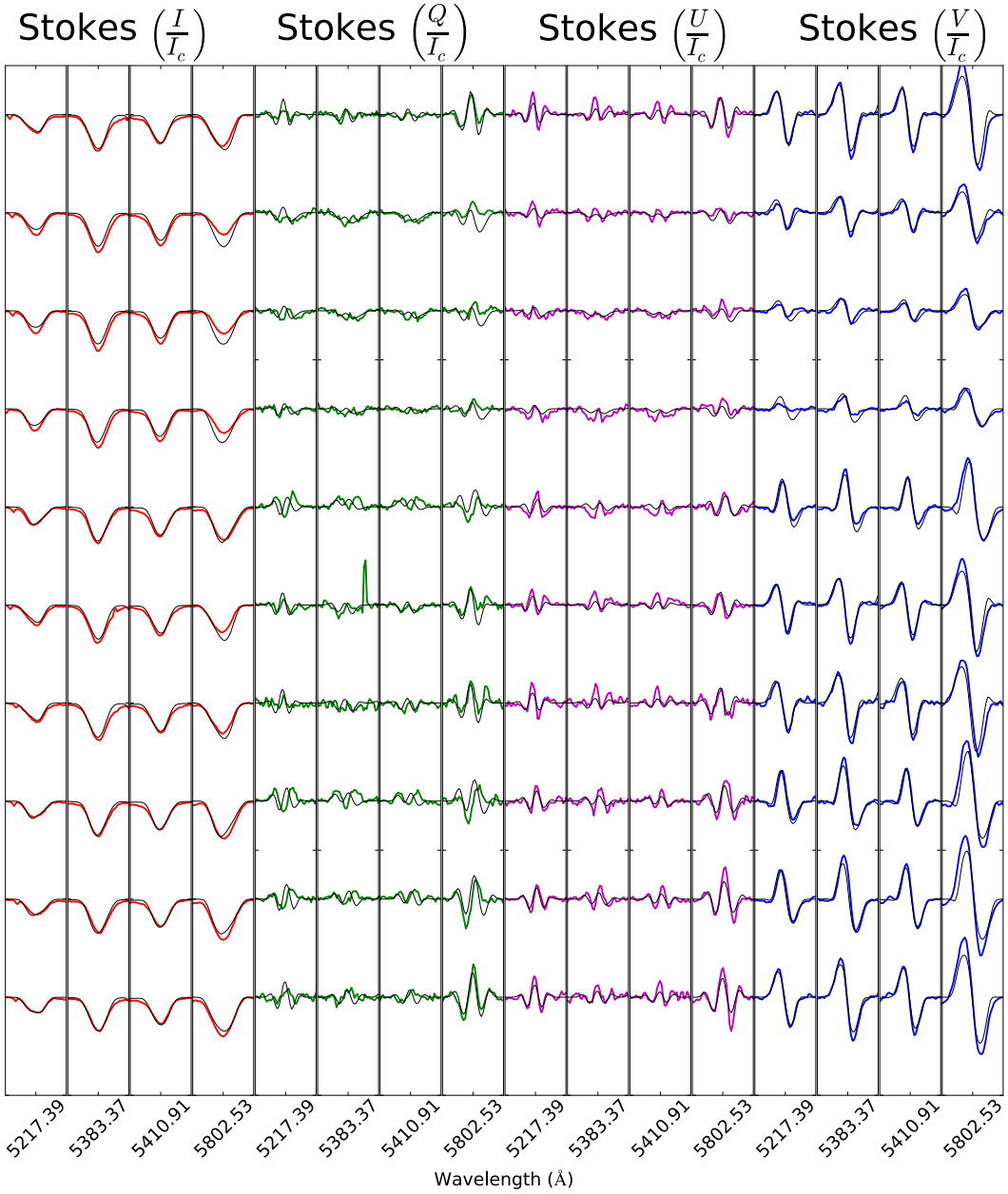

Figure 7.2: A comparison of the observed (solid red line) and synthetic (solid black line) spectra of the star HD24712. The synthetic spectra have been calculated using SPARTI with dipole field morphology and the fit parameters are give in Table 7.3. Three lines are shown at wavelengths, 5677.19 Å, 5802.53 Å and 5851.54 Å and for each Stokes profiles $IQUV$, each row of Stokes profiles corresponds to a rotational phase of the star

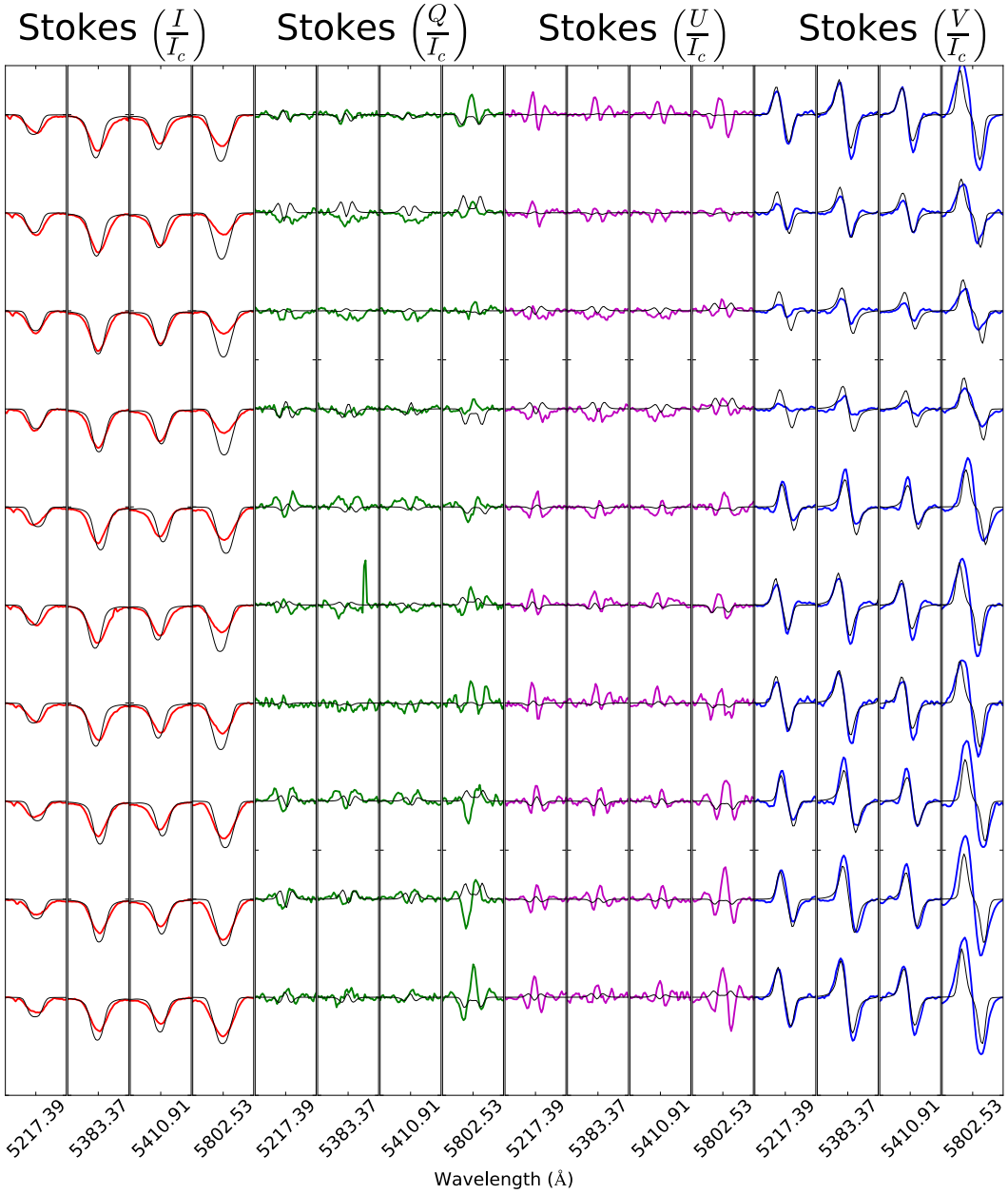

Figure 7.3: A comparison of the observed (solid red line) and synthetic (solid black line) spectra of the star HD24712. The synthetic spectra have been calculated using SPARTI with de-centered dipole field morphology and the fit parameters are give in Table 7.3. Three lines are shown at wavelengths, 5677.19 Å, 5802.53 Å and 5851.54 Å and for each Stokes profile $IQUV$, each row of Stokes profiles corresponds to a rotational phase of the star

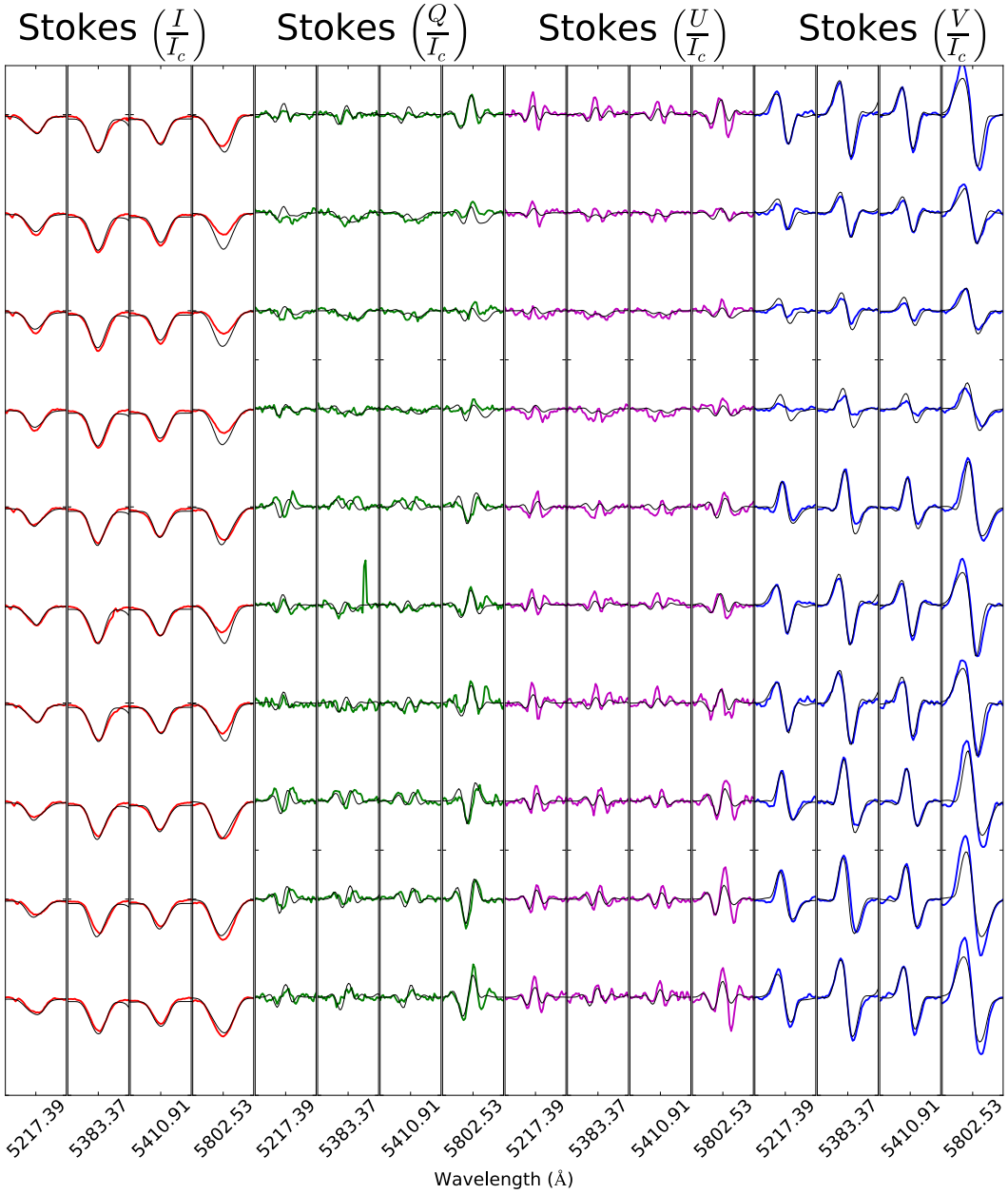

Figure 7.4: A comparison of the observed (solid red line) and synthetic (solid black line) spectra of the star HD24712. The synthetic spectra have been calculated using SPARTI with dipole + quadrupole field morphology and the fit parameters are give in Table 7.3. Three lines are shown at wavelengths, 5677.19 Å, 5802.53 Å and 5851.54 Å and for each Stokes profile $IQUV$, each row of Stokes profiles corresponds to a rotational phase of the star.

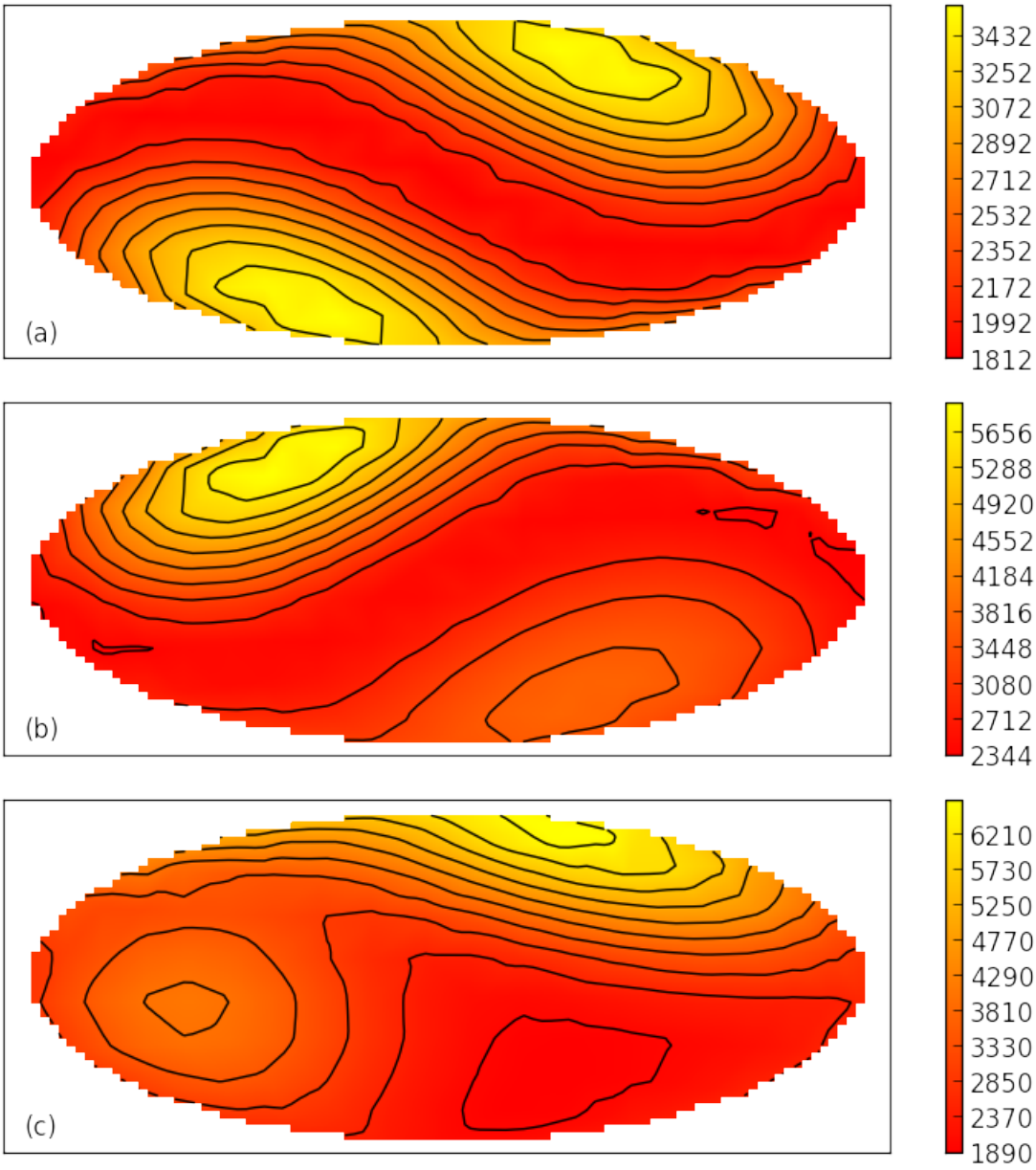

Figure 7.5: The field maps of HD24712 for each field morphology, dipole, de-centered dipole and dipole + quadrupole using the magnetic field parameters shown in Table 7.3. The vertical bars beside each surface plot show the magnetic field strength in gauss.

Table 7.4: The parameters associated with a dipole + quadrupole magnetic field morphology of βCrB as determined by Bagnulo et al. (2000).

Parameter	Bagnulo et al. (2000) Eq.22	Bagnulo et al. (2000) Eq. 23
$i(^\circ)$	168 ± 1	162 ± 1
$\beta(^\circ)$	88 ± 1	93 ± 1
$\beta_1(^\circ)$	12 ± 1	40 ± 2
$\beta_2(^\circ)$	79 ± 1	114 ± 2
$\gamma_1(^\circ)$	350 ± 5	143 ± 2
$\gamma_2(^\circ)$	331 ± 1	35 ± 1
B_d (G)	12165 ± 55	8810 ± 370
B_q (G)	14420 ± 70	15145 ± 90
f_0	5 ± 2	0 ± 2
$v \sin i$ (km s^{-1})	1.8 ± 0.2	2.8 ± 0.4
$\theta(^\circ)$	124 ± 2	35 ± 2

7.2.3 Discussion

The model generated using a dipole and using a dipole + quadrupole morphology fit well to the observed data. The quality of the fits are comparable to those achieved by Rusomarov et al. (2015) which shows that I am able to achieve results comparable to those which are considered "state of the art". The dipole + quadrupole fits better than the dipole model showing that this star potentially has a slightly more complex structure than previously found. It can be seen that the Nd line does not fit well. I have attempted to model this using an abundance spot as was used by Lüftinger et al. (2010). However, I found this unable to fit the variability in phases of both the Nd line Stokes I and Stokes V profiles.

7.3 βCrB

The second star I have analysed using Sparti is βCrB. This star has an extremely complex spectrum which varies remarkably with rotational phase as shown in Fig. 7.9.

The ability to model this star would present a major step forward for our understanding of this star, but also it would show that SPARTI is capable of modelling stars with complex magnetic fields and strongly non-solar photospheric abundances.

The star βCrB is a binary star system with a bright star currently classified as A9SrEuCr and a dimmer F2V type companion. Bagnulo et al. (2000) closely examined the spectra of βCrB and found no evidence of the F2V component which is 1.7mag fainter in the V filter (Tokovinin 1985). As a result from here on in, when I refer to βCrB I am only considering the bright A9SrEuCr component of the binary star system.

For the purposes of this analysis I took the values of $T_{\rm eff}$ and $\log g$ from the literature, as 7800 K and 4.25 (Bagnulo et al. 2001b) respectively. These values are based on the measurements by Hauck & North (1982), Hauck & North (1993), Adelman (1985) and Faraggiana & Gerbaldi (1993). When I obtain a better fit to the Stokes $IQUV$ profiles with both the abundances and magnetic field, it will be possible to further refine these values.

Studies by Hatzes & Mkrtichian (2004) and Kochukhov et al. (2002) show evidence of pulsations, each finding different periods. These observed pulsations point to βCrB being a roAp star, however re-analysis by Kurtz & Leone (2006) found no evidence for of any pulsations.

The magnetic field of βCrB has been well studied because it is very bright (visual magnitude 3.68). A number of mean longitudinal field measurements are given in Mathys (1991) and mean field modulus measurements are given in Mathys et al. (1997). Bychkov, Bychkova & Madej (2005) presents a catalogue of measurements of the effective magnetic field strength as a function of phase showing a periodic sinusoidal variation. The measurements presented in Bychkov, Bychkova & Madej (2005) are taken from Borra & Vaughan (1977), Borra & Landstreet (1980), Vogt, Tull & Kelton (1980), Borra, Fletcher & Poeckert (1981) and Wade et al. (2000a).

Previous modelling of βCrB by Bagnulo et al. (2000) has yielded two sets of parameters describing the dipole+quadrupole morphology of the magnetic field. These parameters are shown in Table 7.4. Bagnulo et al. (2001b) took the results from Bagnulo et al. (2000) and used as inputs to COSSAM, they found it necessary to use

a vertical stratification to be able to simultaneously model the weak and strong lines. However, they were unable to fit the Fe II lines 4923.927Å and 5018.440Å Bagnulo et al. (2001b) were unable to determine which model was better since both contained differences between the observed and synthetic spectra of comparable magnitude. This thesis represents the first attempt to model the vertical stratification and magnetic field of βCrB simultaneously based on the inversion of a time series of Stokes $IQUV$ profiles.

7.3.1 Observations

The data I have used in this section comes in part from observations I carried out using the Catania Astrophysical Observatory Spectropolarimeter (CAOS; Leone et al. 2016) and the remainder is from archival data observed using the same instrument.

7.3.1.1 Serra La Nave Observatory

To obtain data of βCrB, I observed using the 91cm telescope at Serra La Nave (SLN) observatory located in Catania, Italy, on the southern side of Mt Etna at an altitude of 1725m. The telescope has a small aperture but is ideal for the monitoring bright stars. βCrB has an apparent magnitude of 3.68 in the V band so it was possible to achieve high signal-to-noise spectra.

Using CAOS it is possible to obtain high resolution Stokes $IQUV$ spectra with dense phase coverage of a large number of bright magnetic stars. The spectrograph has an echelle grating with a spectral range of 3000 Å to 10000 Å, with optimal performance between 3880 Å and 7250 Å. It is bench-mounted in a sealed room and the CCD is kept at a temperature of $-135°$C. The spectrograph is fiber-fed by two optical fibers which are optimised for UV transmission. These fibers have an aperture of 3" which compares to a general seeing of ~ 2 at the Serra La Nave Observatory.

The retarder wave plates used as part of CAOS are achromatic, this is because low- and zero-order ones were not suitable (Leone 2003) and the super-achromatic

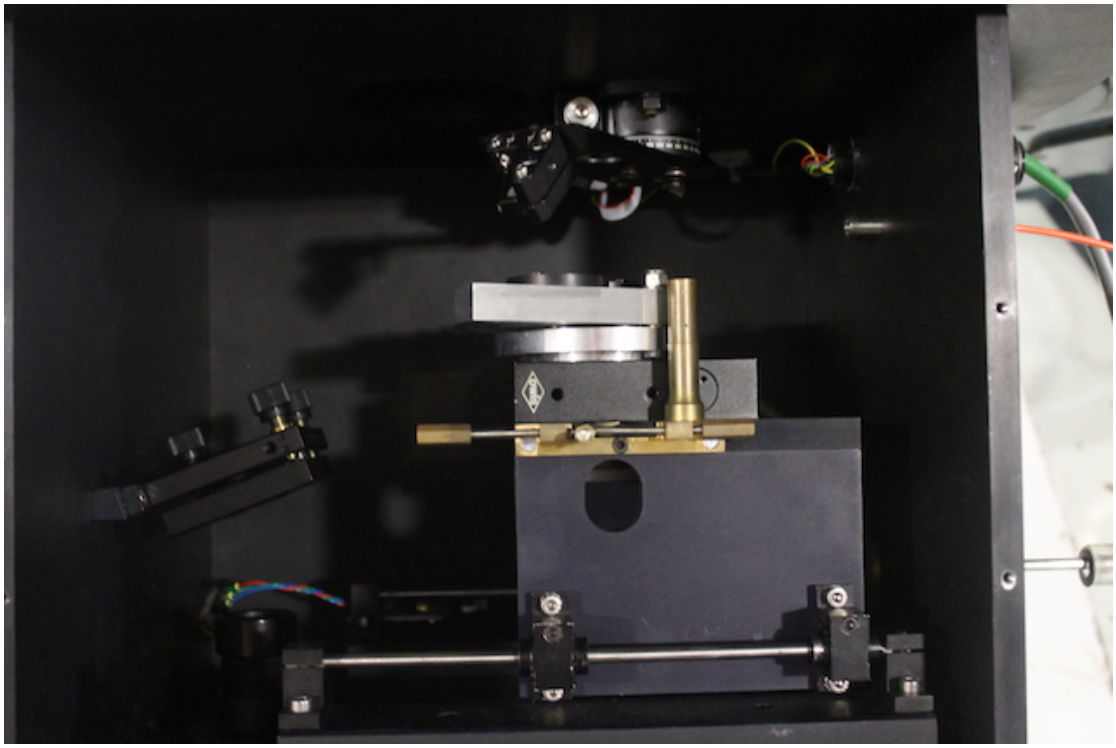

Figure 7.6: The polarimeter used as part of CAOS (Catania Astrophysical Observatory Spectrograph) attached to the 91cm telescope at Serra La Nave Observatory. This is an image I photographed during my first observing run at the Serra La Nave observatory.

Figure 7.7: An observational challenge when observing using the Serra La Nave telescope. This is an image I photographed on the 16th June 2014 during my first observing run at the Serra La Nave observatory, it is an active eruption of Mount Etna's Southern crater.

retarders have been shown to be a source of ripples at resolving powers as low as 35000 (Donati et al. 1999)

The calibration and reliability of the Stokes profiles observed using CAOS has been tested using the observations of βCrB at multiple phases. The results of this are shown in Fig. 7.8, which provides a comparison between the spectra of βCrB observed with CAOS, ESPaDOnS (an Echelle SpectroPolarimetric Device for the Observation of Stars) at the Canada France Hawaii Telescope (CFHT) and MuSiCoS at the Télescope Bernard Lyot at Pic du Midi. Both ESPaDOnS and CAOS have similar resolving powers of 60000 and 55000 ± 5500 respectively so a direct comparison is possible. The resolving power of MuSiCoS is lower at 35000 however it is still possible to compare the shape of the profiles. Fig. 7.8 shows very good agreement between the profiles of all three instruments. This shows that it is likely that CAOS is reliable and calibrated in the same way as ESPaDOnS and MuSiCoS.

7.3.1.2 Data

The data consists of Stokes profiles at 22 different phases calculated starting from a zero phase at Julian date 2434204.70, which is consistent with Wade et al. (2000a). The Julian and Gregorian date of each observation is given in Table 7.5 along with the phase rotation of the star between 0.0 and 1.0 where the rotational phase is calculated using Eq. 4.12 and the observations for which I was the observer.

7.3.2 Results

Using the Fe lines, 4918.99Å, 4923.92Å, 5018.44Å, 5129.15Å and 5133.69Å at 20 of the 22 rotational phases I have calculated the best fit parameters for the observed spectrum of βCrB dipole + quadrupole magnetic field morphologies shown in Table 7.4. The difference between the observed and model Stokes $IQUV$ profiles are shown, for each of the magnetic field parameterisations, in Fig 7.9. The map of the magnetic field strength over the entire stellar surface is shown in Fig. 7.10.

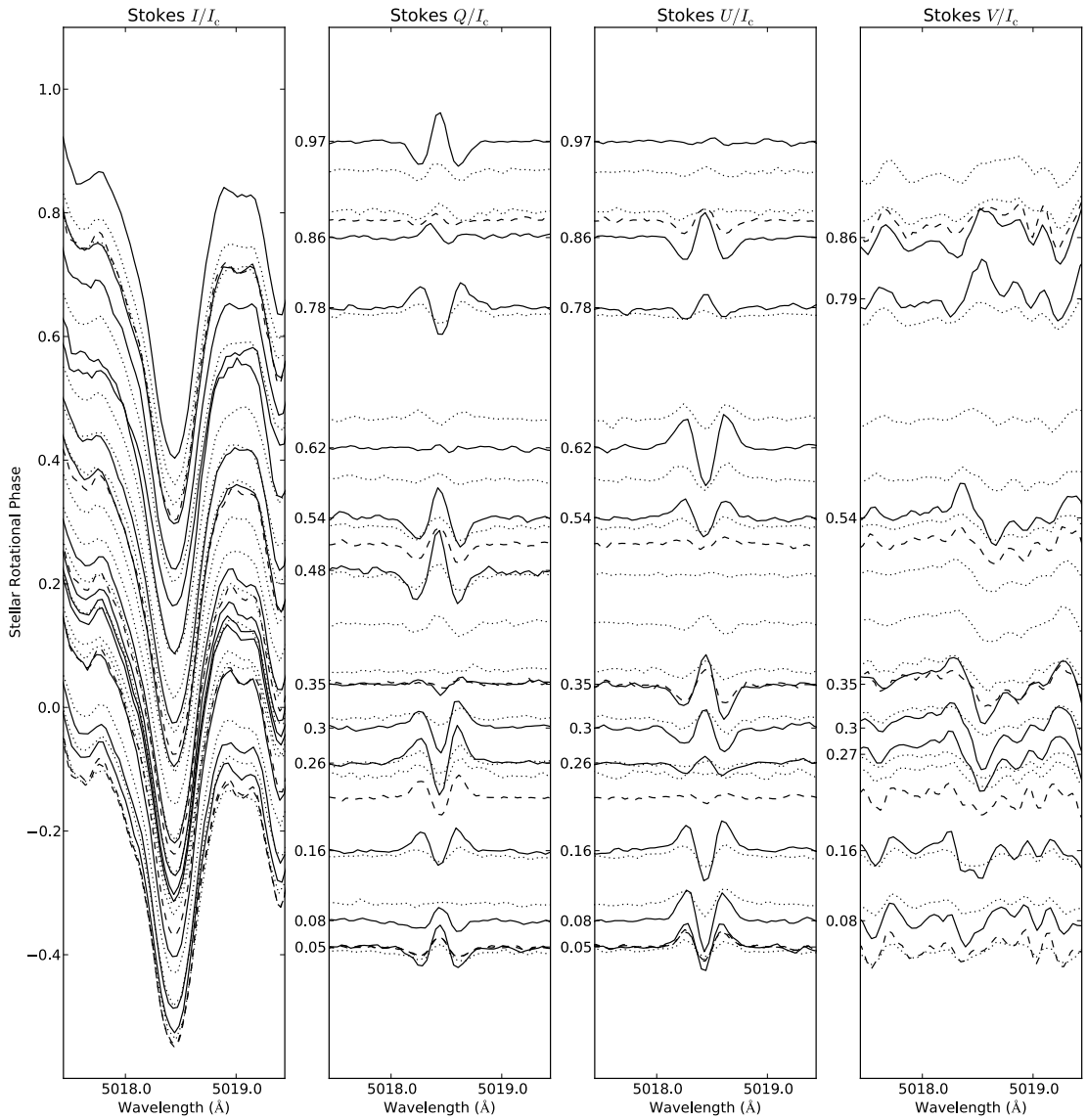

Figure 7.8: Observations of βCrb taken at different rotational phases by ESPaDOnS (dashed line), MuSiCoS (dotted line) and CAOS (solid line). Where the rotational phase between 0.0 and 1.0 equates to one full revolution of the star about it's rotation axis. The four boxes correspond to each of the Stokes parameters $IQUV$ normalised to the continuum (I_c)

Table 7.5: The date, time and rotational phase of each of the observations of βCrb observed using CAOS, the final column indicates whether I was the observer (Y) or not (N).

Julian Date	Gregorian Date	Observation Start Time (UT)	Rotational Phase	A. Martin Observed
2456778.539	1st May 2014	00:56	0.079	N
2456787.528	10th May 2014	00:40	0.565	N
2456788.585	11th May 2014	02:02	0.622	N
2456799.498	21st May 2014	23:57	0.212	N
2456807.530	30th May 2014	00:43	0.647	N
2456809.475	31st May 2014	23:24	0.752	N
2456815.500	7th June 2014	00:00	0.078	N
2456816.488	7th June 2014	23:42	0.132	N
2456820.499	11th June 2014	23:58	0.348	N
2456822.404	13th June 2014	21:41	0.452	Y
2456826.379	17th June 2014	21:05	0.667	Y
2456830.510	22nd June 2014	00:14	0.890	Y
2456831.394	22nd June 2014	21:27	0.938	Y
2456833.449	24th June 2014	22:46	0.049	Y
2456835.379	26th June 2014	21:05	0.153	Y
2456836.378	27th June 2014	21:04	0.207	Y
2456848.380	9th July 2014	21:07	0.857	N
2457129.589	17th April 2014	02:08	0.068	N
2457189.426	15th June 2015	22:13	0.305	Y
2457190.380	16th June 2015	21:07	0.356	Y
2457191.376	17th June 2015	21:01	0.410	Y
2457193.398	19th June 2015	21:33	0.520	Y

Table 7.6: The model parameters found during the analysis of βCrB, with SPARTI, for the dipole+quadrupole morphology. The uncertainty is calculated using Eq. 4.16. The final nine rows of the table are the parameters used in the step function given in Section 4.8.1.1.

Parameter	Dipole + Quadrupole	
$i(^\circ)$	24 $\pm$	7
$\beta(^\circ)$	102 $\pm$	7
$\beta_1(^\circ)$	56 $\pm$	6
$\beta_2(^\circ)$	34 $\pm$	6
$\gamma_1(^\circ)$	232 $\pm$	14
$\gamma_2(^\circ)$	114 $\pm$	14
$B_d(G)$	8100 $\pm$	2200
$B_q(G)$	18700 $\pm$	1300
f_0	0.14 $\pm$	0.04
$v \sin i$ (km s^{-1})	3.7 $\pm$	1.0
$\theta(^\circ)$	20 $\pm$	5
Fe II (A)	7.5 $\pm$	0.3
Fe II (B)	44 $\pm$	9
Fe II (C)	8.1 $\pm$	0.4
Gd (A)	3.9 $\pm$	0.11
Gd (B)	65.03 $\pm$	0.01
Gd (C)	4.34 $\pm$	0.01
Dy (A)	5.5 $\pm$	1.8
Dy (B)	7.00 $\pm$	0.01
Dy (C)	3.5 $\pm$	2.7

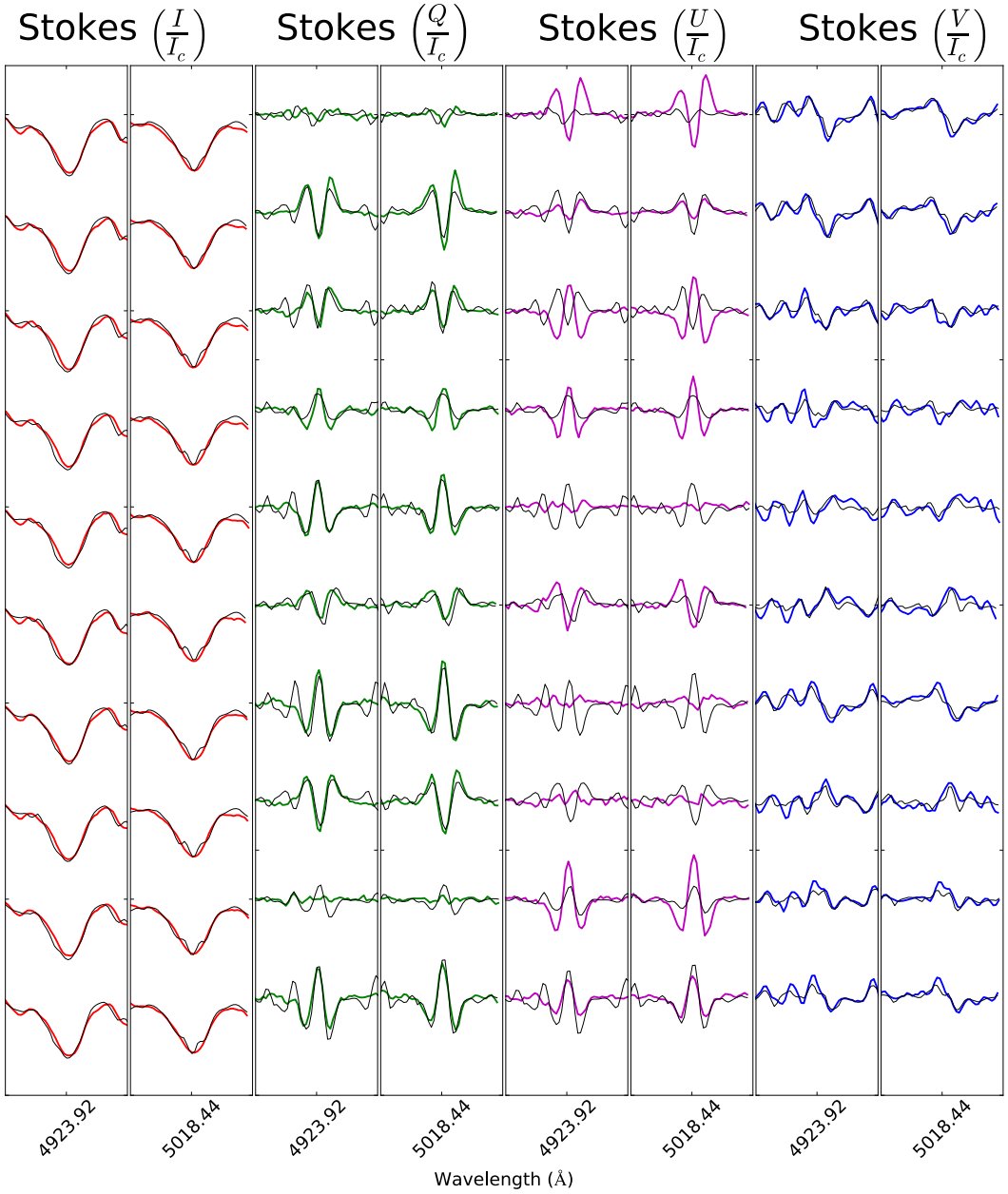

Figure 7.9: A comparison of the observed (solid red line) and synthetic (solid black line) spectra of the star βCrB. The synthetic spectra have been calculated using SPARTI with dipole + quadrupole field morphology and the fit parameters are give in Table 7.4. Three lines are shown at wavelengths, 4923.92 Å, 5018.44 Å and 5129.15 Å and for each Stokes profile $IQUV$, each row of Stokes profiles corresponds to a rotational phase of the star

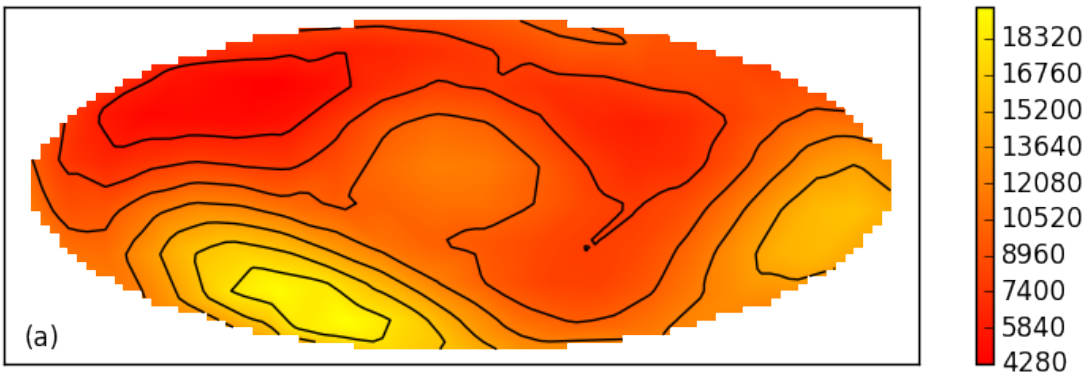

Figure 7.10: The field maps of βCrB for each field morphology, dipole, de-centered dipole and dipole + quadrupole using the magnetic field parameters shown in Table 7.6. The vertical bar beside the surface plot shows the magnetic field strength in gauss.

7.3.3 Discussion

The complex nature of βCrB means it was not possible for me to fit the star with a dipolar field. However, after numerous modelling attempts using the dipole+quadrupole morphology, it was possible to produce a model which provides a reasonable fit to the Stokes $IQUV$ profiles of βCrB. Previous modelling of the magnetic fields in Ap stars, has been limited to stars for which the rotational axis is perpendicular to the observers line of sight. However, we observe βCrB pole on, which, in a star with minimal Stokes QU, would present problems. However, due to the complex nature of the field I observe in βCrB, there is a remarkably strong QU, which allowed me to complete a detailed modelling. The model synthetic Stokes I profiles shown in Fig. 7.9 fit the width of the observed profiles unlike the profiles presented in Bagnulo et al. (2001b). The fits to Stokes Q and V are also good, however Stokes U does not fit well at all, in addition the Stokes I profile of the 5018.44Å line shows a strange shape in the core. In both cases this may be the result of the dipole+quadrupole morphology not being a realistic model for this star. This explains the shape of the Stokes I core because Sparti is trying to fit the abundances and magnetic morphology simultaneously. If the magnetic morphology does not have the necessary degrees of freedom to allow Sparti to model the Stokes profiles, then it will try and compensate by adjusting the other parameters, including the abundances, leading to the model core shape.

My analysis of βCrB is the first Zeeman Doppler mapping (ZDM) of a time series Stokes $IQUV$ for this star. Previously, using *longitudinal field*, *mean field modulus* and *broadband linear polarization* measurements, it was determined that this star likely had a dipole + quadrupole magnetic field (Bagnulo et al. 2001b). My results confirm this conclusion and show that even with the addition of vertical stratification and horizontal inhomogeneities of elements, it is still not possible to model this star using a magnetic field of dipole morphology.

Current theory shows that a fossil field origin is the most likely origin for magnetic fields in Ap stars (e.g., Donati & Landstreet 2009). As a result, theoretically, the magnetic fields in Ap stars should have a large scale simple magnetic geometry

stable over time. The magnetic field of HD 24712 appears to be essentially dipolar, however, the field of βCrB has a far more complex field. A potential explanation for this difference could be the age of the stars. However, both stars are of similar age (βCrB [$\log t = 8.95 \pm 0.02$ year] and HD24712 [$\log t = 9.07 \pm 0.10$ year]; Kochukhov & Bagnulo 2006) and so the difference in complexity is not likely to be an age effect. Since the analysis of Ap stars using ZDM of a time series of full Stokes profiles is still in its infancy, it is important to analyse a large sample of such stars to determine whether βCrB is exceptionally complicated or whether there is a wide range of observed complexity. Either result would provide strong constraints to the theory of how dynamo fields transition into fossil fields.

The results of the abundance analysis are inconclusive without a more complex stratification pattern. However, it appears the the abundance of Fe in the lower layers of the atmosphere is higher in βCrB than HD24712. This is consistent with the findings of Bailey, Landstreet & Bagnulo (2014), who found a positive trend between Fe abundance and magnetic field strength. On the other hand, for the upper layers of the atmosphere, the Fe abundance appears to be higher in HD24712 than βCrB which is inconsistent with Bailey, Landstreet & Bagnulo (2014). As a result, to be able to draw accurate conclusions about abundance patterns in Ap stars it is necessary to consider not just the average abundance but also the vertical and horizontal stratification of the chemical elements in the stellar atmosphere.

7.4 Summary of Results

In this chapter I have presented my analysis of the stars HD24712 and βCrB. I have described the instruments used to observe and the data reduction techniques used to obtain the Stokes $IQUV$ profiles. My analysis of HD24712 shows good agreement between the model I calculate and the results from Rusomarov et al. (2015). My analysis of βCrB has shown that the star may have a field with a structure that is

more complicated than a dipole+quadrupole. The model calculated using SPARTI fits the profiles better than previous studies, but is not able to correctly model the Stokes U signal. This analysis, in combination with previous works, shows that Ap stars do not only have simple dipole fields but also have more complicated fields. This has an impact on theories which relate to the transition from a magnetic field with a dynamo origin to a magnetic field with a fossil field origin. I have shown that when analysing the abundance patterns of Ap stars, it is important to consider the stratification of abundances not just the average abundance. In addition, I have shown that SPARTI gives the capability to efficiently analyse the magnetic fields of a large number of stars.

8 Conclusions and Future Work

This thesis presents the development of two spectral inversion codes: SPARTI SIMPLE, which models the intensity spectra of non-magnetic stars and SPARTI, which models the Stokes $IQUV$ profiles of magnetic stars. For spectral synthesis they use modified versions of the radiative transfer codes COSSAM SIMPLE and COSSAM respectively[1].

The inversion codes are based on the Levenberg-Marquardt algorithm (LMA) developed by Levenberg (1944) and Marquardt (1963), and include a number of routines to account for: radial velocity shifts, instrument resolving power, rejection of spectral lines to be fit (e.g. to avoid spectral lines formed in non-local thermodynamic equilibrium). Most importantly, SPARTI SIMPLE and SPARTI account for the stratification of chemical elements in the stellar photosphere, surface abundance spots and the presence of a magnetic field. The latter can be parameterised in different forms, namely a de-centered dipole (Stift 1975) and dipole + quadrupole (Landolfi, Bagnulo & Landi Degl'Innocenti 1998).

Both codes were thoroughly tested using numerical simulations which accounted for synthetic photon-noise, instrument resolution and crosstalk between different Stokes parameters. The level to which instrumental effects can be tolerated was tested, with the conclusion that, a resolving power of 60000 and a signal-to-noise ratio of 200 were typically sufficient to recover the model parameters. Further to this, the code was tested through the analysis of stars that are well studied in the literature. Using spectra of the Sun, HD32115 and 21 Peg, SPARTI SIMPLE was tested to confirm that the fundamental parameters and chemical abundances calculated for each star match previous results by Asplund et al. (2009), Fossati et al. (2011b) and Fossati et al. (2009) respectively. SPARTI was applied to the analysis of the magnetic stars HD24712 and β Coronae Borealis (βCrB). The aim for this analysis was to determine whether SPARTI is able to model an observed spectrum, and also to test whether the recovered

[1]Both COSSAM SIMPLE and COSSAM are written by M.J. Stift (**http://www.ada2012.eu/cossam_multi/index.html**).

magnetic configurations are unique or whether it finds a number of solutions. After approximately 30 runs of Sparti, starting from random initial parameters, the results found for HD24712, at convergence, were all consistent. The modelling of HD24712 returned values close to those previously found in the literature. The fit to the observed spectrum is as good as previously published results, however the current spot model was unable to fit the variable depth of the Nd lines. The star HD137909 shows evidence of a stronger and more complicated magnetic field with complex abundance distributions. The model Stokes $IQUV$ profiles calculated by Sparti were able to fit the the width of the spectral lines in Stokes I unlike the model by Bagnulo et al. (2001b). The fits to the Stokes Q and V profiles were also good, however the fit to Stokes U was not. This may be the result of the star having a field with more complexity than a dipole + quadrupole morphology. As a result of this finding, it is clear that the analysis of a large sample of such stars is necessary to determine whether βCrB is uncommonly complex or whether Ap stars exhibit a wide range of observed complexity. Either result would provide strong constraints to the theory of how dynamo fields transition into fossil fields. Furthermore, the analysis of abundance patterns in Ap stars requires the consideration of stratification of elements in the stellar atmosphere not just the average abundance.

Sparti Simple was used for the analysis of the young open cluster NGC 6250. This study is part of a large collaborative effort to investigate the correlation between the structure of the stellar photosphere and stellar age. Previous analysis of clusters as part of this collaboration include the work by Kılıçoğlu et al. (2016) (NGC6405) and by Fossati et al. (2007), Fossati et al. (2008a), Fossati et al. (2010), and Fossati et al. (2011a) (Praesape cluster and NGC 5460). In the course of the study of NGC 6250 an in-depth cluster membership analysis was completed, using the proper motions, radial velocity and $BVJHK$ photometry (where available) for each of the observed stars. As a result of this analysis 19 stars were found to be cluster members and new values for the cluster mean proper motions, mean radial velocity, distance, age and reddening parameters were provided. After completing the cluster membership analysis, the spectra of the member stars were normalised and their fundamental parameters were

determined. Then, the chemical abundances of the elements in the photospheres of each of the member stars were calculated. The abundances obtained show that the cluster has a metallicity of $Z_{\rm cluster} = 0.018 \pm 0.005$ which is very close to solar. A spectroscopic H-R diagram was constructed to determine masses and radii and it was concluded that there was no evidence of statistically significant trends between the stellar fundamental parameters and any of the chemical abundances contrary to what was found by Fossati et al. (2011a). There is, however, the hint of an increase in mean Ba abundance with cluster age but more clusters should be analysed to confirm this trend.

During the course of my thesis I have obtained and reduced a number of spectropolarimetric observations, using ISIS at the William Herschel Telescope and CAOS at the Serra La Nave Telescope. The data obtained with CAOS of βCrB is used in this thesis. The results from observations using ISIS are not strictly related to this thesis but some are presented in the papers, for which I was a co-author, by Landstreet et al. (2015) (*A novel and sensitive method for measuring very weak magnetic fields of DA white dwarfs*) and by Landstreet et al. (2016) (*Discovery of an extremely weak magnetic field in the white dwarf LTT 16093 = WD2047+372*). The remaining results including observations of the interstellar medium, solar system objects and more white dwarfs will be presented in further papers which are in preparation. In addition to observing the data, I reduced and in some cases calculated the magnetic field strength.

In summary, this thesis provides the tools necessary to efficiently perform the chemical abundance analysis of main sequence stars, and to model the Stokes $IQUV$ spectra of magnetic main sequence stars. This will make it possible to add a large amount of data to constrain atomic diffusion theory in stellar photospheres and for the testing of the uniqueness and robustness of previous Zeeman/Magnetic Doppler Imaging/Mapping (Z/MDI/M) results.

8.1 Future Work

The work presented in this thesis continues the study of the evolution of chemical elements in the atmospheres of non-magnetic main-sequence F-, A- and B-type stars but also presents the tools to study the evolution of chemical elements in the atmospheres of magnetic main-sequence F-, A- and B-type stars. Furthermore with the inclusion of molecular abundances and physics into COSSAM, it will be possible to model the magnetic fields of stars earlier than F-type using SPARTI.

The work on NGC 6250 is not the only contribution that I have made to the analysis of open cluster stars. A second open cluster NGC 6633 is being analysed with SPARTI SIMPLE by Cesare Scalia (University of Catania). Cesare Scalia and I have already established membership, determined the fundamental parameters and performed a preliminary abundance analysis. This cluster is an order of magnitude older than NGC 6250 and so already allows us to directly compare two sets of data obtained with the same methods. We took advantage of the efficiency of SPARTI SIMPLE and decided to analyse not only the member stars but also the non-member stars of both NGC 6633 and NGC 6250, this allows us to determine whether any trends seen in the member stars are unique to that cluster or are also seen in the field stars. It is anticipated that a paper presenting this work will be published by early Autumn 2016. After the completion of the study of NGC 6633 the results of all of the analysed clusters will be combined, to investigate whether there is evidence for correlation between the abundance of the chemical elements in the photospheres of stars and their age.

Further development of SPARTI SIMPLE is necessary to add $T_{\rm eff}$ and $\log g$ of each analysed star as free parameters in the Levenberg-Marquardt algorithm, which would make the analysis of numerous stars very efficient. This is not as simple as including $T_{\rm eff}$ and $\log g$ in the array of free parameters in SPARTI SIMPLE. A number of steps are performed prior to it being possible to run COSSAM SIMPLE, these include extracting data from a model atmosphere at a certain $T_{\rm eff}$ and $\log g$ to determine various line properties. This is not in itself a problem since, this can and in fact is already part of SPARTI SIMPLE to allow it to calculate $v_{\rm mic}$ which is handled prior to COSSAM

Simple. The major challenge is that of memory allocation. Using Sparti Simple it is quite normal to model synthetic spectra covering a range >1000Å, this involves keeping a very large amount of line information in memory for access. Currently, however, to prevent overflow errors, allocation of memory is handled at the initiation of a Sparti Simple run and cannot be changed throughout. The amount of memory assigned and the size of various arrays in Cossam Simple are determined by the number of lines that are in the spectra of a star which has a particular $T_{\rm eff}$ and $\log g$, however this can vary significantly when the $T_{\rm eff}$ and $\log g$ are changed. This means if the code begins from a certain $T_{\rm eff}$ and $\log g$ and then, in the process of finding the best solution, it changes these values, the number of lines will also change which would lead to a memory error. Considerations must also be given to the reliability and uniqueness of the results calculated using this new code, since by adding $T_{\rm eff}$ and $\log g$, Sparti Simple suddenly has a much greater degree of freedom than previously and so it is important to thoroughly test results using both numerical simulations and observed spectra. Once accomplished however this would represent a large upgrade to Sparti Simple, given an observed spectrum and only very rough estimates of the stellar fundamental parameters it would be possible to efficiently and accurately model a non-magnetic star.

The inclusion of $T_{\rm eff}$ and $\log g$ as free parameters in Sparti Simple coupled with the extraordinary increase in data resulting from missions such as GAIA, means that the analysis of the abundance evolution of elements in stellar photospheres will not be limited to members of open clusters. GAIA will allow us to calculate the distance, photometry and age of stars to an unprecedented accuracy. This means it will be possible to include field stars into the study of chemical abundance evolution in stellar photospheres. Large amounts of data is available in the archive for example that of UVESPOP (Bagnulo et al. 2003) which includes the high resolution high signal-to-noise spectra of over 300 stars covering a spectral range of 3040Å–10400Å. Sparti Simple is ideally suited to performing chemical abundance analysis of a large number of stars efficiently and so would make it possible to make good use of this dataset.

Further development of Sparti is also imperative, the first step is to include

the possibility of a multipolar magnetic morphology. This would enable more realistic modelling of stars with complex magnetic morphologies. Depending on the access to large computer facilities, it would also be possible to parallelise not only individual wavelength ranges, but also each model parameter. Since I currently run the code on a 60-thread machine, it would not be unreasonable to require a computer with several hundred cores. This would vastly reduce the execution time of Sparti, however once again this would be challenging because of the large number of code structures which would need to be moved. Currently, however, it is already possible to analyse magnetic stars and so, in parallel with code development it will be possible to include magnetic stars into the study of open clusters to investigate how magnetic fields and photospheric chemical abundances evolve over the main sequence lifetime of stars.

Finally as a result of observing at the William Herschel Telescope using the ISIS instrument, I have created a new data reduction pipeline (Isispipe) for spectropolarimetric data. This code will be the first published pipeline dedicated to the reduction of spectropolarimetric data for this instrument, and is efficient and well tested. I have a paper in preparation to publish this code along with a characterisation of the instrument.

Previously questions have been raised about the uniqueness and reliability of the results obtained by Zeeman/Magnetic Doppler Imaging/Mapping, but also how best to constrain diffusion theory (Michaud 1970) using the results found by observation. For an interesting discussion on the topic see Stift, Leone & Cowley (2012) and the response by Kochukhov, Wade & Shulyak (2012). By applying Sparti Simple and Sparti to a large sample of stars, with well defined ages, we should be able to answer these questions.

Bibliography

Abramowitz M., Stegun I., 1965, Handbook of Mathematical Functions, Dover Publications

Adelman S. J., 1985, PASP, 97, 970

Alecian G., Stift M. J., 2004, A&A, 416, 703

Alecian G., Stift M. J., 2007, A&A, 475, 659

Alecian E., Wade G. A., Catala C., Folsom C., Grunhut J., Donati J.-F., Petit P., Bagnulo S., Boehm T., Bouret J.-C., Landstreet J. D., 2007, in Bouvier J., Chalabaev A., Charbonnel C., eds, SF2A-2007: Proceedings of the Annual meeting of the French Society of Astronomy and Astrophysics, p. 431

Alecian E., Wade G. A., Catala C., Grunhut J. H., Landstreet J. D., Bagnulo S., Böhm T., Folsom C. P., Marsden S., Waite I., 2013, MNRAS, 429, 1001

Asplund M., Grevesse N., Sauval A. J., Scott P., 2009, ARA&A, 47, 481

Aster R., Borchers B., Thurber C., 2013, *Academic Press*, Parameter Estimation and Inverse Problems, Academic Press

Auer L. H., Heasley J. N., House L. L., 1977, ApJ, 216, 531

Aurière M., Wade G. A., Silvester J., Lignières F., Bagnulo S., Bale K., Dintrans B., Donati J. F., Folsom C. P., Gruberbauer M., Hui Bon Hoa A., Jeffers S., Johnson N., Landstreet J. D., Lèbre A., Lueftinger T., Marsden S., Mouillet D., Naseri S., Paletou F., Petit P., Power J., Rincon F., Strasser S., Toqué N., 2007, A&A, 475, 1053

Aurière M., Konstantinova-Antova R., Petit P., Charbonnel C., Dintrans B., Lignières F., Roudier T., Alecian E., Donati J. F., Landstreet J. D., Wade G. A., 2008, A&A, 491, 499

Aurière M., Wade G. A., Konstantinova-Antova R., Charbonnel C., Catala C., Weiss W. W., Roudier T., Petit P., Donati J.-F., Alecian E., Cabanac R., van Eck S., Folsom C. P., Power J., 2009, A&A, 504, 231

Aurière M., Wade G. A., Lignières F., Hui-Bon-Hoa A., Landstreet J. D., Iliev I. K., Donati J.-F., Petit P., Roudier T., Théado S., 2010, A&A, 523, A40

Aznar Cuadrado R., Jordan S., Napiwotzki R., Schmid H. M., Solanki S. K., Mathys G., 2004, A&A, 423, 1081

Babcock H. W., 1947, ApJ, 105, 105

Babcock H. W., 1958, ApJS, 3, 141

Babcock H. W., 1960, ApJ, 132, 521

Bagnulo S., Landi Degl'Innocenti E., Landolfi M., Leroy J. L., 1995, A&A, 295, 459

Bagnulo S., Landolfi M., Mathys G., Landi Degl'Innocenti M., 2000, A&A, 358, 929

Bagnulo S., Szeifert T., Wade G. A., Landstreet J. D., Mathys G., 2001a, The Messenger, 104, 32

Bagnulo S., Wade G. A., Donati J.-F., Landstreet J. D., Leone F., Monin D. N., Stift M. J., 2001b, A&A, 369, 889

Bagnulo S., Landi Degl'Innocenti M., Landolfi M., Mathys G., 2002, A&A, 394, 1023

Bagnulo S., Jehin E., Ledoux C., Cabanac R., Melo C., Gilmozzi R., ESO Paranal Science Operations Team, 2003, The Messenger, 114, 10

Bagnulo S., Landolfi M., Landstreet J. D., Landi Degl'Innocenti E., Fossati L., Sterzik M., 2009, PASP, 121, 993

Bagnulo S., Landstreet J. D., Fossati L., Kochukhov O., 2012, A&A, 538, A129

Bagnulo S., Fossati L., Kochukhov O., Landstreet J. D., 2013, A&A, 559, A103

Bailey J. D., Landstreet J. D., Bagnulo S., 2014, A&A, 561, A147

Baschek B., Holweger H., Traving G., 1966, Astronomische Abhandlungen der Hamburger Sternwarte, 8, 26

Bayer C., Maitzen H., Paunzen E., Rode-Paunzen M., Sperl M., 2000, A&AS, 147, 99

Bischof K. M., 2005, Memorie della Societa Astronomica Italiana Supplementi, 8, 64

Borra E. F., Landstreet J. D., 1980, ApJS, 42, 421

Borra E. F., Vaughan A. H., 1977, ApJ, 216, 462

Borra E. F., Fletcher J. M., Poeckert R., 1981, ApJ, 247, 569

Braithwaite J., Spruit H. C., 2004, Nature, 431, 819

Bressan A., Marigo P., Girardi L., Salasnich B., Dal Cero C., Rubele S., Nanni A., 2012, MNRAS, 427, 127

Brown B. P., Browning M. K., Brun A. S., Miesch M. S., Toomre J., 2010, ApJ, 711, 424

Bychkov V. D., Bychkova L. V., Madej J., 2005, A&A, 430, 1143

Calamai G., Landi Degl'Innocenti E., Landi Degl'Innocenti M., 1975, A&A, 45, 297

Carter B., Brown S., Donati J.-F., Rees D., Semel M., 1996, Publ. Astron. Soc. Australia, 13, 150

Castelli F., 2005, Memorie della Societa Astronomica Italiana Supplementi, 8, 25

Catalano F. A., Renson P., 1997, A&AS, 121

Chabrier G., Baraffe I., 1997, A&A, 327, 1039

Chandrasekhar S., 1935, MNRAS, 96, 21

Charbonneau P., 2014, Annual Review of Astronomy and Astrophysics, 52(1), 251

Chen Y., Girardi L., Bressan A., Marigo P., Barbieri M., Kong X., 2014, MNRAS, 444, 2525

Chen Y., Bressan A., Girardi L., Marigo P., Kong X., Lanza A., 2015, MNRAS, 452, 1068

Chmielewski Y., 1979, Spectres stellaires synthetiques : programmes de calcul Chmielewski.

Cowling T. G., 1945, MNRAS, 105, 166

Crutcher R., 1999, ApJ, 520, 706

Cunha M. S., 2007, Communications in Asteroseismology, 150, 48

Dappen W., Anderson L., Mihalas D., 1987, ApJ, 319, 195

Degl'Innocenti E., 2014, *UNITEXT for Physics*, Atomic Spectroscopy and Radiative Processes, Springer Milan

Dias W. S., Assafin M., Flório V., Alessi B. S., Líbero V., 2006, A&A, 446, 949

Donati J.-F., Brown S. F., 1997, A&A, 326, 1135

Donati J.-F., Collier Cameron A., 1997, MNRAS, 291, 1

Donati J.-F., Landstreet J. D., 2009, ARA&A, 47, 333

Donati J.-F., 2001, in Boffin H. M. J., Steeghs D., Cuypers J., eds, Astrotomography, Indirect Imaging Methods in Observational Astronomy, Lecture Notes in Physics, Berlin Springer Verlag Vol. 573, p. 207

Donati J.-F., Brown S. F., Semel M., Rees D. E., 1992, in Giampapa M. S., Bookbinder J. A., eds, Cool Stars, Stellar Systems, and the Sun, Astronomical Society of the Pacific Conference Series Vol. 26, p. 353

Donati J.-F., Catala C., Wade G. A., Gallou G., Delaigue G., Rabou P., 1999, A&AS, 134, 149

Donati J.-F., Gregory S. G., Alencar S. H. P., Hussain G., Bouvier J., Dougados C., Jardine M. M., Ménard F., Romanova M. M., 2012, MNRAS, 425, 2948

Faraggiana R., Gerbaldi M., 1993, in Dworetsky M. M., Castelli F., Faraggiana R., eds, IAU Colloq. 138: Peculiar versus Normal Phenomena in A-type and Related Stars, Astronomical Society of the Pacific Conference Series Vol. 44, p. 169

Feautrier P., 1964, C.R., 258, 3189

Feinstein C., Vergne M. M., Martínez R., Orsatti A. M., 2008, MNRAS, 391, 447

Fensl R. M., 1995, A&AS, 112, 191

Ferrario L., Wickramasinghe D. T., 2007, in Napiwotzki R., Burleigh M. R., eds, 15th European Workshop on White Dwarfs, Astronomical Society of the Pacific Conference Series Vol. 372, p. 163

Folsom C. P., Wade G. A., Bagnulo S., Landstreet J. D., 2007, MNRAS, 376, 361

Fossati L., Bagnulo S., Monier R., Khan S., Kochukhov O., Landstreet J., Wade G., Weiss W., 2007, A&A, 476, 911

Fossati L., Bagnulo S., Landstreet J., Wade G., O.Kochukhov, Monier R., Weiss W., Gebran M., 2008a, A&A, 483, 891

Fossati L., Bagnulo S., Landstreet J., Wade G., O.Kochukhov, Monier R., Weiss W., Gebran M., 2008b, Contr. Astron. Obser. Skalnate Pleso, 38, 123

Fossati L., Ryabchikova T., Bagnulo S., Alecian E., Grunhut J., Kochukhov O., Wade G., 2009, A&A, 503, 945

Fossati L., Mochnacki S., Landstreet J., Weiss W., 2010, A&A, 510, A8

Fossati L., Folsom C. P., Bagnulo S., Grunhut J. H., Kochukhov O., Landstreet J. D., Paladini C., Wade G. A., 2011a, MNRAS, 413, 1132

Fossati L., Ryabchikova T., Shulyak D. V., Haswell C. A., Elmasli A., Pandey C. P., Barnes T. G., Zwintz K., 2011b, MNRAS, 417, 495

Gebran M., Monier R., 2008, A&A, 483, 567

Gebran M., Vick M., Monier R., Fossati L., 2010, A&A, 523, 71

Gebran M., Monier R., Richard O., 2008, A&A, 479, 189

Glazunova L. V., Yushchenko A. V., Tsymbal V. V., Mkrtichian D. E., Lee J. J., Kang Y. W., Valyavin G. G., Lee B.-C., 2008, AJ, 136, 1736

Gompertz B., 1832, Phil. Trans. Roy. Soc. London, 123, 513

González-García B. M., Zapatero Osorio M. R., Béjar V. J. S., Bihain G., Barrado Y Navascués D., Caballero J. A., Morales-Calderón M., 2006, A&A, 460, 799

Gray D., 2005, The Observation and Analysis of Stellar Photospheres, Cambridge University Press

Gregory S. G., Donati J.-F., Morin J., Hussain G. A. J., Mayne N. J., Hillenbrand L. A., Jardine M., 2012, ApJ, 755, 97

Grunhut J. H., Wade G. A., Hanes D. A., Alecian E., 2010, MNRAS, 408, 2290

Grunhut J. H., Wade G. A., MiMeS Collaboration, 2012, in Hoffman J. L., Bjorkman J., Whitney B., eds, American Institute of Physics Conference Series, American Institute of Physics Conference Series Vol. 1429, p. 67

Hale G. E., 1908, PASP, 20, 220

Hale G. E., Ellerman F., Nicholson S. B., Joy A. H., 1919, ApJ, 49, 153

Hatzes A. P., Mkrtichian D. E., 2004, MNRAS, 351, 663

Hauck B., North P., 1982, A&A, 114, 23

Hauck B., North P., 1993, A&A, 269, 403

Heisenberg W., 1927, Zeitschrift für Physik, 43(3), 172

Henden A. A., Templeton M., Terrell D., Smith T. C., Levine S., Welch D., 2016, VizieR Online Data Catalog, 2336

Herbst W., 1977, AJ, 82, 902

Hog E., Fabricius C., Makarov V. V., Urban S., Corbin T., Wycoff G., Bastian U., Schwekendiek P., Wicenec A., 2000, A&A, 355, L27

Holland J. H., 1975, Adaptation in natural and artificial systems. an introductory analysis with applications to biology, control and artificial intelligence

Hubeny I., Lanz T., 1995, ApJ, 439, 875

Hubeny I., Mihalas D., 2014, Theory of Stellar Atmospheres

Hubeny I., Hummer D. G., Lanz T., 1994, A&A, 282, 151

Hubrig S., Briquet M., Schöller M., De Cat P., Mathys G., Aerts C., 2006, MNRAS, 369, L61

Hubrig S., Yudin R. V., Pogodin M., Schöller M., Peters G. J., 2007, Astronomische Nachrichten, 328, 1133

Hubrig S., Briquet M., De Cat P., Schöller M., Morel T., Ilyin I., 2009, Astronomische Nachrichten, 330, 317

Hubrig S., Ilyin I., Schöller M., Briquet M., Morel T., De Cat P., 2011, ApJ, 726, L5

Hui A. K., Armstrong B. H., Wray A. A., 1978, J. Quantit. Spectrosc. Radiat. Transfer, 19, 509

Hummer D. G., Mihalas D., 1988, ApJ, 331, 794

Hussain G. A. J., 2012, Astronomische Nachrichten, 333, 4

Hussain G. A. J., Collier Cameron A., Jardine M. M., Dunstone N., Ramirez Velez J., Stempels H. C., Donati J.-F., Semel M., Aulanier G., Harries T., Bouvier J., Dougados C., Ferreira J., Carter B. D., Lawson W. A., 2009, MNRAS, 398, 189

Johns-Krull C. M., 2007, ApJ, 664, 975

Jordan S., Bagnulo S., Werner K., O'Toole S. J., 2012, A&A, 542, A64

Jordan S., Werner K., O'Toole S. J., 2005, A&A, 432, 273

Kawka A., Vennes S., 2012, MNRAS, 425, 1394

Kepler S. O., Pelisoli I., Jordan S., Kleinman S. J., Koester D., Külebi B., Peçanha V., Castanheira B. G., Nitta A., Costa J. E. S., Winget D. E., Kanaan A., Fraga L., 2013, MNRAS, 429, 2934

Kharchenko N. V., Piskunov A. E., Schilbach E., Röser S., Scholz R.-D., 2013, A&A, 558, A53

Kılıçoğlu T., Monier R., Richer J., Fossati L., Albayrak B., 2016, AJ, 151, 49

Kochukhov O., Bagnulo S., 2006, A&A, 450, 763

Kochukhov O., Piskunov N., 2002, A&A, 388, 868

Kochukhov O., Wade G. A., 2007, A&A, 467, 679

Kochukhov O., Wade G. A., 2010, A&A, 513, A13

Kochukhov O., Landstreet J. D., Ryabchikova T., Weiss W. W., Kupka F., 2002, MNRAS, 337, L1

Kochukhov O., Bagnulo S., Wade G. A., Sangalli L., Piskunov N., Landstreet J. D., Petit P., Sigut T. A. A., 2004, A&A, 414, 613

Kochukhov O., Tsymbal V., Ryabchikova T., Makaganyk V., Bagnulo S., 2006, A&A, 460, 831

Kochukhov O., Makaganiuk V., Piskunov N., Jeffers S. V., Johns-Krull C. M., Keller C. U., Rodenhuis M., Snik F., Stempels H. C., Valenti J. A., 2013, A&A, 554, A61

Kochukhov O., Makaganiuk V., Piskunov N., 2010, A&A, 524, A5

Kochukhov O., Wade G. A., Shulyak D., 2012, MNRAS, 421, 3004

Kolenberg K., Bagnulo S., 2009, A&A, 498, 543

Konstantinova-Antova R., Aurière M., Charbonnel C., Drake N. A., Schröder K.-P., Stateva I., Alecian E., Petit P., Cabanac R., 2010, A&A, 524, A57

Konstantinova-Antova R., Aurière M., Petit P., Charbonnel C., Tsvetkova S., Lèbre A., Bogdanovski R., 2012, A&A, 541, A44

Kudryavtsev D. O., Romanyuk I. I., Elkin V. G., Paunzen E., 2006, MNRAS, 372, 1804

Kurtz D. W., Leone F., 2006, A&A, 458, 915

Kurtz D. W., Marang F., 1987, MNRAS, 229, 285

Kurtz D. W., 1981, Information Bulletin on Variable Stars, 1915

Kurtz D. W., 1982, MNRAS, 200, 807

Kurtz D. W., Cameron C., Cunha M. S., Dolez N., Vauclair G., Pallier E., Ulla A., Kepler S. O., da Costa A., Kanaan A., Fraga L., Giovannini O., Wood M. A., Silvestri N., Kawaler S. D., Riddle R. L., Reed M. D., Watson T. K., Metcalfe T. S., Mukadam A., Nather R. E., Winget D. E., Nitta A., Kleinman S. J., Guzik J. A., Bradley P. A., Matthews J. M., Sekiguchi K., Sullivan D. J., Sullivan T., Shobbrook R., Jiang X., Birch P. V., Ashoka B. N., Seetha S., Girish V., Joshi

S., Moskalik P., Zola S., O'Donoghue D., Handler G., Mueller M., Gonzalez Perez J. M., Solheim J.-E., Johannessen F., Bigot L., 2005, MNRAS, 358, 651

Kurucz R. L., 2005, Memorie della Societa Astronomica Italiana Supplementi, 8, 14

Landi Degl'Innocenti E., Landolfi M., Polarization in Spectral Lines, Springer Netherlands, Dordrecht, 2004

Landi Degl'Innocenti E., 1979, Sol. Phys., 63, 237

Landi Degl'Innocenti E., Bagnulo S., Fossati L., 2007, ASP Conf. Ser., 364, 495

Landolfi M., Landi Degl'Innocenti E., 1982, Sol. Phys., 78, 355

Landolfi M., Bagnulo S., Landi Degl'Innocenti M., 1998, A&A, 338, 111

Landstreet J. D., Borra E. F., 1978, ApJ, 224, L5

Landstreet J. D., Mathys G., 2000, A&A, 359, 213

Landstreet J. D., 1988, ApJ, 326, 967

Landstreet J. D., Barker P. K., Bohlender D. A., Jewison M. S., 1989, ApJ, 344, 876

Landstreet J. D., Bagnulo S., Andretta V., Fossati L., Mason E., Silaj J., Wade G. A., 2007, A&A, 470, 685

Landstreet J. D., Silaj J., Andretta V., Bagnulo S., Berdyugina S. V., Donati J.-F., Fossati L., Petit P., Silvester J., Wade G. A., 2008, A&A, 481, 465

Landstreet J. D., Bagnulo S., Fossati L., Jordan S., O'Toole S. J., 2012a, A&A, 541, A100

Landstreet J. D., Bagnulo S., Valyavin G. G., Fossati L., Jordan S., Monin D., Wade G. A., 2012b, A&A, 545, A30

Landstreet J. D., Bagnulo S., Valyavin G. G., Gadelshin D., Martin A. J., Galazutdinov G., Semenko E., 2015, A&A, 580, A120

Landstreet J. D., Bagnulo S., Martin A., Valyavin G., 2016, ArXiv e-prints

Langer N., Kudritzki R. P., 2014, A&A, 564, A52

Leone F., 2003, in Trujillo-Bueno J., Sanchez Almeida J., eds, Solar Polarization, Astronomical Society of the Pacific Conference Series Vol. 307, p. 51

Leone F., Martínez González M. J., Corradi R. L. M., Privitera G., Manso Sainz R., 2011, ApJ, 731, L33

Leone F., Corradi R. L. M., Martínez González M. J., Asensio Ramos A., Manso Sainz R., 2014, A&A, 563, A43

Leone F., Avila G., Bellassai G., Bruno P., Catalano S., Di Benedetto R., Di Stefano A., Gangi M., Giarrusso M., Greco V., Martinetti E., Miraglia M., Munari M., Pontoni C., Scalia C., Scuderi S., Spanó P., 2016, AJ, 151, 116

Levenberg K., 1944, Quart. Appl. Math., 2, 164

Livingston W., Harvey J. W., Malanushenko O. V., Webster L., 2006, Sol. Phys., 239, 41

Lüftinger T., Kochukhov O., Ryabchikova T., Piskunov N., Weiss W. W., Ilyin I., 2010, A&A, 509, A71

MacGregor K. B., Cassinelli J. P., 2003, ApJ, 586, 480

MacQueen J., 1967, Proceedings of the Fifth Berkeley Symposium on Mathematical Statistics and Probability, Volume 1: Statistics, University of California Press, p. 281, Berkeley, Calif.

Makaganiuk V., Kochukhov O., Piskunov N., Jeffers S. V., Johns-Krull C. M., Keller C. U., Rodenhuis M., Snik F., Stempels H. C., Valenti J. A., 2011, A&A, 525, A97

Marquardt D., 1963, Journal of the Society for Industrial and Applied Mathematics, 11, 431

Marsden S. C., Petit P., Jeffers S. V., Morin J., Fares R., Reiners A., do Nascimento J.-D., Aurière M., Bouvier J., Carter B. D., Catala C., Dintrans B., Donati J.-F., Gastine T., Jardine M., Konstantinova-Antova R., Lanoux J., Lignières F., Morgenthaler A., Ramìrez-Vèlez J. C., Théado S., Van Grootel V., BCool Collaboration, 2014, MNRAS, 444, 3517

Martin A. J., Stift M. J., Fossati L., Bagnulo S., Scalia C., Leone F., Smalley B., 2017, MNRAS, 466, 613

Mathys G., Lanz T., 1992, A&A, 256, 169

Mathys G., 1989, Fundamentals Cosmic Phys., 13, 143

Mathys G., 1991, A&AS, 89, 121

Mathys G., 1994, A&AS, 108

Mathys G., Hubrig S., Landstreet J. D., Lanz T., Manfroid J., 1997, A&AS, 123

Mathys G., Hubrig S., Mason E., Michaud G., Schöller M., Wesemael F., 2012, Astronomische Nachrichten, 333, 30

Mendigutía I., Calvet N., Montesinos B., Mora A., Muzerolle J., Eiroa C., Oudmaijer R. D., Merín B., 2011, A&A, 535, A99

Mestel L., 1999, Int. Ser. Monogr. Phys., Vol. 99,

Michaud G., 1970, ApJ, 160, 641

Michaud G., Alecian G., Richer J., 2015, Atomic Diffusion in Stars, Springer International Publishing

Michaud G., Charland Y., Megessier C., 1981, A&A, 103, 244

Moffat A., Vogt N., 1975, A&AS, 20, 155

Morin J., Donati J.-F., Petit P., Delfosse X., Forveille T., Jardine M. M., 2010, MNRAS, 407, 2269

Muzerolle J., Calvet N., Hartmann L., 1998, ApJ, 492, 743

O'Toole S. J., Jordan S., Friedrich S., Heber U., 2005, A&A, 437, 227

Paletou F., 2012, A&A, 544, A4

Parker E. N., 1979, ApJ, 230, 905

Pasquini L., et al., 2002, The Messenger, 110, 1

Pershan P. S., 1967, Journal of Applied Physics, 38(3)

Petit P., Donati J.-F., Aurière M., Landstreet J. D., Lignières F., Marsden S., Mouillet D., Paletou F., Toqué N., Wade G. A., 2005, MNRAS, 361, 837

Petit P., Lignières F., Wade G. A., Aurière M., Böhm T., Bagnulo S., Dintrans B., Fumel A., Grunhut J., Lanoux J., Morgenthaler A., Van Grootel V., 2010, A&A, 523, A41

Petit P., Van Grootel V., Bagnulo S., Charpinet S., Wade G. A., Green E. M., 2012, in Kilkenny D., Jeffery C. S., Koen C., eds, Fifth Meeting on Hot Subdwarf Stars and Related Objects, Astronomical Society of the Pacific Conference Series Vol. 452, p. 87

Piskunov N., Kochukhov O., 2002, A&A, 381, 736

Piskunov N., 1998, in Donahue R. A., Bookbinder J. A., eds, Cool Stars, Stellar Systems, and the Sun, Astronomical Society of the Pacific Conference Series Vol. 154, p. 2029

Piskunov N. E., Kupka F., Ryabchikova T. A., Weiss W. W., Jeffery C. S., 1995, A&AS, 112, 525

Piskunov N., Snik F., Dolgopolov A., Kochukhov O., Rodenhuis M., Valenti J., Jeffers S., Makaganiuk V., Johns-Krull C., Stempels E., Keller C., 2011, The Messenger, 143, 7

Press W. H., Teukolsky S. A., Vetterling W. T., Flannery B. P., 1992, Numerical recipes in C. The art of scientific computing

Preston T., 1898, Philosophical Magazine Series 5, 45(275), 325

Prsa A., Harmanec P., Torres G., Mamajek E., Asplund M., Capitaine N., Christensen-Dalsgaard J., Depagne E., Haberreiter M., Hekker S., Hilton J., Kopp G., Kostov V., Kurtz D. W., Laskar J., Mason B. D., Milone E. F., Montgomery M., Richards M., Schmutz W., Schou J., Stewart S. G., 2016, ArXiv e-prints

Rae A., 2008, Quantum mechanics, Taylor & Francis Group

Rees D. E., Durrant C. J., Murphy G. A., 1989, ApJ, 339, 1093

Reetz J. K., 1991, Diploma Thesis, Universitä München

Robichon N., Arenou F., Mermilliod J.-C., Turon C., 1999, A&A, 345, 471

Roeser S., Demleitner M., Schilbach E., 2010, AJ, 139, 2440

Rusomarov N., Kochukhov O., Ryabchikova T., Piskunov N., 2015, A&A, 573, A123

Ryabchikova T. A., Landstreet J. D., Gelbmann M. J., Bolgova G. T., Tsymbal V. V., Weiss W. W., 1997, A&A, 327, 1137

Ryabchikova T., Wade G. A., Aurière M., Bagnulo S., Donati J.-F., Jeffers S. V., Johnson N., Landstreet J. D., Lignières F., Lueftinger T., Marsden S., Mouillet D., Paletou F., Petit P., Reegen P., Silvester J., Strasser S., Toque N., 2005, A&A, 429, L55

Sanders W. L., 1971, A&A, 14, 226

Schwabe S. H., 1843, Astronomische Nachrichten, 21, 235

Seaton M. J., 1990, Bulletin of the American Astronomical Society, Bulletin of the American Astronomical Society Vol. 22, p. 844

Semel M., Li J., 1996, Sol. Phys., 164, 417

Semel M., 1967, Annales d'Astrophysique, 30, 513

Semel M., 1989, A&A, 225, 456

Shorlin S. L. S., Wade G. A., Donati J.-F., Landstreet J. D., Petit P., Sigut T. A. A., Strasser S., 2002, A&A, 392, 637

Shultz M., Wade G. A., Grunhut J., Bagnulo S., Landstreet J. D., Neiner C., Alecian E., Hanes D., MiMeS Collaboration, 2012, ApJ, 750, 2

Shultz M., Wade G. A., Petit V., Grunhut J., Neiner C., Hanes D., MiMeS Collaboration, 2014, MNRAS, 438, 1114

Shulyak D., Ryabchikova T., Mashonkina L., Kochukhov O., 2009, A&A, 499, 879

Silvester J., Wade G. A., Kochukhov O., Bagnulo S., Folsom C. P., Hanes D., 2012, MNRAS, 426, 1003

Skrutskie M. F., Cutri R. M., Stiening R., Weinberg M. D., Schneider S., Carpenter J. M., Beichman C., Capps R., Chester T., Elias J., Huchra J., Liebert J., Lonsdale C., Monet D. G., Price S., Seitzer P., Jarrett T., Kirkpatrick J. D., Gizis J. E., Howard E., Evans T., Fowler J., Fullmer L., Hurt R., Light R., Kopan E. L., Marsh K. A., McCallon H. L., Tam R., Van Dyk S., Wheelock S., 2006, AJ, 131, 1163

Snik F., Jeffers S., Keller C., Piskunov N., Kochukhov O., Valenti J., Johns-Krull C., 2008, Ground-based and Airborne Instrumentation for Astronomy II, Proc. SPIEVol. 7014, p. 70140O

Snik F., Kochukhov O., Piskunov N., Rodenhuis M., Jeffers S., Keller C., Dolgopolov A., Stempels E., Makaganiuk V., Valenti J., Johns-Krull C., 2011, in Kuhn J. R., Harrington D. M., Lin H., Berdyugina S. V., Trujillo-Bueno J., Keil S. L., Rimmele T., eds, Solar Polarization 6, Astronomical Society of the Pacific Conference Series Vol. 437, p. 237

Spiegel E. A., Zahn J.-P., 1992, A&A, 265, 106

Stibbs D. W. N., 1950, MNRAS, 110, 395

Stift M. J., Alecian G., 2012, MNRAS, 425, 2715

Stift M. J., 1975, MNRAS, 172, 133

Stift M. J., 1985, MNRAS, 217, 55

Stift M. J., 2000, A Peculiar Newsletter, 23, 27

Stift M. J., Leone F., Cowley C. R., 2012, MNRAS, 419, 2912

Stokes G. G., 1852, Philosophical Transactions of the Royal Society of London, 142, 463

Struve O., 1929, ApJ, 69, 173

Stütz C., Bagnulo S., Jehin E., Ledoux C., Cabanac R., Melo C., Smoker J. V., 2006, A&A, 451, 285

Swets D., Punch B., 1995, Unpublished

Tang J., Bressan A., Rosenfield P., Slemer A., Marigo P., Girardi L., Bianchi L., 2014, MNRAS, 445, 4287

Tipler P., Llewellyn R., 2003, Modern Physics, W. H. Freeman

Tokovinin A. A., 1985, A&AS, 61, 483

Unno W., 1956, PASJ, 8, 108

Valenti J. A., Piskunov N., 1996, A&AS, 118, 595

VanderNoot T., Abrahams I., 1998, Journal of Electroanalytical Chemistry, 448(1), 17

Vieira S. L. A., Corradi W. J. B., Alencar S. H. P., Mendes L. T. S., Torres C. A. O., Quast G. R., Guimarães M. M., da Silva L., 2003, AJ, 126, 2971

Villanova S., Carraro G., Saviane L., 2009, A&A, 504, 845

Vink J. S., Drew J. E., Harries T. J., Oudmaijer R. D., 2002, MNRAS, 337, 356

Vogt S. S., Penrod G. D., Hatzes A. P., 1987, ApJ, 321, 496

Vogt S. S., Tull R. G., Kelton P. W., 1980, ApJ, 236, 308

Wade G. A., Donati J.-F., Landstreet J. D., Shorlin S. L. S., 2000a, MNRAS, 313, 823

Wade G. A., Donati J.-F., Landstreet J. D., Shorlin S. L. S., 2000b, MNRAS, 313, 851

Wade G. A., Bagnulo S., Kochukhov O., Landstreet J. D., Piskunov N., Stift M. J., 2001, A&A, 374, 265

Wade G. A., Drouin D., Bagnulo S., Landstreet J. D., Mason E., Silvester J., Alecian E., Böhm T., Bouret J.-C., Catala C., Donati J.-F., 2005, A&A, 442, L31

Wade G. A., Bagnulo S., Drouin D., Landstreet J. D., Monin D., 2007, MNRAS, 376, 1145

Walborn N. R., 1972, AJ, 77, 312

Wittmann A., 1971, Sol. Phys., 20, 365

Zacharias N., Urban S. E., Zacharias M. I., Wycoff G. L., Hall D. M., Monet D. G., Rafferty T. J., 2005, AJ, 127, 3043

Zeeman P., 1897, ApJ, 5, 332